

AD-A124 365

AN EXPERIMENTAL STUDY OF THE DYNAMICS OF AN UNSTEADY  
TURBULENT BOUNDARY LAYER(U) STANFORD UNIV CA  
THERMOSCIENCES DIV R JAYARAMAN ET AL. DEC 82 TF-18

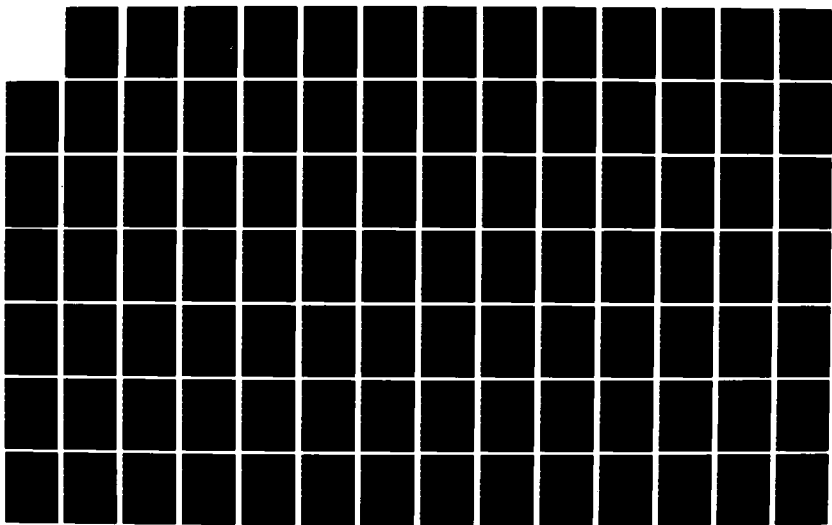
1/3

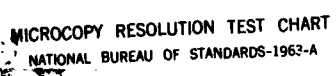
UNCLASSIFIED

ARO-16768. 2-EG ARO-1-80

.F/G 28/4

NL





DA 124365

# AN EXPERIMENTAL STUDY OF THE DYNAMICS OF AN UNSTEADY TURBULENT BOUNDARY LAYER

by

Rangarajan Jayaraman  
Pradip Parikh  
William C. Reynolds

Prepared under the joint support of

Army Research Office  
Aeromechanics Laboratory, RTL (AVRADCOM)  
NASA/Ames Research Center



Technical Report Number TF-18

Thermosciences Division  
Department of Mechanical Engineering  
Stanford University  
Stanford, California

December 1982

83 02 014 074

Unclassified

SECURITY CLASSIFICATION OF THIS PAGE (When Data Entered)

112

## REPORT DOCUMENTATION PAGE

READ INSTRUCTIONS  
BEFORE COMPLETING FORM

1. REPORT NUMBER 16760.2-EG		2. GOVT ACCESSION NO. AD-A224365	3. RECIPIENT'S CATALOG NUMBER 365
4. TITLE (and Subtitle) An Experimental Study of the Dynamics of an Unsteady Turbulent Boundary Layer		5. TYPE OF REPORT & PERIOD COVERED Final: 1 Oct 79 - 30 Sep 82	
7. AUTHOR(s) Rangarajan Jayaraman Pradip Parikh William C. Keynolds		6. PERFORMING ORG. REPORT NUMBER	
9. PERFORMING ORGANIZATION NAME AND ADDRESS Stanford University Stanford, CA		8. CONTRACT OR GRANT NUMBER(s) ARO 1-80; 2-81; 1-82	
11. CONTROLLING OFFICE NAME AND ADDRESS U. S. Army Research Office Post Office Box 12211 Research Triangle Park, NC 27709		10. PROGRAM ELEMENT, PROJECT, TASK AREA & WORK UNIT NUMBERS	
14. MONITORING AGENCY NAME & ADDRESS (if different from Controlling Office)		12. REPORT DATE Dec 82	
		13. NUMBER OF PAGES 208	
		15. SECURITY CLASS. (of this report) Unclassified	
		15a. DECLASSIFICATION/DOWNGRADING SCHEDULE	
16. DISTRIBUTION STATEMENT (of this Report) Approved for public release; distribution unlimited.			
17. DISTRIBUTION STATEMENT (of the abstract entered in Block 20, if different from Report) DTIC FEB 15 1983 H			
18. SUPPLEMENTARY NOTES The view, opinions, and/or findings contained in this report are those of the author(s) and should not be construed as an official Department of the Army position, policy, or decision, unless so designated by other documentation			
19. KEY WORDS (Continue on reverse side if necessary and identify by block number) turbulent boundary layers fluid dynamics free stream velocity			
20. ABSTRACT (Continue on reverse side if necessary and identify by block number) Turbulent boundary layers with a time-dependent free-stream velocity occur in many fluid dynamic devices. The main objectives of the present work are as follows: to understand the characteristics of a turbulent boundary layer that develops under steady, zero-pressure gradient conditions upstream, and is subjected to well-defined and sinusoidally varying adverse free-stream gradient downstream, and to provide a definitive data set that would serve as a test case for evaluating the performance of calculation procedures and turbulence models for such flows.			

AD-A 124365

DTIC FILE COPY

DD FORM 1 JAN 73 1473 EDITION OF 1 NOV 65 IS OBSOLETE

UNCLASSIFIED

SECURITY CLASSIFICATION OF THIS PAGE (When Data Entered)

**AN EXPERIMENTAL STUDY OF THE DYNAMICS  
OF AN UNSTEADY TURBULENT BOUNDARY LAYER**

**by**

**Rangarajan Jayaraman  
Pradip Parikh  
William C. Reynolds**

**Prepared under the joint support of**

**Army Research Office  
Aeromechanics Laboratory, RTL (AVRADCOM)  
NASA/Ames Research Center**

**Technical Report No. TF-18**

**Thermosciences Division  
Department of Mechanical Engineering  
Stanford University  
Stanford, California 94305**

**December 1982**

## Acknowledgments

We gratefully acknowledge the continued sponsorship of the Army Aeromechanics Laboratory, NASA-Ames Research Center, and the Army Research Office. Dr. Larry Carr of the Army Research Office attended all our weekly meetings and provided us with many valuable suggestions. We thank Dr. Carr and Prof. Stephen Kline for carefully reviewing the manuscript and suggesting many improvements.

Messrs. Robin Birch, Tots Ikebe, and Roy Niegel provided excellent shop support throughout this work. Mrs. Ruth Korb has done an outstanding job with all phases of the preparation of this report. Her efforts and editorial expertise are very much appreciated.

Accession For	
NTIS GRA&I	<input checked="checked" type="checkbox"/>
DTIC TAB	<input type="checkbox"/>
Unannounced	<input type="checkbox"/>
Justification	
By _____	
Distribution/	
Availability Codes	
Dist	Avail and/or Special
A	



## Abstract

Turbulent boundary layers with a time-dependent free-stream velocity occur in many fluid dynamic devices. The main objectives of the present work are as follows:

- to understand the characteristics of a turbulent boundary layer that develops under steady, zero-pressure gradient conditions upstream, and is subjected to well-defined and sinusoidally varying adverse free-stream gradient downstream, and
- to provide a definitive data set that would serve as a test case for evaluating the performance of calculation procedures and turbulence models for such flows.

The experiments were done in a unique closed-loop water channel especially constructed for the study. A single-color, forward-scatter, frequency-shifted, Laser-Doppler Anemometer system was used with a frequency tracker to measure the streamwise component of velocity. A laboratory microcomputer system was set up to control the experiment and automate the data-acquisition process. Two major series of experiments with relative amplitudes (of free-stream oscillations at the end of the test section) of about 5% and 25% were done. Several frequencies and  $X$  stations were covered in each, to provide a wide range in Strouhal number ( $0.04 < S_x < 1.6$ ). Phase-averaged streamwise velocity and square of streamwise turbulent fluctuations were measured; from these, other quantities of interest were computed.

The results show that the time-averaged velocity and turbulence are insensitive to the imposed unsteadiness, while the periodic components are very strongly affected by the frequency. The periodic velocity field exhibits two distinct regimes of behavior with respect to the Strouhal number ( $S_x$ , based on the local mean free-stream velocity and the streamwise distance in the test section). For  $S_x < 1$ , the flow is primarily governed by inertia, while for  $S_x > 1$ , the flow is dominated by increasing pressure-gradient oscillations that overcome inertia. The high Strouhal number results agree quite well with the Stokes solution. The steady form of the law of the wall seems to be inapplicable to the phase-averaged velocity profiles at high frequencies. Over the range of frequencies and amplitudes studied, there seem to be no dramatic interactions between the organized oscillations and the disorganized turbulent fluctuations.

# Table of Contents

	Page
Acknowledgments . . . . .	iii
Abstract . . . . .	iv
List of Figures . . . . .	vii
List of Tables . . . . .	xii
Nomenclature . . . . .	xiii
Chapter	
1 INTRODUCTION . . . . .	1
1.1 General . . . . .	1
1.2 Previous Work . . . . .	1
1.3 Summary of Previous Research and Unanswered Questions . . . . .	6
1.4 Data Requirements in Unsteady Turbulent Boundary Layers . . . . .	7
1.5 Objectives . . . . .	9
1.6 Summary of Present Work . . . . .	9
2 THEORETICAL BACKGROUND . . . . .	11
2.1 Triple Decomposition . . . . .	11
2.2 Averaging . . . . .	11
2.3 Fourier Analysis . . . . .	13
2.4 Governing Equations . . . . .	14
2.5 Simplification of Governing Equations . . . . .	17
2.5.1 Primary Estimates . . . . .	17
2.5.2 Analysis of Continuity Equations . . . . .	19
2.5.3 Analysis of Mean Momentum Equations . . . . .	20
2.5.4 Analysis of Periodic Momentum Equations . . . . .	22
3 EXPERIMENTAL SETUP AND PROCEDURES . . . . .	29
3.1 Apparatus . . . . .	29
3.1.1 Design Objective . . . . .	29
3.1.2 Stanford Unsteady Turbulent Boundary Layer Research Water Channel . . . . .	30
3.1.3 Oscillation Mechanism . . . . .	33
3.1.4 Water Treatment and Control . . . . .	34
3.1.5 LDA Mount . . . . .	35
3.2 Data-Acquisition and Control System . . . . .	35
3.2.1 Laboratory Computer System . . . . .	36
3.2.2 Laser Doppler Anemometer System . . . . .	36
3.2.3 Shaft Encoder System . . . . .	37
3.2.4 LDA Mount Traverse System . . . . .	38
3.2.5 Pressure Measurement System . . . . .	38
3.3 Data-Acquisition and Control Procedures . . . . .	39
3.3.1 LDA Probe Volume Positioning . . . . .	39
3.3.2 Frequency Control . . . . .	39
3.3.3 LDA Calibration . . . . .	40
3.3.4 Experimental Run Procedures . . . . .	41
3.4 Data-Reduction Procedure . . . . .	42



<b>4</b>	<b>EXPERIMENTAL RESULTS . . . . .</b>	<b>43</b>
4.1	General Considerations . . . . .	44
4.1.1	Number of Cycles . . . . .	44
4.1.2	Zero Frequency Measurements . . . . .	44
4.1.3	Very Near-Wall Data Restrictions . . . . .	45
4.1.4	Estimated Uncertainties . . . . .	45
4.2	Flow Qualification . . . . .	46
4.2.1	Spanwise Uniformity . . . . .	46
4.2.2	Zero Pressure Gradient Boundary Layer Development . . . . .	47
4.2.3	Upstream Disturbance . . . . .	49
4.3	Imposed Free-Stream Excitation in Test Section . . . . .	50
4.4	Mean Velocity and Turbulence . . . . .	51
4.5	Periodic Velocity . . . . .	52
4.5.1	Amplitude . . . . .	52
4.5.2	Phase . . . . .	53
4.6	Periodic Turbulence . . . . .	54
4.6.1	Amplitude . . . . .	54
4.6.2	Phase . . . . .	55
4.7	Phase-Averaged Velocity Profiles . . . . .	55
4.8	Phase-Averaged Turbulence Profiles . . . . .	56
4.9	Computed Quantities . . . . .	57
4.10	Summary of Results . . . . .	58
<b>5</b>	<b>DISCUSSION . . . . .</b>	<b>59</b>
5.1	Mean Velocity and Turbulence . . . . .	59
5.2	Behavior of Design Pressure Gradient . . . . .	60
5.3	Flow Regimes . . . . .	63
5.4	Importance of Strouhal Number: Behavior of Displace- ment Thickness. . . . .	64
5.5	High Strouhal Number Behavior . . . . .	65
5.6	Expected Wall Shear-Stress Behavior . . . . .	67
5.7	Log Linear Region . . . . .	72
5.8	Periodic Turbulence . . . . .	74
<b>6</b>	<b>CONCLUSIONS AND RECOMMENDATIONS . . . . .</b>	<b>77</b>
6.1	Conclusions . . . . .	77
6.2	Recommendations for Future Work . . . . .	78
	<b>References . . . . .</b>	<b>79</b>
	<b>Tables . . . . .</b>	<b>83</b>
	<b>Figures . . . . .</b>	<b>87</b>
	<b>Appendices . . . . .</b>	<b>181</b>

## List of Figures

Figure	Page
3.1. Desired free-stream velocity variation . . . . .	87
3.2. Schematic of the water channel . . . . .	87
3.3. Data-acquisition and control system . . . . .	88
3.4. MINC microcomputer system . . . . .	89
4.1. Spanwise uniformity: $X' = 0.94$ , $f = 1.0$ Hz, $Y/\delta = 0.2$ .	
a) Low amplitude: Mean velocity . . . . .	90
b) Low amplitude: Mean turbulence . . . . .	90
c) Low amplitude: First harmonic velocity amplitude . . . . .	91
d) Low amplitude: First harmonic velocity phase . . . . .	91
e) High amplitude: Mean velocity . . . . .	92
f) High amplitude: Mean turbulence . . . . .	92
g) High amplitude: First harmonic velocity amplitude . . . . .	93
h) High amplitude: First harmonic velocity phase . . . . .	93
4.2. Zero-pressure gradient: Free-stream velocity variation . . . . .	94
4.3. Zero-pressure gradient: Mean velocity profile development upstream . . . . .	95
4.4. Zero-pressure gradient:	
a) Coles boundary layer thickness development . . . . .	96
b) Displacement thickness development . . . . .	96
4.5. Zero-pressure gradient: Skin-friction coefficient development . . . . .	97
4.6. Defect velocity profile at $X' = -0.36$ : Comparison to Klebanoff . . . . .	98
4.7. Mean turbulence profile at $X' = -0.36$ : Comparison to Klebanoff . . . . .	98
4.7.1 Zero-pressure gradient: Momentum balance . . . . .	99
4.8. Rms upstream disturbance: High amplitude . . . . .	100
4.9. Unsteady upstream mean velocity profiles, High amplitude . . . . .	101
4.10. Unsteady upstream mean turbulence profiles, High amplitude . . . . .	102
4.11. Imposed free-stream mean velocity in test section:	
a) Low amplitude . . . . .	103
b) High amplitude . . . . .	104

4.12.	Imposed free-stream amplitude in test section:	
a)	Low amplitude . . . . .	105
b)	High amplitude . . . . .	106
4.13.	Imposed free-stream phase in test section:	
a)	Low amplitude . . . . .	107
b)	High amplitude . . . . .	108
4.14.	Phase-averaged free stream in test section: $f = 0.5$ Hz, High amplitude.	
a)	0, 15, 30, 45, 60, 75° . . . . .	109
b)	90, 105, 120, 135, 150, 165° . . . . .	109
c)	180, 195, 210, 225, 240, 255° . . . . .	110
d)	270, 285, 300, 315, 330, 345° . . . . .	110
4.15.	Phase-averaged free stream in test section: $f = 0.5$ Hz, Low amplitude.	
a)	0, 15, 30, 45, 60, 75° . . . . .	111
b)	90, 105, 120, 135, 150, 165° . . . . .	111
c)	180, 195, 210, 225, 240, 255° . . . . .	112
d)	270, 285, 300, 315, 330, 345° . . . . .	112
4.16.	Unsteady mean velocity profiles in test section:	
a)	Low amplitude: $X' = 0.88$ , $f = 0.1, 0.2, 0.5, 1.0,$ 2.0 Hz . . . . .	113
b)	High amplitude: $X' = 0.94$ , $f = 0.1, 0.2, 0.5, 1.0,$ 2.0 Hz . . . . .	114
4.17.	Unsteady mean turbulence profiles in test section:	
a)	Low amplitude: $X' = 0.88$ , $f = 0.1, 0.2, 0.5, 1.0,$ 2.0 Hz . . . . .	115
b)	High amplitude: $X' = 0.94$ , $f = 0.1, 0.2, 0.5, 1.0,$ 2.0 Hz . . . . .	116
4.18.	First harmonic velocity amplitude profiles in test section:	
a)	Low amplitude: $X' = 0.88$ , $f = 0.1, 0.2, 0.5, 1.0,$ 2.0 Hz . . . . .	117
b)	High amplitude: $X' = 0.94$ , $f = 0.1, 0.2, 0.5, 1.0,$ 2.0 Hz . . . . .	118
4.19.	First harmonic velocity phase profiles in test section:	
a)	Low amplitude: $X' = 0.88$ , $f = 0.1, 0.2, 0.5, 1.0,$ 2.0 Hz . . . . .	119
b)	High amplitude: $X' = 0.94$ , $f = 0.1, 0.2, 0.5, 1.0,$ 2.0 Hz . . . . .	120
4.20.	First harmonic turbulence amplitude profiles in test section:	
a)	Low amplitude: $X' = 0.88$ , $f = 0.1, 0.2, 0.5, 1.0,$ 2.0 Hz . . . . .	121
b)	High amplitude: $X' = 0.94$ , $f = 0.1, 0.2, 0.5, 1.0,$ 2.0 Hz . . . . .	122

4.21.	First harmonic turbulence phase profiles in test section:	
a)	Low amplitude: $X' = 0.88$ , $f = 0.1, 0.2, 0.5, 1.0,$	
	2.0 Hz . . . . .	123
b)	High amplitude: $X' = 0.94$ , $f = 0.1, 0.2, 0.5, 1.0,$	
	2.0 Hz . . . . .	124
4.22.	Phase-averaged velocity profiles in test section: Low	
	amplitude, $X' = 0.88$ , $f = 0.2$ Hz.	
a)	0, 15, 30, 45, 60, 75° . . . . .	125
b)	90, 105, 120, 135, 150, 165° . . . . .	125
c)	180, 195, 210, 225, 240, 255° . . . . .	126
d)	270, 285, 300, 315, 330, 345° . . . . .	126
4.23.	Phase-averaged velocity profiles in test section: Low	
	amplitude, $X' = 0.88$ , $f = 0.5$ Hz.	
a)	0, 15, 30, 45, 60, 75° . . . . .	127
b)	90, 105, 120, 135, 150, 165° . . . . .	127
c)	180, 195, 210, 225, 240, 255° . . . . .	128
d)	270, 285, 300, 315, 330, 345° . . . . .	128
4.24.	Phase-averaged velocity profiles in test section: Low	
	amplitude, $X' = 0.88$ , $f = 2.0$ Hz.	
a)	0, 15, 30, 45, 60, 75° . . . . .	129
b)	90, 105, 120, 135, 150, 165° . . . . .	129
c)	180, 195, 210, 225, 240, 255° . . . . .	130
d)	270, 285, 300, 315, 330, 345° . . . . .	130
4.25.	Phase-averaged velocity profiles in test section: High	
	amplitude, $X' = 0.94$ , $f = 0.2$ Hz.	
a)	0, 15, 30, 45, 60, 75° . . . . .	131
b)	90, 105, 120, 135, 150, 165° . . . . .	131
c)	180, 195, 210, 225, 240, 255° . . . . .	132
d)	270, 285, 300, 315, 330, 345° . . . . .	132
4.26.	Phase-averaged velocity profiles in test section: High	
	amplitude, $X' = 0.94$ , $f = 0.5$ Hz.	
a)	0, 15, 30, 45, 60, 75° . . . . .	133
b)	90, 105, 120, 135, 150, 165° . . . . .	133
c)	180, 195, 210, 225, 240, 255° . . . . .	134
d)	270, 285, 300, 315, 330, 345° . . . . .	134
4.27.	Phase-averaged velocity profiles in test section: High	
	amplitude, $X' = 0.94$ , $f = 2.0$ Hz.	
a)	0, 15, 30, 45, 60, 75° . . . . .	135
b)	90, 105, 120, 135, 150, 165° . . . . .	135
c)	180, 195, 210, 225, 240, 255° . . . . .	136
d)	270, 285, 300, 315, 330, 345° . . . . .	136
4.28.	Phase-averaged turbulence profiles in test section: Low	
	amplitude, $X' = 0.83$ , $f = 0.2$ Hz.	
a)	0, 15, 30° . . . . .	137
b)	45, 60, 75° . . . . .	137
c)	90, 105, 120° . . . . .	138
d)	135, 150, 165° . . . . .	138

e)	180, 195, 210°	139
f)	225, 240, 255°	139
g)	270, 285, 300°	140
h)	315, 330, 345°	140

4.29. Phase-averaged turbulence profiles in test section: Low amplitude,  $X' = 0.88$ ,  $f = 0.5$  Hz.

a)	0, 15, 30°	141
b)	45, 60, 75°	141
c)	90, 105, 120°	142
d)	135, 150, 165°	142
e)	180, 195, 210°	143
f)	225, 240, 255°	143
g)	270, 285, 300°	144
h)	315, 330, 345°	144

4.30. Phase-averaged turbulence profiles in test section: Low amplitude,  $X' = 0.88$ ,  $f = 2.0$  Hz.

a)	0, 15, 30°	145
b)	45, 60, 75°	145
c)	90, 105, 120°	146
d)	135, 150, 165°	146
e)	180, 195, 210°	147
f)	225, 240, 255°	147
g)	270, 285, 300°	148
h)	315, 330, 345°	148

4.31. Phase-averaged turbulence profiles in test section: High amplitude,  $X' = 0.94$ ,  $f = 0.2$  Hz.

a)	0, 15, 30°	149
b)	45, 60, 75°	149
c)	90, 105, 120°	150
d)	135, 150, 165°	150
e)	180, 195, 210°	151
f)	225, 240, 255°	151
g)	270, 285, 300°	152
h)	315, 330, 345°	152

4.32. Phase-averaged turbulence profiles in test section: High amplitude,  $X' = 0.94$ ,  $f = 0.5$  Hz.

a)	0, 15, 30°	153
b)	45, 60, 75°	153
c)	90, 105, 120°	154
d)	135, 150, 165°	154
e)	180, 195, 210°	155
f)	225, 240, 255°	155
g)	270, 285, 300°	156
h)	315, 330, 345°	156

4.33. Phase-averaged turbulence profiles in test section: High amplitude,  $X' = 0.94$ ,  $f = 2.0$  Hz.

a)	0, 15, 30°	157
b)	45, 60, 75°	157
c)	90, 105, 120°	158

d)	135, 150, 165°	158
e)	180, 195, 210°	159
f)	225, 240, 255°	159
g)	270, 285, 300°	160
h)	315, 330, 345°	160
4.34.	Computed shape factor and thicknesses in test section: Low amplitude, $X' = 0.88$ .	
a)	$f = 0.1$ Hz	161
b)	$f = 0.2$ Hz	162
c)	$f = 0.5$ Hz	163
d)	$f = 1.0$ Hz	164
e)	$f = 2.0$ Hz	165
4.35.	Computed shape factor and thicknesses in test section: High amplitude, $X' = 0.94$ .	
a)	$f = 0.1$ Hz	166
b)	$f = 0.2$ Hz	167
c)	$f = 0.5$ Hz	168
d)	$f = 1.0$ Hz	169
e)	$f = 2.0$ Hz	170
5.1.	Behavior of design pressure gradient: First harmonic amplitude	171
5.2.	Behavior of design pressure gradient: First harmonic phase	172
5.3.	Behavior of design pressure gradient: Second harmonic amplitude	173
5.4.	Displacement thickness: First harmonic amplitude	174
5.5.	Displacement thickness: First harmonic phase	175
5.6.	High Strouhal number behavior: Stokes layer amplitude	176
5.7.	High Strouhal number behavior: Stokes layer phase	177
5.8.	First harmonic velocity amplitude in test section: $X' = 0.94$ , $f = 0.1, 0.2, 0.5, 1.0, 2.0$ Hz	178
5.9.	Wall shear amplitude (expected)	179
5.10.	Wall shear phase (expected)	180

## List of Tables

Table	Page
1.1 Experimental Flow Parameters . . . . .	83
2.1 Simplified Governing Equations . . . . .	84
4.1 High-Amplitude Experimental Cases . . . . .	85
4.2 Low-Amplitude Experimental Cases . . . . .	85
4.3 Estimated N <sup>th</sup> -Order Uncertainties . . . . .	86
A.1 Contents of Microfiche 1 . . . . .	182
A.2 Types of Plots . . . . .	183
A.3 Types of Tables . . . . .	184
A.4 Nomenclature Used in Tables . . . . .	185
A.5 Identification of Groups of Experimental Cases . . . . .	186
A.6 Plot Locations . . . . .	187
A.7 Table Locations . . . . .	188

# Nomenclature

$A$	First harmonic amplitude of free-stream velocity oscillations; used in order-of-magnitude analysis.
$A_{n,f}$	$n^{\text{th}}$ harmonic amplitude of variable $f$ , unless noted otherwise.
$A_{1,D1}$	First harmonic amplitude of $\langle \delta_1 \rangle$ ; used in plots.
$A_{1,U}$	$= A_{1,u}$ ; used in plots.
$A_{1,UE}$ $A_{1,Ue}$	$= A_{1,Ue}$ ; used in plots.
$A_{1,U'U'}$	$= A_{1,u'u'}$ ; used in plots.
$A_{1,u_\tau}$	First harmonic amplitude of $\langle u_\tau \rangle$ .
$a$	$= A_{1,Ue}/U_0$ evaluated at $X' = 1$ ; first harmonic amplitude of free-stream velocity at the end of the test section normalized by the mean free-stream velocity at the entrance to the test section.
$C$	$= 5.0$ ; constant in log law of the wall.
$C_F$	$= C_f$ ; used in plots.
$C_p$	$= C_p$ ; used in plots.
$C_f$	$= 2\tau_w/\rho U_e^2$ ; skin-friction coefficient of the mean velocity profile determined by Coles analysis procedure; not an instantaneous quantity.
$C_p$	$= 2(p-p_0)/\rho U_0^2$ ; coefficient of pressure.
$C_{ps}$	$= 2(p_s-p_0)/\rho U_0^2$ ; steady static pressure coefficient.
$D_c$	$= \delta$ ; used in plots.
$\overline{D}_c$	$= D_c$ ; not a time average.
$\overline{D}_{99}$	Mean value of $\langle \delta_{99} \rangle$ ; used in plots.
$D_1$	$= \delta_1$ ; used in plots.
$\overline{D}_1$	Mean value of $\langle \delta_1 \rangle$ ; used in plots.
$D_2$	$= \delta_2$ ; used in plots.
$\langle D_{99} \rangle$	$= \langle \delta_{99} \rangle$ ; used in plots.



$\langle D_1 \rangle$  =  $\langle \delta_1 \rangle$ ; used in plots.  
 $\langle D_2 \rangle$  =  $\langle \delta_2 \rangle$ ; used in plots.  
 $f$  Frequency in Hz; also any flow variable.  
 $G$  =  $dC_p/dx'$ ; normalized streamwise gradient of coefficient of pressure.  
 $H$  Shape factor of the mean velocity profile; not an instantaneous quantity.  
 $\langle H \rangle$  Shape factor computed from phase-averaged velocity profiles; not a phase-averaged quantity; used in plots.  
 $\bar{H}$  Mean value of  $\langle H \rangle$ ; used in plots.  
 $i$  Index in subscript notation.  
 $j$  Pure imaginary number; also used as a second index in subscript notation.  
 $L$  Length of the test section, 61 cm; also typical streamwise length scale used in order-of-magnitude analysis.  
 $L_S$  =  $\lambda_S$ ; used in plots.  
 $PL$  Left-hand side of normalized momentum integral equation.  
 $P_L$  =  $\phi_{1,U_e}$  at the last measured  $x$  station in recovery section; used in plots.  
 $P_{1,dCp/dx'}$  =  $\phi_{1,dC_p/dx'}$ ; used in plots.  
 $P_{1,D1}$  First harmonic phase of  $\langle \delta_1 \rangle$ ; used in plots.  
 $P_{1,U}$  =  $\phi_{1,u}$ ; used in plots.  
 $\left. \begin{matrix} P_{1,UE} \\ P_{1,Ue} \end{matrix} \right\}$  =  $\phi_{1,U_e}$ ; used in plots.  
 $P_{1,U'U'}$  =  $\phi_{1,u'u'}$ ; used in plots.  
 $PR$  Right-hand side of normalized momentum integral equation.  
 $p$  Instantaneous static pressure.  
 $P_0$  Reference static pressure at the entrance to the test section.  
 $P_S$  Steady static pressure

$Re_{D2}$	$= \bar{U}_e \delta_2 / \nu$ ; momentum thickness Reynolds number for mean velocity profile; used in plots.
$S$	$= \omega L / \bar{U}_e$ ; Strouhal number used in order-of-magnitude analysis based on the typical length scale in the streamwise direction and the mean free-stream velocity.
$S_\delta$	$= \omega \delta / \bar{U}_e$ ; Strouhal number based on local values of the thickness of the mean boundary layer and the free-stream mean velocity.
$S_x$	$= \omega (X - X_0) / \bar{U}_e$ ; Strouhal number based on the streamwise distance in the test section at the measuring station and the local mean free-stream velocity.
$t$	Time.
$t_i$	Discrete times at which a variable is sampled.
$\bar{U}$	$= \bar{u}$ ; time average of streamwise velocity.
$U_e$	$= \bar{U}_e$ ; used in order-of-magnitude analysis.
$U_0$	Uniform mean free-stream velocity in the upstream development section; approximately 730 mm/s.
$U^+$	$= \bar{U} / u_\tau$ .
$U'U'$	$= u'u'$ ; used in plots.
$U^*$	$= u_\tau$ ; used in plots.
$\tilde{U}$	$= \tilde{u}$ ; used in plots.
$\langle U \rangle$	$= \langle u \rangle$ .
$u$	Instantaneous streamwise component of velocity.
$u_i$	$i = 1, 2, 3$ ; components of the velocity vector in subscript notation.
$u_\tau$	Wall shear velocity of the mean velocity profile computed by Coles analysis procedure; not an instantaneous quantity.
$\langle u_\tau \rangle$	"Wall shear velocity" parameter used in the log-linear region analysis; not necessarily related to the phase-averaged wall shear stress.
$\bar{V}$	$= \bar{v}$ ; time average of normal-to-wall velocity.
$v$	Instantaneous normal-to-wall component of velocity.

$W$	Channel width, 30.48 cm.
$w$	Spanwise component of velocity.
$X$	Streamwise distance in the experimental rig measured with respect to the nozzle exit.
$X_0$	Streamwise distance of the entrance to the test section with respect to the nozzle exit, 205.1 cm.
$X'$	$= (X - X_0)/L$ ; streamwise distance of the measuring station with respect to the entrance to the test section normalized by the test-section length.
$x$	$= X$ .
$\underline{x}$	Position vector in 3D space.
$x_i$	$i = 1, 2, 3$ ; components of the position vector in subscript notation.
$Y$	Normal-to-wall distance in the experimental rig measured with respect to the wall.
$Y^+$	$= y u_\tau / \nu$ .
$y_s$	$= y / \delta_s$ ; normal-to-wall distance normalized by Stokes layer thickness parameter.
$y$	$= Y$ .
$Z$	Spanwise distance in the experimental rig measured with respect to the centerline of the channel.
$z$	$= Z$ .

#### Greek Symbols

$\alpha$	$= A/U_e$ ; first harmonic amplitude of free-stream velocity normalized by the mean free-stream velocity; used in order-of-magnitude analysis.
$\delta$	Thickness of the mean velocity profile; usually determined by Coles analysis procedure (see Coles [1968]).
$\delta f_N$	$N^{\text{th}}$ -order uncertainty in variable $f$ .
$\langle \delta_{99} \rangle$	99% thickness computed from phase-averaged velocity profiles; not a phase-averaged quantity.

$\delta_1$	Displacement thickness of the mean velocity profile; not an instantaneous quantity.
$\langle \delta_1 \rangle$	Displacement thickness computed from phase-averaged velocity profiles.
$\delta'$	Typical length scale in the normal-to-wall direction for periodic quantities used in the order-of-magnitude analysis; not a turbulent quantity.
$\delta_2$	Momentum thickness of the mean velocity profile; not an instantaneous quantity.
$\langle \delta_2 \rangle$	Momentum thickness computed from phase-averaged velocity profiles; not a phase-averaged quantity.
$e^2$	Multiplicative factor used in order-of-magnitude analysis.
$\gamma$	$= \left( \frac{A_{1,\tau_w}}{\bar{\tau}_w} \right) \left( \frac{A_{1,U_e}}{\bar{U}_e} \right)^{-1} \left( \frac{C_f}{2} \right) \left( \frac{\bar{U}_e (x-x_0)}{v} \right)^{1/2}$
$\kappa$	Von-Karman constant used in log law of the wall, 0.41.
$l_s$	$= \sqrt{\frac{2\nu}{\omega}}$ ; Stokes layer thickness parameter.
$\nu$	Kinematic viscosity.
$\omega$	Circular frequency in radians/sec.
$\phi_{n,f}$	Phase of $n^{\text{th}}$ harmonic component of periodic variable $f$ .
$\phi_{1,u_\tau}$	First harmonic phase of $\langle u_\tau \rangle$ .
$\rho$	Density.
$\tau$	$= 2\pi/\omega$ ; time period of imposed excitation.
$\tau_w$	Wall shear stress.
$\theta$	Cycle phase angle.

#### Special Symbols and Usage

$A_{n,f}$	$n^{\text{th}}$ harmonic amplitude of variable $f$ unless noted otherwise.
$\phi_{n,f}$	Phase of $n^{\text{th}}$ harmonic component of periodic variable $f$ unless noted otherwise.
—	Used over a variable denotes its time average, unless noted otherwise.

- ~      Used over a variable denotes its periodic component.
- ~      Used after a variable denotes its typical value of order-of-magnitude accuracy.
- '      Used as a superscript to a variable denotes its turbulent component unless noted otherwise.
- e,E    Used as a subscript to a variable denotes its free-stream value.
- Used under a variable denotes that it is a vector.
- Δ      Used before a variable denotes changes in that variable.
- < >    Used around a variable denotes its phase average unless noted otherwise.
- rms    Used as a subscript to a variable denotes its root-mean-squared value.

## Chapter 1

### INTRODUCTION

#### 1.1 General

Turbulent boundary layers with a time-dependent (unsteady) free-stream velocity occur in many fluid dynamic devices. Examples of such flows are flow over the blades of a helicopter in forward flight, flow over the wings of an accelerating aircraft, and flow over the stator blades downstream of a rotary stage in a turbomachine.

The work described in this report deals with an experimental study of the dynamics of a turbulent boundary layer subjected to an oscillatory, mean adverse, free-stream velocity gradient. It is part of an ongoing research program at Stanford investigating the effects on turbulence of imposed organized unsteadiness.

There are two major objectives for the present study. First, the work seeks to provide an understanding of the physics of unsteady turbulent boundary layers. Second, the experiments are intended to provide a definitive data base for the evaluation and development of turbulence models for such flows.

To provide further motivation and background for the present work, a brief review of previous research which is believed to be most relevant is given in the next section.

#### 1.2 Previous Work

Table 1.1 is a summary of important parameters and pertinent information from several of the experiments reviewed below. Experiments on unsteady, fully developed channel and pipe flows are also included, since the near-wall turbulence structure in such flows is similar to the turbulent boundary layer.

Two important parameters included in the table are an amplitude parameter which is the free-stream oscillation amplitude normalized by the mean free-stream velocity ( $\alpha$ ) and a frequency parameter in the form of a Strouhal number based on the boundary layer thickness and the mean free-stream velocity ( $S_\delta$ ). For fully developed pipe flows, the

radius, and, for fully developed channel flows, the channel half-gap are used in place of the boundary layer thickness; the mean centerline velocity is used in place of the mean free-stream velocity. Some of the parameters had to be obtained from very small plots in poorly reproduced reports, and hence could have substantial errors.

In the following chronological review, no direct quantitative comparison of any two of these experiments will be attempted. Such an attempt is precluded by the variety of different flow parameters and excitations involved. Only qualitative consensus on the response to unsteadiness will be sought.

The first systematic study of a flat-plate turbulent boundary layer subjected to uniform sinusoidal free-stream oscillations about a constant mean was performed by Karlsson [1959]. Measurements of the mean velocity, the amplitudes of the in- and the out-of-phase components of the first harmonic of the periodic velocity and the intensity of higher harmonics and turbulence were made using a hot-wire anemometer (HWA), over a wide range of frequencies and amplitudes. Karlsson found the mean velocity to be independent of both amplitude and frequency of excitation. The near-wall velocity always led the free-stream oscillations in phase, and for the high-amplitude, high-frequency excitation, there were periodic flow reversals near the wall.

Hussain and Reynolds [1970a, 1970b, 1972] and Reynolds and Hussain [1972] reported on the effect of a weak planar disturbance on a fully developed channel flow. The measurements of the amplitude and the relative phase of the induced streamwise velocity components were made in air using HWAs. The wave-induced velocities were found to be small and to decay exponentially in the mean-flow direction. The decay rates increased while the wave lengths decreased as the frequency was increased. The authors concluded that, even for such small disturbances, the induced oscillations in the Reynolds stresses cannot be neglected for predicting the observed wave behavior.

Acharya and Reynolds [1975] subjected the same fully developed channel flow to periodic variations in the through-flow rate. They found that the time-averaged velocity and the longitudinal turbulence intensity were practically the same as for the corresponding steady

flow. The amplitude and the phase of the periodic component of the velocity were constant over the central portion of the channel, indicating a "slug-like" response. All the variations were confined to a thin region near the wall, and the behavior for the two frequencies studied was very different. This was attributed to the fact that the higher frequency was very close to the turbulent "burst" frequency. It must be noted that the very small signal-to-noise ratios resulting from the small amplitudes of excitation employed caused considerable scatter in the near-wall data. Several of the common turbulence closure schemes were found to perform poorly in post-dicting the flow, and the authors conjectured that higher levels of closure might be needed to improve the computations.

Schachenmann and Rockwell [1976] reported measurements on a mean adverse pressure gradient boundary layer in a conical diffuser subjected to sinusoidal variations in core velocity. Over the range of frequencies studied, they found no detectable effect of unsteadiness on the mean velocity profiles. They found that the amplitude of the velocity oscillations in the boundary layer could exceed the core velocity amplitude by as much as 100%. For low-frequency excitation, the phase of velocity in the boundary layer was consistently ahead of the core velocity phase; for high-frequency excitation, the boundary-layer velocity phase lagged that of the core flow, and the amplitude could exhibit more than one peak. It must be observed, however, that there are only a few points in the profiles, and the data scatter is quite large for amplitudes and phases.

The group at ONERA/CERT in France has been very active in studies on a turbulent boundary layer subjected to sinusoidal free-stream oscillations. Cousteix, Desopper, and Houdeville [1977], Houdeville and Cousteix [1979], and Cousteix, Houdeville, and Javelle [1981] reported extensive measurements of phase-averaged velocity and turbulence normal and shear stresses using HWAs and a Laser Doppler Anemometer (LDA) on turbulent boundary layers with and without mean adverse pressure gradients. The mean-flow development was unaffected by unsteadiness. The phase and the amplitude of boundary layer parameters, like the displacement and the momentum thicknesses, exhibited an oscillatory behavior



with respect to the Strouhal number based on the length of boundary layer development. The phase-averaged boundary layer profiles followed the logarithmic law of the wall; and the wall shear velocity, computed using Clauser technique, showed increase in amplitude while its phase reduced to zero as the Strouhal number increased. The velocity phase plots showed a local maximum near the wall but varied considerably very close to the wall. The authors conjectured that a universal near-wall law, such as for steady flows, was perhaps not valid for unsteady flows.

Patel [1977] reported investigations on a flat-plate turbulent boundary layer subjected to harmonic oscillations of the free stream velocity associated with a traveling wave. The mean flow and turbulent intensity were unaffected by the unsteadiness. The amplitude-ratio distributions across the boundary layer were found to be independent of the free-stream velocity amplitude. For low-amplitude cases, this was true of the phase-angle profiles as well. For higher-amplitude cases, the phase-lag levels were found to increase with the free-stream velocity amplitude. A linearized high-frequency analysis using an eddy-viscosity turbulence model compared reasonably well with the experiments. More important, the analysis showed the dominant influence of the traveling-wave convection velocity on the response of the turbulent boundary layer to free-stream velocity oscillations.

Following Patel's work, Kenison [1977] studied the effect of a traveling wave on the behavior of a separating turbulent boundary layer. The mean distributions of velocity and turbulence profiles and skin friction were unaffected by the unsteadiness for the range of frequencies and amplitudes studied. The velocity amplitudes in the boundary layer were dependent on the frequency and the distance along the plate. There was a thin region of periodic reversed flow ahead of the mean separation point, but it had no significant effect on the variation of momentum thickness or shape factor. The phase of the velocity oscillations was always a lag with respect to that of the free stream. The lag levels generally increased with downstream distance and were much larger than the results from Patel in the same facility, but with no streamwise pressure gradient.

Ramaprian and Tu [1979, 1980, 1981] have reported experiments on a fully-developed pipe flow with sinusoidal variation in through-flow rate. Measurements were made in oil and water using LDA, and a range of frequencies was covered. The authors found that at the highest frequency of oscillation the Reynolds stresses remained frozen at an average value over the oscillation cycle. The time-averaged mean velocity exhibited a point of inflection and an increase in time-mean shear stress at the wall. The authors argued that the frequency of oscillation was very close to the turbulent burst frequency, causing the turbulence to interact with the organized fluctuations, resulting in a change in the mean-velocity profile. It must be noted, however, that this result was based on a single data point near the wall, and the time-mean shear stress at the wall was found by the gradient of the mean velocity profile at the wall, a highly uncertain procedure.

Binder and Kuney [1981] studied the near-wall region of a fully-developed channel flow subjected to small periodic velocity oscillations, using LDA. The time-averaged velocity and turbulent intensity were unaffected by the oscillations. For high frequencies, the near-wall amplitude and the phase were found to follow the laminar Stokes solution.

Shemer [1981] reported measurements on a pulsating, fully-developed pipe flow in both laminar and turbulent regimes at the same Reynolds number. For both regimes, he found that the time-mean properties of the flow were independent of the oscillations. The radial dependence of the amplitude and the phase of the velocity oscillations were found to be different for laminar and turbulent flows. The maximum of the velocity amplitude for the turbulent flow occurred at the center for low frequencies, but shifted toward the wall as frequency increased. The near-wall velocity oscillations always lagged that at the center of the pipe, and the lag increased with frequency.

As an extension of their experiments on a steady, separating, turbulent boundary layer, Simpson [1977] and later on Simpson et al. [1980, 1983] studied the effect of a low-frequency sinusoidal variation of the free-stream velocity on the same flow. Extensive measurements were made of mean and turbulent quantities and the forward-flow fraction using a

number of measurements, including HWA, LDA, and thermal tufts. Upstream of detachment, the mean profiles were unaffected by the unsteadiness, and the turbulence structure was said to be quasi-steady. During the detachment process, large amplitude and phase variations developed throughout the flow. The anomalous near-wall phase variations in the upstream flow were attributed to small oscillations in the probe position with respect to the wall at the exciting frequency.

Finally, some review articles of interest should be mentioned. For an excellent overview of the many different areas of unsteady fluid flows and applications, see McCroskey [1977]. Telionis [1977] and Cousteix [1979] have reviewed both experiments and calculations of unsteady boundary layers, both laminar and turbulent. A comprehensive review of existing unsteady turbulent boundary layer experiments is given by Carr [1981a, 1981b]. The compilation included descriptions of experimental apparatus, flow conditions, summaries of acquired data, and significant conclusions. Carr has created a magnetic data-tape library containing the data from these experiments. The above review and the data library should prove to be invaluable for present and future unsteady, turbulent boundary layer flow experimenters and computers. The present data are being added to Carr's library.

### 1.3 Summary of Previous Research and Unanswered Questions

The only clear conclusion to be drawn from the above works is that, over a fairly large range of amplitudes and frequencies of excitation, the time-averaged flow is practically unaffected by the imposed organized unsteadiness. Several unanswered questions remain.

- What are the parameters that govern unsteady flows?

Definitely, a frequency parameter in the form of a Strouhal number and an amplitude parameter should be on the list. Depending on the choice of the length scale (for example, streamwise distance, boundary layer thickness, boundary layer integral thicknesses are all possible candidates), different Strouhal numbers can be defined. None seems to emerge as a clear choice.

- What is the interaction, if any, between the organized fluctuations and the disorganized turbulent fluctuations?

No clear answer to this very important question emerges from the available literature. There is a more important and related question: how would one go about detecting any such interaction? It would seem that any correlations between an organized quantity and a turbulence quantity that one might look for to detect interactions would be suppressed by the phase-averaging process employed by almost all researchers.

- At what range of frequencies can one expect interactions between the organized and the turbulent fluctuations?

There is an expectation among most researchers that the frequencies of excitation have to be in the range characteristic of turbulent fluctuations before any interactions will take place. The Strouhal number based on the boundary layer thickness for the turbulent "burst" frequency is about 1.26, based on the results from Rao, Narasimha, and Narayanan [1971]. With a few exceptions, in the experiments above, the excitation frequencies were considerably lower than the "burst" frequency. No definite reasons or arguments emerge from the literature, explaining why sub-harmonic interactions are impossible or unlikely.

The works reviewed above point to the lack of sufficient experimental data on unsteady turbulent boundary layers. Some important considerations in meeting these data requirements are discussed next.

#### 1.4 Data Requirements in Unsteady, Turbulent Boundary Layers

Two needs emerge from a careful review of the above literature:

- need for very carefully done experiments on very clearly defined unsteady turbulent flows;
- need for systematic and careful evaluation of the performance of existing turbulence models in such flows.

Some important considerations in fulfilling the first of these needs in turbulent boundary layers is addressed below.

A good physical understanding of unsteady, turbulent boundary layers can be gained only through careful study of their dynamic behavior when subjected to different types of unsteadiness. The organized unsteadiness imposed on a turbulent flow can be of several different types. It could be periodic or transient. If periodic, then it could

be of different wave forms. The wave forms could correspond to a standing wave pattern or could be traveling at a speed more or less than the reference flow speed. If the phenomenon in question were a linear one, one could construct the response for a given type of unsteadiness from a superposition of the responses to elementary harmonic excitations over the relevant frequency range. If the phenomenon is a nonlinear one, the response could be potentially very different for different types of excitations. Turbulence is essentially a nonlinear phenomenon. There is no reason to expect that the response of turbulent flows to organized unsteadiness will be linear except perhaps for very small amplitudes. Viewed from this perspective, the available data on unsteady turbulent boundary layers are very meager.

For a given type of imposed unsteadiness, it is important to cover a large region in the parameter space to identify different flow regimes, if any. In most of the experiments reviewed above, independent variation of parameters was difficult, if not impossible. In particular, most of the above experiments do not cover a wide range in the frequency parameter. Even for those that do (Karlsson [1959] and Schachermann and Rockwell [1976]), the data are available only in the form of a few plots in the cited references; moreover, these results suffer from lack of definition and deficiencies in instrumentation and data-processing.

In developing an understanding of the dynamics of unsteady turbulent boundary layers, it is very important to minimize effects due to other causes. All of the works reviewed above are characterized by unsteadiness throughout the flow field. The effects of organized unsteadiness on transition to turbulence and the subsequent development of the turbulent flow are wholly untested, and remain open questions. Thus it is not clear how much of the effects seen in the above works should be attributed to unsteady transition. Certainly, from the computational point of view, it would be desirable to start from steady conditions, and then impose unsteadiness.

The present experiments were specifically designed to address many of the above requirements.

### 1.5 Objectives

The primary motivations for the Stanford Unsteady Turbulent Boundary Layer Research Program are two-fold:

- to explore the possibilities of controlling, reducing, or eliminating unsteady fluid dynamic effects such as dynamic stall by carefully tailored and externally imposed excitations, and
- to provide design guidelines for the improvement in performance of fluid dynamic devices with inherent unsteadiness, such as turbomachinery and internal combustion engines.

The overall objectives of the Stanford Program are to provide a fundamental understanding of the fluid dynamical and heat-transfer characteristics of unsteady, turbulent boundary layers in general, and to acquire a comprehensive data base. From the overall objectives of the Program, the following specific objectives of the research reported here were formulated:

- To understand the characteristics of a turbulent boundary layer with well-defined initial and boundary conditions.
- To provide a definitive data set on such an unsteady, turbulent boundary layer that will serve as a test case for evaluating the performance of calculation procedures and as input for turbulence models of such flows.

A brief outline of how these objectives were met is given next.

### 1.6 Summary of Present Work

To meet the above objectives, a closed-loop water channel was specially constructed for the experiments. In the upstream development section of the channel, a turbulent boundary layer was grown under steady, zero-pressure gradient conditions. This provided a well-defined inlet condition to the test section, where the boundary layer was subjected to a sinusoidally varying, adverse, free-stream gradient. A laboratory computer was set up to automate the data acquisition and control procedure.

Two major series of experiments with relative amplitudes (of free-stream oscillations at the end of the test section) of 5% and 25% were

carried out. Several frequencies and X stations were covered in each, to provide a wide range of Strouhal number. Measurements of phase-averaged streamwise velocity and square of streamwise turbulent fluctuations were made, from which other quantities of interest were computed.

The time-averaged flow was found to be insensitive to the imposed unsteadiness. The periodic flow was strongly affected by frequency and showed two distinct regimes of behavior. The high-frequency results agreed well with the Stokes solution. Over the range of frequencies and amplitudes studied, no dramatic interactions between the organized oscillations and the disorganized turbulent fluctuations were found.

An extensive data set has been obtained. This is documented in this report and a separate microfiche report [Jayaraman, Parikh and Reynolds, 1982]. A digital magnetic tape containing all the data is available from Dr. Lawrence W. Carr, U. S. Army Aeromechanics Laboratory, Ames Research Center, MS 215-1, Moffett Field, California 94035.

## Chapter 2

### THEORETICAL BACKGROUND

#### 2.1 Triple Decomposition

Following Hussain and Reynolds [1970], any flow variable  $f(\underline{x}, t)$  such as velocity or pressure, can be decomposed into three components:

$$f(\underline{x}, t) = \bar{f}(\underline{x}) + \tilde{f}(\underline{x}, t) + f'(\underline{x}, t) \quad (2.1)$$

Here  $\bar{f}(\underline{x})$  is the time-averaged or mean value of  $f(\underline{x}, t)$  at a given location,  $\tilde{f}(\underline{x}, t)$  is the organized response component due to the imposed organized unsteadiness, and  $f'(\underline{x}, t)$  is the turbulent fluctuation. Several unsteady turbulent flow investigations to date have used the above decomposition.

#### 2.2 Averaging

In order to separate the three components of a flow variable, two different averaging procedures are employed, namely, time average and ensemble average. The time average is conventionally defined as follows:

$$\bar{f}(\underline{x}) = \lim_{T \rightarrow \infty} \frac{1}{T} \int_0^T f(\underline{x}, t) dt \quad (2.2)$$

When the variable is sampled at discrete times, the time average is the average of a large number of samples in a record of sufficiently long duration. In other words,

$$\bar{f}(\underline{x}) = \lim_{N \rightarrow \infty} \frac{1}{N} \sum_{i=1}^N f(\underline{x}, t_i) \quad (2.3)$$

where  $t_i$  are the discrete times (usually equally spaced) when samples were taken. It is also understood that the total time duration in which all the samples were taken is large compared to both the imposed excitation period and the longest turbulent fluctuation period.

In order to extract the organized component, an ensemble-averaging procedure is used. An ensemble average is defined as the average over a



large number of realizations of the same phenomenon. This is expressed as:

$$\langle f(\underline{x}, t) \rangle = \lim_{N \rightarrow \infty} \frac{1}{N} \sum_{i=1}^N f_i(\underline{x}, t) \quad (2.4)$$

where  $i$  identifies a particular realization. Further, each realization is understood to have begun at  $t = 0$ .

For an imposed periodic excitation, the organized response component will also be periodic with the same period; thus the realization,  $i$ , will occur at the same point in each cycle, and the organized component can be called the periodic component. The ensemble average for this case becomes

$$\langle f(\underline{x}, t) \rangle = \lim_{N \rightarrow \infty} \frac{1}{N} \sum_{n=0}^{N-1} f(\underline{x}, t + n\tau) \quad (2.5)$$

where  $\tau$  is the time period of the imposed excitation.

It is easier to think of the ensemble averaging, for periodic excitations, as phase averaging. A phase average is defined as the average of samples from a large number of cycles at a fixed cycle phase angle. That is,

$$\langle f(\underline{x}, \theta) \rangle = \lim_{N \rightarrow \infty} \frac{1}{N} \sum_{n=0}^{N-1} f(\underline{x}, \theta + 2\pi n) \quad , \quad 0 \leq \theta \leq 2\pi \quad (2.6)$$

where  $\theta$  is the cycle phase angle. Definitions (2.5) and (2.6) are entirely equivalent. In practice,  $N$  is always finite but large.

By definition,

$$\langle f(\underline{x}, t) \rangle = \bar{f}(\underline{x}) + \tilde{f}(\underline{x}, t) \quad (2.7)$$

and the time average (or, equivalently, the average over all phases) of the phase average is the mean. That is,

$$\overline{\langle f(\underline{x}, t) \rangle} = \bar{f}(\underline{x}) \quad (2.8)$$

Therefore

$$\tilde{f}(\underline{x}, t) = \langle f(\underline{x}, t) \rangle - \bar{f}(\underline{x}) \quad (2.9)$$

and

$$f'(\underline{x}, t) = f(\underline{x}, t) - \langle f(\underline{x}, t) \rangle \quad (2.10)$$

From the above definitions, the following useful relations can be developed:

$$\begin{aligned} \langle f' \rangle &= 0 & \langle \tilde{f}g \rangle &= \tilde{f} \langle g \rangle \\ \overline{\tilde{f}g} &= \bar{f} \bar{g} & \langle \bar{f} \rangle &= \bar{f} \\ \overline{\tilde{f}} &= 0 & \langle \bar{f}g \rangle &= \bar{f} \langle g \rangle \quad (2.11) \\ \overline{f'} &= 0 & \overline{\tilde{f}g'} &= 0 \\ \langle \tilde{f}g' \rangle &= 0 \end{aligned}$$

### 2.3 Fourier Analysis

Fourier analysis is useful in determining the amplitudes and the phase angles of the harmonic components of the periodic response. Any periodic waveform can be split up into its Fourier components as follows:

$$\tilde{f}(\underline{x}, t) = \sum_{n=1}^{\infty} A_{n,f}(\underline{x}) \cos \left[ n\omega t + \phi_{n,f}(\underline{x}) \right] \quad (2.12)$$

where  $A_{n,f}(\underline{x})$  and  $\phi_{n,f}(\underline{x})$  are the amplitude and the phase of the  $n^{\text{th}}$  harmonic of the periodic component  $\tilde{f}(\underline{x}, t)$  at that location and

$$\omega = \frac{2\pi}{\tau} \quad (2.13)$$

where  $\tau$  is the time period of the imposed periodic excitation.

Complete description of  $\tilde{f}$  requires specification of  $A_{n,f}$  and  $\phi_{n,f}$  for all values of  $n$ . Only the first few harmonics are usually important in the response of physical systems to a purely sinusoidal excitation.

## 2.4 Governing Equations

The equations of motion provide considerable insight into the physics of the flow. The governing equations (using Cartesian tensor notation) for an incompressible flow of a Newtonian fluid are as follows:

$$\text{Continuity:} \quad \frac{\partial u_i}{\partial x_i} = 0 \quad (2.14)$$

$$\text{Momentum:} \quad \frac{\partial u_i}{\partial t} + u_j \frac{\partial u_i}{\partial x_j} = -\frac{1}{\rho} \frac{\partial p}{\partial x_i} + \nu \frac{\partial^2 u_i}{\partial x_j \partial x_j} \quad (2.15)$$

Let

$$u_i = \bar{u}_i + \tilde{u}_i + u'_i \quad (2.16a)$$

$$p = \bar{p} + \tilde{p} + p' \quad (2.16b)$$

Substituting Eqs. (2.16) into (2.14) and performing phase and time averaging,

$$\frac{\partial \bar{u}_i}{\partial x_i} = 0 \quad (2.17a)$$

$$\frac{\partial \tilde{u}_i}{\partial x_i} = 0 \quad (2.17b)$$

$$\frac{\partial u'_i}{\partial x_i} = 0 \quad (2.17c)$$

Substituting Eqs. (2.16) into (2.15),

$$\begin{aligned} \frac{\partial}{\partial t} (\bar{u}_1 + \tilde{u}_1 + u'_1) + \frac{\partial}{\partial x_j} \left[ (\bar{u}_j + \tilde{u}_j + u'_j)(\bar{u}_1 + \tilde{u}_1 + u'_1) \right] \\ = -\frac{1}{\rho} \frac{\partial}{\partial x_1} (\bar{p} + \tilde{p} + p') + \nu \frac{\partial^2}{\partial x_j \partial x_j} (\bar{u}_1 + \tilde{u}_1 + u'_1) \end{aligned}$$

or

$$\begin{aligned} \frac{\partial}{\partial t} (\bar{u}_1 + \tilde{u}_1 + u'_1) + \frac{\partial}{\partial x_j} (\bar{u}_1 \bar{u}_j + \bar{u}_1 \tilde{u}_j + \bar{u}_1 u'_j + \tilde{u}_1 \bar{u}_j + \tilde{u}_1 \tilde{u}_j + \tilde{u}_1 u'_j + \\ + u'_1 \bar{u}_j + u'_1 \tilde{u}_j + u'_1 u'_j) = -\frac{1}{\rho} \frac{\partial}{\partial x_1} (\bar{p} + \tilde{p} + p') + \\ + \nu \frac{\partial^2}{\partial x_j \partial x_j} (\bar{u}_1 + \tilde{u}_1 + u'_1) \end{aligned} \quad (2.18)$$

Phase averaging (2.18),

$$\begin{aligned} \frac{\partial \tilde{u}_1}{\partial t} + \frac{\partial}{\partial x_j} (\bar{u}_1 \bar{u}_j + \bar{u}_1 \tilde{u}_j + \tilde{u}_1 \bar{u}_j + \tilde{u}_1 \tilde{u}_j + \langle u'_1 u'_j \rangle) \\ = -\frac{1}{\rho} \frac{\partial}{\partial x_1} (\bar{p} + \tilde{p}) + \nu \frac{\partial^2}{\partial x_j \partial x_j} (\bar{u}_1 + \tilde{u}_1) \end{aligned} \quad (2.19)$$

Time averaging (2.18),

$$\frac{\partial}{\partial x_j} (\bar{u}_1 \bar{u}_j + \overline{\tilde{u}_1 \tilde{u}_j} + \overline{u'_1 u'_j}) = -\frac{1}{\rho} \frac{\partial \bar{p}}{\partial x_1} + \nu \frac{\partial^2 \bar{u}_1}{\partial x_j \partial x_j} \quad (2.20)$$

Subtracting (2.20) from (2.19),

$$\frac{\partial \tilde{u}_1}{\partial t} + \frac{\partial}{\partial x_j} (\bar{u}_1 \tilde{u}_j + \tilde{u}_1 \bar{u}_j + \widetilde{\tilde{u}_1 \tilde{u}_j} + \widetilde{u'_1 u'_j}) = -\frac{1}{\rho} \frac{\partial \tilde{p}}{\partial x_1} + \nu \frac{\partial^2 \tilde{u}_1}{\partial x_j \partial x_j} \quad (2.21)$$

Equation (2.20) can be expressed in the more usual form as

$$\frac{\partial}{\partial x_j} (\bar{u}_1 \bar{u}_j) = -\frac{1}{\rho} \frac{\partial \bar{p}}{\partial x_1} + \nu \frac{\partial^2 \bar{u}_1}{\partial x_j \partial x_j} - \frac{\partial}{\partial x_j} (\overline{u'_1 u'_j} + \overline{\tilde{u}_1 \tilde{u}_j}) \quad (2.22)$$

Equation (2.21) can be rewritten as

$$\frac{\partial \tilde{u}_1}{\partial t} + \frac{\partial}{\partial x_j} (\bar{u}_1 \tilde{u}_j + \tilde{u}_1 \bar{u}_j) = -\frac{1}{\rho} \frac{\partial \tilde{p}}{\partial x_1} + \nu \frac{\partial^2 \tilde{u}_1}{\partial x_j \partial x_j} - \frac{\partial}{\partial x_j} (\widetilde{\tilde{u}_1 \tilde{u}_j} + \widetilde{u'_1 u'_j}) \quad (2.23)$$

For a 2-D phase-averaged flow, let

$$u_i = (u, v, w)$$

$$\bar{u}_i = (\bar{U}, \bar{V}, 0)$$

$$x_i = (x, y, z)$$

Equations (2.17) can be rewritten as

$$\frac{\partial \bar{U}}{\partial x} + \frac{\partial \bar{V}}{\partial y} = 0 \quad (2.24a)$$

$$\frac{\partial \tilde{u}}{\partial x} + \frac{\partial \tilde{v}}{\partial y} = 0 \quad (2.24b)$$

Equation (2.22) can be expressed as

$$\begin{aligned} \frac{\partial}{\partial x} (\bar{U} \bar{U}) + \frac{\partial}{\partial y} (\bar{U} \bar{V}) &= -\frac{1}{\rho} \frac{\partial \bar{p}}{\partial x} + \nu \left( \frac{\partial^2 \bar{U}}{\partial x^2} + \frac{\partial^2 \bar{U}}{\partial y^2} \right) - \frac{\partial}{\partial x} (\bar{u}' u') - \frac{\partial}{\partial y} (\bar{u}' v') \\ &\quad - \frac{\partial}{\partial x} (\tilde{u} \tilde{u}) - \frac{\partial}{\partial y} (\tilde{u} \tilde{v}) \end{aligned} \quad (2.25a)$$

and

$$\begin{aligned} \frac{\partial}{\partial x} (\bar{V} \bar{U}) + \frac{\partial}{\partial y} (\bar{V} \bar{V}) &= -\frac{1}{\rho} \frac{\partial \bar{p}}{\partial y} + \nu \left( \frac{\partial^2 \bar{V}}{\partial x^2} + \frac{\partial^2 \bar{V}}{\partial y^2} \right) - \frac{\partial}{\partial x} (\bar{v}' u') - \frac{\partial}{\partial y} (\bar{v}' v') \\ &\quad - \frac{\partial}{\partial x} (\tilde{v} \tilde{u}) - \frac{\partial}{\partial y} (\tilde{v} \tilde{v}) \end{aligned} \quad (2.25b)$$

Equation (2.23) can be rewritten as

$$\begin{aligned} \frac{\partial \tilde{u}}{\partial t} + 2 \frac{\partial}{\partial x} (\tilde{u} \bar{U}) + \frac{\partial}{\partial y} (\bar{U} \tilde{v} + \tilde{u} \bar{V}) &= -\frac{1}{\rho} \frac{\partial \tilde{p}}{\partial x} + \nu \left( \frac{\partial^2 \tilde{u}}{\partial x^2} + \frac{\partial^2 \tilde{u}}{\partial y^2} \right) \\ &\quad - \frac{\partial}{\partial x} (\tilde{u} \tilde{u} + \tilde{u}' u') - \frac{\partial}{\partial y} (\tilde{u} \tilde{v} + \tilde{u}' v') \end{aligned} \quad (2.26a)$$

and

$$\begin{aligned} \frac{\partial \tilde{v}}{\partial t} + \frac{\partial}{\partial x} (\bar{V} \tilde{u} + \tilde{v} \bar{U}) + 2 \frac{\partial}{\partial y} (\bar{V} \tilde{v}) &= -\frac{1}{\rho} \frac{\partial \tilde{p}}{\partial y} + \nu \left( \frac{\partial^2 \tilde{v}}{\partial x^2} + \frac{\partial^2 \tilde{v}}{\partial y^2} \right) \\ &\quad - \frac{\partial}{\partial x} (\tilde{v} \tilde{u} + \tilde{v}' u') - \frac{\partial}{\partial y} (\tilde{v} \tilde{v} + \tilde{v}' v') \end{aligned} \quad (2.26b)$$

## 2.5 Simplification of Governing Equations

The purpose of this section is to simplify the governing equations given in Section 2.4 for the special case of a 2-D incompressible boundary layer. This will be achieved by performing an order of magnitude analysis on the equations and eliminating terms that are small compared to others. For convenience, the simplified equations are summarized in Table 2.1. The details of the analysis are given in Sections 2.5.1, 2.5.2, 2.5.3 and 2.5.4.

### 2.5.1 Primary Estimates

In performing the order-of-magnitude analysis, variables will be replaced by "typical" (order of magnitude) values. The changes in variables are expected to be of the same order as typical values. In the following, the symbol " $\sim$ " is used to indicate a typical value or order-of-magnitude accuracy without regard to the sign. This should not be confused with the " $\sim$ " used over a periodic variable. The symbol " $\Delta$ " in front of a variable is used to indicate changes in that variable.

For a 2-D incompressible boundary layer flow, the following orders of magnitude are assumed:

$$\Delta x \sim L \quad \text{for both mean and periodic variables,}$$

$$\Delta t \sim 1/\omega,$$

$$\Delta y \sim \delta \quad \text{for mean variables,}$$

$$\sim \delta' \quad \text{for periodic quantities,}$$

$$U, \Delta U \sim U_e,$$

$$\tilde{u}, \Delta \tilde{u} \sim A,$$

where

$L$  is a typical length scale in the streamwise direction over which typical changes in mean and periodic variables take place,

$\omega$  is the circular frequency of oscillation,

$\delta$  is the mean boundary layer thickness ( $\delta \ll L$ ),

$\delta'$  is a typical length scale in the normal-to-wall direction over which typical changes in periodic variables occur (normally  $\delta' \leq \delta$ ),

$U_e$  is the mean free-stream velocity, and

$A$  is the amplitude of the free-stream velocity oscillations.

It is further assumed that

$$\Delta(\overline{u'u'}) , \quad \Delta(\overline{u'v'}) \sim \epsilon^2 U_e^2$$

and

$$\Delta(\widetilde{u'u'}) , \quad \Delta(\widetilde{u'v'}) \sim \epsilon^2 \alpha U_e^2 ,$$

where

$\epsilon^2$  is a multiplicative factor (usually  $\ll 1$ ) whose order of magnitude will be determined later in the analysis and

$$\alpha = A/U_e.$$

The order of magnitude of the changes in  $(\widetilde{u'u'})$  and  $(\widetilde{u'v'})$  may be arrived at by the following reasoning. Assume that, under quasi-steady ( $\omega = 0$ ) conditions,

$$\langle u'u' \rangle \sim \epsilon^2 \langle u_e \rangle^2$$

where  $\langle u_e \rangle$  is phase-averaged free-stream velocity and

$$\langle u_e \rangle = U_e + A \cos(\omega t)$$

Therefore,

$$\begin{aligned} \langle u_e \rangle^2 &= U_e^2 + 2AU_e \cos(\omega t) + A^2 \cos^2(\omega t) \\ &= U_e^2 \left[ 1 + 2\alpha \cos(\omega t) + \alpha^2 \cos^2(\omega t) \right] \end{aligned}$$

Usually  $\alpha < 1$  and  $\alpha^2$  is small compared to  $\alpha$ . Thus

$$(\widetilde{u'u'}) , \quad \Delta(\widetilde{u'u'}) \sim \epsilon^2 \alpha U_e^2 .$$

A similar reasoning holds for  $\Delta(\widetilde{u'v'})$ . Experimental data presented in Chapter 4 show that the estimate for  $\Delta(\widetilde{u'u'})$  is good over all the frequencies studied.

Each of Equations (2.24), (2.25), and (2.26) will be analyzed individually in the following sections.

### 2.5.2 Analysis of Continuity Equations

Consider Eq. (2.24a):

$$\frac{\partial \bar{U}}{\partial x} \sim \frac{U_e}{L} \quad \text{and} \quad \frac{\partial \bar{V}}{\partial y} \sim \frac{\Delta \bar{V}}{\delta} .$$

Since both terms must be significant,

$$\Delta \bar{V} \sim U_e \frac{\delta}{L} .$$

Consider Eq. (2.24b):

$$\frac{\partial \tilde{u}}{\partial x} \sim \frac{A}{L} \quad \text{and} \quad \frac{\partial \tilde{v}}{\partial y} \sim \frac{\Delta \tilde{v}}{\delta'} .$$

This implies that

$$\Delta \tilde{v} \sim A \frac{\delta'}{L}$$



### 2.5.3 Analysis of Mean Momentum Equation

Eq. (2.25a) has nine terms. Their orders of magnitude are estimated as follows:

$$\text{Term 1:} \quad \left[ \frac{\partial}{\partial x} (\bar{U} \bar{U}) \right] \sim \frac{U_e^2}{L}$$

$$\text{Term 2:} \quad \left[ \frac{\partial}{\partial y} (\bar{U} \bar{V}) \right] \sim \frac{U_e U_e \delta}{\delta L} = \frac{U_e^2}{L}$$

$$\text{Term 3:} \quad \left[ \frac{1}{\rho} \frac{\partial \bar{p}}{\partial x} \right] \sim \frac{1}{\rho} \frac{\Delta \bar{p}_e}{L}$$

$$\text{Term 4:} \quad \left[ \nu \frac{\partial^2 \bar{U}}{\partial x^2} \right] \sim \nu \frac{U_e}{L^2} = \frac{U_e^2}{L} \frac{\nu}{U_e L}$$

$$\text{Term 5:} \quad \left[ \nu \frac{\partial^2 \bar{U}}{\partial y^2} \right] \sim \nu U_e \frac{1}{\delta^2} = \frac{U_e^2}{L} \frac{\nu}{U_e L} \frac{L^2}{\delta^2}$$

$$\text{Term 6:} \quad \left[ \frac{\partial}{\partial x} (\bar{u' u'}) \right] \sim \frac{1}{L} \epsilon^2 U_e^2 = \frac{U_e^2}{L} \epsilon^2$$

$$\text{Term 7:} \quad \left[ \frac{\partial}{\partial y} (\bar{u' v'}) \right] \sim \frac{1}{\delta} \epsilon^2 U_e^2 = \frac{U_e^2}{L} \epsilon^2 \frac{L}{\delta}$$

$$\text{Term 8:} \quad \left[ \frac{\partial}{\partial x} (\bar{\tilde{u} \tilde{u}}) \right] \sim \frac{1}{L} A^2 = \frac{U_e^2}{L} \frac{A^2}{U_e^2}$$

$$\text{Term 9:} \quad \left[ \frac{\partial}{\partial y} (\bar{\tilde{u} \tilde{v}}) \right] \sim \frac{1}{\delta'} A \frac{A \delta'}{L} = \frac{U_e^2}{L} \frac{A^2}{U_e^2}$$

Term 4 is negligible compared to Term 5, and Term 6 is negligible compared to Term 7, since  $(\delta/L) \ll 1$ . For the viscous term to be significant (Term 5), we require that

$$\left(\frac{U_e L}{\nu}\right) \sim \left(\frac{L}{\delta}\right)^2 \quad \text{or} \quad \left(\frac{\delta}{L}\right) \sim \left(\frac{U_e L}{\nu}\right)^{-1/2}$$

For the pressure gradient term to be significant, we note that

$$\Delta \bar{p}_e \sim \frac{\rho L U_e^2}{L} = \rho U_e^2$$

Further note that Terms 8 and 9 are of order  $\alpha^2$  compared to Terms 1 and 2 and hence are negligible even for  $\alpha$  as great as 0.3.

Finally, for the only turbulent term to be of any significance (Term 7), we note that

$$\epsilon^2 \sim \frac{\delta}{L}.$$

Consider Eq. (2.25b); there are nine terms. The order of magnitude of each is estimated as follows.

$$\text{Term 1:} \quad \left[ \frac{\partial}{\partial x} (\bar{U} \bar{V}) \right] \sim \frac{U_e \delta U_e}{L L} = \frac{U_e^2 \delta}{L^2}$$

$$\text{Term 2:} \quad \left[ \frac{\partial}{\partial y} (\bar{V} \bar{V}) \right] \sim \frac{1}{\delta} \frac{\delta U_e}{L} \frac{\delta U_e}{L} = \frac{U_e^2 \delta}{L^2}$$

$$\text{Term 4:} \quad \left[ \nu \frac{\partial^2 \bar{V}}{\partial x^2} \right] \sim \nu \frac{\delta U_e}{L} \frac{1}{L^2} = \frac{U_e^2 \delta}{L^2} \frac{\nu}{U_e L}$$

$$\text{Term 5:} \quad \left[ \nu \frac{\partial^2 \bar{V}}{\partial y^2} \right] \sim \nu \frac{\delta U_e}{L} \frac{1}{\delta^2} = \frac{U_e^2 \delta}{L^2} \frac{\nu}{U_e L} \frac{L^2}{\delta^2}$$

$$\text{Term 6:} \quad \left[ \frac{\partial}{\partial x} (\bar{u}' v') \right] \sim \frac{1}{L} \epsilon^2 U_e^2 = \frac{U_e^2 \delta}{L^2} \epsilon^2 \frac{L}{\delta}$$

$$\text{Term 7:} \quad \left[ \frac{\partial}{\partial y} (\bar{v}' v') \right] \sim \frac{\epsilon^2 U_e^2}{\delta} = \frac{U_e^2 \delta}{L^2} \epsilon^2 \frac{L^2}{\delta^2}$$

$$\text{Term 8: } \left[ \frac{\partial}{\partial x} (\tilde{u} \tilde{v}) \right] \sim \frac{1}{L} A \frac{A \delta'}{L} = \frac{A^2 \delta'}{L^2} = \frac{U_e^2 \delta}{L^2} \frac{A^2}{U_e^2} \frac{\delta'}{\delta}$$

$$\text{Term 9: } \left[ \frac{\partial}{\partial y} (\tilde{v} \tilde{v}) \right] \sim \frac{1}{\delta'} \frac{\delta' A}{L} \frac{\delta' A}{L} = \frac{U_e^2 \delta}{L^2} \frac{A^2}{U_e^2} \frac{\delta'}{\delta}$$

With the above estimates, for Eq. (2.25b), Terms 1, 2, 4, 5, 6, 8 and 9 are negligible (for  $\alpha < 0.3$ ) compared to Term 7. Thus

$$\frac{\partial \bar{p}}{\partial y} \sim \frac{\rho U_e^2}{L}$$

or

$$(\bar{p}_\delta - \bar{p}_0) \sim \rho U_e^2 \frac{\delta}{L} \ll 1.$$

Therefore,

$$\frac{\partial \bar{p}}{\partial y} = 0 \quad (2.27)$$

and Eq. (2.25a) simplifies to

$$\frac{\partial}{\partial x} (\bar{U} \bar{U}) + \frac{\partial}{\partial y} (\bar{U} \bar{V}) = -\frac{1}{\rho} \frac{\partial \bar{p}}{\partial x} + \nu \frac{\partial^2 \bar{U}}{\partial y^2} - \frac{\partial}{\partial y} (\overline{u'v'}) , \alpha < 0.3 . \quad (2.28)$$

This equation is the same as the steady boundary layer momentum equation.

#### 2.5.4 Analysis of Periodic Momentum Equations

Equation (2.26a) has 11 terms. Their orders of magnitude are estimated as follows:

$$\text{Term 1: } \left[ \frac{\partial \tilde{u}}{\partial t} \right] \sim A \omega$$

$$\text{Term 2: } \left[ \frac{\partial}{\partial x} (\tilde{u} \bar{U}) \right] \sim \frac{A U_e}{L}$$

$$\text{Term 3:} \quad \left[ \frac{\partial}{\partial y} (\bar{u} \tilde{v}) \right] \sim \frac{1}{\delta'} u_e \frac{A \delta'}{L} = \frac{AU_e}{L}$$

$$\text{Term 4:} \quad \left[ \frac{\partial}{\partial y} (\tilde{u} \bar{v}) \right] \sim \frac{1}{\delta'} A \frac{U_e \delta}{L} = \frac{AU_e}{L} \frac{\delta}{\delta'}$$

$$\text{Term 5:} \quad \left[ \frac{1}{\rho} \frac{\partial \tilde{p}}{\partial x} \right] \sim \frac{\Delta \tilde{p}}{\rho L}$$

$$\text{Term 6:} \quad \left[ v \frac{\partial^2 \tilde{u}}{\partial x^2} \right] \sim v \frac{A}{L^2} = \frac{AU_e}{L} \frac{v}{U_e}$$

$$\text{Term 7:} \quad \left[ v \frac{\partial^2 \tilde{u}}{\partial y^2} \right] \sim v \frac{A}{\delta'^2} = \frac{AU_e}{L} \frac{v}{U_e} \frac{L^2}{\delta'^2} \frac{\delta^2}{\delta'^2} \sim \frac{AU_e}{L} \frac{\delta^2}{\delta'^2}$$

$$\text{Term 8:} \quad \left[ \frac{\partial}{\partial x} (\tilde{u} \tilde{u}) \right] \sim \frac{1}{L} A^2 = \frac{AU_e}{L} \frac{A}{U_e} = \frac{AU_e}{L} \alpha$$

$$\text{Term 9:} \quad \left[ \frac{\partial}{\partial x} (\tilde{u}' \tilde{u}') \right] \sim \frac{1}{L} \varepsilon^2 \alpha U_e^2 = A \frac{AU_e}{L^2} = \frac{AU_e}{L} \frac{\delta}{L}$$

$$\text{Term 10:} \quad \left[ \frac{\partial}{\partial y} (\tilde{u} \tilde{v}) \right] \sim \frac{1}{\delta'} A \frac{A \delta'}{L} = \frac{A^2}{L} = \frac{AU_e}{L} \alpha$$

$$\text{Term 11:} \quad \left[ \frac{\partial}{\partial y} (\tilde{u}' \tilde{v}') \right] \sim \frac{1}{\delta'} \varepsilon^2 \alpha U_e^2 = \frac{1}{\delta'} \frac{\delta}{L} AU_e = \frac{AU_e}{L} \frac{\delta}{\delta'}$$

Clearly, Terms 6 and 9 are negligible compared to Term 2.

Three different cases need to be considered.

Case 1 (very low frequencies)

$$A\omega \ll \frac{AU_e}{L}$$

or

$$\frac{\omega L}{U_e} = S \ll 1$$

For the present experiments,  $L \sim 0.6$  m,  $U_e \sim 0.7$  m; the above requirement translates into

$$\omega \ll 1 \text{ rad/s}$$

For this case, the unsteady term can be neglected in comparison to other terms. Further, if viscosity has to be important, then  $\delta' \sim \delta$ , i.e., the thickness of region over which unsteady effects are important is of the same order as the boundary layer thickness. The pressure oscillations are of the order of  $\rho A U_e = \rho U_e^2 \alpha$ . Thus the governing equation for  $\tilde{u}$  becomes (anticipating the result for  $\tilde{p}$  to be shown later):

$$2 \frac{\partial}{\partial x} (\tilde{u} \bar{U}) + \frac{\partial}{\partial y} (\bar{U} \tilde{v} + \tilde{u} \bar{V}) = - \frac{1}{\rho} \frac{\partial \tilde{p}_e}{\partial x} + \nu \frac{\partial^2 \tilde{u}}{\partial y^2} - \frac{\partial}{\partial y} (\widetilde{u'v'}) - \left[ \frac{\partial}{\partial x} (\widetilde{\tilde{u}\tilde{u}}) + \frac{\partial}{\partial y} (\widetilde{\tilde{u}\tilde{v}}) \right] \quad (2.29)$$

The terms in square brackets are of order  $\alpha$  and hence are probably important only for  $\alpha > 0.1$ .

#### Case 2 (very high frequencies)

$$A\omega \gg \frac{AU_e}{L}$$

or

$$\frac{\omega L}{U_e} \gg 1$$

For the present experiments, this means

$$\omega \gg 1 \text{ rad/s}$$

In this case, for the viscous term to be significant,

$$\frac{1}{A\omega} \frac{AU_e}{L} \frac{\delta^2}{\delta'^2} \sim 1$$

or

$$\frac{\delta'}{\delta} \sim \left[ \frac{1}{(\omega L/U_e)} \right]^{1/2}$$

i.e.,

$$\frac{\delta'}{\delta} \sim \frac{1}{S^{1/2}}$$

Clearly, at very high Strouhal numbers, the unsteady effects are confined to a very thin region near the wall.

For this case the pressure oscillations are of the order of  $\rho A \omega L = \rho U_e^2 \alpha S$ . Thus the pressure oscillations increase with Strouhal number. The governing equation reduces to the Stokes equation, as shown below:

$$\frac{\partial \tilde{u}}{\partial t} = -\frac{1}{\rho} \frac{\partial \tilde{p}_e}{\partial x} + \nu \frac{\partial^2 \tilde{u}}{\partial y^2} \quad (2.30)$$

Case 3 (intermediate frequencies):

$$A \omega \sim \frac{A U_e}{L}$$

or

$$\frac{\omega L}{U_e} = S \sim 1$$

For this case, the unsteady term has to be added to Eq. (2.29).

$$\begin{aligned} \frac{\partial \tilde{u}}{\partial t} + 2 \frac{\partial}{\partial x} (\tilde{u} \bar{U}) + \frac{\partial}{\partial y} (\bar{U} \tilde{v} + \tilde{u} \bar{V}) &= -\frac{1}{\rho} \frac{\partial \tilde{p}_e}{\partial x} + \nu \frac{\partial^2 \tilde{u}}{\partial y^2} - \frac{\partial}{\partial y} (\widetilde{u'v'}) \\ &\quad - \left[ \frac{\partial}{\partial x} (\widetilde{\tilde{u} \tilde{u}}) + \frac{\partial}{\partial y} (\widetilde{\tilde{u} \tilde{v}}) \right] \end{aligned} \quad (2.31)$$

Once again, the terms in square brackets are of order  $\alpha$  and hence need to be retained only for  $\alpha > 0.1$ .

To complete the order of magnitude analysis, it will be shown that  $\frac{\partial \tilde{p}}{\partial y} = 0$  for an unsteady boundary layer. Equation (2.26b) has 11 terms. Their orders of magnitude are estimated as follows:

$$\text{Term 1:} \quad \left[ \frac{\partial \tilde{v}}{\partial t} \right] \sim \frac{A \omega \delta'}{L}$$

$$\text{Term 2:} \quad \left[ \frac{\partial}{\partial x} (\bar{v} \tilde{u}) \right] \sim \frac{1}{L} \frac{U_e \delta}{L} A = \frac{AU_e \delta}{L^2} = \frac{AU_e}{L} \frac{\delta}{L}$$

$$\text{Term 3:} \quad \left[ \frac{\partial}{\partial x} (\tilde{v} \bar{u}) \right] \sim \frac{1}{L} U_e \frac{A \delta'}{L} = \frac{AU_e \delta'}{L^2} = \frac{AU_e}{L} \frac{\delta'}{L}$$

$$\text{Term 4:} \quad \left[ \frac{\partial}{\partial y} (\bar{v} \tilde{v}) \right] \sim \frac{AU_e \delta}{L^2} \quad \text{or} \quad \frac{AU_e \delta'}{L^2} = \frac{AU_e}{L} \left( \frac{\delta}{L} \quad \text{or} \quad \frac{\delta'}{L} \right)$$

$$\text{Term 6:} \quad \left[ v \frac{\partial^2 \tilde{v}}{\partial x^2} \right] \sim v \frac{A \delta'}{L} \frac{1}{L^2} = v \frac{A \delta'}{L^3} = \frac{AU_e}{L} \frac{v}{U_e} \frac{\delta'}{L}$$

Term 7:

$$\left[ v \frac{\partial^2 \tilde{v}}{\partial y^2} \right] \sim v \frac{A \delta'}{L} \frac{1}{\delta'^2} = v \frac{A}{L \delta'} = \frac{AU_e}{L} \frac{v}{U_e} \frac{L}{\delta'} \sim \frac{AU_e}{L} \frac{\delta}{L} \frac{\delta}{\delta'}$$

$$\text{Term 8:} \quad \left[ \frac{\partial}{\partial x} (\tilde{u} \tilde{v}) \right] \sim \frac{1}{L} A \frac{A \delta'}{L} = \frac{A^2 \delta'}{L^2} = \frac{AU_e}{L} \alpha \frac{\delta'}{L}$$

$$\text{Term 9:} \quad \left[ \frac{\partial}{\partial x} (\tilde{u}' \tilde{v}') \right] \sim \frac{1}{L} \epsilon^2 \sigma U_e^2 = \frac{1}{L} \frac{\delta}{L} \frac{A}{U_e} U_e^2 = \frac{\delta AU_e}{L^2} = \frac{AU_e}{L} \frac{\delta}{L}$$

$$\text{Term 10:} \quad \left[ \frac{\partial}{\partial y} (\tilde{v} \tilde{v}) \right] \sim \frac{1}{\delta'} \frac{A^2 \delta'^2}{L^2} = \frac{A^2 \delta'}{L^2} = \frac{AU_e}{L} \alpha \frac{\delta'}{L}$$

$$\text{Term 11:} \quad \left[ \frac{\partial}{\partial y} (\tilde{v}' \tilde{v}') \right] \sim \frac{1}{\delta'} \epsilon^2 \alpha U_e^2 = \frac{\delta AU_e}{L \delta'} = \frac{AU_e}{L} \frac{\delta}{\delta'}$$

Case 1:

$S \ll 1$ ,  $\delta' \sim \delta$ . In this case,

$$\frac{\partial \tilde{p}}{\partial y} \sim \frac{\rho A U_e}{L} = \frac{\rho U_e^2 \alpha}{L}$$

or

$$\Delta \tilde{p} \Big|_0^\delta \sim \rho U_e^2 \alpha \frac{\delta}{L} \ll 1$$

Case 2:

$S \gg 1$ ;  $(\delta'/\delta) \sim 1/S^{1/2}$  In this case,

$$\frac{\partial \tilde{p}}{\partial y} \sim \rho \frac{A U_e}{L} \frac{\delta}{\delta'} = \frac{\rho A U_e}{L} \left( \frac{\omega L}{U_e} \right)^{1/2}$$

or

$$\Delta \tilde{p} \Big|_0^\delta \sim \rho U_e^2 \alpha \frac{\delta}{L} \left( \frac{\omega L}{U_e} \right)^{1/2} = \rho U_e^2 \alpha \frac{v \omega}{U_e^2} \ll 1$$

since usually

$$\frac{U_e L}{v} \gg S$$

Case 3:

$S \sim 1$ ;  $\delta' \sim \delta$ . This is the same as Case 1.

Thus, for a boundary layer,

$$\frac{\partial \tilde{p}}{\partial y} \approx 0 \quad (2.32)$$

Hence

$$\frac{\partial \tilde{p}}{\partial x} \approx \frac{\partial \tilde{p}_e}{\partial x} \quad (2.33)$$

as had been used earlier.



## Chapter 3

### EXPERIMENTAL SETUP AND PROCEDURES

The experimental setup consists of the apparatus and the data-acquisition and control system. The experimental procedures consist of the data-acquisition and control procedures and the data-reduction procedures. Each one of these will be briefly described below.

#### 3.1 Apparatus

The apparatus consists primarily of the water channel and the oscillation mechanism used to produce the free-stream oscillations. The objectives behind the design of the apparatus will be described first. After a description of the water channel and the means of producing controlled oscillations, the treatment and control of water quality and the LDA mount will be briefly touched upon.

##### 3.1.1 Design Objective

Figure 3.1 shows the desired free-stream variation in the experimental apparatus. In the upstream development section, the free-stream velocity is steady in time and uniform in the  $X$  direction. In the test section, the free-stream velocity decreases linearly with  $X$ , with the rate of decrease dependent on the cycle-phase angle. At  $0^\circ$  cycle-phase angle, the free-stream gradient is 0 and its value is the same as upstream. In the recovery section, the free-stream velocity is again uniform in  $X$  but is a function of cycle-phase angle.

During operation, the free-stream velocity gradient in the test section oscillates sinusoidally at the desired frequency, between 0 and the desired maximum value. The time-averaged free-stream velocity decreases linearly with  $X$ . The amplitude of the free-stream oscillations increases linearly with  $X$ . Thus the boundary layer in the upstream development section grows under zero pressure-gradient conditions as a steady, flat-plate boundary layer. In the test section, it is subjected to an oscillatory adverse free-stream gradient with a nonzero mean.

The experimental parameters that can be varied are the frequency of oscillation and the amplitude of free-stream oscillations at the end of the test section. The actual details of the implementation of the design objective in the test apparatus are given below.

### 3.1.2 Stanford Unsteady Turbulent-Boundary-Layer-Research Water Channel

A special and unique water tunnel facility in which unsteady turbulent boundary layers can be studied in great detail was constructed for the research program. Water was chosen as the working fluid for the following important reasons:

- The fluid velocities required are low, and hence the turbulence frequencies of interest will be low. Free-stream oscillations at such frequencies (0-2 Hz) can be achieved easily with relatively simple mechanical arrangements.
- Forward-scatter Laser-Doppler Anemometry with frequency-tracking is easy to use in water.
- Water permits easy visualization of the flow field.
- Unsteady compressibility effects are much less severe in water than in air.

Figure 3.2 shows a schematic diagram of the Stanford Unsteady Turbulent-Boundary-Layer-Research water channel. Water pumped from the sump is supplied to the overhead tank (section  $1.5 \times 1$  m) through a standing pipe with several holes. The water level is maintained constant to within 2 mm  $H_2O$  by an overflow weir. An open rectangular header (not shown in the figure) is placed inside the tank around the entrance to the downcomer. The header has a honeycomb for one of its vertical faces through which water can enter the header. The purpose is to make the flow inside the header as quiescent as possible.

The entrance to the downcomer is through a honeycomb. At the bottom of the downcomer, water is turned through  $90^\circ$  by a triangular header and honeycomb combination into the screen box. The screen box is made of plexiglas, and the screens are made of stainless steel wire (24 gauge, 70% porosity) and are stretched onto plexiglas frames. There are three screens, spaced 12 cm apart, and they are inserted into the box

much like printed circuit cards. The sides of the box can be disassembled for removal and cleaning of the screens. Once in place, the screens can be put into tension by bolts that reach from the sides of the box. It was found necessary to keep the screens clean and their surface as planar as possible to achieve very good spanwise uniformity in the development and test sections (see Figs. 4.1). The cross-section of the screen box is  $1\text{ m} \times 1\text{ m}$ . The screen box is followed by a nozzle that contracts the flow in both directions to the channel cross-section ( $35\text{ cm} \times 15\text{ cm}$ ).

The nozzle, the overhead tank, the downcomer, and the  $90^\circ$  turn header were all constructed of 32 mm steel plates reinforced by structural channels. The inside surfaces of these components were sandblasted, washed with acetone, and coated with epoxy resin to prevent rusting.

The nozzle is followed by a 2 m long development section of cross-section  $35\text{ cm} \times 15\text{ cm}$ . At the end of the nozzle (i.e., at the beginning of the development section), two rows of closely spaced bleed holes are provided for removal of side- and top-wall boundary layers from the nozzle. This permits growth of a new test boundary layer on the top wall of the development section. As the boundary layers grow, the free-stream velocity in the core increases due to the increasing blockage. Part of the flow needs to be bled off to keep the free-stream velocity uniform. For this purpose, rows of bleed holes are provided in the bottom wall every 15 cm throughout the development section. The flow through each bleed hole row is controlled by a valve. These valves are carefully adjusted to achieve a very uniform free-stream velocity in the development section (see Fig. 4.2).

The top- and the side-wall boundary layers are tripped by a sandpaper-type rough tape placed 12 cm downstream of the nozzle exit. At the end of the development section, the side-wall boundary layers are removed by splitter plates, and the channel width is reduced from 35 cm to 30 cm. This forces growth of new side-wall boundary layers in the test section that will be thinner than the top-wall study boundary layer and hence be more resistant to separation. The amount of flow removed is carefully adjusted to give a smooth flow at the leading edge of the splitter plates, visualized by dye, injected just upstream of the plates.

The test section that follows the development section is 61 cm long and 30 cm x 15 cm in cross section. The bottom wall of the test section consists of a porous plate, through which flow can be extracted. The test section is followed by a short recovery section and then an exit section. The exit section also has a porous plate similar to that in the test section. These porous plates have several holes spaced 1.3 cm apart in rows spaced every 2 cm along the plates.

To have uniform suction in the bottom-wall porous plate in the test section, the pressure drop across the plate should be large compared to the change in static pressure in the channel along the plate. The size of the holes in the plates is chosen for each amplitude such that the above requirement is met.

The top wall of the channel forms a smooth working surface for the test boundary layer. Probe access ports, approximately 2 cm in diameter, are provided along the centerline of the channel and spanwise at several locations. These ports are fitted with individually fitted plugs, which can be removed for insertion of probe traverse mechanisms, etc. Several static pressure taps are provided on the top surface of the channel throughout. Both the probe ports and the pressure taps are spaced 7.6 cm along the channel length.

The development section, the test section, the recovery section, and the exit section are constructed of 1.3 cm thick plexiglas reinforced at periodic intervals by plexiglas ribs. The use of transparent plexiglas permitted easy optical access for the application of laser anemometry.

In order to permit LDA measurements close to the wall, the top wall around the measurement location in the test section is deflected slightly into the channel. A large bolt, extending from a rigid aluminum frame placed around the measurement location, is used to press down on the top wall and deflect it inward.

Significant errors in the near-wall unsteady measurements can result from periodic variation at the exciting frequency of the probe location with respect to the wall (see Acharya and Reynolds [1975], Simpson et al. [1983]). The bolt and frame combination mentioned above

served the additional purpose of stiffening the top wall of the channel around the measurement location and therefore reducing any oscillations of the top wall during unsteady operation. From a careful evaluation of the near-wall unsteady data (see Appendix B), it is believed that the present experiments do not have significant errors due to relative movement of the LDA measuring volume with respect to the top wall.

### 3.1.3 Oscillation Mechanism

Water that enters the test section exits the system through two different paths. Some of it is bled off through the porous bottom wall of the test section. The rest of it passes through the recovery section and exits via the porous plate in the exit section. These paths lead to two adjacent but separated ducts. A plate with a number of slots acts as a gate valve that controls the exit of both ducts. There is a specially fabricated Teflon gasket between the exit of the ducts and one of the sides of the gate valve. The gasket serves as a water seal. The other side of the gate valve is open to the atmosphere. Water that passes through the slots in the gate valve drains down into the sump.

The gate valve can slide back and forth freely on ball-bearing supports. The slot area presented to each duct varies as the valve moves, but the total slot area seen by both ducts is always a constant. This area is the main controlling resistance for the flow of water from the overhead tank to the sump below. Since it is a constant, the total flow through the valve is a constant independent of the valve position. Thus the flow rate through the system is independent of the position of the valve.

The fraction of the total slot area seen by the duct connected to the test section is a linear function of the valve position. Thus, to the first order, the proportion of the total flow bled off in the test section is a linear function of the valve position. The gate valve is oscillated back and forth sinusoidally by a Scotch-yoke mechanism driven by a constant-speed DC motor. This causes the fraction of the total flow bled off in the test section to oscillate nearly sinusoidally. Since the suction through the porous plate is distributed throughout the length of the test section, the free-stream velocity decreases nearly linearly with  $x$  and oscillates in response to the oscillating valve.

To compensate for the required pressure drop across the bottom-wall porous plate in the test section, extra correction slots that are exposed only during some portions of the oscillation cycle are used in the gate valve. These slots are carefully trimmed for each of the oscillation amplitudes, to minimize the residual variation in the flow rate upstream, as the valve oscillates.

The system is carefully adjusted so that the free-stream velocity remains a constant throughout the test section when the valve is kept stationary at the position corresponding to the  $0^\circ$  cycle-phase angle. By varying the speed of the DC motor, the frequency of test-section free-stream velocity oscillations can be varied over a range of 0 to 2 Hz. By varying the amplitude of the gate valve oscillations, the amplitude of free-stream velocity oscillations can be varied. The maximum usable free-stream velocity amplitude at the end of the test section, normalized by the mean free stream velocity at the entrance is about 30%. This limit is set by the excessive growth of the boundary layer at low frequencies, for large free-stream adverse gradients, in comparison to the channel height.

#### 3.1.4 Water Treatment and Control

Tap water contains a large number of microscopic particles. For proper operation of the Laser Anemometer system, it was found necessary to filter the water to remove particles larger than about 5 microns. In order to maintain a constant flow temperature over long periods, cooling is continuously provided by passing part of the flow through a water-chiller unit. A thermistor located in the exit section is used to sense the water temperature, and a closed-loop electronic controller is used to vary the duty cycle of the chiller. With this arrangement, the water temperature can be maintained to within  $0.1^\circ\text{C}$ . All experiments were conducted at a nominal temperature of  $17^\circ\text{C}$ .

Chemical treatment of the water to prevent algae growth was not possible, since the chemicals available for this purpose caused excessive numbers of air bubbles to remain in the water, rise to the top wall, and prevent near-wall measurements. The relatively low water temperature was therefore important in minimizing algae growth.

### 3.1.5 LDA Mount

The sending and receiving optics of the laser anemometer system are mounted on two arms of a U-shaped rigid structure constructed out of aluminum channels. These arms hang on either side of the channel. The structure is mounted on a machine slide with fine traverse capability in the Y (vertical) direction. The slide is attached to a carriage that can move in the Z (spanwise) direction on precision guide rods. The guide rods are mounted on a platform that can move in the X direction on wheels supported by I-beams that run parallel to the channel. The platform can be locked in a given place to the I-beams. Since the collecting and receiving optics are fixed to the same rigid structure, the alignment of the optics is not affected as the system is moved about.

### 3.2 Data-Acquisition and Control System

Much of the experimental data acquisition and control procedure was automated to meet the present research objectives in a reasonable amount of time. The typical data-acquisition times were very long. For a good profile definition, a large number of points (30-50) was needed in the boundary layer. For a good signal-to-noise ratio in the phase-averaged velocity and turbulence (especially in the low-amplitude experiment), a large number of cycles (500) was needed. For 0.1 Hz, the above requirements translate to over 100 hours of data collection. The frequency of oscillation needed to be maintained constant over such long times. Several frequencies and X stations needed to be studied to provide a good understanding of the flow behavior and to provide an extensive data set. A computer-based and automated data-acquisition and control system was ideally suited to meet the above requirements.

The data-acquisition and control system (Fig. 3.3) consists of the laboratory computer system, the Laser-Doppler Anemometer system, the shaft position encoder system, the LDA traverse system, the frequency control system, and the pressure-measurement system. Each of these sub-systems will be briefly described below.

### 3.2.1 Laboratory Computer System

The data-acquisition and control system is based on a MINC micro-computer system (Fig. 3.4) consisting of a Digital Equipment Corporation LSI 11/2 processor with 64 KB of memory. Two single-sided double-density diskette drives provide 1 MB of mass storage. The system is equipped with a VT105 Graphics Terminal for interactive usage, an IDS460 Paper Tiger Matrix Printer, and a HP9872C Graphics Plotter interfaced through an IEEE-488 Instrument Bus controller. The system has been configured with the following hardware to facilitate interfacing with laboratory instruments and control systems for real-time data acquisition and control:

Real Time Clock: The clock can be programmed to provide periodic interrupts from 0.002 Hz to  $10^6$  Hz and to time external events; the clock also permits synchronization with external events.

Analog-to-Digital Converter: The A/D has eight fully differential channels, a programmable gain amplifier (gains of 1, 2, 4, and 8), 12-bit accuracy, 35 KHz conversion rate, and a switch-selectable range of (0 to 10) V or (-10 to +10) V.

Digital-to-Analog Converter: The D/A has four channels of 12-bit accuracy and switch-selectable ranges of (0 to 5) V, (0 to 10) V, or (-10 to +10) V.

Digital Input and Output: Two channels of DIN and two channels of DOUT are provided. Each channel is 16-bits wide and includes lines for triggering and sensing service requests from external devices.

All the input and output connectors and switches of the above interface boards are brought to the front panel of the computer for easy connection to laboratory instruments.

### 3.2.2 Laser Doppler Anemometer System

The LDA system is a one-component forward-scatter, differential, Doppler-mode system employing frequency shifting. The Doppler signal is processed by a frequency tracker working on the phase-locked loop principle. The system is composed of the following DISA 55X Modular LDA Optical components.



5 mW He-Ne coaxial laser head,  
55X24 beam splitter,  
55X29 Bragg cell (40 MHz frequency shift),  
55X28 beam displacer,  
55X52 front lens (focal length 600 mm),  
55X34 photo-multiplier optics,  
55X08 photo-multiplier section,  
55N10 frequency shifter,  
55N20 frequency tracker.

The sending and receiving optics are mounted on two rigid arms of the laser mount structure that extend down on either side of the water channel. Two optical-quality mirrors are used for turning the beams into the water channel and for focusing of the collecting optics. The frequency shifter unit can electronically vary the frequency (around 40 MHz) by which one of the beams is shifted with respect to the other. The frequency tracker has both a front-panel digital readout of the velocity and an analog voltage output proportional to the instantaneous tracking frequency, which in turn is proportional to the average velocity of particles in the measuring volume at that instant.

### 3.2.3 Shaft Encoder System

The shaft encoder system consists of a Litton Model 76 Absolute Shaft Position Encoder and the associated electronics. The encoder is connected to the shaft of the DC motor that drives the oscillation mechanism and provides a 10-bit Gray coded output of the angular position of the shaft. The 0° output of the encoder is made to correspond to the 0° cycle-phase angle. The encoder electronics provides the power needed to operate the encoder and converts the Gray code to natural binary code for input to the computer. In addition, the encoder electronics provides sampling triggers at 512 equally spaced phases in the cycle and a pulse at the occurrence of the 0° cycle-phase angle.

### 3.2.4 LDA Mount Traverse System

A SLO-SYN Stepping Motor (Model M093-FC07) is geared to the shaft of the slide of the LDA Mount system. The motor is energized by a SLO-SYN Translator (Type ST101). The translator is controlled by an electronic Probe Controller. The probe-controller electronics can be operated from the front panel or can be controlled by the computer. The controller can be set to provide digital LED readouts of the Y location with respect to the wall of the measuring volume of the LDA in units of 0.0025 cm. Each step of the stepping motor corresponds to 0.00032 cm movement of the measuring volume.

### 3.2.5 Pressure Measurement System

The pressure measurement system is based on a 48-channel scanivalve pressure switch and a Validyne Model MP245 pressure transducer. Pressure transmitting lines from all the pressure taps in the water channel are brought to the Scanivalve. There is provision for purging these lines of trapped air bubbles. The pressure switch is capable of rapid scanning of the channels without imposing a volume change on the transducer. The transducer cavities can also be purged of air bubbles.

The range of differential pressure that the transducer can measure is from 0 to 10 cm  $H_2O$ . The actual range over which the transducer was used in the present experiments was from 2 to 3 cm  $H_2O$ . Over this range, the transducer and the associated electronics were calibrated to an accuracy better than 0.1%. Two columns of water whose height difference could be measured to better than 0.025 mm were used to provide the calibration differential pressure for the transducer.

The pressure measurement system was used in the present work only for measuring the free-stream velocity in the channel under steady operating conditions, and for the calibration of the LDA system (see Section 3.3.3). The free-stream velocity could be measured to an accuracy of better than 0.1%.

### 3.3 Data-Acquisition and Control Procedures

The data-acquisition and control procedures deal with the LDA probe volume positioning, the calibration of the LDA system, the long-term control of frequency, and the experimental run procedure. Each of these is described below.

#### 3.3.1 LDA Probe Volume Positioning

The LDA traverse system permits very precise movement (0.025 cm) of the LDA probe volume in the Y direction. However, each time the LDA system is moved to a different X location, it is necessary to position the measuring volume accurately with respect to the wall. The means and the procedure for doing this are described below.

A standard tunnel port plug was modified to accommodate at its center a stainless steel stem with a disk on the end toward the inside of the tunnel. The stem is spring-loaded so that, in its normal retracted position, the disk would be flush with the wall of the tunnel. The stem and the disk can be pushed into the tunnel and locked in place. A slot is cut on the stem surface perpendicular to the stem axis. A sharp needle is cemented in the slot. The distance of the needle from the surface of the plug is carefully measured using an optical comparator.

The LDA-mount carriage is moved to the desired X location and locked in place. The LDA-mount slide is moved so that the probe volume intersects the tip of the needle. The needle casts a sharp shadow behind, and the bright streaks of laser light on either side of the shadow are made equal in extent in order to position the center of the probe volume with the tip of the needle. This positioning is accurately repeatable to within 0.025 mm.

#### 3.3.2 Frequency Control

The DC motor controller is capable of keeping the frequency of oscillation constant to within 0.2% in the short term. Over the long term, however, due to thermal drift of analog components used in the controller, the frequency can vary considerably. This is especially acute for low frequencies, since the total data-acquisition time needed

for a given number of cycles is large. The problem was overcome by controlling the set-point voltage for the controller externally by the computer.

The transfer function from the external DC voltage input of the motor-speed controller to the oscillation frequency was found to be very highly linear. One channel of the D/A is connected to this input. First, the D/A output is set at the nominal voltage corresponding to the desired frequency, and the real-time clock is set up to time external events. The clock is started on an occurrence of the 0° position and stopped on the next occurrence. The output of the clock is then the period of oscillation from which the actual frequency is calculated. The error in the actual frequency is used to correct the D/A output voltage appropriately and the procedure repeated until the actual and the desired frequencies differ by less than 0.2%. With this procedure, it was possible to keep the oscillation frequency constant to within 0.2% over any desired length of time.

### 3.3.3 LDA Calibration

An LDA system is a linear transducer of velocity to Doppler frequency. Ideally, if the separation of the beams, the front lens focal length and the details and properties of the media along the beam path are known, then the proportionality constant can be easily calculated. In practice, lack of precise knowledge of any of the parameters makes it desirable to do a one-point calibration using another means of independent measurement of velocity. Certainly, it is advisable to cross-check any computed calibration factor with a measured one. The procedure adopted in the present case is described below.

The LDA measuring volume and a pitot tube were positioned in the free stream. The pressure difference between the pitot tube and a static pressure tap at the same  $X$  location was measured very accurately using the pressure transducer, and the free-stream velocity was calculated. From the average Doppler frequency measured by the LDA and the free-stream velocity, the calibration factor for the LDA was easily calculated. This procedure was repeated over a 20% range of free-stream velocities, and the results were averaged. The measured calibration

factor was used in all data reduction. An estimate of the calibration factor made from the beam separation, the focal length of the front lens, and the refractive index of water is only 1.3% different from the measured value.

When the channel is set up for uniform free-stream velocity throughout the rig, the LDA measurements of free-stream velocity along the channel are within 0.5% of the values given by pressure measurements. This indicates that the LDA calibration factor is good to within 0.5% throughout the channel.

### 3.3.4 Experimental Run Procedure

Figure 3.3 shows a schematic of the interconnections among the different parts of the data-acquisition and control system. Only a very brief listing of the different steps involved in running the experiment will be given below. Much of the procedure is automated, and extensive software was developed for data acquisition, control, and processing. The listing of all programs relevant to the running of the experiment can be found in Jayaraman [1982]. The program listings should be consulted for the exact procedural details.

The LDA is moved to the desired  $X$  location, and the probe volume is positioned as described above. The desired frequencies, the  $Y$  locations, the number of cycles to average over, and the run title are input to the data-acquisition program. The program moves the LDA to a desired  $Y$  location (starting from the wall and moving out), sets up a desired frequency, and starts collecting data. Every ten cycles, it verifies the frequency of oscillation and re-synchronizes the data collection with the  $0^\circ$  cycle-phase angle. After data have been collected over the desired number of cycles, the program stores the data on the disk, sets up the next frequency, and repeats the process until all frequencies are done at that  $Y$  location. The program then moves the LDA to the next  $Y$  location and repeats the process until all  $Y$  locations are done.

The whole system has been reliably operated in such an automated mode over periods as long as 240 hours with very minimal operator inter-

vention. This would not have been possible without the precise and continuous control of water temperature, described previously.

### 3.4 Data-Reduction Procedure

Extensive software was developed for the purposes of analyzing the data obtained by the data-acquisition programs. Software packages for plotting of the results using the plotter were also developed. All these programs are listed in Jayaraman [1982] and should be consulted for precise details of the data-reduction and plotting procedures.

The data-acquisition programs obtained phase-averaged streamwise velocity component ( $\langle u \rangle$ ) and its square ( $\langle u^2 \rangle$ ). From these the mean and the periodic components of the streamwise velocity component and the square of streamwise turbulent fluctuations were calculated as shown below.

$$\bar{U} = \overline{\langle u \rangle} ; \quad \tilde{u} = \langle u \rangle - \bar{U} ;$$

$$\langle u'u' \rangle = \langle u^2 \rangle - \langle u \rangle^2 ;$$

$$\overline{(u'u')} = \overline{\langle u'u' \rangle} ; \quad \widetilde{(u'u')} = \langle u'u' \rangle - \overline{u'u'} .$$

The mean velocity data were analyzed using the procedure described by Coles [1968] to determine the wall shear stress and the boundary layer thicknesses. The boundary layer thickness so determined will be referred to as the "Coles boundary layer thickness" in the rest of the report. It is a much more definite parameter than the 99% thickness.

The periodic component of the velocity and the turbulence were analyzed using an FFT procedure to determine the amplitude and the phase of the first harmonic. The variation over the cycle of displacement and momentum thickness and shape factor was computed easily from the phase-averaged velocity profiles.

## Chapter 4

### EXPERIMENTAL RESULTS

Two major series of experiments were done. In the first, the amplitude of free-stream oscillations at the end of the test section normalized by the upstream free-stream mean velocity was about 5%; in the second, it was about 25%. These experiments will be referred to as the "low-amplitude" and the "high-amplitude" experiment, respectively. In both experiments, data were collected at several different frequencies and  $X$  stations. Tables 4.1 and 4.2 summarize all the cases covered by the two experiments and include the corresponding Strouhal numbers, defined as follows:

$$S_x = \frac{\omega(X-X_0)}{\bar{U}} ; \quad S_\delta = \frac{\omega\delta}{\bar{U}} ,$$

where

$X$  is the streamwise distance at the measurement station,

$X_0$  is the streamwise distance of the entrance to the test section,

$\omega$  is the circular frequency in radians/second,

$\bar{U}_e$  is the local free-stream mean velocity, and

$\delta$  is the thickness of the mean boundary layer determined by Coles analysis procedure (Section 3.4).

The streamwise distance in the test section is normalized by the test-section length as follows:

$$x' = \frac{(X-X_0)}{L}$$

where  $L$  is the length of the test section, 60.9 cm. It can be seen that the experiments cover a very wide range in Strouhal number.

Detailed results for all the cases studied are available in a separate report [Jayaraman, Parikh, and Reynolds, 1982] on microfiches. Refer to Appendix A for the organization and contents of the microfiches. In the following presentation of the results of the experiments, only representative cases will be used. They will be primarily

from the high-amplitude experiment supplemented by the low-amplitude cases, where needed to show the effect of amplitude, if any. The term "turbulence" is used to denote the square of streamwise turbulent fluctuations ( $u'u'$ ).

#### 4.1 General Considerations

In evaluating the results to be presented, several important considerations should be kept in mind. These are addressed below.

##### 4.1.1 Number of Cycles

In all cases, phase-averaged streamwise velocity and the square of streamwise turbulent velocity fluctuations were computed over 500 cycles of oscillation. The number of cycles chosen was a compromise between very long run times and good signal-to-noise ratios in the averages. Naturally, the high-amplitude cases have much better signal-to-noise ratios than do the low-amplitude cases. For this reason, the high-amplitude experiment is more extensive than the low-amplitude one.

##### 4.1.2 Zero Frequency Measurements

There is one important difference between the two experiments. In the case of the low-amplitude experiment, the flow-oscillation gate valve could be kept stationary at different locations, and the resulting steady velocity profiles could be measured and used for constructing the response of the boundary layer when subjected to extremely low frequencies of oscillation. This could not be done in the high-amplitude experiment, since under large adverse free-stream gradient conditions the boundary layer separated catastrophically from the wall and a viscous region filled up the entire channel. However, it was found that flow oscillation at frequencies as low as 0.1 Hz was sufficient to prevent the boundary layer from such separation, and meaningful unsteady data could be collected.



#### 4.1.3 Very Near-Wall Data Restrictions

The size of the LDA probe volume in the  $Y$  direction is estimated to be approximately 0.3 mm. The size of the actual measuring volume is determined by the probe volume and the collecting optics, and is likely to be of the order of 0.3 mm. The output signal of the photomultiplier is an average of signals from particles in different parts of the measuring volume. If the probe volume center is moved closer to the wall than its radius, then part of the volume is cut off by the wall. The effective center of such a truncated volume is farther from the wall than the probe volume center. It is estimated that data closer to the wall than 0.2 mm suffer from the above restrictions, due to finite measuring volume size.

The effect on mean velocity is to measure higher velocity than actual at a given distance from the wall. Another way to look at this is to say that the measured velocity is to be ascribed to a location from the wall farther than the nominal location. Data from such locations are still included in the results to be presented below. It is believed that they are useful for extracting qualitative trends. No conclusions will be drawn based solely on data from such locations without attendant warnings to that effect.

It should be mentioned that the effect of these points near the wall on computation of boundary layer integral thicknesses and shape factor is very small. This can be seen by comparing the results of computing these parameters for the mean profiles by two different methods. In one method, standard wall functions are used up to a  $Y^+$  of 50 and the experimental data beyond, as suggested by Coles [1968]. In the other scheme, only experimental data are used throughout. The difference between the two methods in all cases is found to be less than 0.2%.

#### 4.1.4 Estimated Uncertainties

Recall that one of the main objectives of this work is to provide a definitive data set on a well-defined unsteady turbulent boundary layer for the purposes of evaluating the performance of computational methods and turbulence models for such flows. As pointed out by Moffat [1981], such a comparison is meaningful only in the light of the  $N^{\text{th}}$ -order

uncertainties in the measured and computed results. The  $N^{\text{th}}$ -order uncertainty in a measured value is an estimate of its absolute accuracy and includes the scatter on repeated trials ( $1^{\text{st}}$ -order uncertainty).

The estimated  $N^{\text{th}}$ -order uncertainties in the measured and calculated quantities are shown in Table 4.3. The associated confidence level is 20 to 1. The  $N^{\text{th}}$ -order uncertainties were propagated using the procedure set forth by Kline and McClintock [1953]. Note that many of the estimates are dependent on the location in the boundary layer and the amplitude of oscillation.

#### 4.2 Flow Qualification

The purpose of this section is to establish that the flow in the test rig is spanwise uniform, the growth of the boundary layer in the rig under zero pressure-gradient conditions is normal, and the induced disturbance upstream during unsteady operation is acceptably small. Each of these issues is discussed below.

##### 4.2.1 Spanwise Uniformity

To determine the two-dimensionality of the flow in the tunnel, closely sampled spanwise surveys of velocity at a fixed location from the wall in the boundary layer were taken by moving the LDA measuring volume in the spanwise direction. In the pre-test operation of the test rig, with 60% open area ratio screens, it was found that the mean velocity varied periodically in the spanwise direction, with the peak-to-peak variation being more than 10% of the free-stream velocity. The cause of this variation was ultimately traced to the screens upstream. It appears that the screen surface should be stretched tight to eliminate any wrinkles that cause longitudinal vorticity, which causes spanwise variation in velocity. Reconstruction of the screen box with plexiglas permitted very easy detection of deterioration of cleanliness of the screens. Use of 70% open area ratio screens that can be removed periodically for cleaning and kept very tightly stretched in place put the problem under complete control.

Figures 4-1a-d show typical spanwise variations in the mean velocity (normalized by the mean free-stream velocity at the entrance to the test section,  $U_0$ ), the mean turbulence (normalized by the square of  $U_0$ ), the amplitude of velocity oscillations (normalized by  $U_0$ ) and its phase angle at  $X' = 0.94$  for the low-amplitude experiment. Figures 4.1e-f show the same for the high-amplitude experiment. The spanwise uniformity is worst at the end of the test section, and this point was chosen for that reason. The abscissas are normalized by the channel width. Note that the data points cover the central half of the channel and that they are closely spaced (about a quarter of the mean boundary layer thickness).

The mean velocity is constant to within 1% across the span, while the root-mean-squared turbulence is uniform to within 1.5%. The variation in the amplitude of velocity oscillations is within 0.3%, while that of the phase angle is less than  $3^\circ$  across the span. The worst spanwise nonuniformity is found in the mean turbulence in the high-amplitude case. It is interesting that this variation does not show up in the mean velocity, the amplitude, or the phase.

The results presented are at one fixed location from the wall for one frequency of oscillation. Measurements at other  $Y$  locations,  $X$  stations, and frequencies show variation of the same order. Thus it can be concluded that the flow in the central half of the channel is very highly two-dimensional with respect to both the mean and the periodic flow fields.

#### 4.2.2 Zero Pressure-Gradient Boundary Layer Development

Figure 4.2 shows the free-stream velocity variation with respect to  $X$  in the test rig when the flow-oscillation gate valve is set at the position corresponding to  $0^\circ$  cycle-phase angle. Note that, with careful adjustment of the bottom-wall suction in the development section to account for the blockage due to the growth of boundary layers, the free-stream velocity is uniform to within 0.3%. This adjustment needed very little changes over very long periods of operation of the rig.

Figure 4.3 shows the development of the mean velocity in the development section in inner coordinates. For comparison, the corresponding

Coles velocity profiles are also shown in the figure. Note the normal log-linear region and the growth of the wake component as the boundary layer grows.

Figures 4.4a-b show the development of the Coles boundary layer thickness and the displacement thickness under zero pressure gradient conditions in the rig. Both grow as a power of  $X$  somewhat less than 1 ( $\approx 0.8$ ).

Figure 4.5 shows the skin-friction coefficient variation with respect to momentum thickness Reynolds number compared to results from Anderson et al. [1972] for the same range of Reynolds numbers. The agreement is quite good.

Figure 4.6 shows the defect velocity profile at the last measurable  $X$  station in the upstream development section. The data are compared with data from Klebanoff [1955], and the agreement is excellent. The mean turbulence profile in the same boundary layer is compared to Klebanoff's data in Fig. 4.7. The agreement is very good in the outer part of the boundary layer, but the present data are somewhat lower in the near-wall region. The boundary layer momentum thickness Reynolds number for the present boundary layer is about 2500, whereas that of Klebanoff is 7300. This is thought to be the cause of this difference.

A global check on the two-dimensionality of the flow is to perform a momentum balance on the data. The procedure followed is the same as that described in Coles and Hirst [1968]. As pointed out by Moffat [1981], this balance is a useless exercise without an assessment of the significance of any imbalance, in light of the estimated  $N^{\text{th}}$ -order uncertainty in closing the momentum integral equation. Figure 4.7.1 is a plot of the left- and the right-hand sides of the integrated form of the momentum integral equation, normalized by the momentum deficit at the first profile. Shown also is the estimated  $N^{\text{th}}$ -order uncertainty in closing the equation. It is clear that the momentum balance is within the estimated uncertainty.

Thus one can conclude that the growth of the boundary layer in the test rig under zero pressure-gradient conditions is normal and two-dimensional. For reference purposes, some of the parameters associated

with the boundary layer at the entrance to the test section are given below.

Free-stream velocity, $U_0$	732 mm/s
Coles boundary layer thickness, $\delta$	35.5 mm
Displacement thickness, $\delta_1$	5.9 mm
Momentum thickness, $\delta_2$	4.2 mm
Shape factor, $H$	1.42
Momentum thickness Reynolds Number, $R_{\delta_2}$	2790
Skin friction coefficient, $C_f$	$3.22 \times 10^{-3}$
Kinematic viscosity, $\nu$	$1.09 \times 10^{-6} \text{ m}^2/\text{s}$

#### 4.2.3 Upstream Disturbance

Ideally, there would be no variation in the upstream flow as the flow is oscillated in the test section. This would be the case if there were no flow capacitance in the system and if the only resistance to the flow were due to the slots in the gate valve. Neither of the above requirements is met exactly in reality. There is a finite flow capacitance in the system, due perhaps to the flexibility of plexiglas. To have uniform suction in the bottom-wall porous plate in the test section, there needs to be sufficient pressure drop across the plate, compared to the static pressure change in the test section. Nonuniformity of suction in the test section would result in phase variation in the free stream, causing the phase-averaged free stream to be nonlinear. Extra correction slots that are exposed only during some portion of the oscillation cycle were needed in the gate valve to compensate for the required pressure drop across the porous plate. Both the correction slot and the sizing of the holes in the porous plate needed to be carefully trimmed for each of the oscillation amplitudes studied. Thus it should be understood that the actual upstream disturbance and the imposed free-stream excitation in the experiments to be presented below were the best achievable in the test facility without resorting to more active control.

Figure 4.8 shows the root-mean-square value of the velocity oscillations in the boundary layer at the last measurable  $X$  station in the development section, expressed as a percentage of the free-stream mean velocity. The reason for using rms values is that the organized disturbance velocity upstream is not sinusoidal for some frequencies. Several frequencies are shown for the high-amplitude experiment. It is clear that the disturbance level is essentially constant within the boundary layer and that the level increases with frequency. Even for the highest frequency, it is only about 1.6%. The disturbance levels for the low-amplitude experiments (not shown) are even lower.

Figures 4.9 and 4.10 show the mean velocity and mean turbulence profiles at the same  $X$  location at different frequencies. The profiles show no effects due to the small unsteadiness in the free stream.

Thus the upstream flow, for all practical purposes, can be considered to be a normal, standard, steady, flat-plate boundary layer, unaffected by the downstream flow oscillations.

#### 4.3 Imposed Free-Stream Excitation in the Test Section

The design objectives for the imposed free-stream oscillations in the test section were as follows:

- linear decrease in time-averaged free-stream velocity;
- linear increase in the amplitude of oscillations;
- linear variation of phase-averaged free-stream velocity.

These requirements implied that there would be no phase variation in the free-stream oscillations. How well these objectives were met in the actual test rig is discussed below.

Figures 4.11a-b show the variation of the free-stream mean velocity in the test section at different frequencies for the high- and the low-amplitude experiments. The mean velocity in the upstream development section is used for normalization, and the  $X$  distance in the test section is expressed as a fraction of its length. The mean velocity decreases linearly with distance, as per the design objective.

Figures 4.12a-b show the variation of the free-stream amplitude of oscillation normalized by the development section free-stream mean velocity for the two experiments. The amplitude grows linearly with distance, as per the design objective. For the high-amplitude experiment, the slope is somewhat lower at lower frequencies. The large variation in the thickness of the boundary layer over the oscillation cycle at lower frequencies is believed to be the cause of the lower slope.

Figures 4.13a-b show the variation of the free-stream phase angle with respect to the last measured station in the recovery section. The phase lag in the upstream locations in the test section increases with frequency. Rapid variations in phase appear where the oscillation amplitudes are relatively small. The phase variation is less than  $20^\circ$  over two-thirds of the test section downstream and the recovery section. These phase variations are believed to be caused by the non-uniformity in the bottom-wall suction and not by a traveling wave inherent to the flow. They are expected to have very little effect on the behavior of the boundary layer. They have been fully documented for inclusion in any computational scheme.

Figures 4.14a-d show the phase-averaged free-stream velocity variation in the test section for the 0.5 Hz high-amplitude case. The variation in the cycle phase angle range of  $60$  to  $300^\circ$  is linear, as per the design objective. The variation around  $0^\circ$  is distinctly nonlinear. No such problems exist in the low-amplitude experiment, as shown in Figs. 4.15a-d for the 0.5 Hz case.

Thus it is clear that the mean and the amplitude of the imposed free-stream variation in the test section closely match the design requirements, while the phase does not. It is recommended that computational procedures use the actual free-stream variation.

#### 4.4 Mean Velocity and Turbulence

Figures 4.16a-b show the mean velocity profiles at one  $X$  station at different frequencies. The distance from the wall has been normalized by the Coles boundary layer thickness of the mean velocity profile. The mean velocity is normalized by the free-stream mean velocity. No significant variation with frequency can be seen in the low-amplitude

experiment. In the high-amplitude experiment, a small variation is seen at low frequencies.

Figures 4.17a-b show the variation of mean turbulence profiles at the same X station. The results are the same as for the mean velocity profiles. Once again, the high-amplitude experiment low-frequency cases show a small variation with frequency.

Thus it is clear that the mean flow is essentially unaffected by unsteadiness in agreement with all the previous works reviewed in Section 1.2. Results from other X stations are presented in Jayaraman, Parikh, and Reynolds [1982] and show the same behavior. The behavior of the mean flow is discussed further in Section 5.1.

#### 4.5 Periodic Velocity

The free-stream excitation imposed on the test section and the response of the boundary layer in all cases were found to be very nearly sinusoidal. Spectral analysis of the periodic velocity shows that there are no pronounced harmonics but a broad band distribution, due to residual noise from the phase-averaging process. The total harmonic distortion in terms of energy in the worst case was about 1.5%. Typically, it was less than 0.5%. Thus, it is sufficient to present the amplitude and the phase of the periodic velocity component at the exciting frequency.

##### 4.5.1 Amplitude

Figures 4.18a-b show the amplitude of the periodic velocity component at the exciting frequency normalized by the free-stream amplitude at a number of frequencies. The abscissa normalization is the same as in the mean profiles. Several observations can be made, as follows:

- At low frequencies, the oscillation amplitude in the boundary layer exceeds that in the free stream; it can be as large as twice the free-stream amplitude.
- The overshoot seen above is strongly suppressed as the frequency increases; the location of the peak moves closer to the wall.
- At low frequencies, there is a region in which the amplitude variation is log-linear. This region corresponds closely with the log-linear region in the mean velocity



profile. As the frequency increases, the extent and the slope of this region decrease; at high frequencies, there is no evidence of such a region.

- At high frequencies, the outer-region amplitude is very nearly the same as that of the free stream. All the variation is confined to a thin region close to the wall. The size of this region decreases with frequency. There is a region where the amplitude is somewhat larger than the free-stream amplitude.
- The variation in the inner region with frequency is non-monotonic. There are intermediate frequencies for which, throughout the boundary layer, the velocity amplitude is less than that in the free stream.

Thus one can conclude that the periodic velocity field is very strongly affected by the frequency of oscillation. The behavior at other  $X$  stations is similar, as can be seen from the results presented in Jayaraman, Parikh, and Reynolds [1982]. Further evidence of this can be seen in the behavior of the phase of the first harmonic component, presented next.

#### 4.5.2 Phase

Figures 4.19a-b show the variation of the phase angle of the fundamental component of the periodic velocity with respect to the phase angle of the free-stream velocity at different frequencies. Several observations can be made, as follows:

- At very low frequencies ( $f \sim 0$ ), the time for the boundary layer to respond fully to the imposed changes in the free stream will be much less than the oscillation time period; thus there will be no phase difference in the boundary layer with respect to the free stream.
- At low frequencies, almost all of the boundary layer lags with respect to the free stream; this lag increases with frequency up to a certain frequency.
- At low frequencies, rapid changes in the phase take place in the outer region; there is a region extending to the wall in which there are no appreciable phase variations; this region corresponds to the log-linear region of the mean velocity and the amplitude profiles at corresponding frequencies.
- There is a frequency beyond which the inner region leads with respect to regions farther from the wall; the extent

of the region of constant phase in the inner region seems to decrease and disappear altogether at high frequencies.

- At high frequencies, there is no phase variation in the outer region; it lags the free stream by a small angle. Rapid phase variations take place in a thin region close to the wall; this region exhibits phase leads with respect to the free stream. The phase lead increases with frequency.

These results for the phase of the first harmonic component confirm the strong dependence on frequency of the periodic velocity field seen in the behavior of the amplitude. Jayaraman, Parikh, and Reynolds [1982] give results at other  $X$  stations showing the same trends. The periodic flow behavior and its implications on quantities such as the displacement thickness and the wall shear stress are discussed in detail throughout Chapter 5. The results for the periodic streamwise turbulent fluctuations will be presented next.

#### 4.6 Periodic Turbulence

The signal-to-noise ratio in the phase-averaged turbulence ( $\langle u'u' \rangle$ ) is much lower than in the phase-averaged velocity. There could be significant harmonic content in the periodic component of turbulence ( $u'u'$ ). However, only the component at the exciting frequency is considered in the following results.

##### 4.6.1 Amplitude

Figures 4.20a-b show the variation of the amplitude of oscillations in  $\langle u'u' \rangle$  as a function of frequency at one  $X$  station in each experiment. The amplitude is normalized by the square of the free-stream mean velocity and the distance from the wall by the Coles boundary layer thickness of the mean velocity profile. Several points to note are as follows:

- At low frequencies, there are two distinct regions where significant turbulence oscillations take place. One is in the inner region, and the other in the outer region of the boundary layer. Relatively little oscillation is present in the region in between.
- In general, as the frequency increases, the oscillation amplitude decreases throughout the boundary layer.

- At high frequencies, the outer-region oscillations are almost completely suppressed, indicating that the turbulence does not vary through the cycle and is essentially the same as the mean.
- The turbulence structure near the wall does vary somewhat through the cycle, even at high frequencies. The variation is considerably less than at lower frequencies.

The above results demonstrate the dynamical nature of the response of turbulence to the imposed unsteadiness. Further evidence is provided by the phase of the first harmonic component given below.

#### 4.6.2 Phase

Figures 4.21a-b show the variation of the phase of the oscillations in turbulence with respect to the free-stream oscillations. Several frequencies in both experiments are shown. The following observations can be made:

- At low frequencies, there are two distinct regions that are out of phase with each other; the phase variation within each region is small, and the changeover from one region to the other is abrupt.
- As frequency is increased, the constant-phase outer region persists, although at high frequencies the data are rather scattered, due to diminishing oscillation amplitudes in that region.
- A thin region close to the wall seems to be in phase with the free-stream oscillations throughout the frequency range.
- At medium and high frequencies, the turbulent oscillations away from the wall lag the free-stream oscillations; the lag increases with distance from the wall and frequency; there is no region of abrupt phase transition, as in the low-frequency cases.

The results for the amplitude and the phase of the fundamental component of the periodic turbulence clearly show its strong dependence on the frequency of excitation.

#### 4.7 Phase-Averaged Velocity Profiles

Figures 4.22a-d, 4.23a-d, 4.24a-d show the phase-averaged velocity profiles every 15° in the oscillation cycle at  $X' = 0.88$  for the low-

amplitude experiment for three different frequencies. The velocity is normalized by the free-stream mean velocity and the distance from the wall by the mean boundary layer Coles thickness. At this low amplitude, it is seen that the profiles are very similar throughout the cycle. There is a definite region where the profiles are log-linear at all frequencies.

Figures 4.25a-d, 4.26a-d, 4.27a-d show the phase-averaged velocity profiles at the same frequencies as above, at  $X' = 0.94$  in the high-amplitude experiment. The velocity in these figures is normalized by the phase-averaged free-stream velocity. Several observations can be made, as follows:

- The shape of the velocity profiles undergoes large changes over the cycle at all frequencies.
- At low frequencies, the boundary layer thickness varies greatly over the cycle; the variation decreases with frequency. At high frequencies, the boundary layer thickness is essentially constant over the cycle.
- As the cycle-phase angle increases, the wake component of the velocity profile increases while the near-wall velocities decrease. At high frequencies, the flow near the wall is reversed over part of the cycle around  $180^\circ$ .
- When the near-wall velocities are very small and/or negative, there is no appreciable log-linear region in the profiles.
- The size of the region of reversed flow and the phase range over which it occurs increase with frequency; this can be seen from examination of phase-averaged velocity profiles at a number of high frequencies (not shown).

The results for the phase-averaged velocity profiles are in agreement with the amplitude and the phase results presented earlier.

#### 4.8 Phase-Averaged Turbulence Profiles

Figures 4.28a-h, 4.29a-h, 4.30a-h show the phase-averaged turbulence profiles every  $15^\circ$  in the oscillation cycle at  $X' = 0.88$  in the low-amplitude experiment for three different frequencies. The ordinate is normalized by the square of the mean free-stream velocity. The profiles are very similar. The near-wall turbulence is suppressed as cycle angle increases from  $0^\circ$ .

Figures 4.31a-h, 4.32a-h, 4.33a-h show the phase-averaged turbulence profiles for the same frequencies at  $X' = 0.94$  in the high-amplitude experiments. The following observations can be made:

- At low frequencies, the turbulence profile undergoes large changes in shape over the oscillation cycle. The peak moves from the wall to the outer region as the cycle phase angle increases from  $0^\circ$ . The variation decreases as frequency is increased; at the highest frequency, the outer region is essentially invariant, while the near-wall structure varies somewhat over the cycle.
- At low and intermediate frequencies, during the portion of the cycle when the phase-averaged velocity near the wall is very small, the turbulence also is very small near the wall; at the same time, the turbulence in the outer region is very high. Thus the turbulence oscillations in the inner and outer regions are essentially out of phase, as has been observed before.

Once again, these results are in agreement with the behavior of the amplitude and the phase of turbulence presented earlier.

#### 4.9 Computed Quantities

There are 512 phase-averaged velocity profiles available over the oscillation cycle for each case. For each of these velocity profiles, the boundary layer 99% thickness, the displacement and momentum thicknesses, and the shape factor are calculated. Note that these are not necessarily the same as the phase averages of the same variables. The behavior of these parameters in the experiments will be discussed below.

Figures 4.34a-e show the variation of computed thickness and shape parameters over the oscillation cycle at  $X' = 0.88$  in the low-amplitude experiment, for five different frequencies. Figures 4.35a-e show the same at  $X' = 0.94$  for the high-amplitude experiment. The abscissa is the difference between the cycle phase angle from the shaft encoder and the free-stream phase angle at that location. The quantities are normalized by their mean values. The following points can be noted:

- The variation of the computed thicknesses for the low-amplitude cases is essentially sinusoidal; the high-amplitude cases exhibit large harmonic distortions.

- The variation in the shape factor over the cycle is small for the low-amplitude cases; the high-amplitude cases show much higher variation, especially at low frequencies.
- In general, the extent of the variation decreases with increasing frequency; at high frequencies, there is no appreciable variation in the boundary layer thickness.
- In the low-amplitude cases, the thicknesses are essentially in phase over all frequencies; this is definitely not the case in the high-amplitude cases.
- At high frequencies, the displacement thickness is nearly  $180^\circ$  out of phase with the free-stream velocity. It should be noted that, at very low frequencies, all thicknesses are  $180^\circ$  out of phase with the free stream; this phase lag with respect to the free-stream increases as the frequency increases. Apparently, for the displacement thickness, there is a frequency at which its phase lag with respect to the free stream is a maximum. For higher frequencies, its phase lag decreases, and at sufficiently high frequencies, it is nearly  $180^\circ$ .

The results for the variation of the integral thicknesses over the cycle for different frequencies serve to reinforce further the strong dependence of the periodic velocity field on frequency.

#### 4.10 Summary of Results

The results presented in the previous sections are only a representative sample from the very extensive data set that has been created in the present research. Results for all the cases studied in the form of plots and tables are presented in Jayaraman, Parikh, and Reynolds [1982]. A table of contents of the microfiche report is given in Appendix A.

The results shown have demonstrated the insensitivity of the mean flow field to the imposed unsteadiness, while stressing the strong dependence on frequency of the periodic flow field. A rationale for understanding some of the results is given in the next chapter.

## Chapter 5

### DISCUSSION

In the previous chapter, a representative sample of results from the experiments was presented. The results show that the experiments performed provide a definitive data set in a well-defined, unsteady, turbulent boundary layer over a wide range of frequencies and amplitudes. The purpose of this chapter is to try to understand the physical reasons for the observed behavior of the flow. The emphasis will be on major effects without too much attention to very fine detail.

In summarizing previous related research on the subject in Chapter 1, it was pointed out that several unanswered questions remained. Any answers, suggestions, or clarifications that the present experiments may provide for those questions will be looked for in this chapter. Where possible, the results will be compared to some simple analyses.

#### 5.1 Mean Velocity and Turbulence

The results presented in Section 4.4 clearly show that, over a wide range of frequencies, the mean velocity and the mean turbulence are essentially unaffected by the type of free-stream unsteadiness imposed in these experiments. In Section 2.5, the order of magnitude analysis showed that the governing equation for the mean velocity (Eq. (2.28)) is the same as for steady flows, as long as the free-stream amplitude is less than about 30% of the mean. Thus, invariant mean velocity would imply invariant  $\overline{u'v'}$  and vice versa. Only  $\overline{u'u'}$  was measured in the experiments. It would be reasonable to expect that its invariance with frequency is a fair indication of invariance of  $\overline{u'v'}$ . The experimental results show that mean velocity and mean turbulence are virtually constant with frequency; thus they are self-consistent with and supportive of the order of magnitude analysis that led to Eq. (2.38).

The low-frequency, high-amplitude cases (0.1 Hz to 0.2 Hz) do show some small variation with frequency. Figure 4.11b shows that the imposed free-stream mean velocity gradient in the test section for the 0.1 Hz, high-amplitude case is somewhat lower than that for higher frequencies. It was already noted in Section 4.3 (see Fig. 4.12b) that

the rate of increase of free-stream oscillation amplitude was also lower for the same case. Results from Section 4.9 (see Fig. 4.35) show that the boundary layer thickness undergoes very large variation over the cycle at low frequencies and that this variation is suppressed as the frequency increases. Its mean value is also larger for low-frequency cases.

The behavior of the thickness of the boundary layer at low frequencies discussed above causes the imposed free-stream excitation for such cases to be somewhat different from the higher-frequency cases. This is believed to be the cause of the small variation in the mean velocity and the mean turbulence profiles seen in the low-frequency, high-amplitude cases.

## 5.2 Behavior of Design Pressure Gradient

The external pressure gradient imposed on a boundary layer exerts a tremendous influence on its behavior. It will be instructive to study the behavior of the imposed pressure gradient for the present experiments, for different frequencies and amplitudes. As will be shown below, such an analysis is very useful in identifying important parameters that govern the flow and different flow regimes with respect to such parameters. For the sake of simplicity and easy identification of the analytical dependence on flow parameters, only the design pressure gradient is dealt with below.

Let

$$\langle U_e(X,t) \rangle = U_0 \left[ 1 - \frac{a(X-X_0)}{L} (1 - \cos \omega t) \right] \quad (5.1)$$

where

$a$  is the amplitude of oscillation of free-stream velocity at the end of the test section as a fraction of  $U_0$ .

Define

$$C_p = \frac{(p - p_0)}{\frac{1}{2} \rho U_0^2}$$

where



$p$  is the instantaneous static pressure,

$p_0$  is the reference static pressure at the entrance to the test section, and

$\rho$  is density.

Define:

$$S_x = \frac{\omega(X - X_0)}{\bar{U}_e} = \frac{\omega(X - X_0)}{U_0(1 - aX')} = \frac{\omega l}{U_0} \frac{X'}{1 - aX'}$$

and

$$G = \frac{\partial C_p}{\partial X'}$$

Using Eq. (5.1) in the momentum equation applied at the free stream, together with the definitions above, after separating mean and oscillatory components, the following relations can be derived:

$$\bar{G} = 2a(1 - \frac{3}{2} aX') \quad (5.2)$$

$$\frac{A_{1,G}}{\bar{G}} = \frac{\left[ S_x^2 (1 - aX')^2 + (1 - 2aX')^2 \right]^{1/2}}{\left[ 1 - \frac{3}{2} aX' \right]} \quad (5.3)$$

$$\phi_{1,G} = \arctan \left[ S_x \frac{(1 - aX')}{(1 - 2aX')} \right] \quad (5.4)$$

and

$$\frac{A_{2,G}}{A_{1,G}} = \frac{aX'/2}{\left[ S_x^2 (1 - aX')^2 + (1 - 2aX')^2 \right]^{1/2}} \quad (5.5)$$

where

$A_{1,G}$  is the fundamental amplitude of the pressure coefficient gradient,

$A_{2,G}$  is the 2nd harmonic amplitude, and

$\phi_{1,G}$  is the phase of the fundamental component.

The time-averaged free stream is clearly

$$\bar{U}_e = U_0 \left[ 1 - aX' \right] \quad (5.6)$$

and the corresponding steady, pressure-coefficient gradient is easily shown to be

$$\frac{\partial C_{p_s}}{\partial X'} = 2a(1 - aX') \quad (5.7)$$

where  $p_s$  is steady static pressure.

The above derivations clearly show that the design pressure gradient is dependent on two parameters--a local frequency parameter in the form of a Strouhal number ( $S_x$ ) based on the  $X$  distance in the test section and the local mean free-stream velocity, and a local amplitude parameter ( $aX'$ ). For the experiments reported here,  $a$  has values of 0.05 and 0.25, approximately;  $S_x$  ranges from about 0.1 to 10.0. The behavior of each component of the unsteady design pressure gradient will be discussed below.

The time mean-pressure gradient (Eq. (5.2)) is not a function of frequency. It is always less than the steady-pressure gradient corresponding to the time mean free-stream velocity distribution (Eq. (5.7)). The difference between the two is larger for higher amplitudes.

Figure 5.1 shows the variation of the fundamental amplitude of the design pressure gradient normalized by the mean pressure gradient as a function of frequency parameter  $S_x$  and the amplitude parameter ( $aX'$ ). It is clear that the pressure-gradient amplitude is essentially a function only of  $S_x$ . The dependence on the amplitude parameter is very weak.

Figure 5.2 shows the variation of the phase of the first harmonic pressure-gradient oscillations with respect to the free-stream velocity oscillations as a function of  $S_x$  for different ( $aX'$ ) values. For very low  $S_x$  values (i.e.,  $f = 0$  Hz), the pressure gradient is  $180^\circ$  out of phase with respect to the free-stream oscillations, since the

pressure gradient increases as the free-stream velocity decreases. The plot shows that the pressure-gradient oscillations undergo a phase advance as  $S_x$  increases. For very high  $S_x$  values, the pressure gradient lags the free stream by  $90^\circ$ . The dependence on the amplitude parameter is once again much weaker than the dependence on  $S_x$ .

Figure 5.3 shows the amplitude of the second harmonic pressure-gradient oscillations normalized by the fundamental amplitude as a function of  $S_x$  for different values of  $(ax')$ . The harmonic distortion is higher for higher amplitudes; it decreases as  $S_x$  increases. It is utmost about 20% of the fundamental amplitude; for  $S_x > 1$ , it is less than about 10% for all amplitudes. Hence, one can expect appreciable harmonic distortion in the variation of global parameters in the high-amplitude experiment for low-frequency, downstream  $X$  station cases.

To summarize, the behavior of the design pressure gradient clearly shows that, for the present experiments, the frequency parameter,  $S_x$ , is much more important than the amplitude parameter. Further, there are two different flow regimes with respect to  $S_x$ , as discussed below.

### 5.3 Flow Regimes

Figure 5.1 shows two distinct regions. For  $S_x < 1$ , the normalized pressure-gradient amplitude is essentially constant. In this regime, the effect of the pressure-gradient oscillations will not be materially different from that at  $S_x = 0$ . The flow can be expected to be governed by inertia. In general, as the frequency (and hence  $S_x$ ) increases, the effects of inertia are to reduce the amplitude of oscillations of the periodic velocity and to cause it to lag increasingly when compared to the velocity oscillations at  $S_x = 0$ . Ample evidence for this behavior is seen in results presented in Section 4.5.

The pressure-gradient oscillations begin to increase rapidly for  $S_x > 1$ . This pressure-gradient excitation is very strong compared to the mean pressure gradient for high  $S_x$  values. The increasing pressure-gradient oscillations counteract the effects of inertia. One can expect the near-wall velocities, which are governed primarily by pressure gradient, to vary more and more over the cycle in response to

the imposed pressure-gradient oscillations as  $S_x$  increases. This increase in amplitude of near-wall velocity oscillations should cause the wall shear stress to increase in amplitude. Since the pressure-gradient oscillations undergo phase advances as  $S_x$  increases, one would expect the near-wall velocity oscillations and hence the wall shear-stress oscillations to undergo phase advances as well. Once again, results from Section 4.5 bear ample evidence in support of this. The expected wall shear stress will be discussed in Section 5.6.

#### 5.4 Importance of Strouhal Number: Behavior of Displacement Thickness

From the study of the behavior of the unsteady design pressure gradient, one can conclude that  $S_x$  is a very important parameter for the experiments reported here. It should be useful to establish that the behavior of global quantities for all the cases studied can be collapsed into a single curve which is a function of  $S_x$ . It is doubtful that the collapse would be perfect. Definitely there would be history- and perhaps amplitude-related nonlinearities that cannot be collapsed by  $S_x$ . Still, even to establish that  $S_x$  is the dominant parameter for the flow would be very useful, if only in reducing the number of plots to be presented.

The displacement thickness was chosen as the global quantity of interest with which to establish the importance of  $S_x$ . From the phase-averaged velocity profiles, the variation of the displacement thickness was calculated. From that, the amplitude and the phase of the first harmonic component were determined by a Fast Fourier Transform harmonic analysis procedure. It should be noted that, at low  $S_x$  values and at most downstream  $X$  stations in the high-amplitude experiment, there was considerably higher harmonic content in the displacement-thickness variation. The first harmonic was always the most energetic component, however.

Figure 5.4 shows the variation of the amplitude of the displacement thickness as a function of  $S_x$  for all the cases studied. The amplitude has been normalized by the mean displacement thickness and further normalized by the relative amplitude of the free-stream oscillations to remove any amplitude effects. The collapse is reasonably good beyond

$S_x = 1$ . For lower  $S_x$  values, the data for the high- and the low-amplitude experimental cases seem to collapse to different values. This is perhaps due to amplitude-related nonlinearities in the behavior of the displacement thickness. Note that the amplitude falls off rapidly until it reaches a value of about 1 around  $S_x = 3$ . Beyond that, the amplitude is essentially 1, as it should be for a high-frequency, thin Stokes layer (see Section 5.5).

Figure 5.5 shows that the phase of the displacement thickness with respect to the free stream collapses reasonably well as a function of  $S_x$ . At very low  $S_x$  values, the displacement thickness oscillates  $180^\circ$  out of phase with the free stream. As  $S_x$  increases but remains less than about 2, the effect of inertia is to cause the phase to lag increasingly with respect to  $S_x = 0$ . The lag reaches a maximum of about  $45^\circ$ . As  $S_x$  increases beyond 2, the increasing phase advances in the near-wall velocity profile cause the phase of the displacement thickness to advance. At very high  $S_x$  values, the displacement thickness is once again  $180^\circ$  out of phase with the free stream, consistent with the Stokes solution, to be shown later in Section 5.5.

It can be concluded, from the above evidence, that  $S_x$  is a very useful and, indeed, the dominant parameter for the flow studied here. The expected behavior of the wall shear-stress oscillations to be discussed later lends further support to its importance.

### 5.5 High Strouhal Number Behavior

It was shown in Section 2.5 that, for very high Strouhal numbers, the governing equation for the oscillatory component of the velocity reduces to the Stokes equation. The solution to this equation is not dependent on the mean velocity field; it is dependent only on the local free-stream velocity variation. The equation is easily solved, as shown below.

For a periodic free-stream velocity variation of the form

$$U_e = \bar{U}_e + A_{1,U_e} \cos(\omega t) \quad (5.8)$$

where  $\bar{U}_e$  is the time-averaged free-stream velocity and  $A_{1,u_e}$  is the fundamental amplitude of free-stream oscillations. Equation (2.30) can be easily solved. The solution is given below.

$$\frac{A_{1,u}}{A_{1,u_e}} = \left[ \{1 - \exp(-y_s) \cos(y_s)\}^2 + \{\exp(-y_s) \sin(y_s)\}^2 \right]^{1/2} \quad (5.9)$$

$$(\phi_{1,u}) = \arctan \left[ \frac{\exp(-y_s) \sin(y_s)}{1 - \exp(-y_s) \cos(y_s)} \right] \quad (5.10)$$

where

$A_{1,u}$  is the amplitude of the fundamental component of the velocity oscillation,

$\phi_{1,u}$  is the phase of the fundamental component, and

$$y_s = \frac{y}{\lambda_s},$$

with

$$\lambda_s = \sqrt{\frac{2\nu}{\omega}},$$

where

$\nu$  is the kinematic viscosity.

In order to check the validity of Stokes' solution for high-Strouhal-number experimental cases reported here, data from such cases were plotted, along with the Stokes solution. Cases for  $S_x$  of 9.57 and 12.40 are from the low-amplitude experiment; the rest are from the high-amplitude experiment. Cases with  $S_x$  values of 12.40 and 15.68 are from  $X$  stations in the recovery section of the test rig. The first three or so points near the wall for each case suffer from the near-wall data restriction discussed earlier.

Figure 5.6 shows the amplitude of the velocity oscillations in the boundary layer normalized by the free-stream amplitude of oscillation. The distance from the wall is normalized by the Stokes-layer thickness parameter,  $\lambda_s$ , as defined above. To the first order, the experimental results agree quite well with the Stokes solution.

Some differences are worth noting, however. The recovery section cases are somewhat lower than the cases from the test section. It is possible that the boundary layer has not had enough length to adjust to the sudden removal of mean adverse free-stream gradient at the end of the test section. The peak in the data occurs somewhat farther from the wall than for the Stokes solution. Significant changes in the profile for the Stokes solution are confined to about five Stokes layer thicknesses; for the data, it is more like ten. This may be an indication that the  $S_x$  values are not high enough. The approach to the high-frequency limit may also be non-monotonic.

Figure 5.7 shows the phase of the velocity oscillations in the boundary layer with respect to the free-stream oscillations. The abscissa normalization is the same as for the previous figure. Once again, to the first order, the data are in very good agreement with the Stokes solution. The recovery section cases fall above the Stokes solution. The same reason cited in connection with Fig. 5.6 above is believed to be the cause of this.

Other cases seem to approach the solution from below. In the outer region, the data show a small but definite lag with respect to the free stream. Almost all of this lag takes place in the outer intermittent region of the boundary layer and is perhaps related to the dynamics of that region. Just as for the amplitude profiles, the effective thickness of the unsteady region is somewhat larger for the data than for the Stokes solution.

The evidence presented above supports the analysis of Section 2.5 that led to the Stokes equation. The conclusion that the high Strouhal number results follow the Stokes solution closely is in essential agreement with the high-frequency, near-wall, unsteady pipe-flow study of Binder and Kueny [1981].

## 5.6 Expected Wall Shear Stress Behavior

Wall shear stress is a very important parameter in steady turbulent boundary layers. It is of interest to study the variation of the oscillations in the wall shear stress in the experiments reported here. No direct measurements of wall shear stress were made. It will be shown

below that a reasonably good estimate of the wall shear-stress oscillations can be made from near-wall velocity data. The actual values will be different from the estimates. It is believed, however, that important trends will be identified.

Near the wall,  $\bar{U}(y)$  and  $\tilde{u}(y,t)$  can be expanded in Taylor's series, as shown below:

$$\bar{U}(y) = \bar{U}(0) + \left(\frac{\partial \bar{U}}{\partial y}\right)_0 y + \left(\frac{\partial^2 \bar{U}}{\partial y^2}\right)_0 y^2 + \dots \quad (5.11)$$

$$\tilde{u}(y,t) = \tilde{u}(0,t) + \left(\frac{\partial \tilde{u}}{\partial y}\right)_0 y + \left(\frac{\partial^2 \tilde{u}}{\partial y^2}\right)_0 y^2 + \dots \quad (5.12)$$

where

$$\bar{U}(0) = \tilde{u}(0,t) = 0$$

and subscript "0" denotes that the derivatives are evaluated at the wall. Therefore,

$$\begin{aligned} \frac{\tilde{u}(y,t)}{\bar{U}(y)} &= \frac{\left(\frac{\partial \tilde{u}}{\partial y}\right)_0 y + \left(\frac{\partial^2 \tilde{u}}{\partial y^2}\right)_0 y^2 + \dots}{\left(\frac{\partial \bar{U}}{\partial y}\right)_0 y + \left(\frac{\partial^2 \bar{U}}{\partial y^2}\right)_0 y^2 + \dots} \\ &= \frac{\left(\frac{\partial \tilde{u}}{\partial y}\right)_0}{\left(\frac{\partial \bar{U}}{\partial y}\right)_0} \left[ 1 + \frac{(\partial^2 \tilde{u} / \partial y^2)_0}{(\partial \tilde{u} / \partial y)_0} y - \frac{(\partial^2 \bar{U} / \partial y^2)_0}{(\partial \bar{U} / \partial y)_0} y + \dots \right] \\ &= \frac{\tau_w}{\tau_w} \left[ 1 + \frac{(\partial^2 \tilde{u} / \partial y^2)_0}{(\partial \tilde{u} / \partial y)_0} y - \frac{(\partial^2 \bar{U} / \partial y^2)_0}{(\partial \bar{U} / \partial y)_0} y + \dots \right] \quad (5.13) \end{aligned}$$

The orders of magnitude of the terms in square brackets are evaluated using the same estimates as in Section 2.5.



Term 2

$$\frac{A/\delta'^2}{A/\delta'} y = y/\delta'$$

Term 3

$$\frac{U_e/\delta^2}{U_e/\delta} y = y/\delta$$

Clearly, for points very close to the wall, Term 3 is always negligible. Since for low and medium Strouhal numbers,

$$\delta' \sim \delta ,$$

Term 2 is also negligible. For very high Strouhal numbers,

$$\frac{\delta'}{\delta} \sim \frac{1}{S^{1/2}}$$

and hence  $\delta'$  gets smaller as  $S$  increases. The contribution due to Term 2 increases as  $S$  increases.

It is clear from the above order of magnitude estimates that estimates of the wall-shear oscillations made from near-wall velocity amplitude behavior will be quite reasonable for low and moderate Strouhal numbers. For higher Strouhal numbers, the estimates are expected to be lower than actual values. It is also worth mentioning that the near-wall laser probe volume-averaging problem will be similar for both the amplitude and the mean velocity. It is quite likely that their ratio is more accurate than the individual values.

To see how reasonable the above approach may be, profiles of the velocity amplitude normalized by the local mean velocity were plotted as a function of distance from the wall. Figure 5.8 shows one such plot at  $X' = 0.94$  for the high-amplitude experiment at several frequencies. It is seen that, except at higher frequencies, there is a substantial region near the wall where the ratio is reasonably constant. At the higher frequencies, it is clear that the estimates will be lower than the actual values at the wall.

In order to find an appropriate normalization for the amplitude-to-mean ratio, the behavior of the Stokes layer wall shear-stress amplitude is investigated below.

From the Stokes solution, it can be easily shown that

$$A_{1,\tau_w} = \mu A_{1,U_e} \sqrt{\frac{\omega}{\nu}} \quad (5.14)$$

or

$$\frac{A_{1,\tau_w}}{\tau_w} = \mu \frac{A_{1,U_e}}{\bar{U}_e} \cdot \frac{\bar{U}_e}{\tau_w} \sqrt{\frac{\omega}{\nu}}$$

or

$$\begin{aligned} \frac{A_{1,\tau_w} / \tau_w}{A_{1,U_e} / \bar{U}_e} &= \frac{\mu \bar{U}_e}{\tau_w} \sqrt{\frac{\omega}{\nu}} \\ &= \frac{2\mu \bar{U}_e}{\rho \bar{U}_e^2} \cdot \frac{1}{C_f} \sqrt{\frac{\omega}{\nu}} \\ &= \frac{2}{C_f} \sqrt{\frac{\omega \nu}{\bar{U}_e^2}} \\ &= \frac{2}{C_f} \left( \frac{\omega(X-X_0)}{\bar{U}_e} \right)^{1/2} \left( \frac{\nu}{\bar{U}_e(X-X_0)} \right)^{1/2} \end{aligned} \quad (5.15)$$

Define:

$$\gamma = \left( \frac{A_{1,\tau_w}}{\tau_w} \right) \left( \frac{A_{1,U_e}}{\bar{U}_e} \right)^{-1} \left( \frac{C_f}{2} \right) \left( \frac{\bar{U}_e(X-X_0)}{\nu} \right)^{1/2} \quad (5.16)$$

Then, for the Stokes solution,

$$\gamma = \sqrt{S_x} \quad (5.17)$$

Figure 5.9 shows the variation of  $\gamma$  as a function of  $S_x$ . All cases studied (except low-amplitude,  $X' = 0.39$  cases which do not have data close enough to the wall) are included in the plot. The Stokes solution also is plotted. Several important observations can be made, as follows:

- Despite the very wide range of frequencies and local amplitudes and histories that the cases represent, the data collapse quite well and show a very definite trend with respect to  $S_x$ ;
- For small  $S_x$  values, the shear-stress amplitude decreases with increasing  $S_x$ . Since there is no variation in the imposed pressure-gradient excitation with  $S_x$  in this range, the decrease in amplitude is primarily the result of inertia.
- The shear-stress amplitude reaches a minimum around  $S_x$  of 3; for higher  $S_x$  values, the amplitude actually increases. This can be explained by the increasing pressure-gradient oscillations that overcome inertia, especially in the near-wall region.
- At high  $S_x$  values,  $\gamma$  falls consistently below the Stokes solution. There are probably two reasons for this. The  $S_x$  values are not high enough for complete agreement with the Stokes solution. Evidence for this was seen in Section 5.5. Further, it was noted that, for high  $S_x$  cases, estimates of the wall-shear oscillation amplitude from the near-wall velocity amplitude are likely to be lower than actual.

The phase angle of the velocity with respect to the free stream of the first measured point was used as an estimate of the phase of the wall shear-stress oscillations. Several drawbacks of this estimate need to be mentioned. The phase values at this point suffer from the laser finite-probe-volume averaging problem. It is believed that, for the low-frequency cases, this is not a very serious problem, since the phase angle varies very little in the inner region for those cases. The high-frequency cases show rapid variations in velocity phase close to the wall, and the estimates seem likely to be lower than actual values. Since the estimates are based on measurement at a single point, unlike

the case of the wall-shear amplitude, more scatter should be expected. Still, the trends shown by these estimates should be quite representative of the wall shear-phase behavior.

Figure 5.10 shows the expected behavior of the wall shear stress with  $S_x$  for the same cases. Despite all the reservations expressed above, the data follow a well-defined trend with respect to  $S_x$ . The following important observations can be made:

- At very low  $S_x$  values, the wall shear-stress oscillations are in phase with the free-stream oscillations. As  $S_x$  increases, the wall-shear oscillations increasingly lag the free stream. Once again, the cause has to be inertia, since the pressure-gradient oscillations are essentially constant.
- The shear-stress oscillations reach a maximum lag of about  $17^\circ$  around  $S_x$  of 1. Beyond, the increasing pressure-gradient oscillations (which undergo phase advances as  $S_x$  increases) cause the phase lag to decrease and then cause increasing phase leads. At very high frequencies, the wall shear will be  $45^\circ$  ahead of the free-stream oscillations, as per the Stokes solution.

### 5.7 Log Linear Region

Steady turbulent boundary layers follow the so-called law of the wall in a region near the wall, beyond the viscous layer. If the phase-averaged velocity profiles follow the same law, then in that region the phase of the velocity should be constant, as pointed out by Simpson, Shivaprasad and Chew [1983]. The appropriate analysis is as follows:

For the phase-averaged profiles, assume that

$$\frac{\langle u \rangle}{\langle u_\tau \rangle} = \frac{1}{\kappa} \ln \left[ \frac{y \langle u_\tau \rangle}{\nu} \right] + C \quad (5.17)$$

Assume that

$$\langle u \rangle = \bar{U} + A_{1,u} e^{j(\omega t + \phi_{1,u})} \quad (5.18)$$

$$\langle u_\tau \rangle = \bar{u}_\tau + A_{1,u_\tau} e^{j(\omega t + \phi_{1,u_\tau})} \quad (5.19)$$

Considering only the first harmonic terms, the left-hand side becomes

$$\frac{\langle u \rangle}{\langle \bar{u}_\tau \rangle} = \frac{\bar{U}}{\bar{u}_\tau} \left[ 1 + \frac{A_{1,u}}{\bar{U}} e^{j(\omega t + \phi_{1,u})} - \frac{A_{1,u_\tau}}{\bar{u}_\tau} e^{j(\omega t + \phi_{1,u_\tau})} \right] \quad (5.20)$$

The right-hand side is

$$\frac{1}{\kappa} \ln \left( \frac{y \bar{u}_\tau}{v} \right) + C + \frac{1}{\kappa} \frac{A_{1,u_\tau}}{\bar{u}_\tau} e^{j(\omega t + \phi_{1,u_\tau})} \quad (5.21)$$

Equations (5.20) and (5.21) imply

$$\frac{\bar{U}}{\bar{u}_\tau} = \frac{1}{\kappa} \ln \left( \frac{y \bar{u}_\tau}{v} \right) + C \quad (5.22)$$

and

$$\frac{A_{1,u}}{\bar{u}_\tau} = \left[ \frac{\bar{U}}{\bar{u}_\tau} \frac{A_{1,u_\tau}}{\bar{u}_\tau} + \frac{1}{\kappa} \frac{A_{1,u_\tau}}{\bar{u}_\tau} \right] e^{j(\phi_{1,u} - \phi_{1,u_\tau})} \quad (5.23)$$

Equation (5.23) implies that

$$\phi_{1,u} = \phi_{1,u_\tau} = \text{constant} \quad (5.24)$$

and

$$\frac{A_{1,u}}{A_{1,u_\tau}} = \frac{\bar{U}}{\bar{u}_\tau} + \frac{1}{\kappa} = \frac{1}{\kappa} \ln \left( \frac{y \bar{u}_\tau}{v} \right) + C + \frac{1}{\kappa} \quad (5.25)$$

The above analysis shows that the phase of the velocity in the log-linear region would be constant. Further, the amplitude of the velocity oscillations would show a log-linear variation. It must be noted that it has not been established that the "wall shear velocity" parameter in the above analysis is that due to the actual wall shear stress. Thus,

in general, there is no reason to expect the constant phase in the region to equal that of the wall shear stress. If the frequency is included as another parameter that affects the velocity profile in the region, the form of the velocity profiles should be as shown below.

$$\frac{\langle u \rangle}{\langle u_\tau \rangle} = f \left[ \frac{y \langle u_\tau \rangle}{\nu}, \frac{\omega y}{\langle u_\tau \rangle} \right] \quad (5.26)$$

Clearly, this form should reduce to the steady law of the wall for very small frequencies. It should be emphasized again that there is no reason to expect that the above form will be the same as the steady form for all frequencies.

The data shown in Sections 4.5 (see Figs. 4.18 and 4.19) clearly show that, at low frequencies, there is a region of constant velocity phase. Looking at the trend toward the wall of the velocity phase, one might expect that the phase of the wall shear stress is also about the same for such frequencies. The corresponding amplitude profiles do show a log-linear variation in the same region.

As the frequency increases, however, the extent of this region decreases. The wall shear stress seems to be ahead of the log-linear region in phase. At high enough frequencies, there is no evidence of a constant phase or a log-linear amplitude region, indicating that the steady law of the wall is not valid. The smooth transition of amplitude and phase of velocity with frequency lends more credence to the more generalized near-wall law shown above.

## 5.8 Periodic Turbulence

The results presented in Section 4.6 (see Figs. 4.20 and 4.21) clearly demonstrate the strong dependence of periodic turbulence on the frequency of excitation. The results for the first harmonic amplitude of turbulence oscillations (Figs. 4.20) show that the estimates of its order of magnitude made in Chapter 2 (Section 2.5.1) are good over all frequencies. In particular, note that the turbulence amplitudes in the high-amplitude cases (Fig. 4.20b) are larger than those in the low-amplitude cases (Fig. 4.20a) by approximately the ratio of the relative free-stream amplitudes in the two experiments, as per the quasi-steady estimate made in Section 2.5.1.

The turbulence-amplitude profiles show two distinct regions of significant turbulence oscillations. The variation in the outer region over the oscillation cycle is believed to be associated with the variation of the boundary layer thickness over the cycle. First of all, at low frequencies, the boundary layer thickness is essentially  $180^\circ$  out of phase with the free stream (see Figs. 4.34 and 4.35), and so is the outer-region turbulence (see Figs. 4.21). At low frequencies, both undergo large variation over the cycle. Points very near the edge of the boundary layer are in the free stream for portions of the cycle and inside the boundary layer at other times. This shows up as turbulence oscillations at those points. As the frequency increases, the variation in both boundary layer thickness and outer-region turbulence is suppressed, and at high frequencies, both are essentially constant over the cycle (Figs. 4.20, 4.34, and 4.35).

The inner-region turbulence oscillations are also reduced as the frequency is increased (see Figs. 4.20), indicating perhaps an inertial response of turbulence to the imposed periodic changes. The observed increase in the phase lag (with respect to phase at very low frequencies) of turbulence oscillations at locations away from the wall as frequency increases provides further evidence for the inertial response hypothesis. Even at the highest frequency studied, however, there is a thin region near the wall where there are significant variations in turbulence over the cycle. This may mean either that much higher frequencies are needed before the inner-region turbulence variation will be completely suppressed or that the dynamics of the response of turbulence to imposed excitation cannot be completely explained by inertia alone.

## Chapter 6

### CONCLUSIONS AND RECOMMENDATIONS

The following is a summary of the major conclusions of the present study and recommendations for future work. These are primarily drawn from the results and discussion presented in the previous chapters.

#### 6.1 Conclusions

- A definitive data set on an unsteady turbulent boundary layer subjected to well-defined oscillations in the free stream velocity has been obtained and should prove very useful in the evaluation of computational schemes and as input to turbulence models for unsteady turbulent boundary layer flows.
- The time-averaged flow field is essentially unaffected by the imposed unsteadiness.
- The periodic flow is very strongly dependent on the frequency of excitation.
- The Strouhal number ( $S_x$ ) based on the streamwise distance in the test section and the local mean free-stream velocity is a very important parameter for the periodic velocity.
- There are two distinct regimes of periodic velocity behavior with respect to the Strouhal number, namely, the inertial regime ( $S_x < 1$ ) and the pressure-gradient-dominated regime ( $S_x > 1$ ).
- The high-frequency periodic velocity results follow the Stokes solution very closely.
- The steady form of the law of the wall does not seem to be valid for the phase-averaged velocity profiles at high frequencies.
- Over the range of frequencies and amplitudes studied, there seem to be no dramatic interactions between the organized oscillations and the disorganized turbulent fluctuations. This conclusion is specific to the types of data processing and the analyses employed, and the quantities studied in the present experiments.



## 6.2 Recommendations for Future Work

The following are recommendations for future work in the present experimental facility:

- To complete the data set, measurements of other components of phase-averaged turbulent stresses are needed. In particular, measurements of shear stress ( $\langle u'v' \rangle$ ) in the boundary layer and wall shear stress ( $\langle \tau_w \rangle$ ) should be made for a complete understanding of the physical characteristics of the flow.
- The experimental apparatus in which the present study was conducted is a very versatile one. Detailed studies on effects of different types of excitation (for example, abrupt imposition of an adverse free-stream gradient) and unsteady turbulent boundary-layer heat transfer would be very fruitful.

The following recommendations are addressed to the unsteady turbulent boundary layer research community at large:

- Unsteady, turbulent, boundary layer flow with separation is a wide-open field. Potentially, the effects of unsteadiness on such a flow are much more important than for attached boundary layers. Careful study of such flows over a wide range of relevant parameters (for example, the frequency parameter) is essential for a complete understanding of important phenomena, such as dynamic stall.
- The question of interaction between the organized and the disorganized motions is still unanswered. Experiments at frequencies much higher than those studied are perhaps needed to resolve this question. Further analysis of the present data from different perspectives may be helpful in clarifying this important issue.

## References

- Acharya, M., and Reynolds, W. C. [1975]. "Measurements and Predictions of a Fully Turbulent Channel Flow with Imposed, Controlled Oscillations," Report TF-8, Thermosciences Div., Dept. of Mech. Engrg. Stanford University, Stanford, California, May 1975.
- Anderson, P. S., Kays, W. M., and Moffat, R. J. [1972], "The Turbulent Boundary Layer on a Porous Plate: An Experimental Study of the Fluid Mechanics for Adverse Free-Stream Pressure Gradients," Report HMT-15, Thermosciences Div., Dept. of Mech. Engrg. Stanford University, Stanford, California, May 1972.
- Binder, G., and Kueny, J. L. [1981], "Measurements of the Periodic Velocity Oscillations near the Wall in Unsteady Turbulent Channel Flow," IUTAM Symposium on Unsteady Turbulent Shear Flows, Toulouse, France, May 1981, Springer-Verlag.
- Carr, L. W. [1981a], "A Review of Unsteady Turbulent Boundary Layer Experiments," IUTAM Symposium on Unsteady Turbulent Shear Flows, Toulouse, France, May 1981, Springer-Verlag.
- Carr, L. W. [1981b], "A Compilation of Unsteady Turbulent Boundary Layer Experimental Data," AGARDograph No. 265.
- Coles, D. E. [1968], "The Young Person's Guide to the Data," Proceedings of the Computation of Turbulent Boundary Layers--1968 AFOSR-IFP-Stanford Conference, 2, Thermosciences Div., Dept. of Mech. Engrg., Stanford University, Stanford, California.
- Coles, D. E., and Hirst, E. A. [1968]. "Memorandum on Data Selection," Proceedings of the Computation of Turbulent Boundary Layers--1968 AFOSR-IFP-Stanford Conference, 2, Thermosciences Div., Dept. of Mech. Engrg., Stanford University, Stanford, California.
- Cousteix [1979], "Boundary Layers in Oscillatory Flows," European Space Agency Technical Translation, ESA-TT-603, December 1979.
- Cousteix, J., Desopper, A., and Houdeville, R. [1977], "Structure and Development of a Turbulent Boundary Layer in an Oscillatory External Flow," Proceedings of the Symposium on Turbulent Shear Flows, Pennsylvania State University, Pennsylvania, 1977.
- Cousteix, J., Houdeville, R., and Javelle, J. [1981], "Response of a Turbulent Boundary Layer to a Pulsation of the External Flow with and without Adverse Pressure Gradient," IUTAM Symposium on Unsteady Turbulent Shear Flows, Toulouse, France, May 1981, Springer-Verlag.
- Houdeville, R., and Cousteix, J. [1979], "First Results of a Study on Turbulent Boundary Layers in Oscillating Flow with a Mean Adverse Pressure Gradient," NASA TM 75799, November 1979.

AD-A124 365

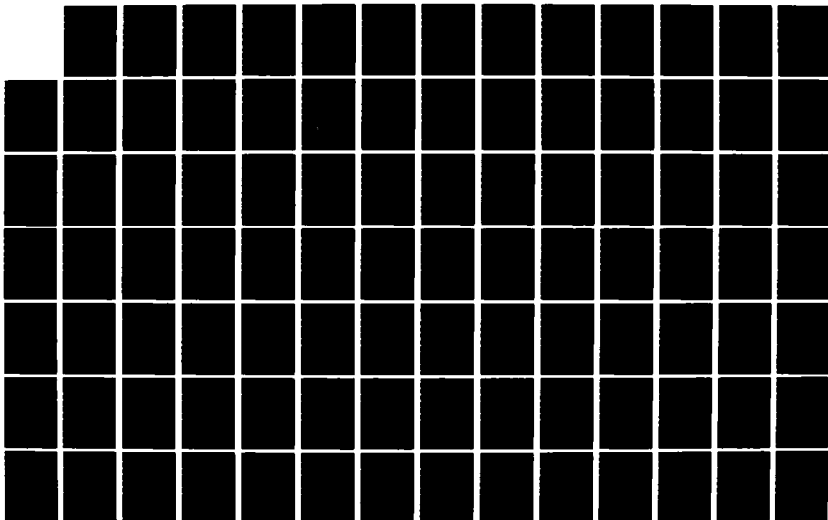
AN EXPERIMENTAL STUDY OF THE DYNAMICS OF AN UNSTEADY  
TURBULENT BOUNDARY LAYER(U) STANFORD UNIV CA  
THERMOSCIENCES DIV R JAYARAMAN ET AL. DEC 82 TF-18  
ARO-16760.2-EG ARO-1-80

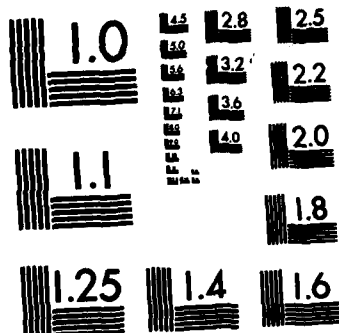
2/3

UNCLASSIFIED

F/G 20/4

NL





MICROCOPY RESOLUTION TEST CHART  
NATIONAL BUREAU OF STANDARDS-1963-A

- Hussain, A.K.M.F., and Reynolds, W. C. [1970a], "The Mechanics of a Perturbation Wave in Turbulent Shear Flow," Report FM-6, Thermosciences Div., Dept. of Mech. Engrg., Stanford University, Stanford, California, May 1970.
- Hussain, A.K.M.F., and Reynolds, W. C. [1970b], "The Mechanics of an Organized Wave in Turbulent Shear Flow," *Journal of Fluid Mechanics*, 41, Part 2, 241-258, 1970.
- Hussain, A.K.M.F., and Reynolds, W. C. [1972], "The Mechanics of an Organized Wave in Turbulent Shear Flow. Part 2: Experimental Results," *Journal of Fluid Mechanics*, 54, 241-261, 1972.
- Jayaraman, R. [1982], "Data Acquisition, Control, and Processing Software for an Automated, Unsteady, Turbulent Boundary Layer Experiment," Report IL-63, Thermosciences Div., Dept. of Mech. Engrg., Stanford University, Stanford, California, December 1982.
- Jayaraman, R., Parikh, P. G., and Reynolds, W. C. [1982], "An Experimental Study of the Dynamics of an Unsteady, Turbulent Boundary Layer--Data Tables and Plots," Microfiche Report No. 1, Thermosciences Div., Dept. of Mech. Engrg., Stanford University, Stanford, California, December 1982.
- Karlsson, S. K. F. [1959], "An Unsteady Turbulent Boundary Layer," *Journal of Fluid Mechanics*, 5, p. 622, 1959.
- Kenison, R. C. [1977], "An Experimental Study of the Effect of Oscillatory Flow on the Separation Region in a Turbulent Boundary Layer," AGARD CP-277, Ottawa, 1977.
- Klebanoff, P. S. [1955], "Characteristics of Turbulence in a Boundary Layer with Zero Pressure Gradient," NACA Report No. 1247, 1955.
- Kline, S. J., and McClintock, F. A. [1953], "Describing Uncertainties in Single-Sample Experiments," *Mechanical Engineering*, January 1953.
- McCroskey, W. F. [1977], "Some Current Research in Unsteady Fluid Dynamics--The 1976 Freeman Scholar Lecture," *Transactions of the ASME*, March 1977.
- Moffat, R. J. [1981], "Contributions to the Theory of Uncertainty Analysis for Single-Sample Experiments," Vol. I, The 1980-81 AFUSK-HTTM-Stanford Conference on Complex Turbulent Flows, Thermosciences Division, Dept. of Mech. Engrg., Stanford University, Stanford, California, 1981.
- Patel, M. H. [1977], "On Turbulent Boundary Layers in Oscillatory Flow," *Proceedings of the Royal Society of London*, A 353, 121-144, 1977.
- Ramaprian, B. R., and Tu, S. W. [1979], "Experiments on Transitional Oscillatory Pipe Flow," IHR Report No. 221, Iowa Institute of Hydraulic Research, University of Iowa, Iowa City, Iowa, August 1979.

- Ramaprian, B. R., and Tu, S. W. [1980], "An Experimental Study of Oscillatory Pipe Flow at Transitional Reynolds Numbers," *Journal of Fluid Mechanics*, 100, p. 513, 1980.
- Ramaprian, B. R., and Tu, S. W. [1981], "Periodic Turbulent Pipe Flow at 'High' Frequencies of Oscillation," *IUTAM Symposium on Unsteady Turbulent Shear Flows*, Toulouse, France, 1981, Springer-Verlag.
- Rao, K. N., Narasimha, R., and Narayanan, M.A.B. [1971], "The 'Bursting' Phenomenon in a Turbulent Boundary Layer," *Journal of Fluid Mechanics*, 48, Part 2, 339-352, 1971.
- Reynolds, W. C., and Hussain, A.K.M.F. [1972], "The Mechanics of an Organized Wave in Turbulent Shear Flow. Part 3," *Journal of Fluid Mechanics*, 54, 262-288, 1972.
- Schachenmann, A. A., and Rockwell, D. O. [1976], "Oscillating Turbulent Flow in a Conical Diffuser," *Transactions of the ASME, Journal of Fluids Engineering*, December 1976.
- Shemer, L. [1981], "Investigation of the Turbulent Characteristics of a Pulsating Pipe Flow," Ph.D. thesis, Tel Aviv University, Israel, June 1981.
- Simpson, R. L. [1977], "Features of Unsteady Turbulent Boundary Layers as Revealed from Experiments," AGARD-CP-227, 1977.
- Simpson, R. L., Chew, Y. T., and Shivaprasad, B. G. [1980], "Measurements of Unsteady Turbulent Boundary Layers with Pressure Gradients," Report WT-6, Dept. of Civil and Mech. Engrg., Southern Methodist University, August 1980.
- Simpson, R. L., Shivaprasad, B. G., and Chew, Y. T. [1983], "The Structure of a Separating Turbulent Boundary Layer. Part 4: Effects of Periodic Freestream Unsteadiness," accepted for publication in *Journal of Fluid Mechanics*, 1983.
- Simpson, R. L., and Shivaprasad, B. G. [1983], "The Structure of a Separating Turbulent Boundary Layer. Part 5: Frequency Effects on Periodic Unsteady Freestream Flows," private communication, submitted to *Journal of Fluid Mechanics*, 1983.
- Telionis, D. P. [1977], "Unsteady Boundary Layers, Separated and Attached," AGARD-CP-227, Ottawa, 1977.

Table 1.1  
Experimental Flow Parameters

Experiment	Medium Flow	$\alpha = A_{1,U} / \bar{U}_e$ (%)	$\bar{U}_e$ (m/s)	f (Hz)	$\delta$ (mm)	$S_\delta = \frac{2\pi f \delta}{\bar{U}_e}$
Hussain	Air/TCF	--	6.7	25-100	32	0.75-3.0
Acharya	Air/TCF	3.6	6.7	24,40	32	0.72-1.2
Ramaprian	Oil/TPF	30	0.55	1.75	25	0.5
Binder	Air/TPF	5	0.18	1.4	50	0.15-2.5
Shemer	Air/TPF	--	1.8	0.2-2	17	0.01-0.1
Karlsson	Air/TBL	34	5.4	0-48	76	0-4.2
Schachermann	Air/TBL	15	3	5-35	10-50	0.02-0.6
Houdeville	Air/TBL	20	20-30	38	10-40	0.1-0.5
Patel	Air/TBL	11	20	4-12	20	0.03-0.08
Kenison	Air/TBL	13	22	0-6	40-80	0-0.14
Simpson	Air/TBL	30	22-12	0.6	25-250	0.004-0.08
Present	Water/TBL	5,25	0.73	0.1-2	41-82	0.04-1.6

Flow Legend: TBL = Turbulent Boundary Layer,  
TPF = fully developed Turbulent Pipe Flow,  
TCF = fully developed Turbulent Channel Flow.

Table 2.1

## SIMPLIFIED GOVERNING EQUATIONS

Mean Equations

Continuity: 
$$\frac{\partial \bar{U}}{\partial x} + \frac{\partial \bar{V}}{\partial y} = 0$$

Momentum ( $\alpha < 0.3$ ):

$$\frac{\partial}{\partial x} (\bar{U} \bar{U}) + \frac{\partial}{\partial y} (\bar{U} \bar{V}) = -\frac{1}{\rho} \frac{\partial \bar{p}_e}{\partial x} + \nu \frac{\partial^2 \bar{U}}{\partial y^2} - \frac{\partial}{\partial y} (\overline{u'v'})$$

Periodic Equations

Continuity: 
$$\frac{\partial \tilde{u}}{\partial x} + \frac{\partial \tilde{v}}{\partial y} = 0$$

Momentum:Case 1: ( $S \ll 1$ )

$$2 \frac{\partial}{\partial x} (\tilde{u} \bar{U}) + \frac{\partial}{\partial y} (\bar{U} \tilde{v} + \tilde{u} \bar{V}) = -\frac{1}{\rho} \frac{\partial \tilde{p}_e}{\partial x} + \nu \frac{\partial^2 \tilde{u}}{\partial y^2} - \frac{\partial}{\partial y} (\widetilde{u'v'}) - \left[ \frac{\partial}{\partial x} (\widetilde{\tilde{u}\tilde{u}}) + \frac{\partial}{\partial y} (\widetilde{\tilde{u}\tilde{v}}) \right]$$

Case 2: ( $S \gg 1$ )

$$\frac{\partial \tilde{u}}{\partial t} = -\frac{1}{\rho} \frac{\partial \tilde{p}_e}{\partial x} + \nu \frac{\partial^2 \tilde{u}}{\partial y^2}$$

Case 3: ( $S \sim 1$ )

$$\frac{\partial \tilde{u}}{\partial t} + 2 \frac{\partial}{\partial x} (\tilde{u} \bar{U}) + \frac{\partial}{\partial y} (\bar{U} \tilde{v} + \tilde{u} \bar{V}) = -\frac{1}{\rho} \frac{\partial \tilde{p}_e}{\partial x} + \nu \frac{\partial^2 \tilde{u}}{\partial y^2} - \frac{\partial}{\partial y} (\widetilde{u'v'}) - \left[ \frac{\partial}{\partial x} (\widetilde{\tilde{u}\tilde{u}}) + \frac{\partial}{\partial y} (\widetilde{\tilde{u}\tilde{v}}) \right]$$

$\alpha$  amplitude of oscillation of the free-stream velocity normalized by the mean free stream.

$S$  Strouhal number based on the typical values for the length scale in the streamwise direction and the mean free-stream velocity.



**Table 4.1**  
**High Amplitude Experimental Cases**

f (Hz)	X'							
	0.39		0.69		0.94		1.19	
	S <sub>x</sub>	S <sub>δ</sub>	S <sub>x</sub>	S <sub>δ</sub>	S <sub>x</sub>	S <sub>δ</sub>	S <sub>x</sub>	S <sub>δ</sub>
0.1	0.225	0.039	0.419	0.061	0.598	0.079	0.777	0.088
0.2	0.450	0.079	0.840	0.117	1.197	0.145	1.555	0.165
0.25	-	-	-	-	-	-	1.973	0.205
0.333	0.751	0.092	1.406	0.189	2.029	0.227	2.622	0.258
0.5	1.128	0.194	2.123	0.277	3.059	0.335	3.940	0.381
0.625	1.411	0.243	2.656	0.343	3.812	0.407	4.920	0.472
0.8	1.808	0.309	3.408	0.440	4.888	0.526	6.286	0.606
1.0	2.264	0.387	4.266	0.548	6.120	0.671	7.847	0.762
1.6	3.638	0.625	6.847	0.894	9.779	1.050	12.55	1.219
2.0	4.556	0.778	8.582	1.116	12.25	1.323	15.68	1.544

**Table 4.2**  
**Low Amplitude Experimental Cases**

f (Hz)	X'							
	0.38		0.63		0.88		1.13	
	S <sub>x</sub>	S <sub>δ</sub>	S <sub>x</sub>	S <sub>δ</sub>	S <sub>x</sub>	S <sub>δ</sub>	S <sub>x</sub>	S <sub>δ</sub>
0.1	0.200	0.036	0.339	0.039	0.478	0.042	0.619	0.046
0.2	-	-	0.675	0.079	0.955	0.083	1.239	0.095
0.333	-	-	1.129	0.132	1.587	0.139	2.067	0.159
0.5	0.996	0.180	1.692	0.197	2.382	0.208	3.106	0.237
0.625	-	-	2.120	0.249	2.990	0.261	3.889	0.297
0.8	-	-	2.711	0.321	3.820	0.335	4.962	0.378
1.0	-	-	3.394	0.397	4.779	0.414	6.211	0.477
1.6	-	-	-	-	7.652	0.672	9.938	0.758
2.0	3.984	0.725	6.795	0.784	9.569	0.838	12.40	0.962

Table 4.3

Estimated  $N^{\text{th}}$ -Order Uncertainties at 20:1 Odds with  $U_0 = 730 \text{ mm/s}$ 

Quantity	$y/\delta > 0.1$	$y/\delta < 0.1$
		$y > 0.2 \text{ mm}$
$\bar{U}/U_0$	0.5%	1.0%
$[(\overline{u'u'})/U_0^2] \times 10^4$	5	20
$\langle u \rangle / U_0$	0.5%	1.0%
$[\langle u'u' \rangle / U_0^2] \times 10^4$	10	40
$A_{1,u}/U_0$	0.3%	0.6%
$\phi_{1,u} \begin{cases} A_{1,u}/U_0: 0.05 \\ A_{1,u}/U_0: 0.25 \end{cases}$	$4^\circ$	$8^\circ$
	$1^\circ$	$2^\circ$
$[A_{1,u'u'}/U_0^2] \times 10^4$	6	25
$\phi_{1,u'u'} \begin{cases} A_{1,u'u'}/U_0^2: 50 \times 10^{-4} \\ A_{1,u'u'}/U_0^2: 10 \times 10^{-4} \end{cases}$	$7^\circ$	$26^\circ$
	$32^\circ$	$130^\circ$
$y$	0.05 mm	
$x$	5 mm	
$z$	5 mm	
$\langle \delta_1 \rangle, \delta_1$	$< 0.6 \text{ mm}$	
$\langle \delta_2 \rangle, \delta_2$	$< 0.5 \text{ mm}$	
$u_\tau$	$< 2 \text{ mm/s}$	

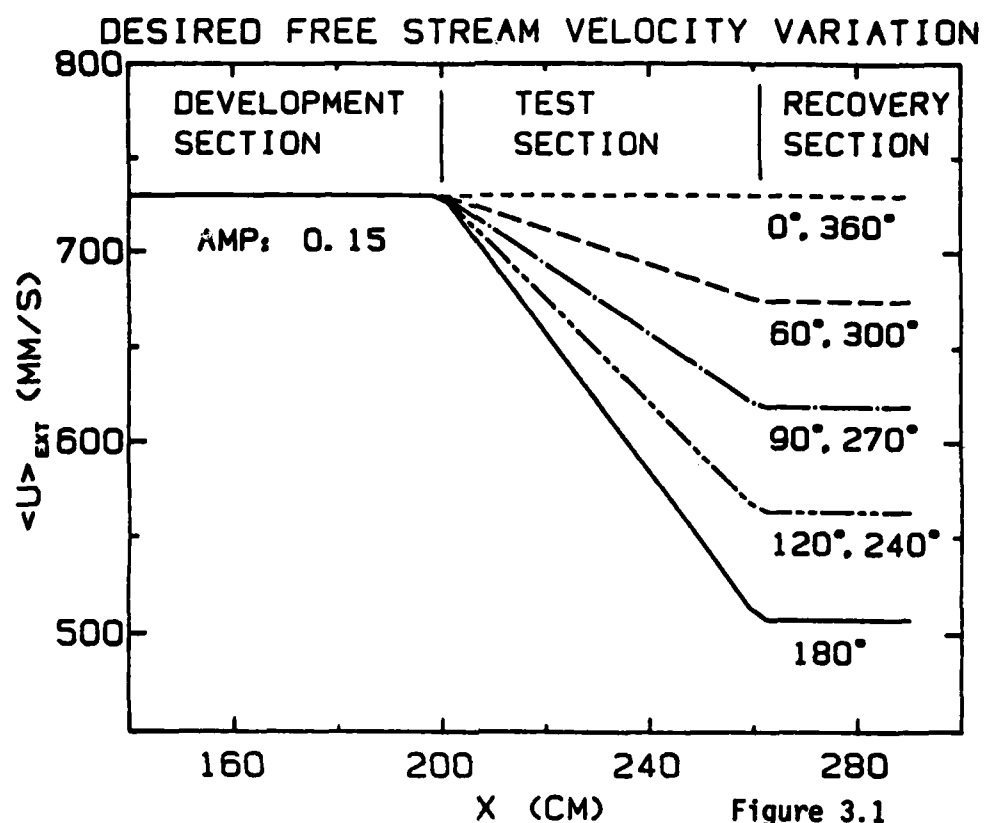


Figure 3.1

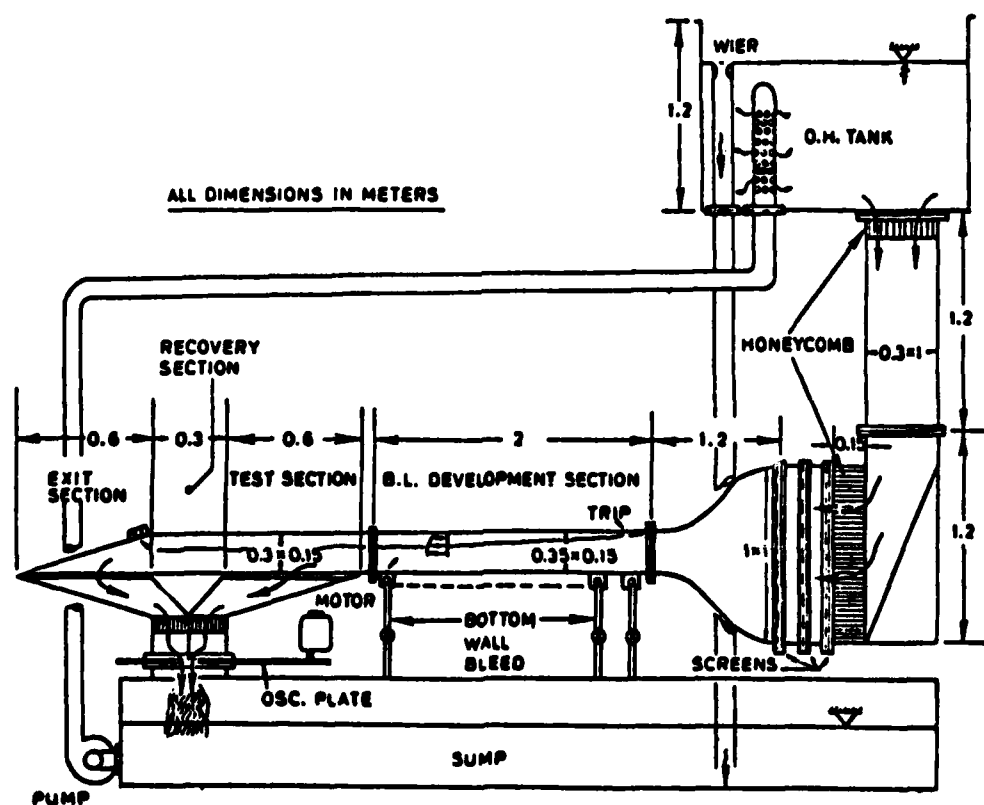


Figure 3.2

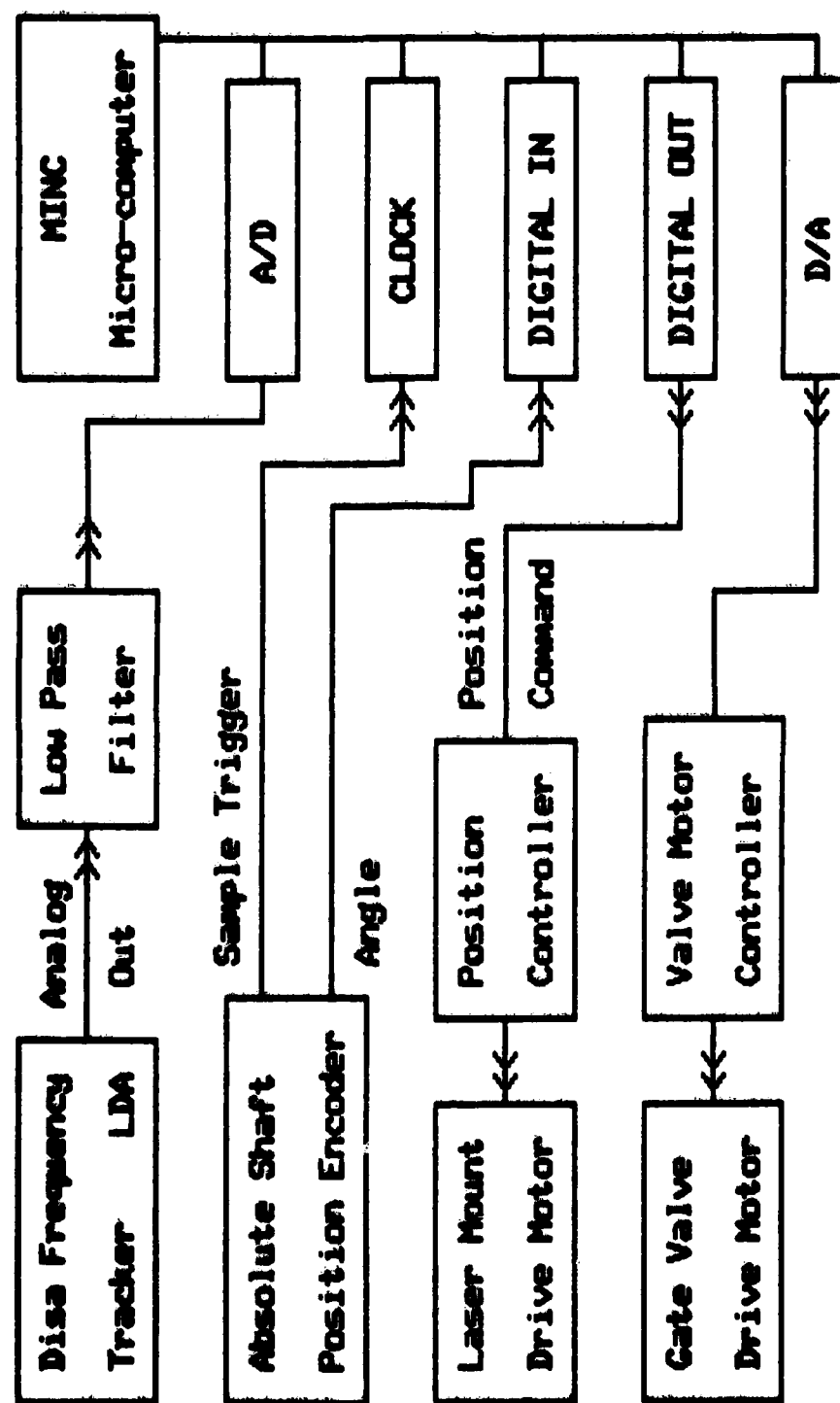


Figure 3.3

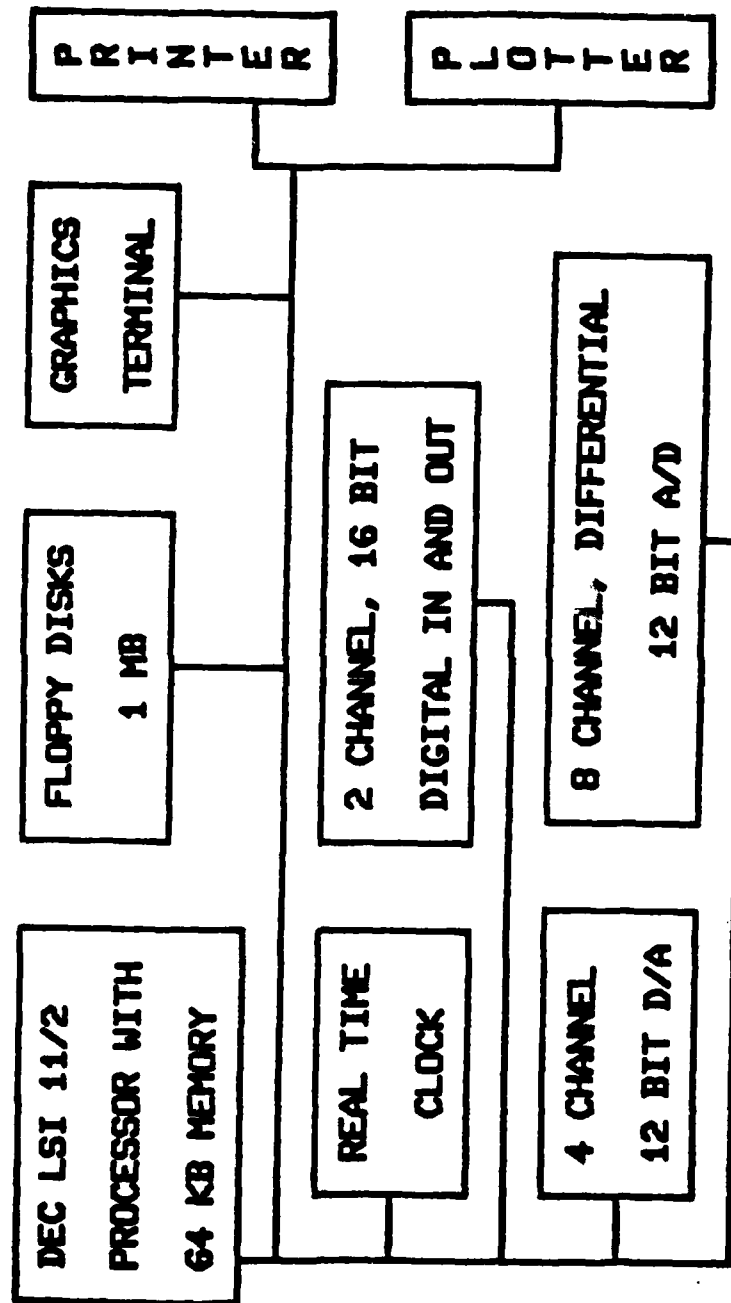
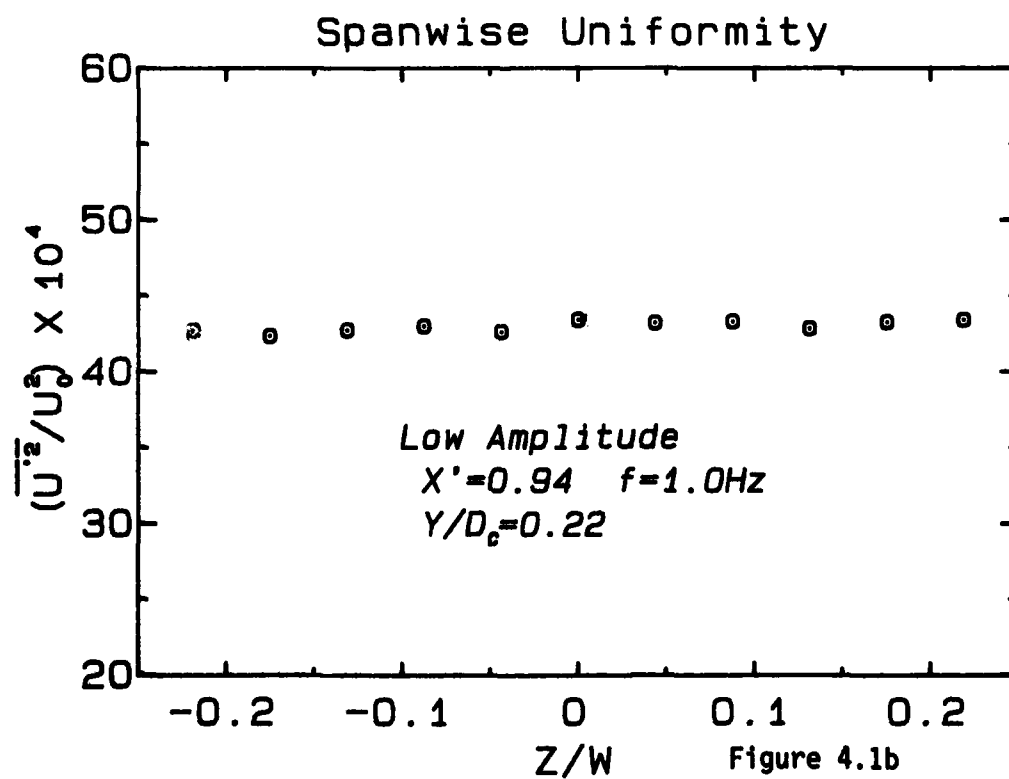
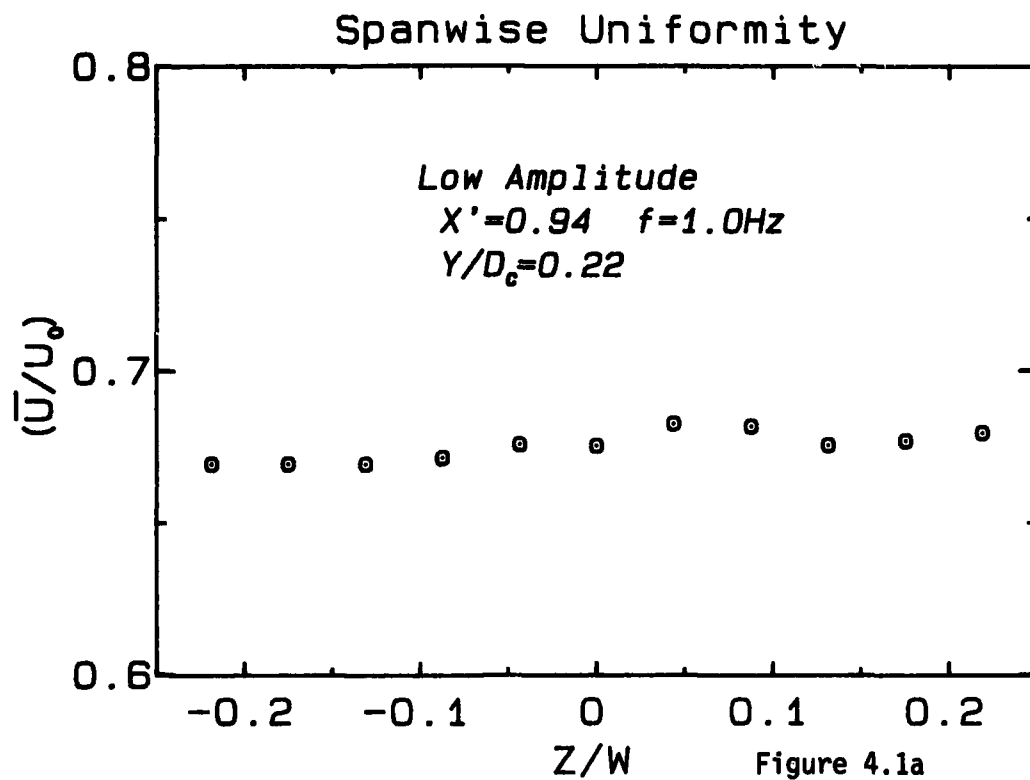
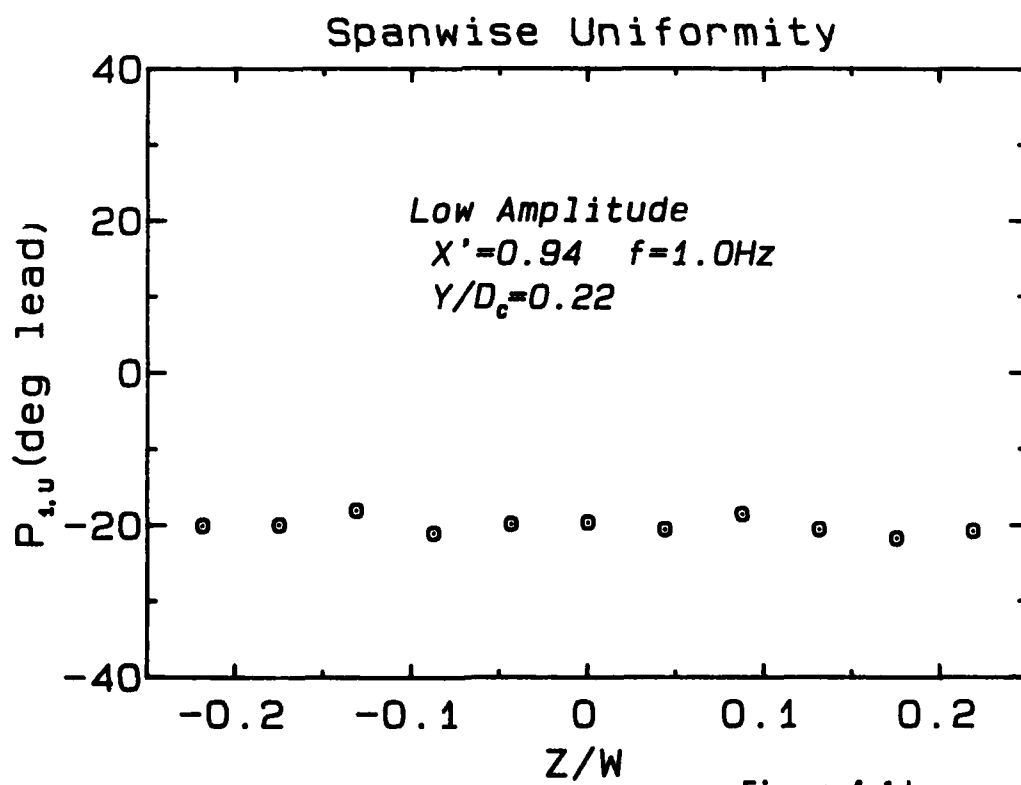
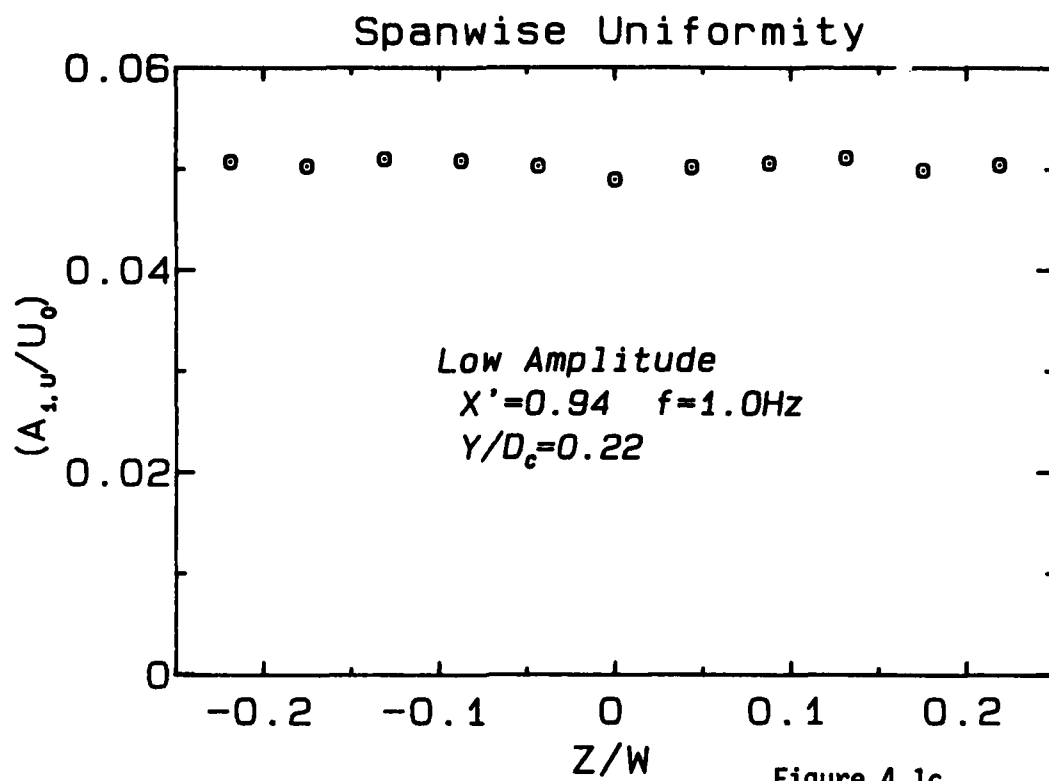


Figure 3.4





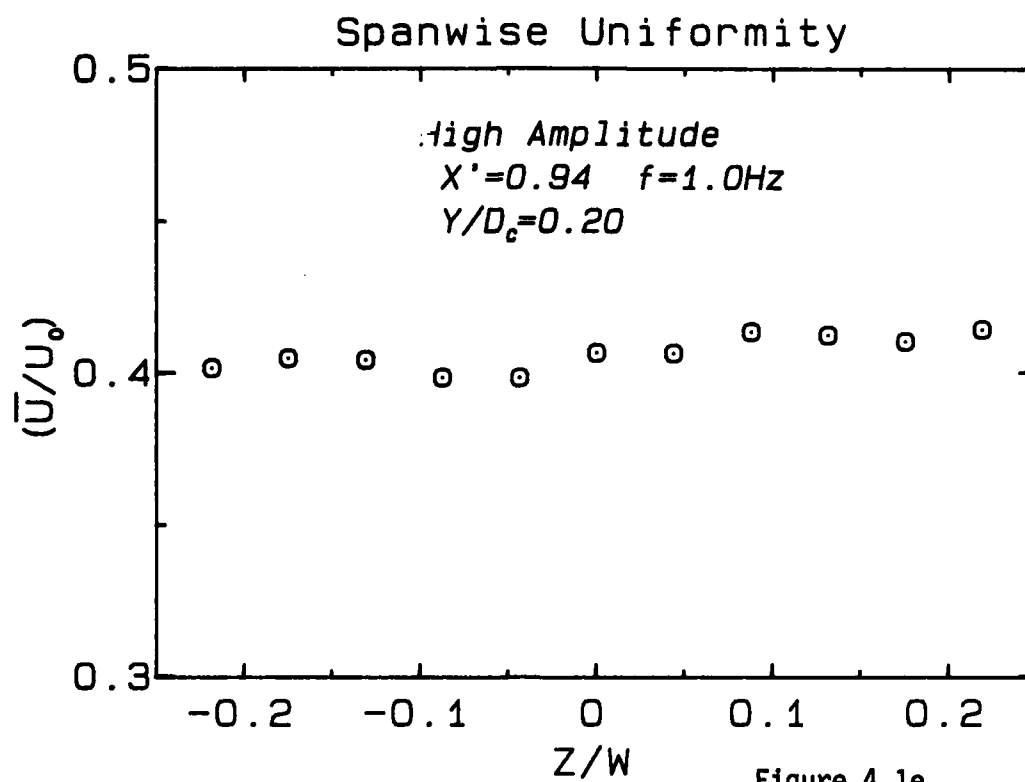


Figure 4.1e

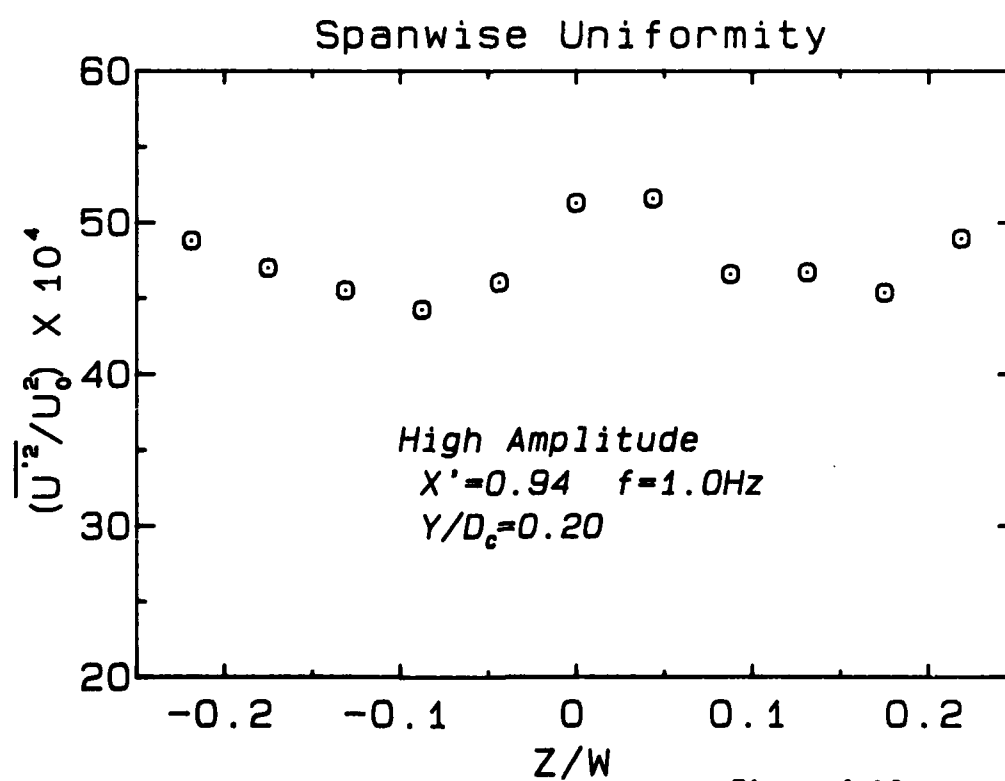
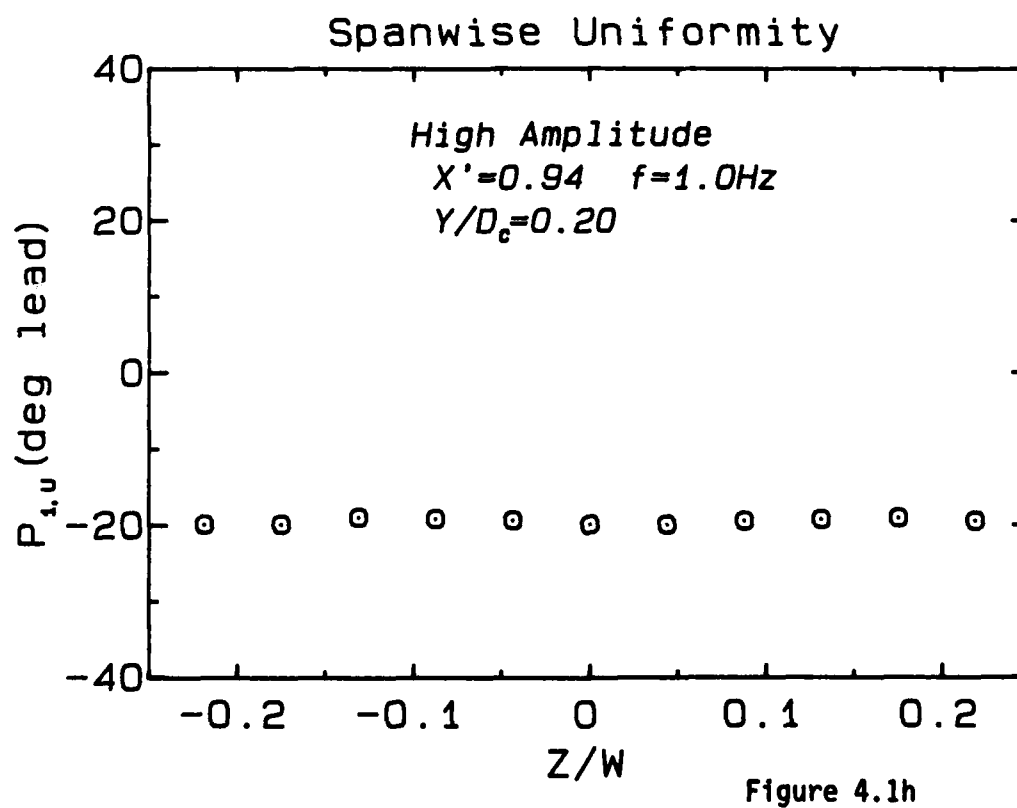
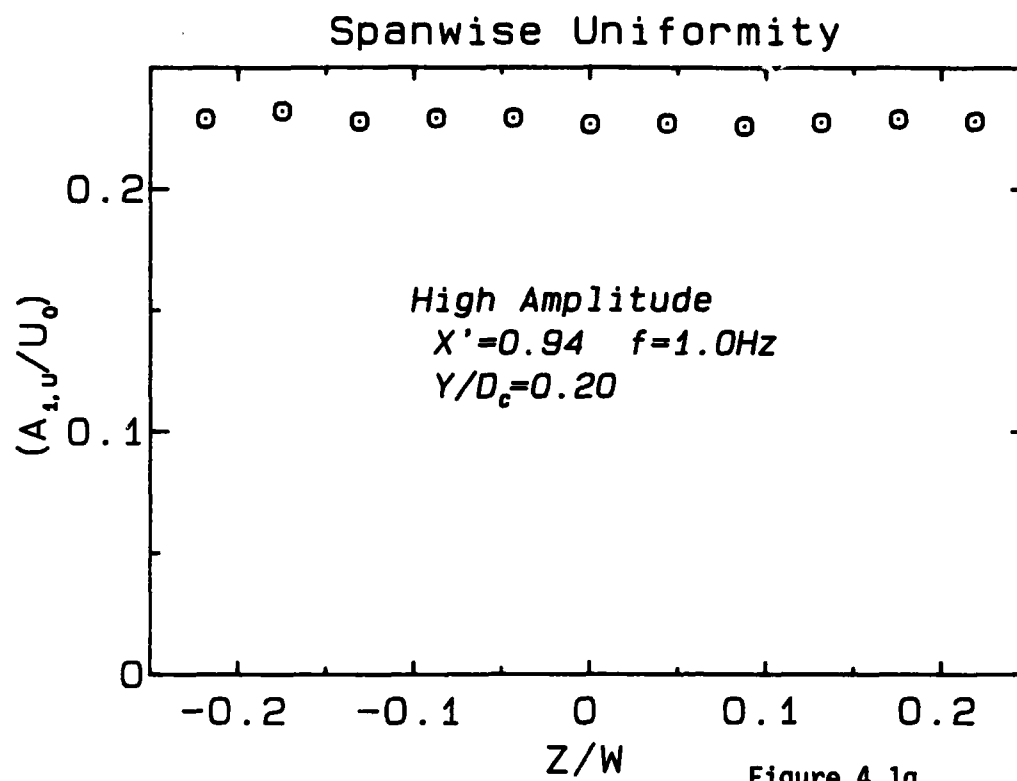


Figure 4.1f





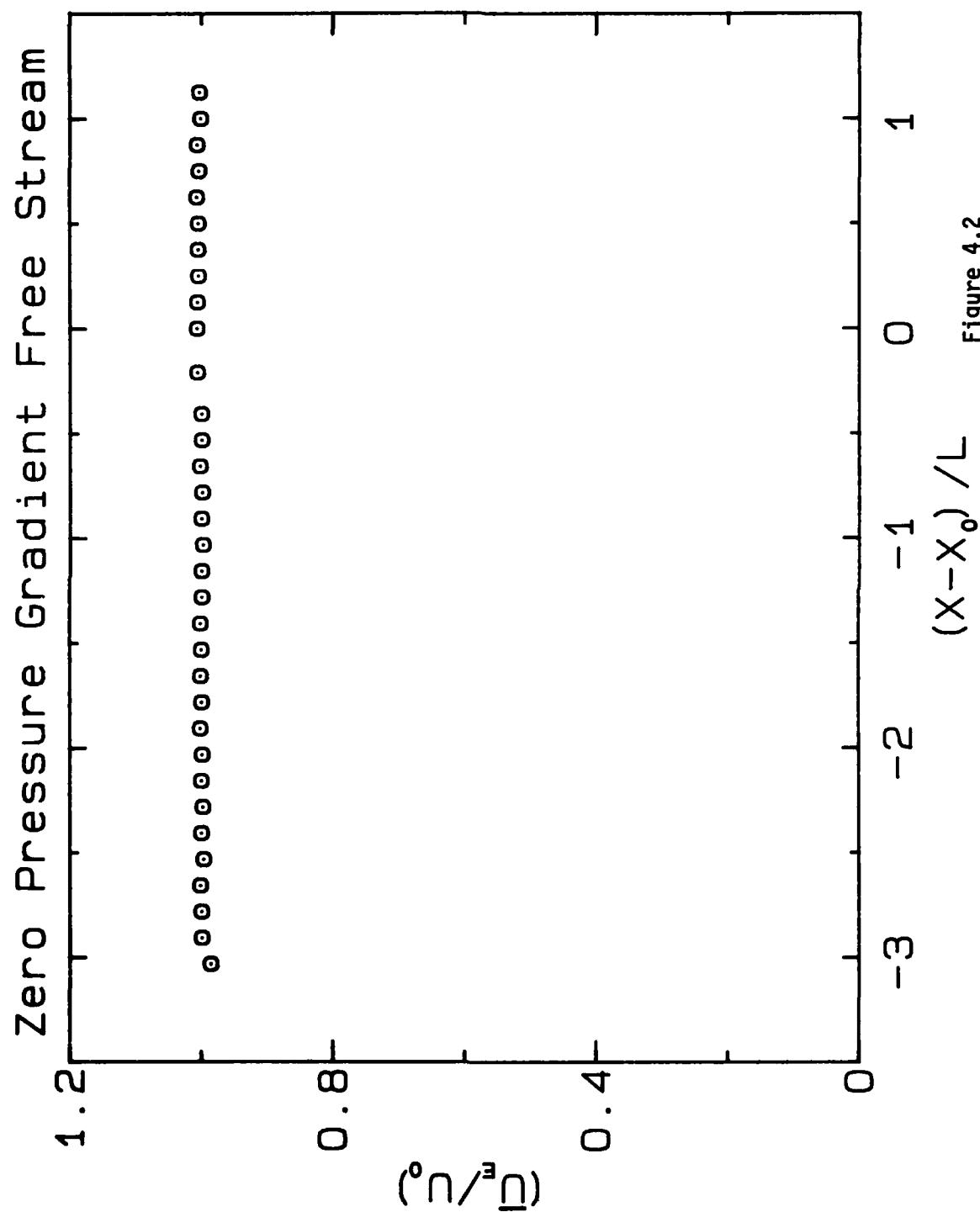


Figure 4.2

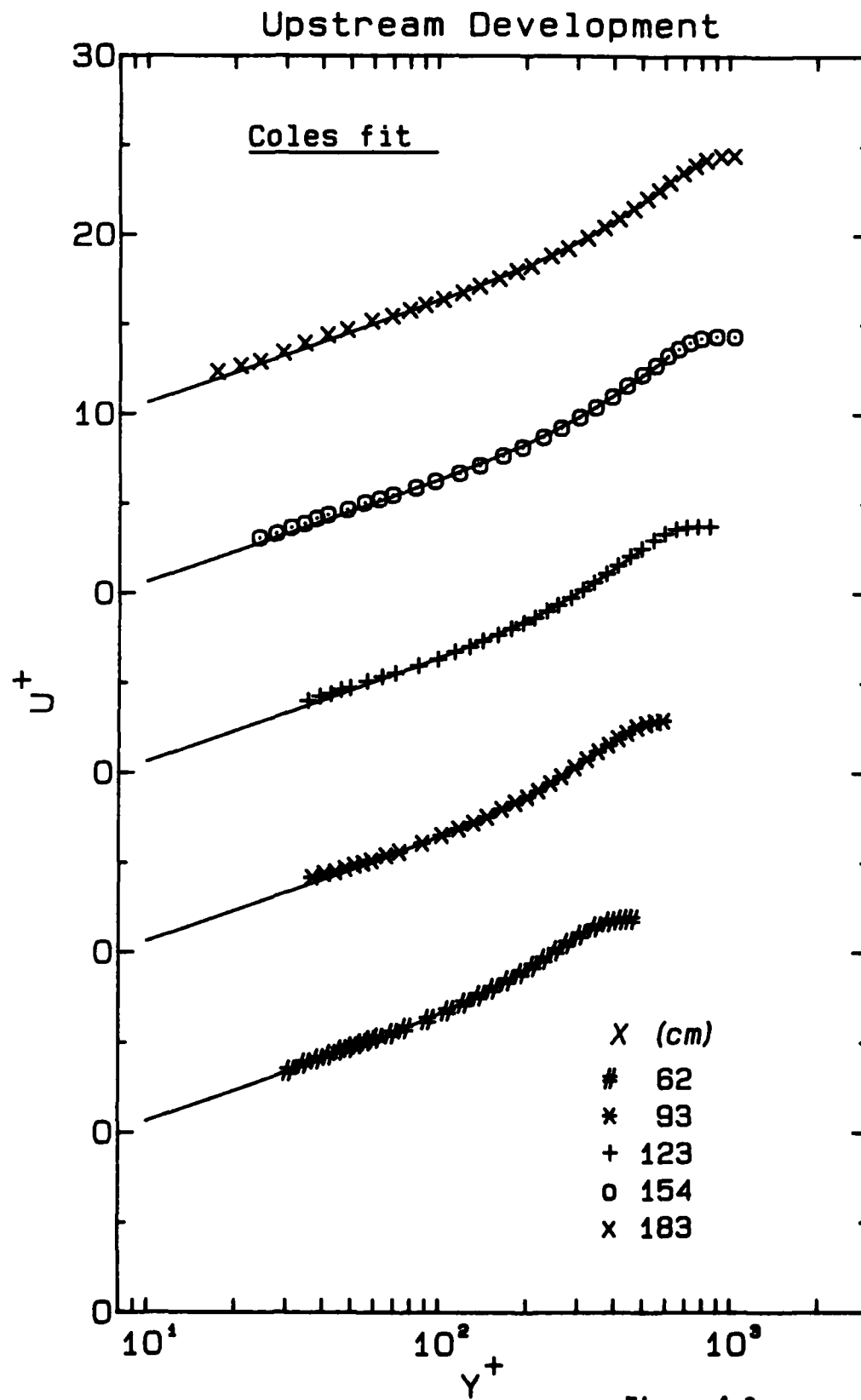


Figure 4.3

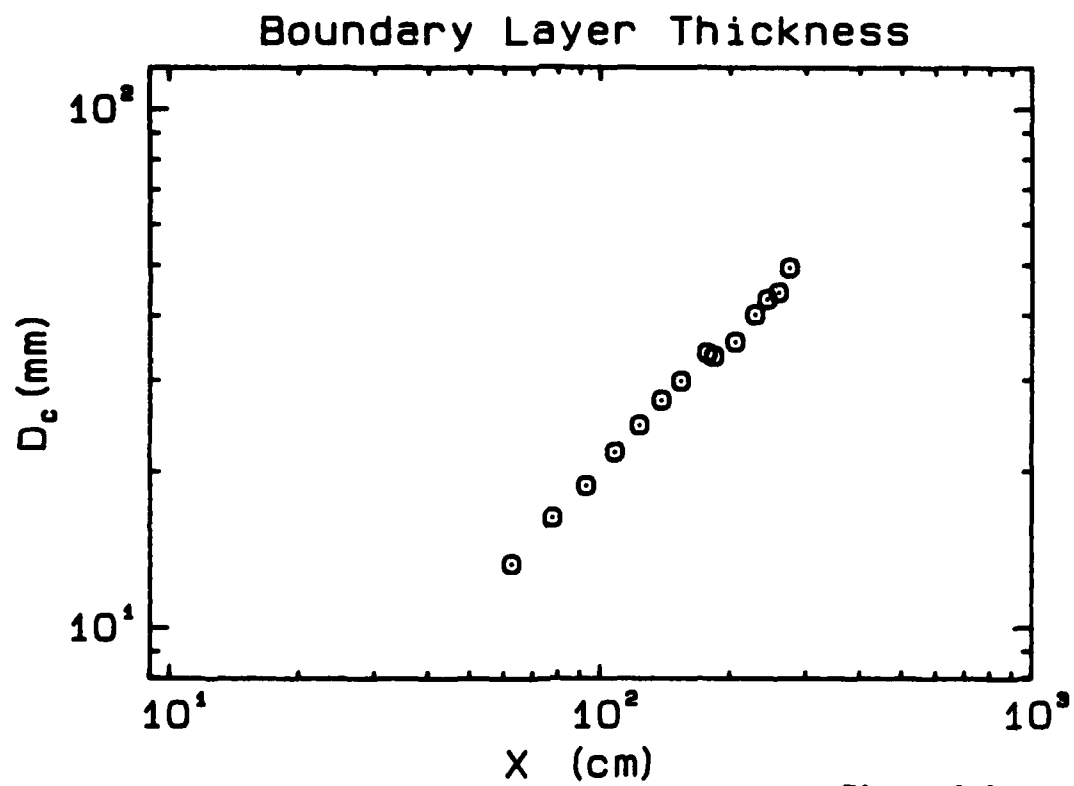


Figure 4.4a

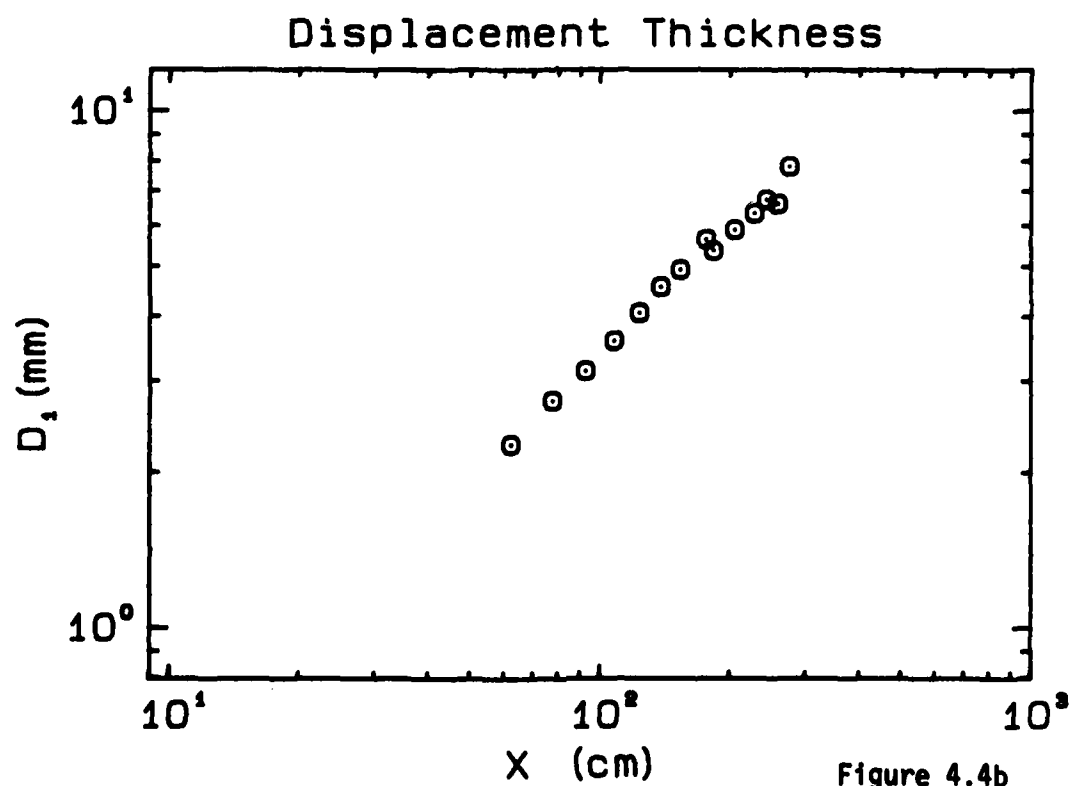


Figure 4.4b

# Skin Friction

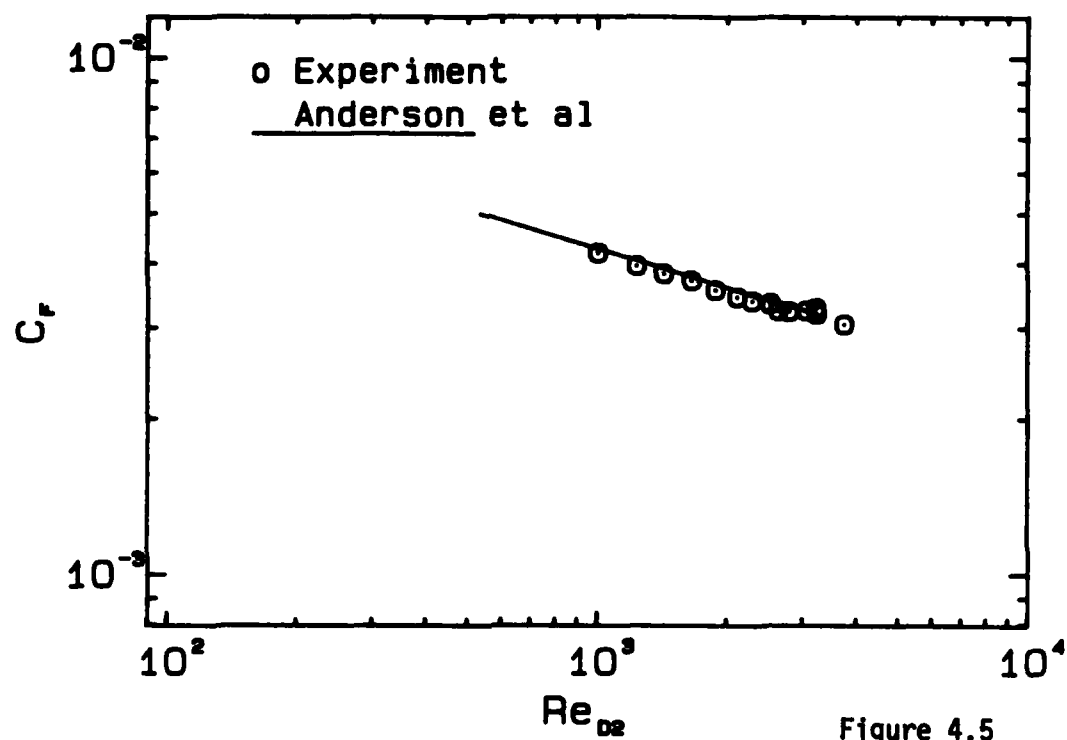


Figure 4.5

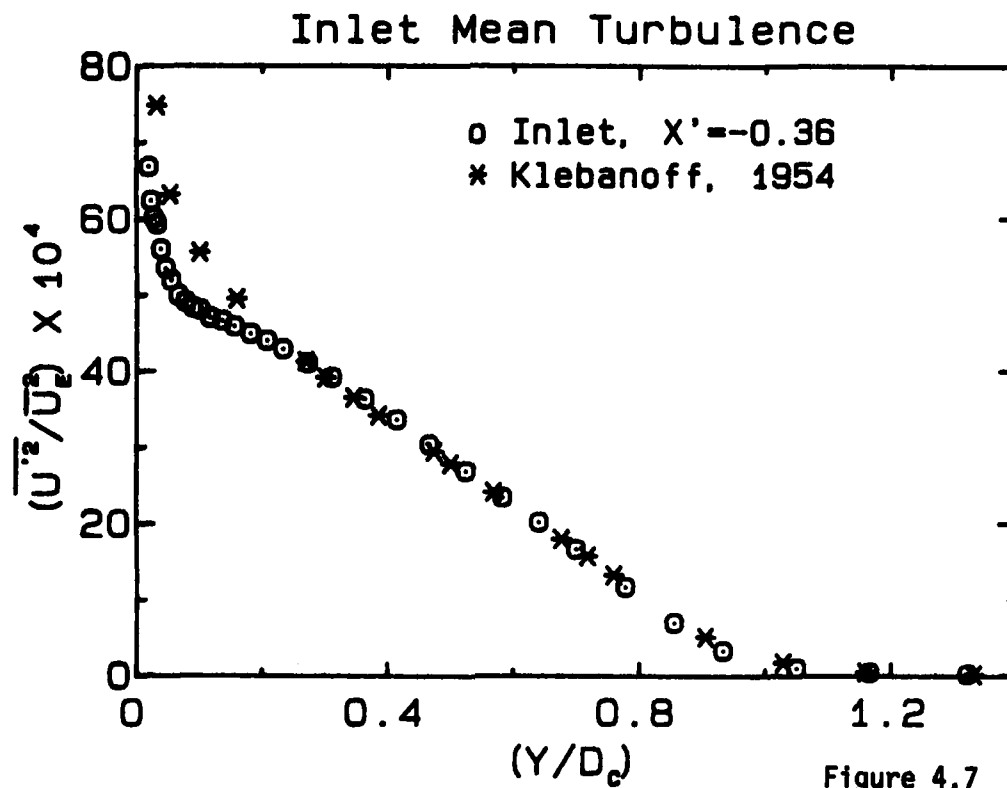


Figure 4.7

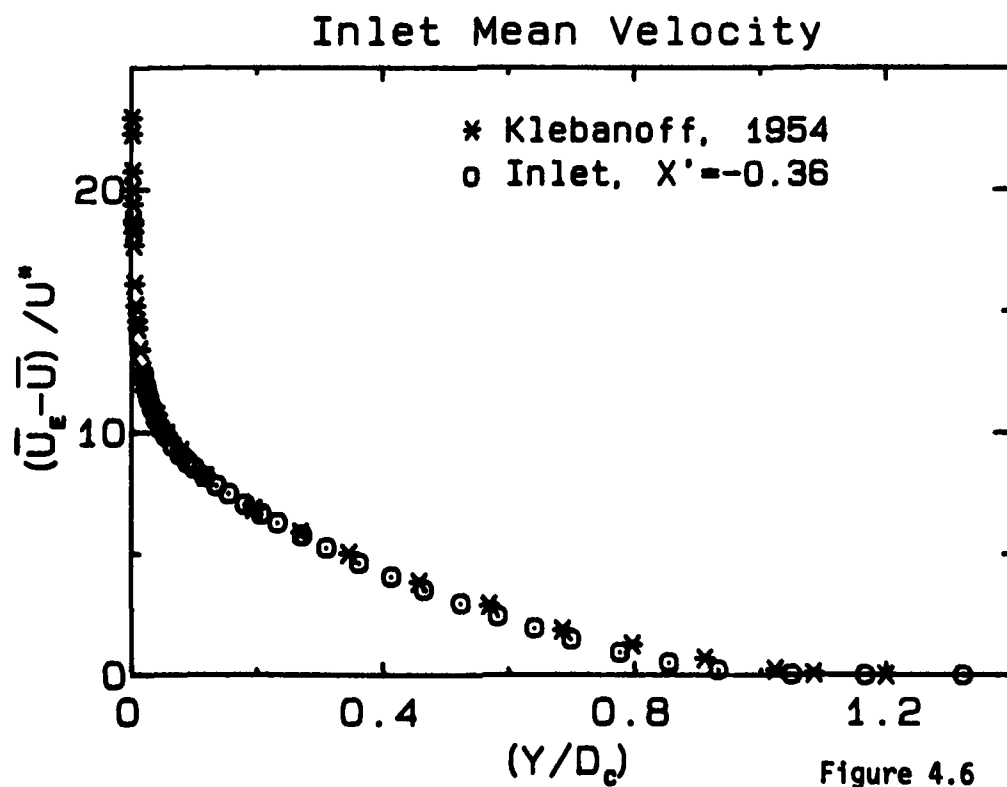


Figure 4.6

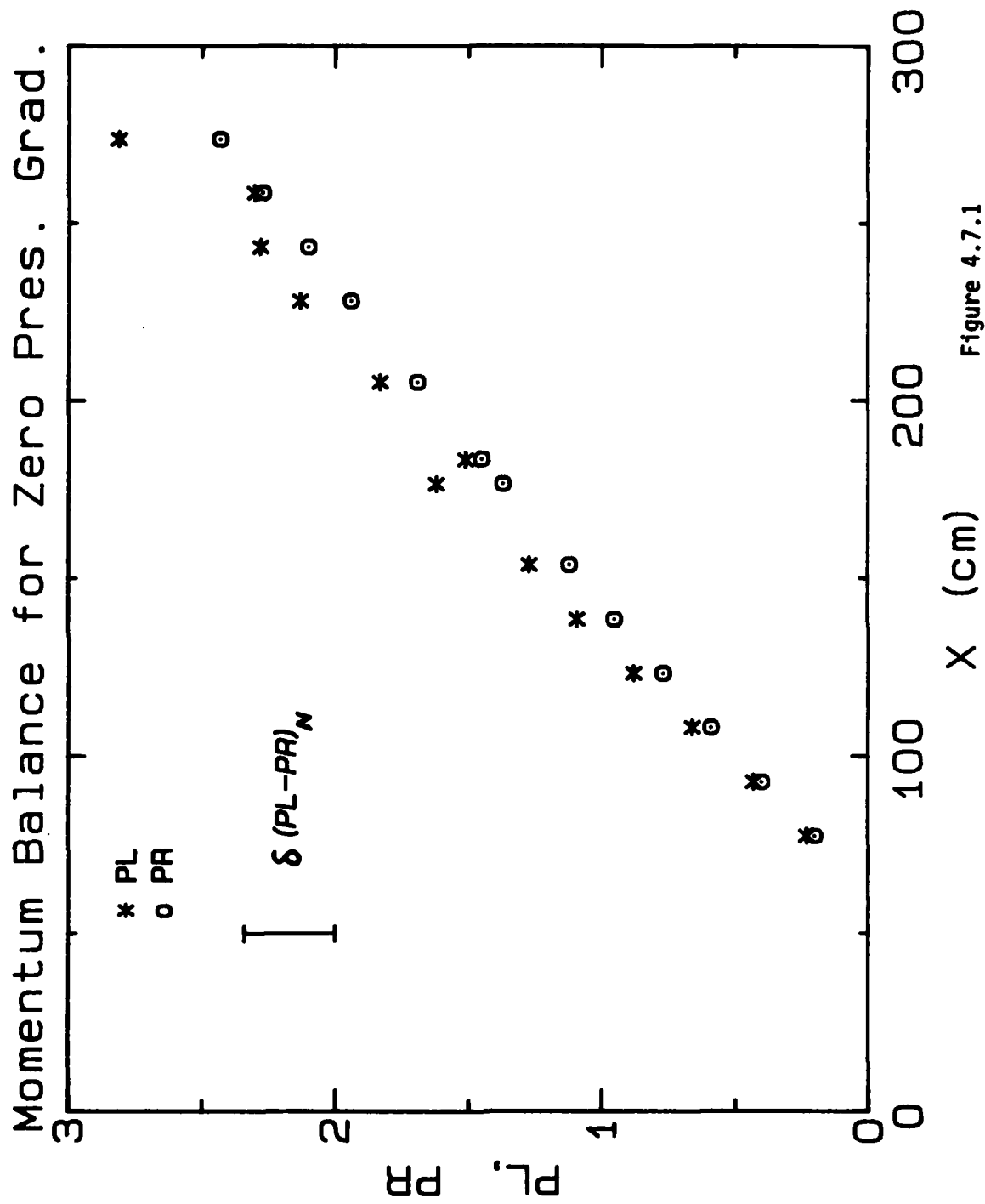


Figure 4.7.1

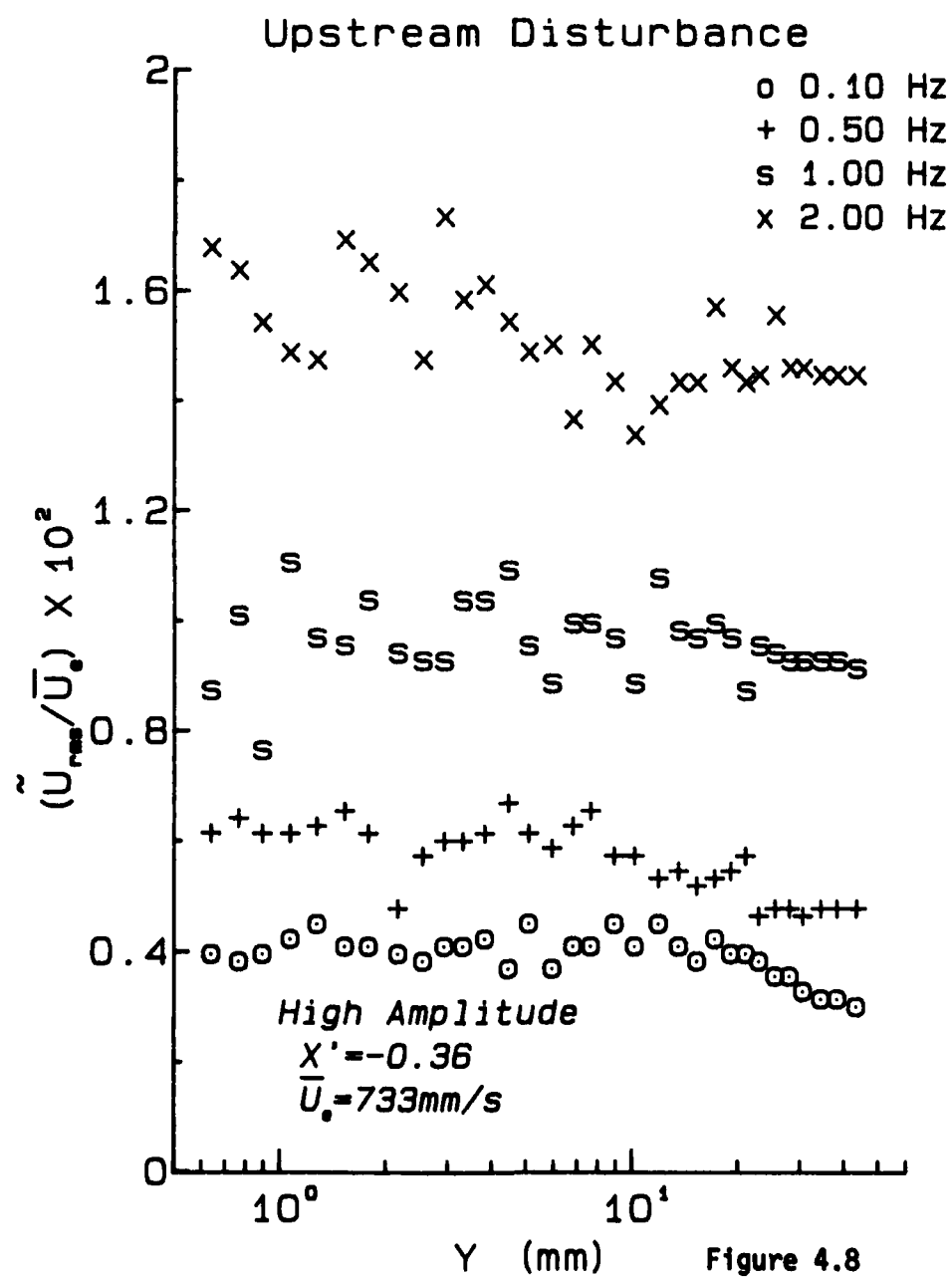


Figure 4.8



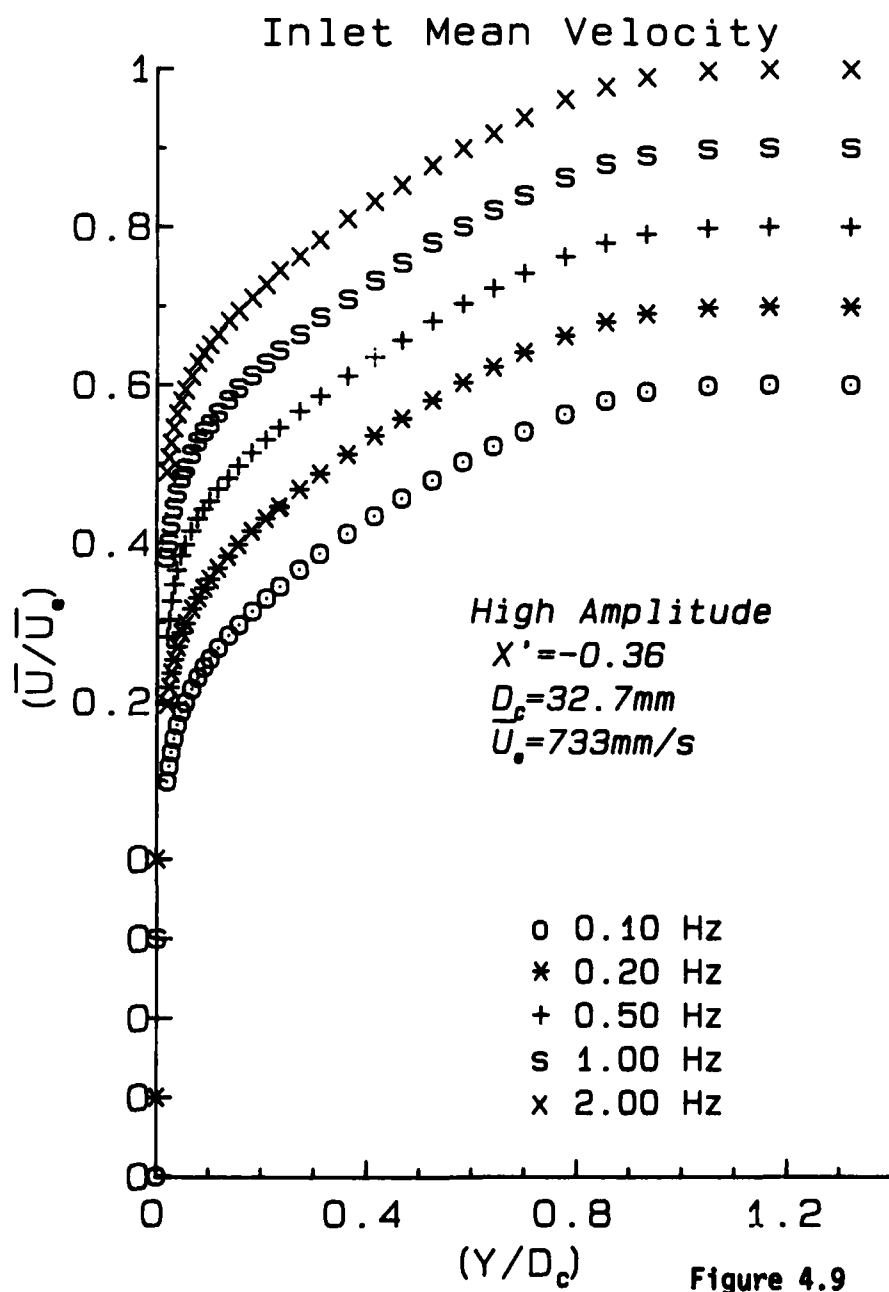


Figure 4.9

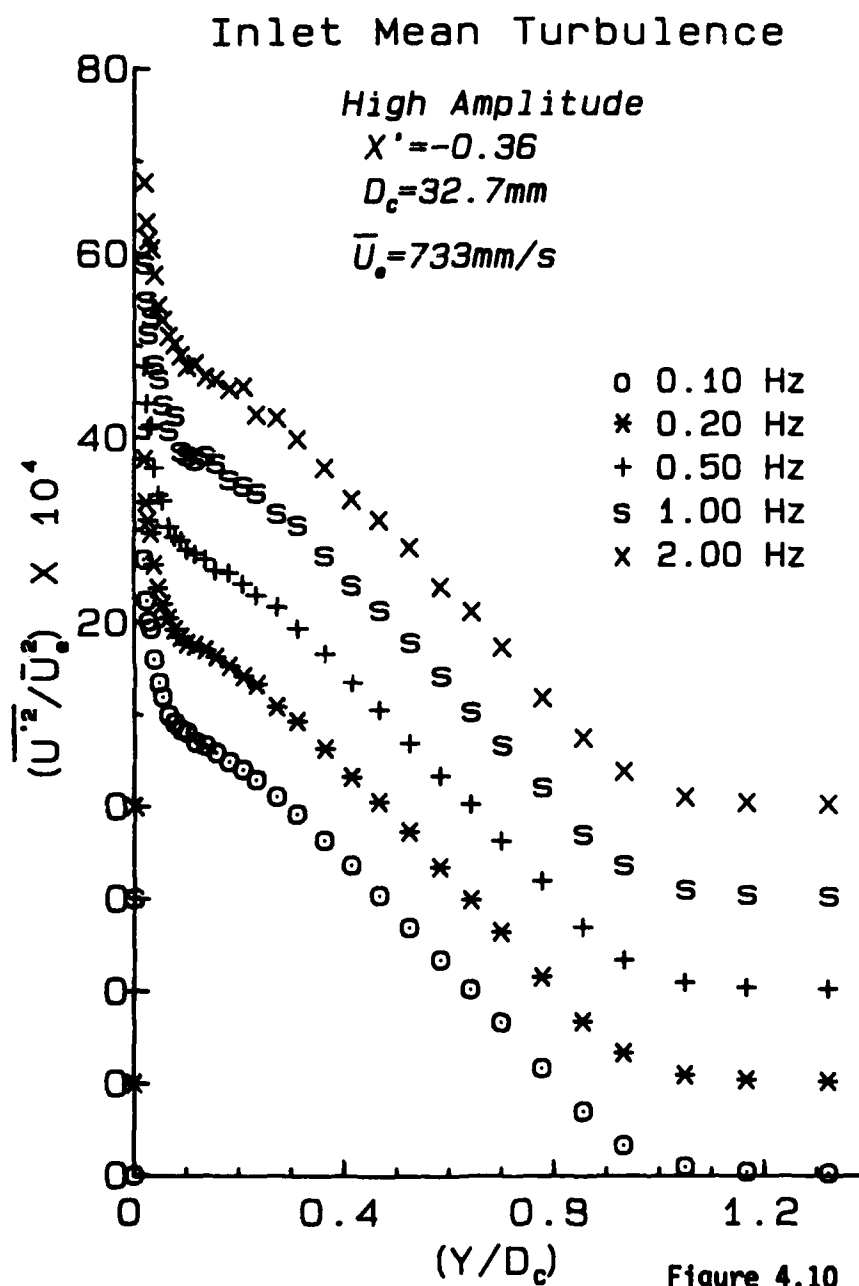


Figure 4.10

# Imposed Free Stream Mean Velocity

Low Amplitude

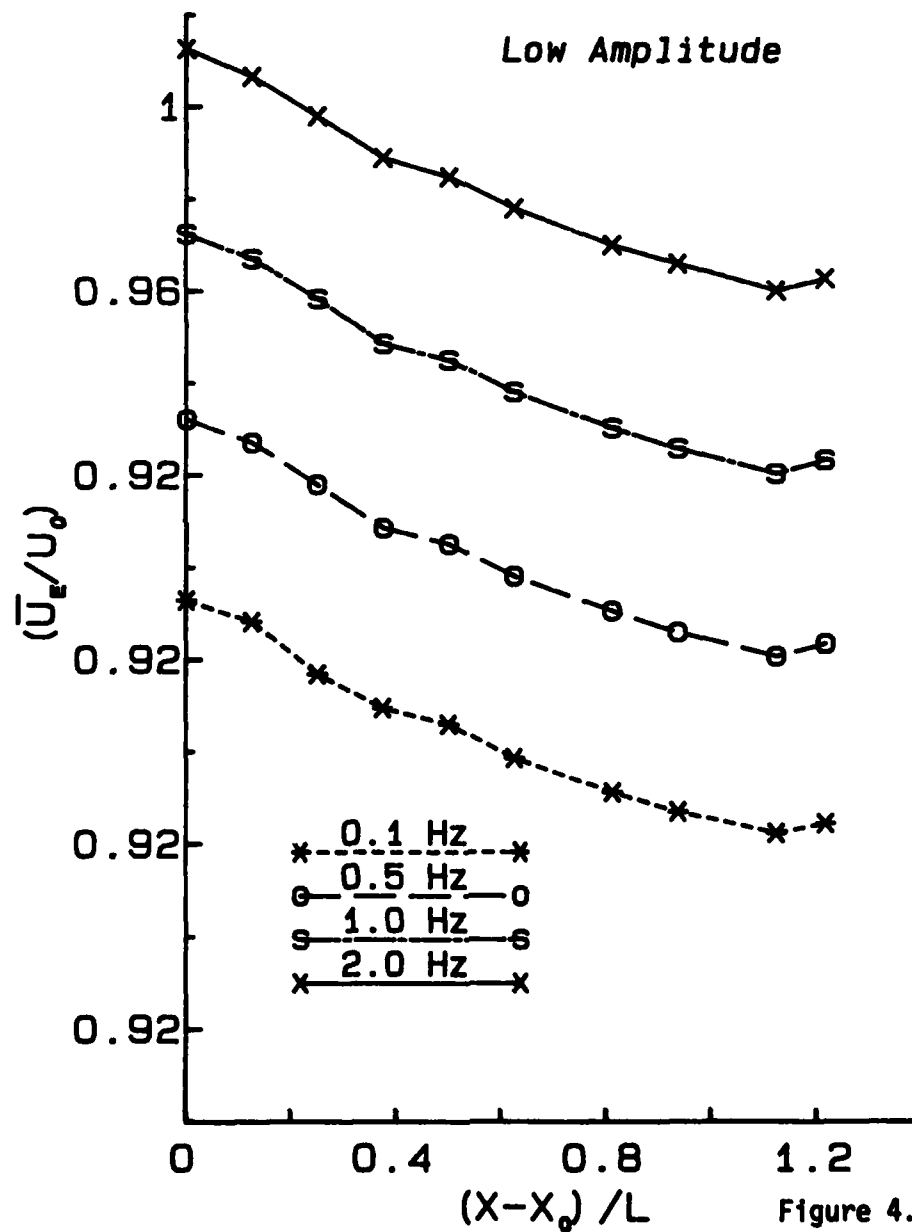


Figure 4.11a

# Imposed Free Stream Mean Velocity

High Amplitude

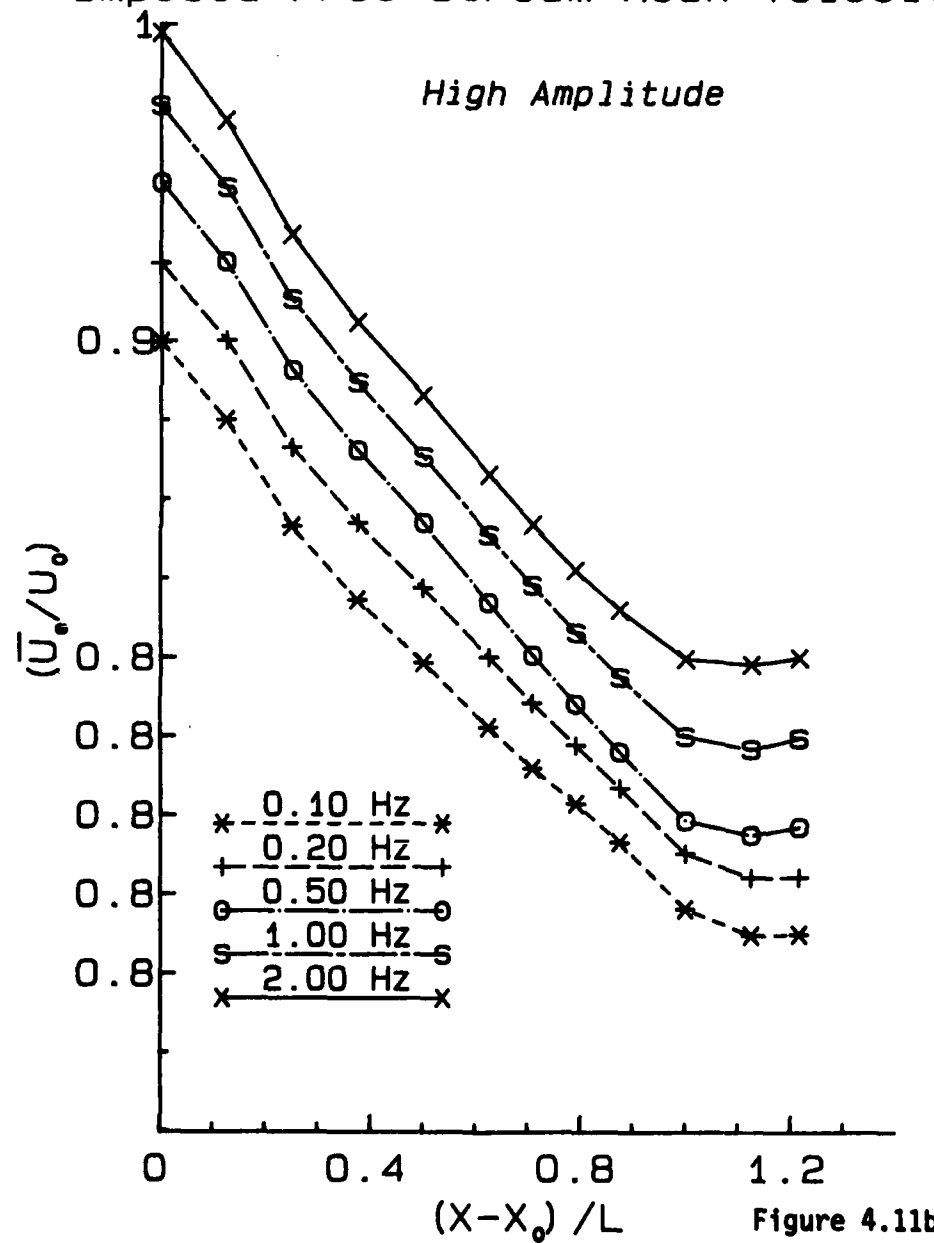


Figure 4.11b

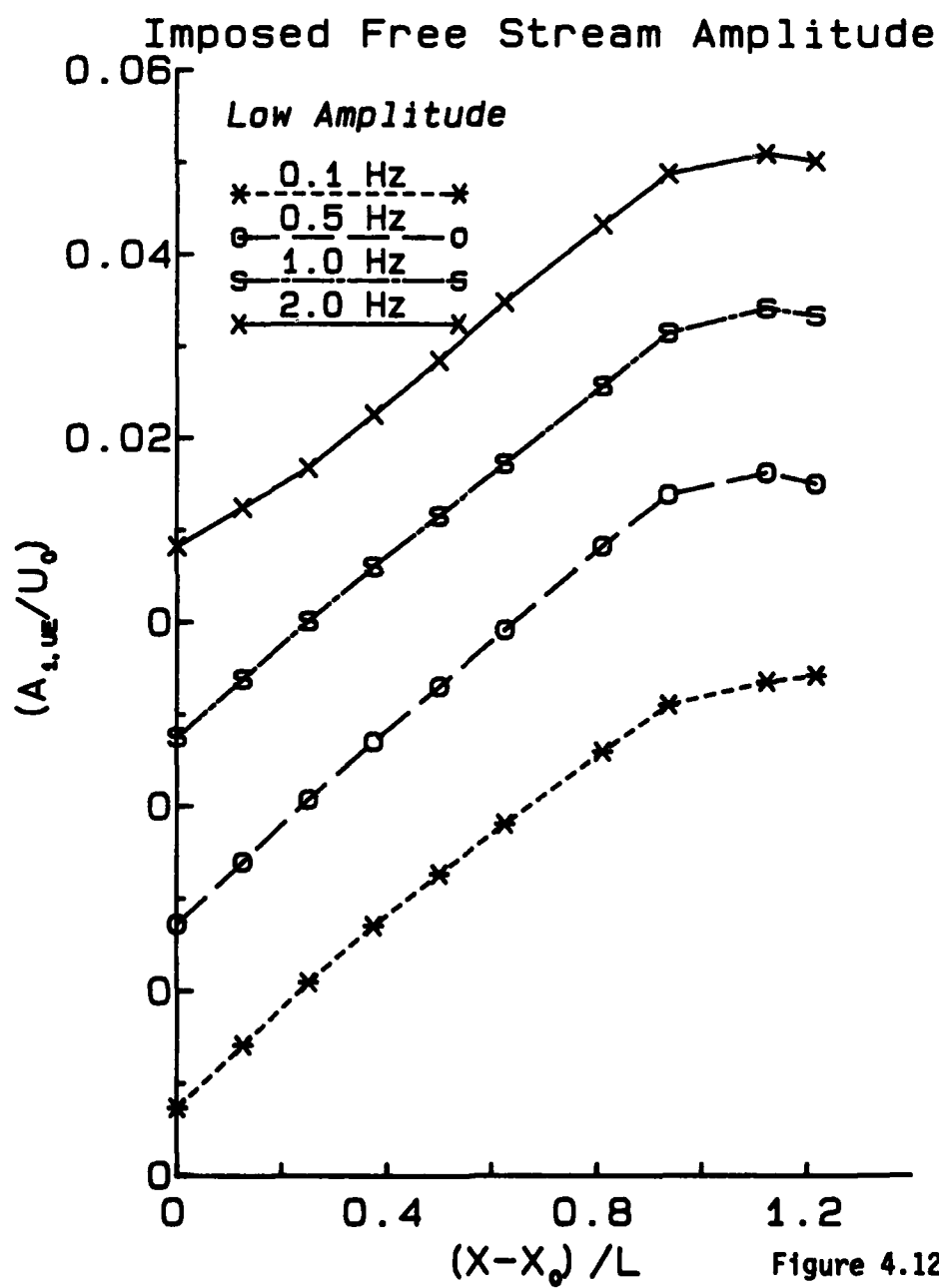
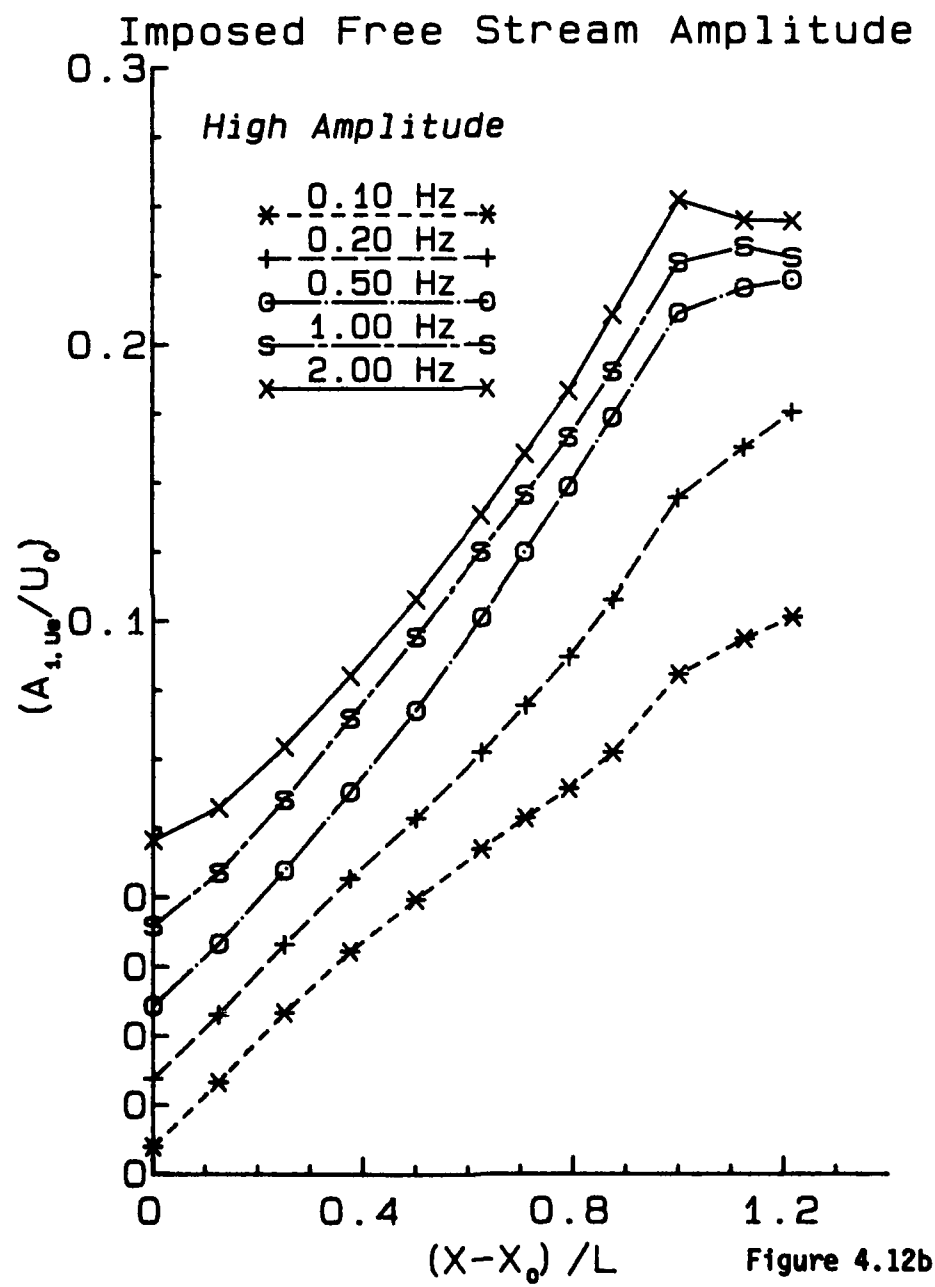
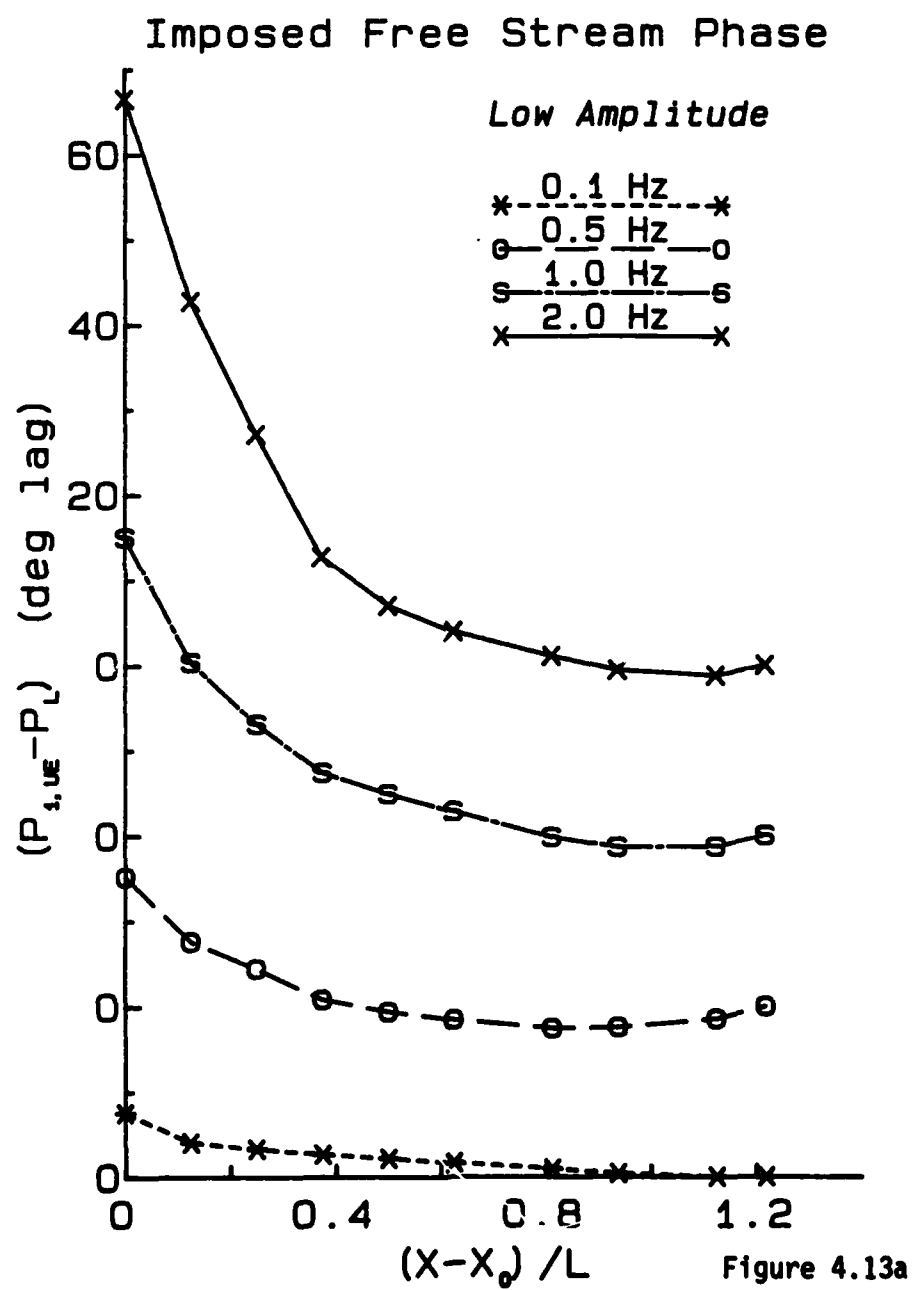


Figure 4.12a





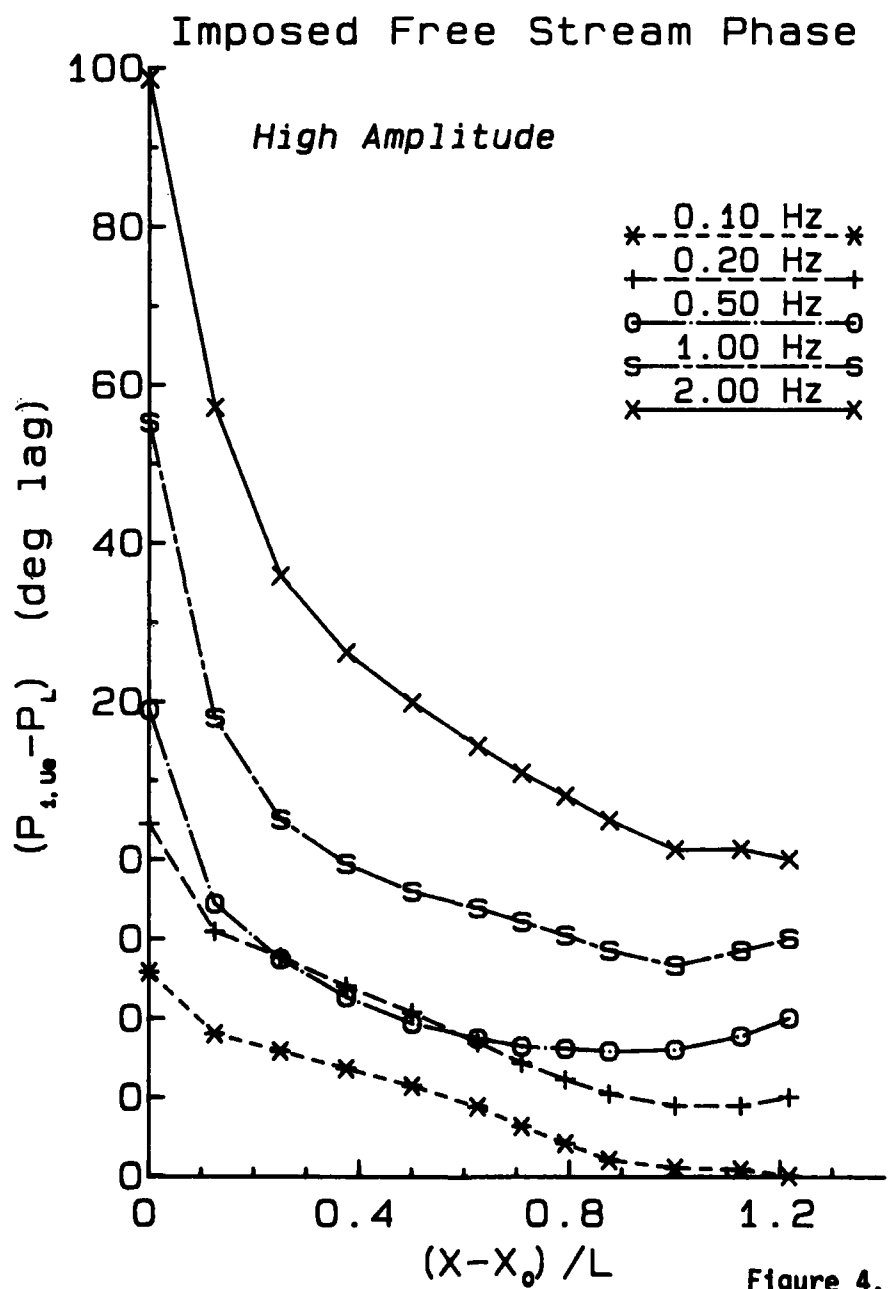


Figure 4.13b



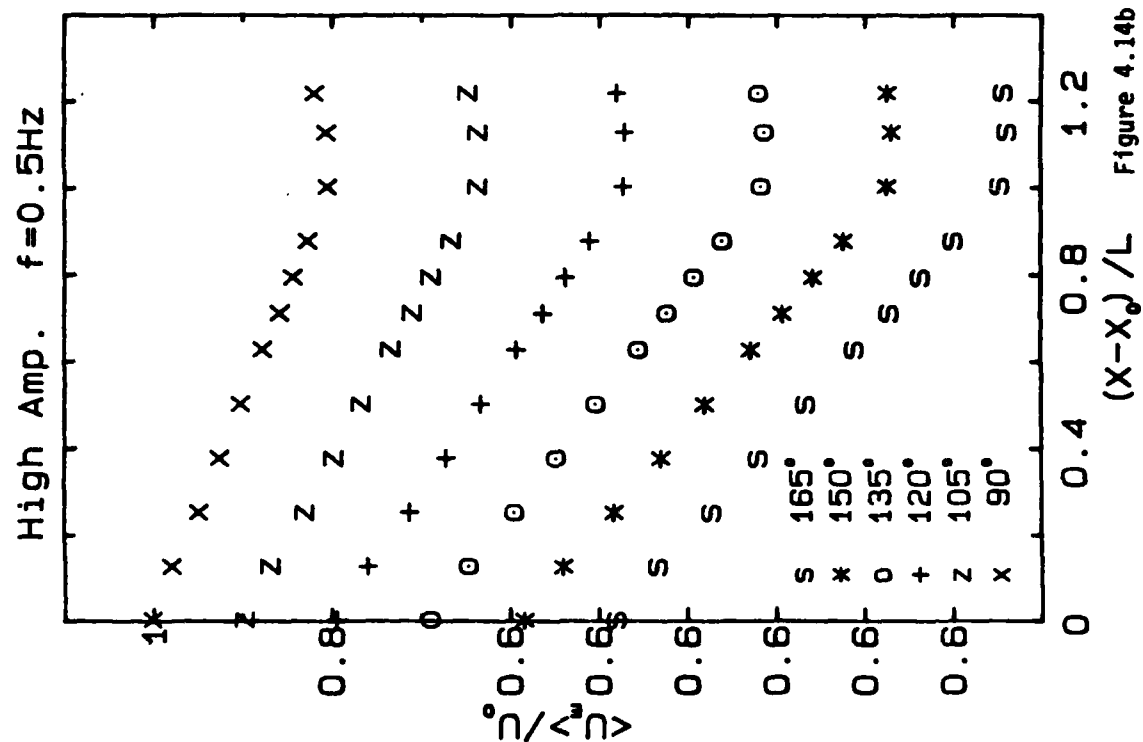


Figure 4.14b

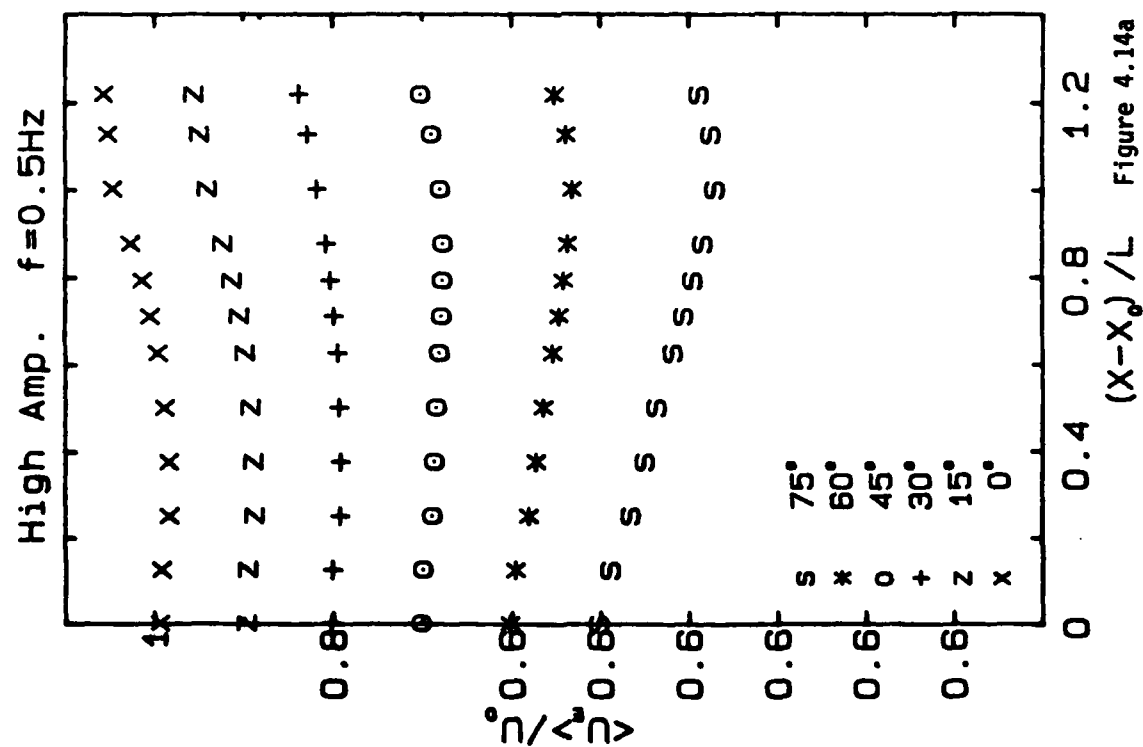


Figure 4.14a

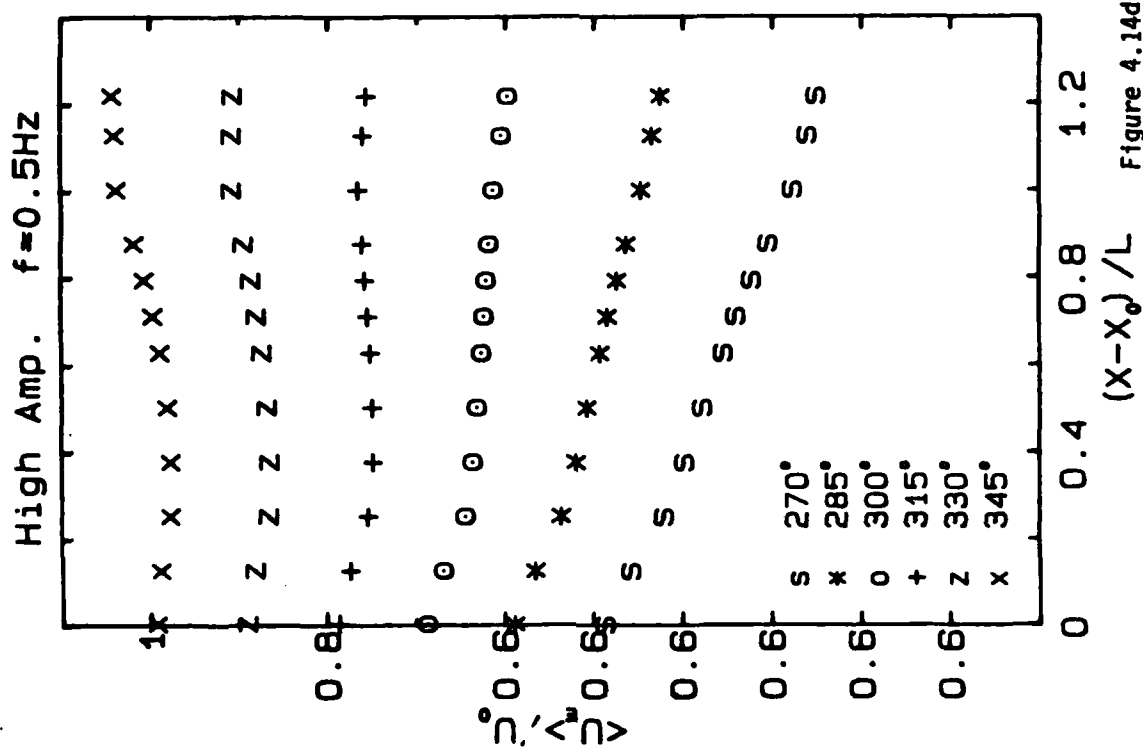


Figure 4.14c

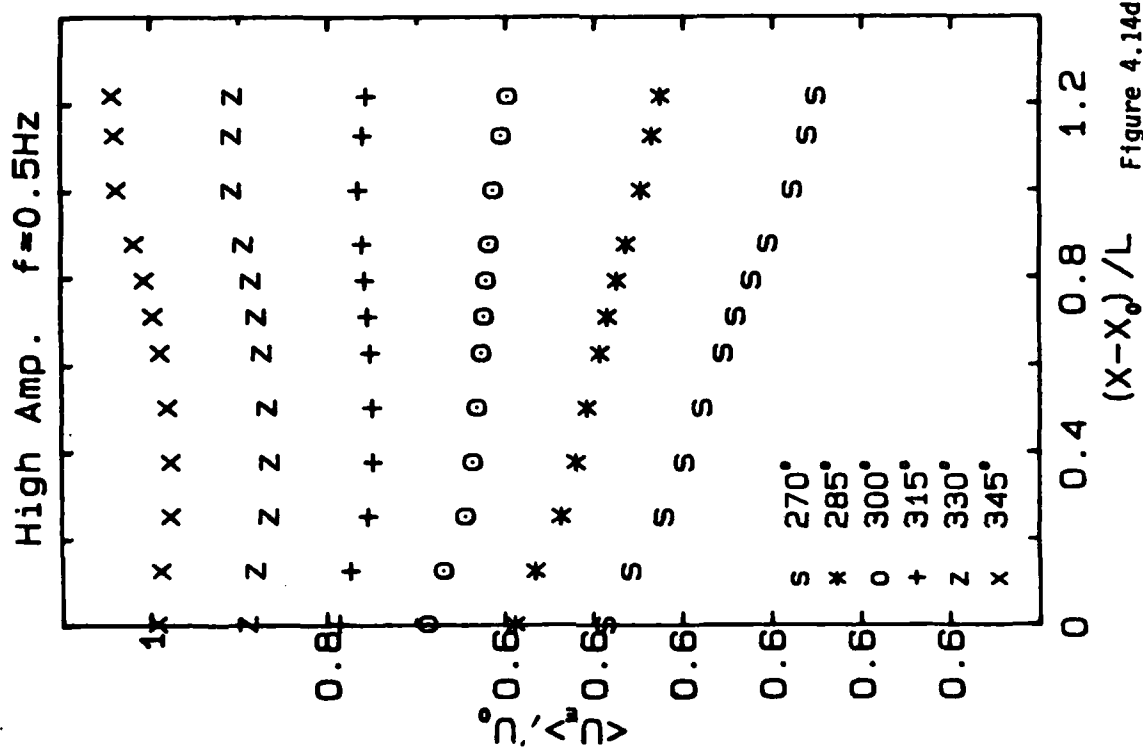


Figure 4.14d

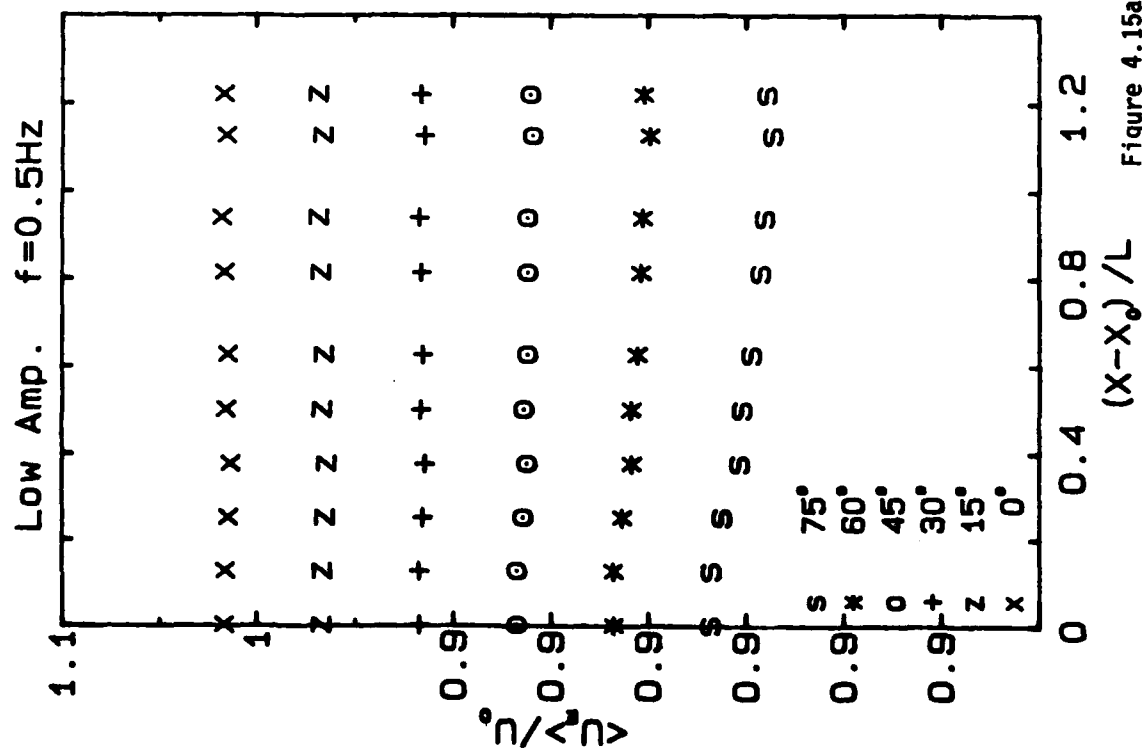


Figure 4.15a

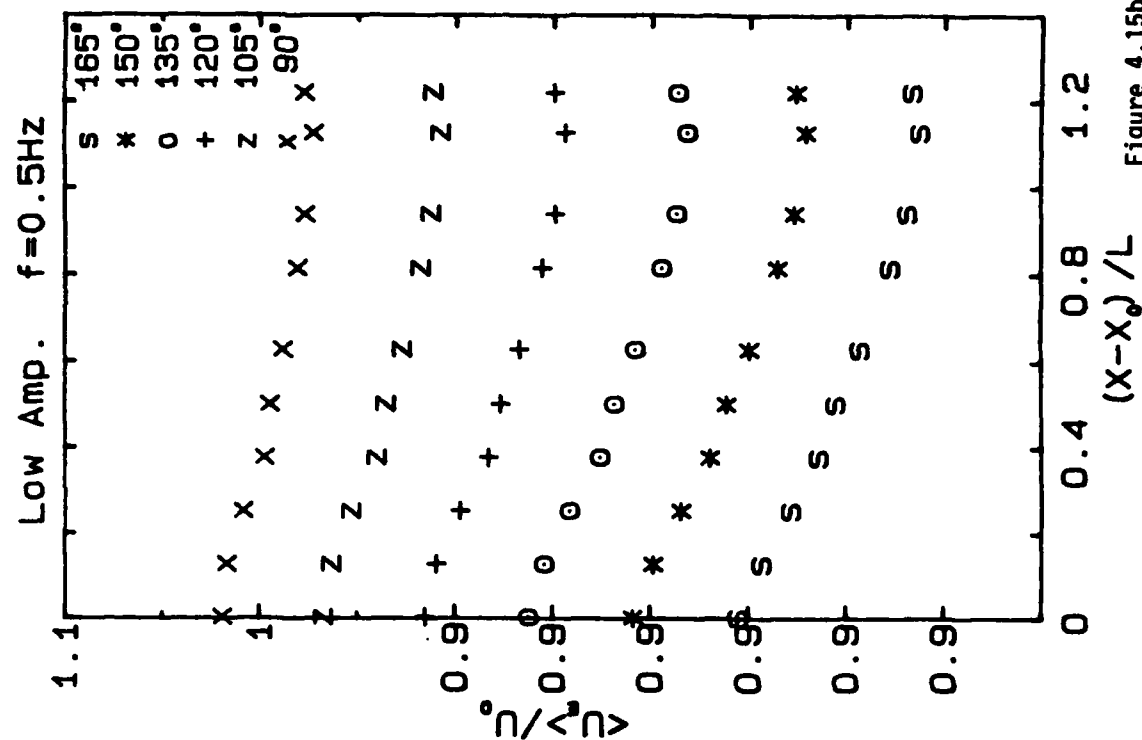


Figure 4.15b

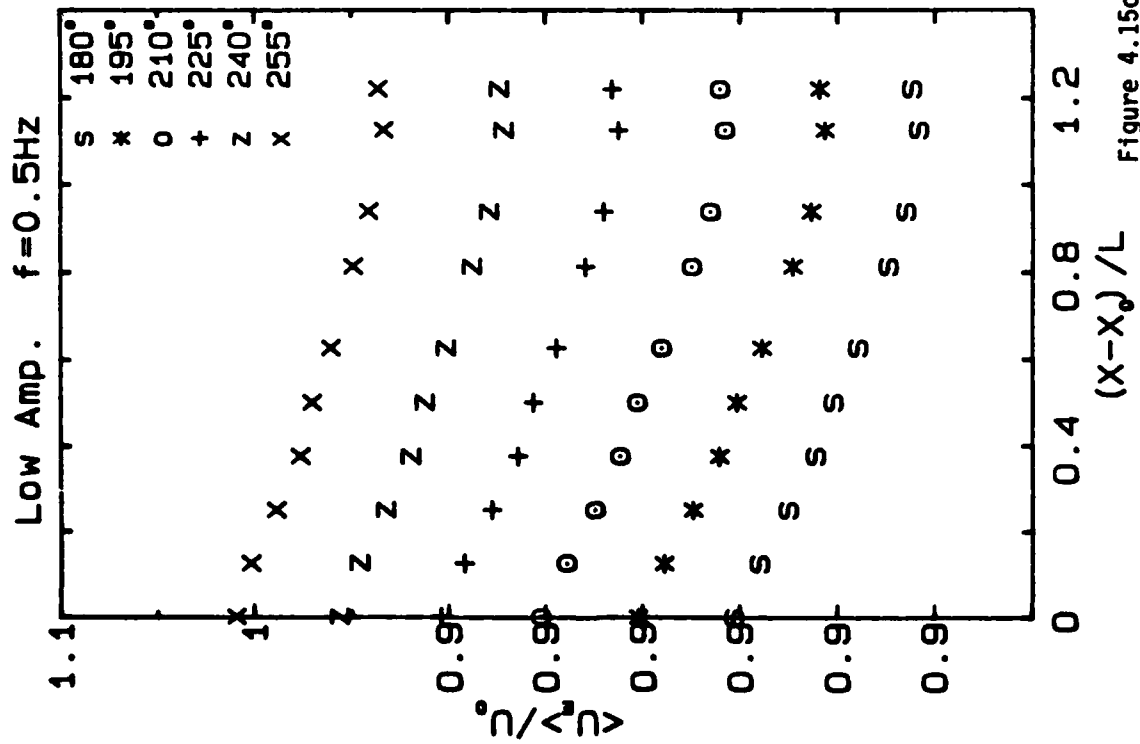


Figure 4.15c

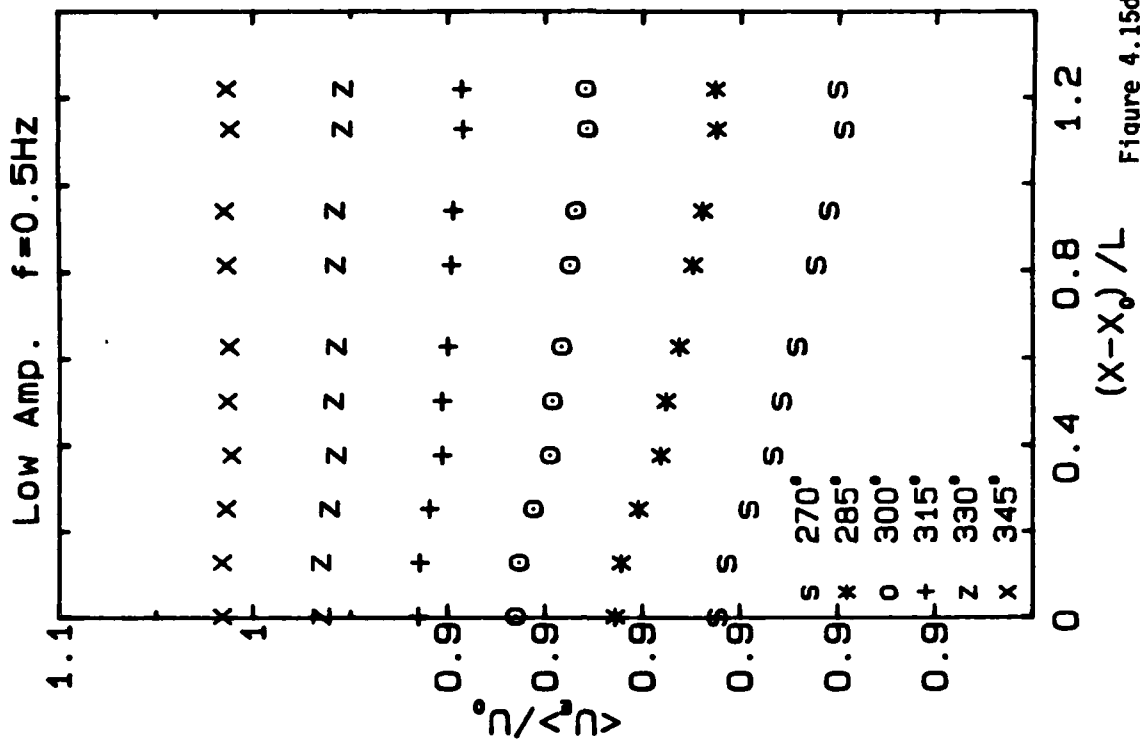
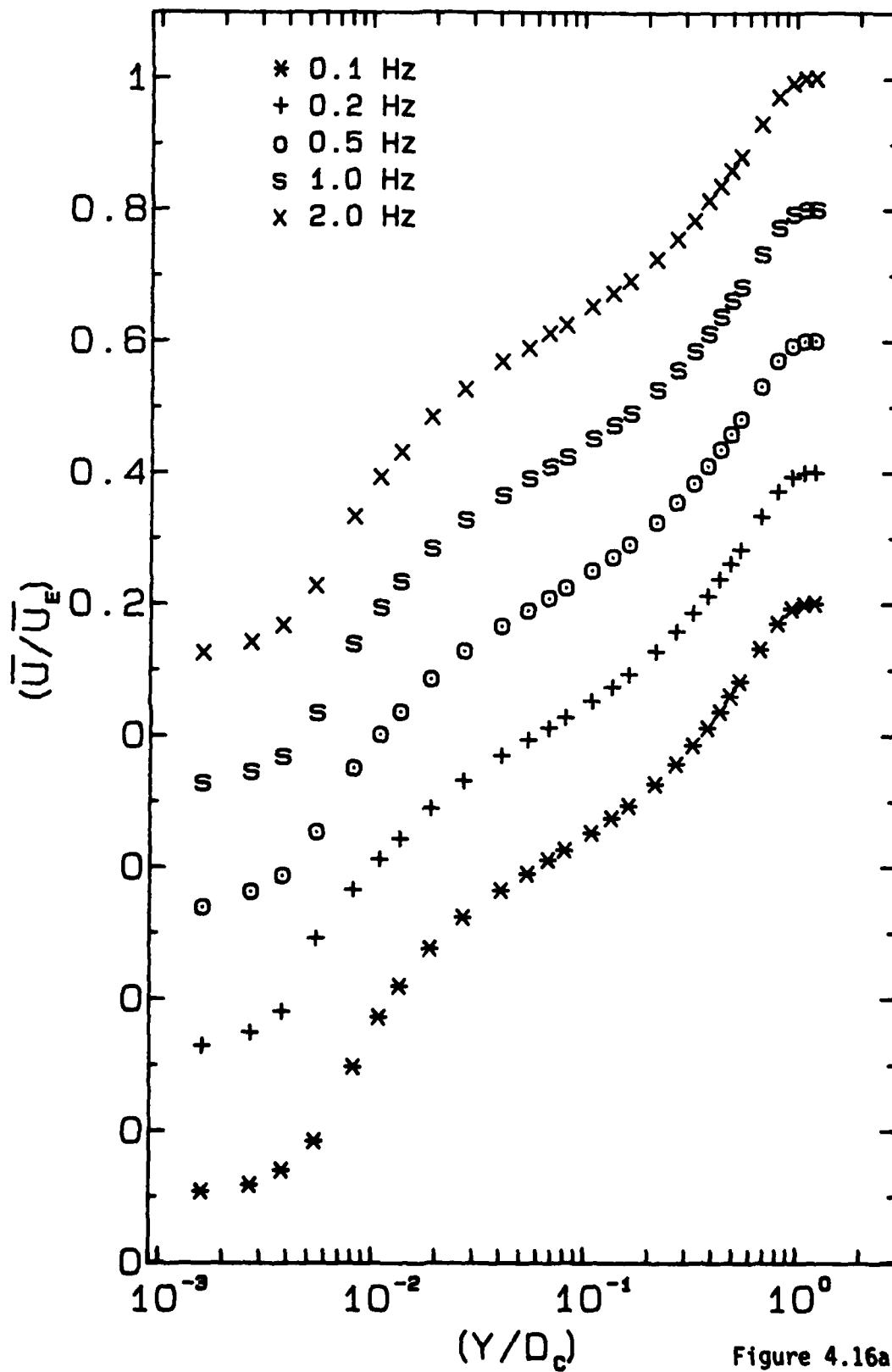
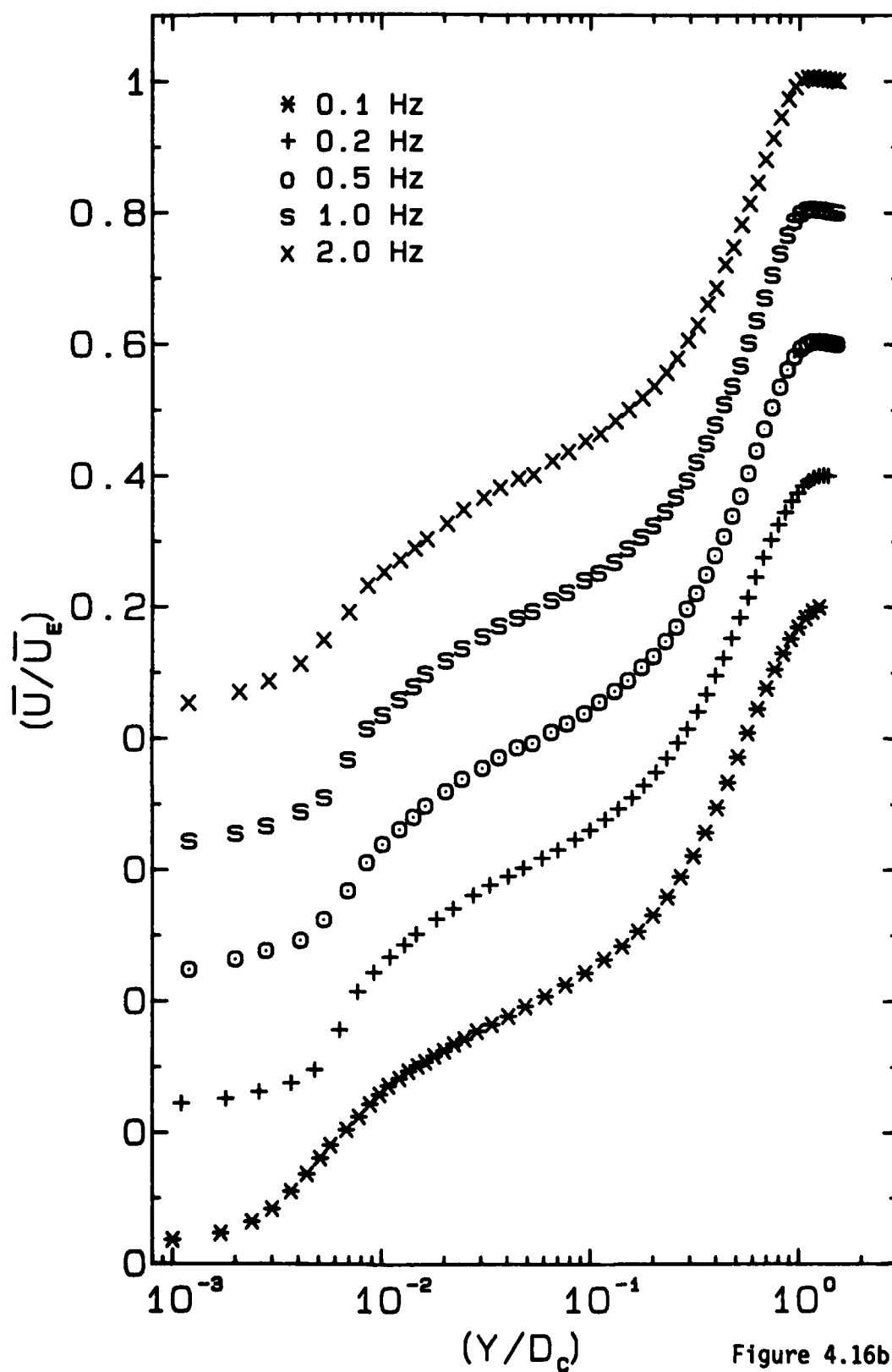


Figure 4.15d

Low Amplitude  $X'=0.88$



High Amplitude  $X'=0.94$



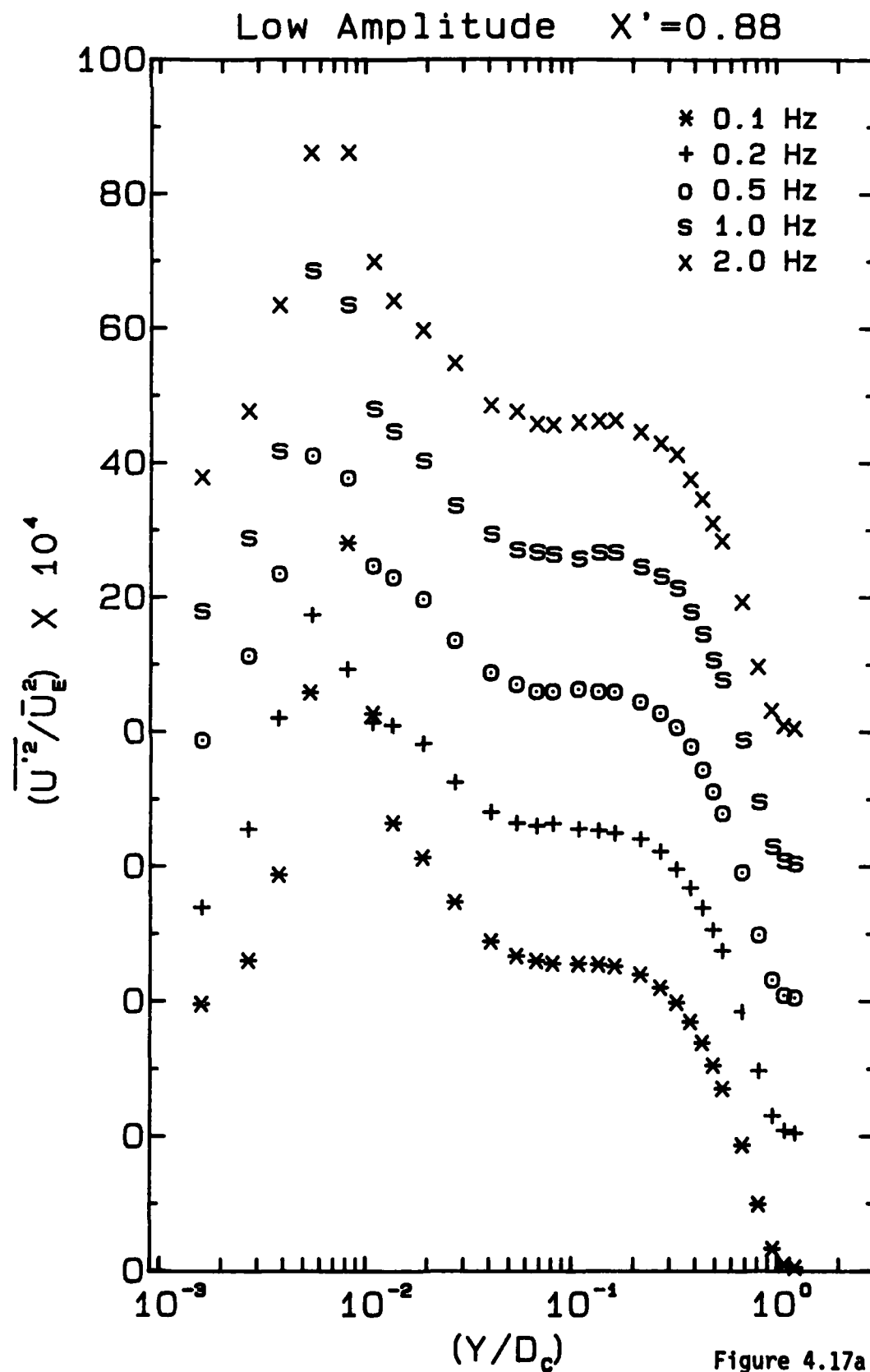
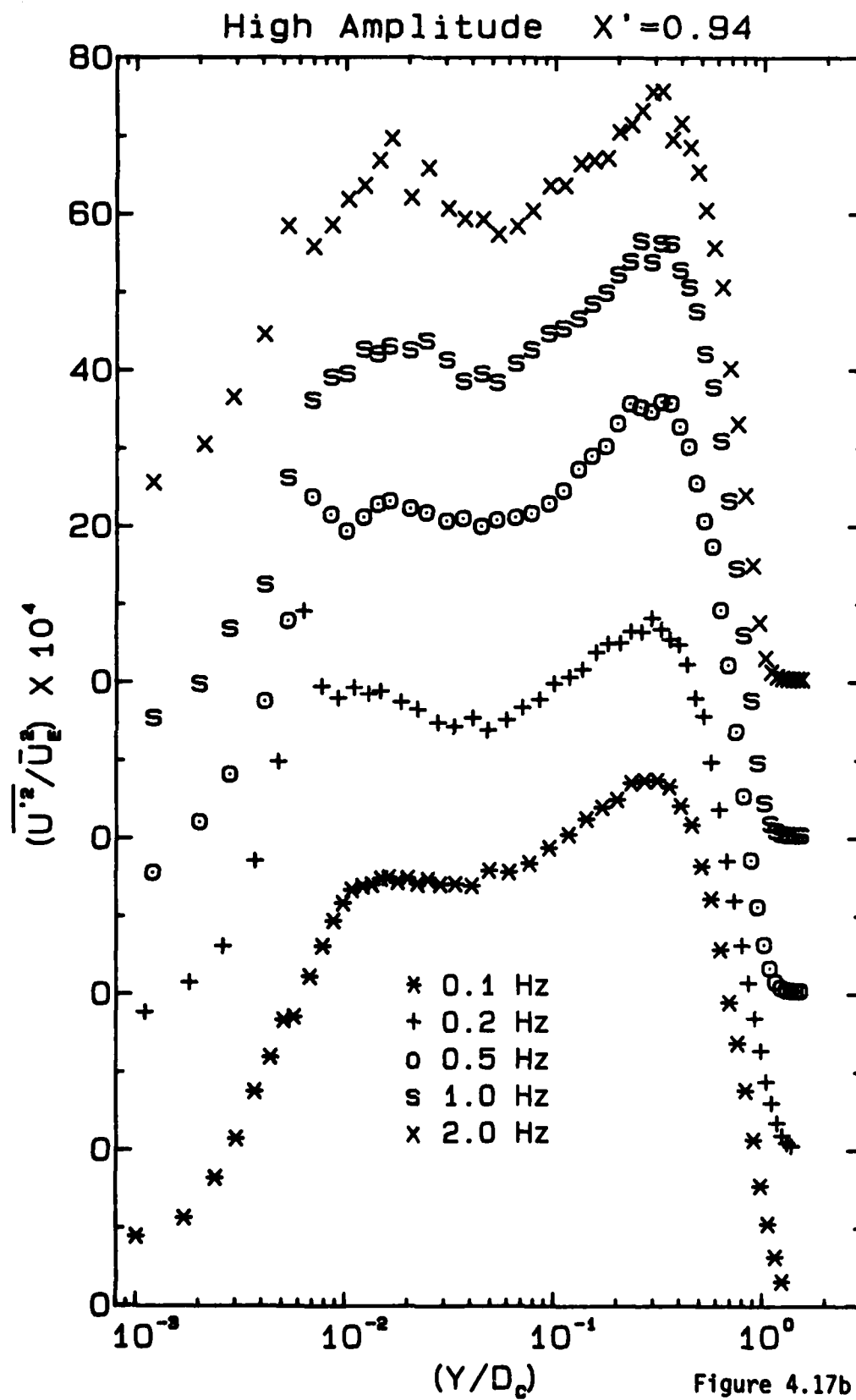
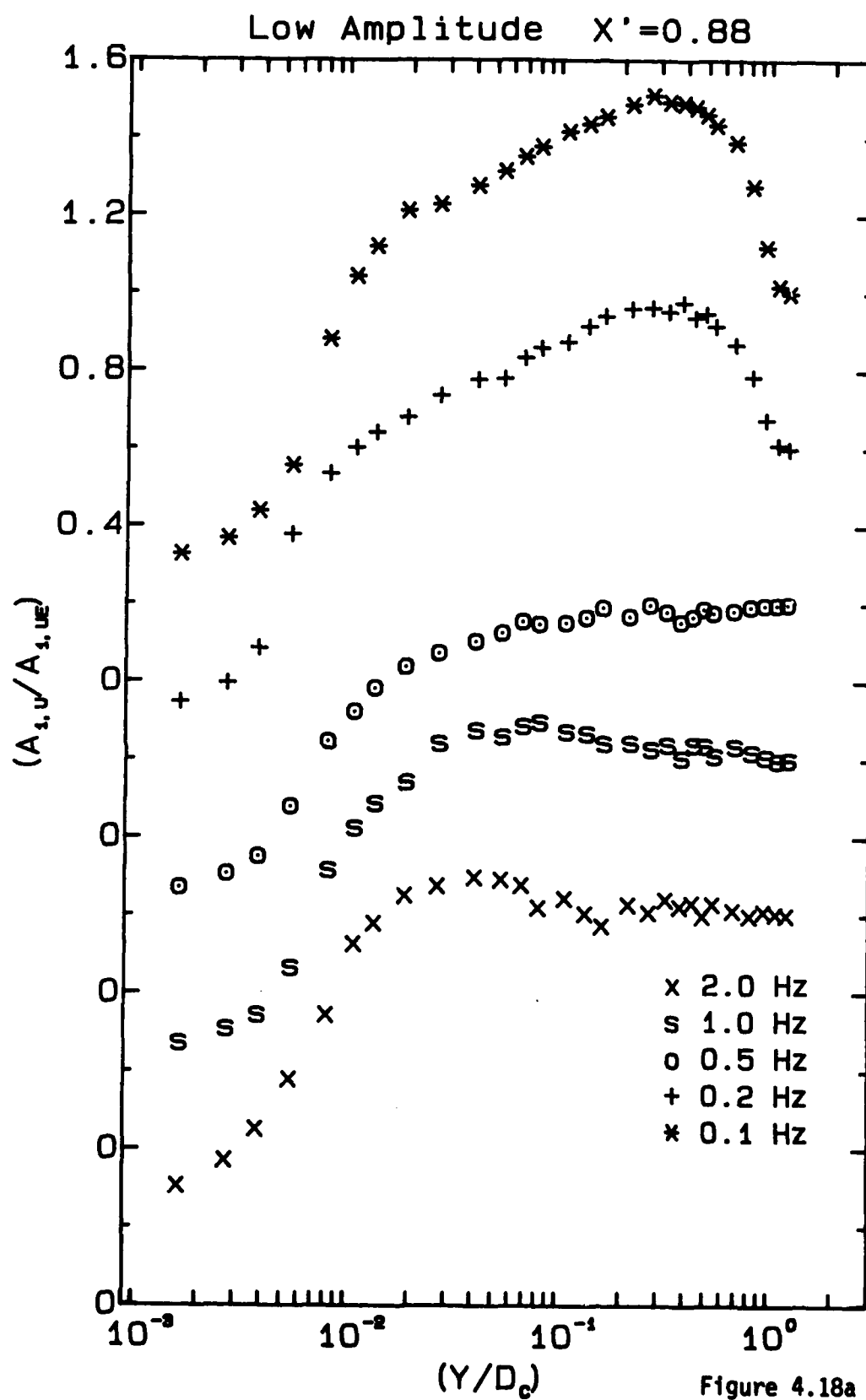


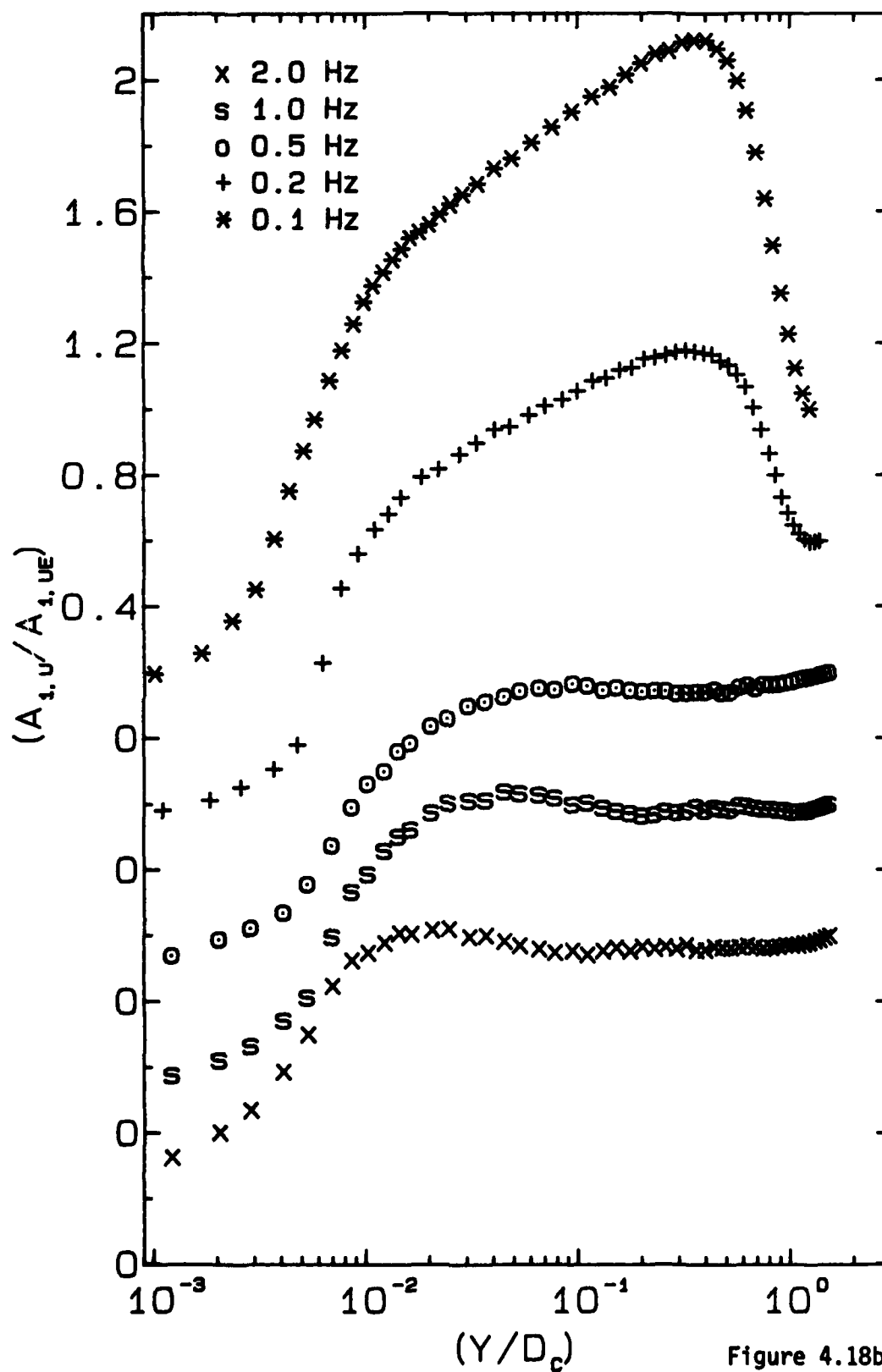
Figure 4.17a

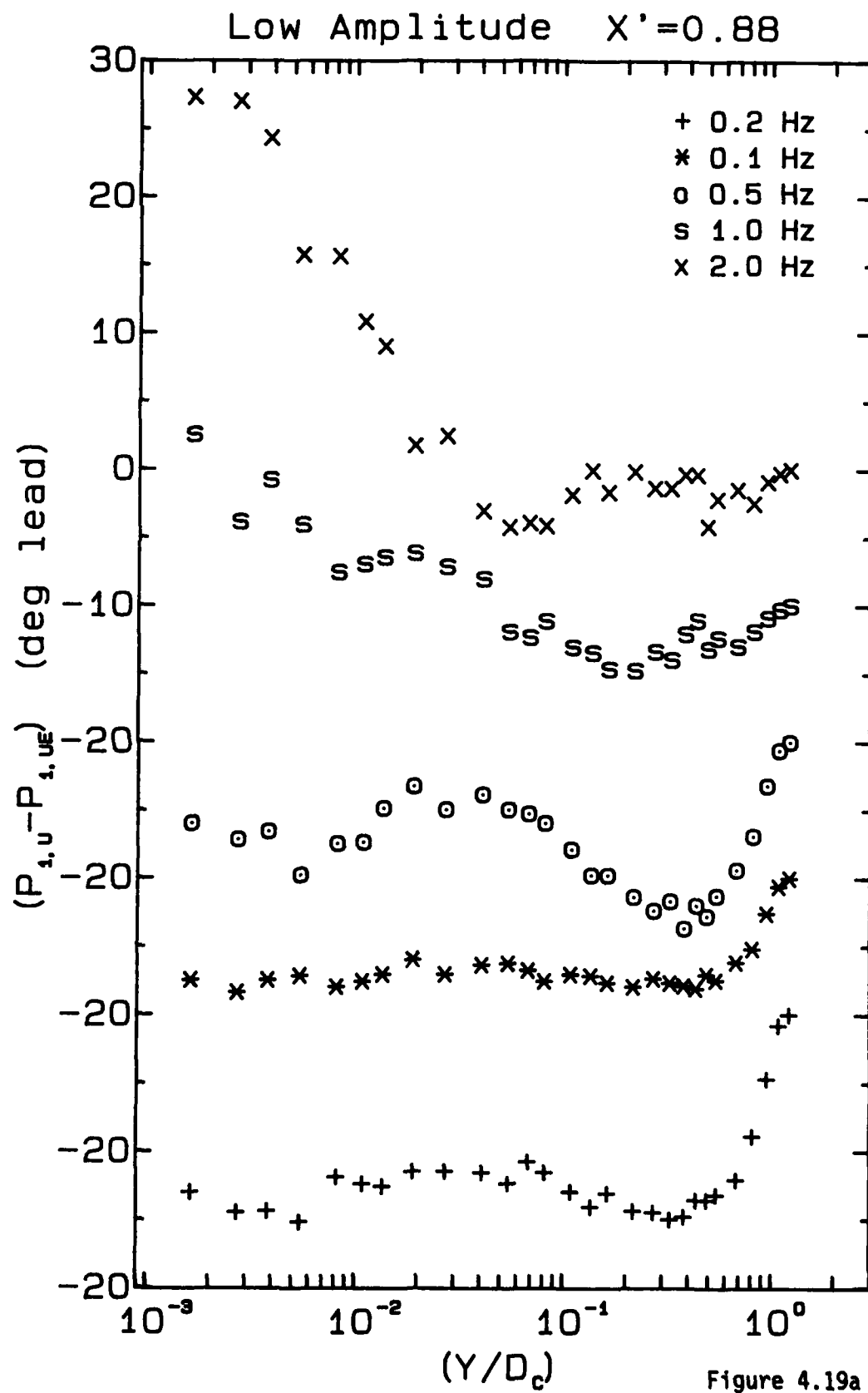


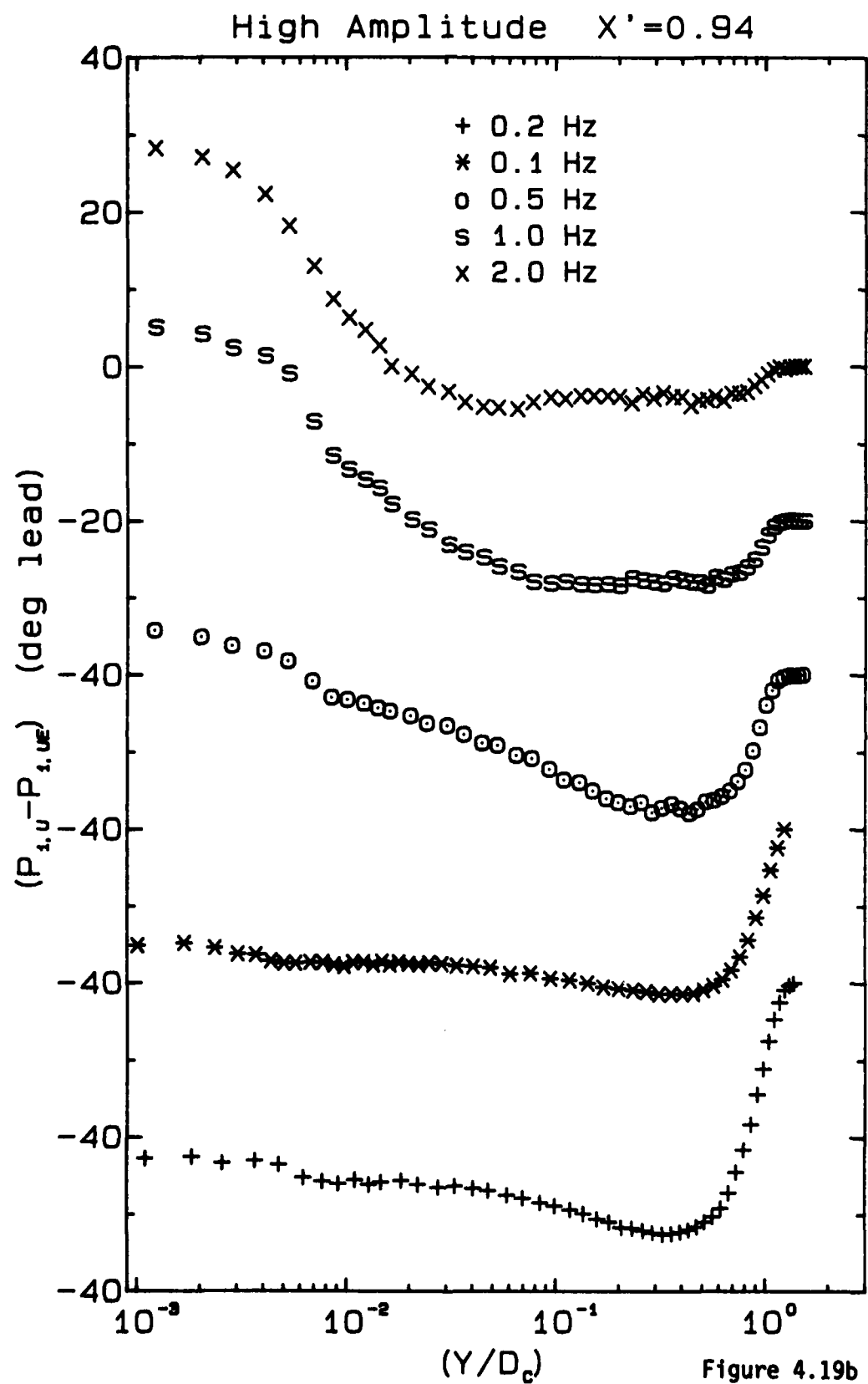




High Amplitude  $X'=0.94$







Low Amplitude  $X'=0.88$

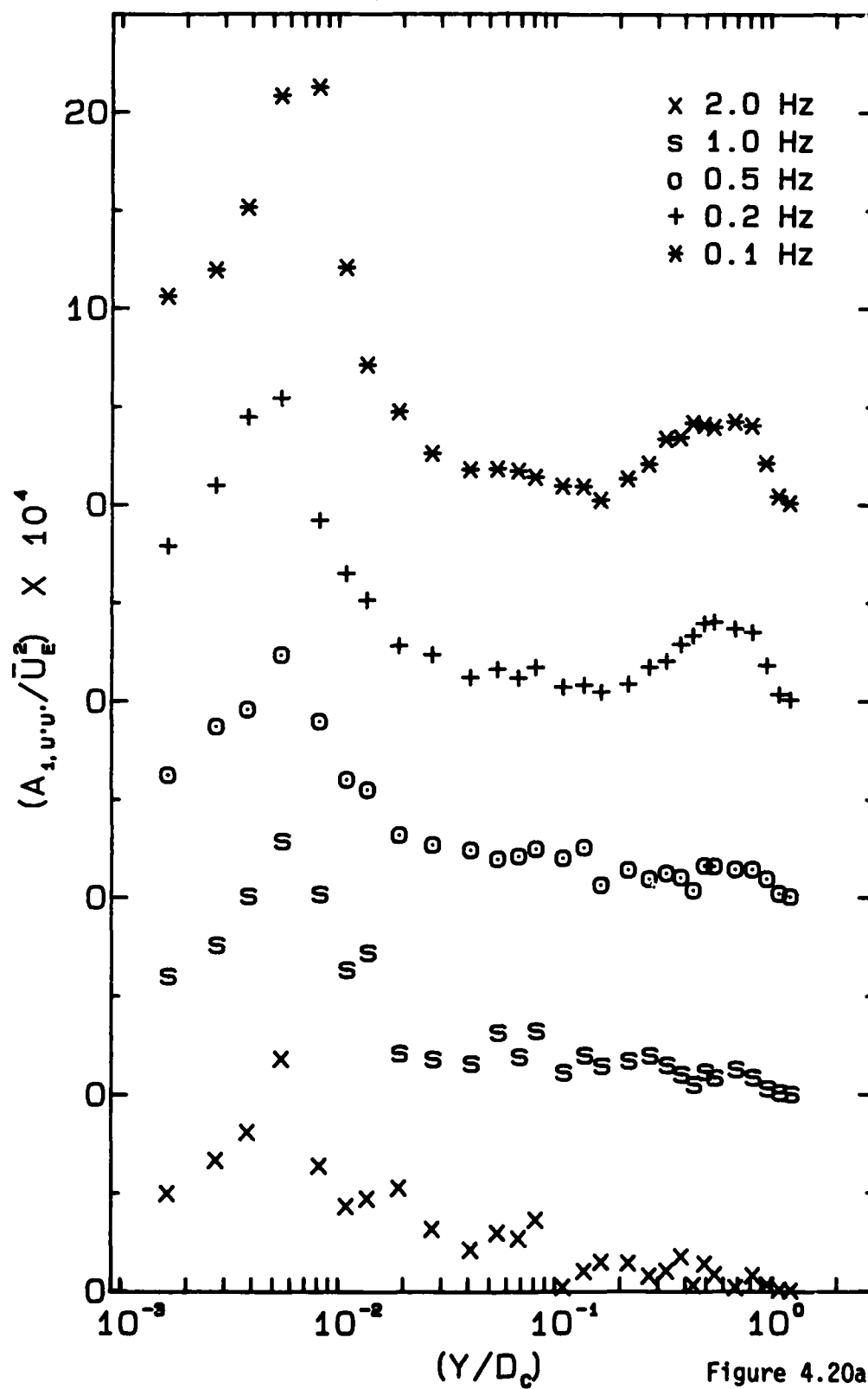


Figure 4.20a

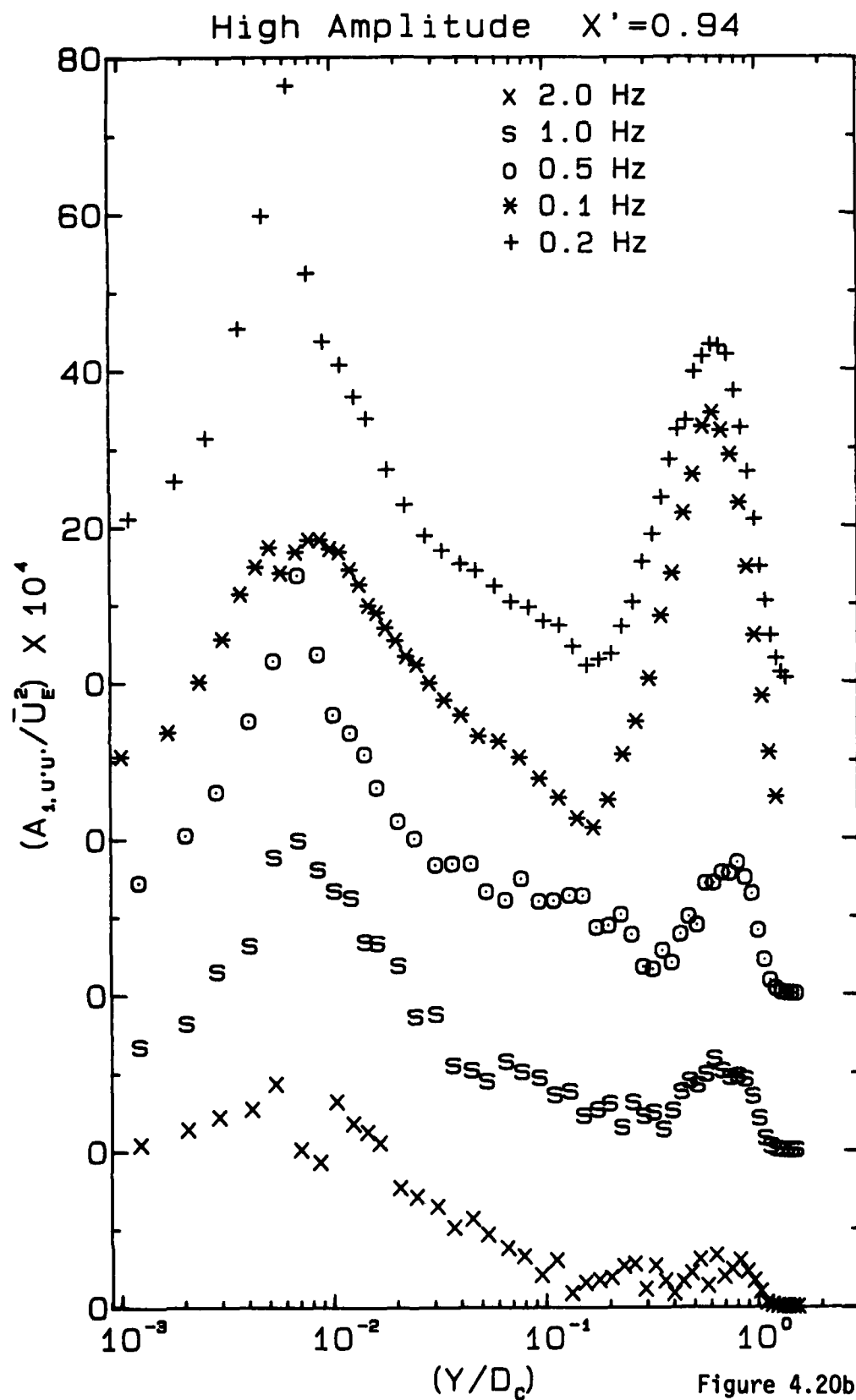


Figure 4.20b

Low Amplitude  $X'=0.88$

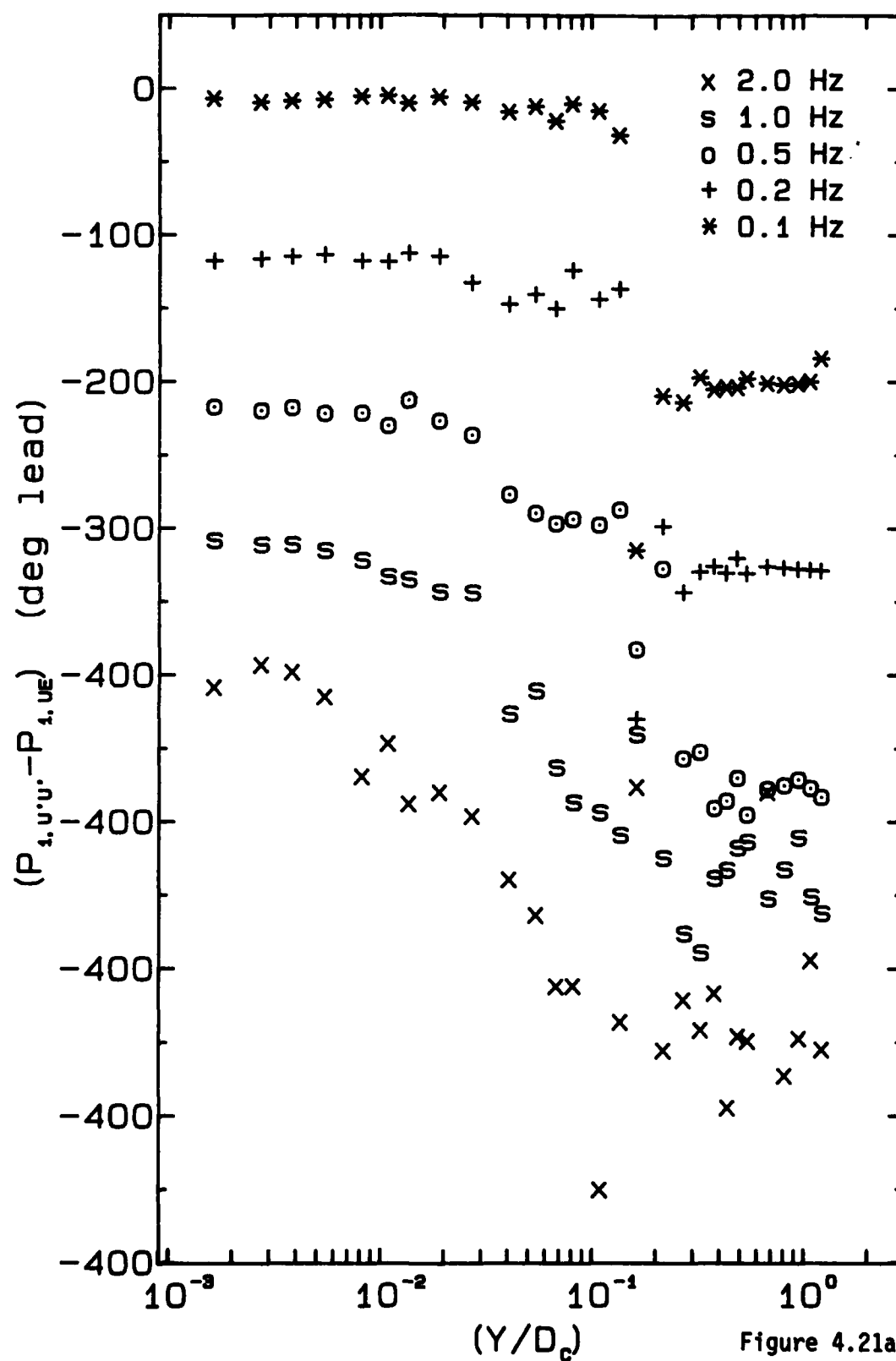


Figure 4.21a

High Amplitude  $X'=0.94$

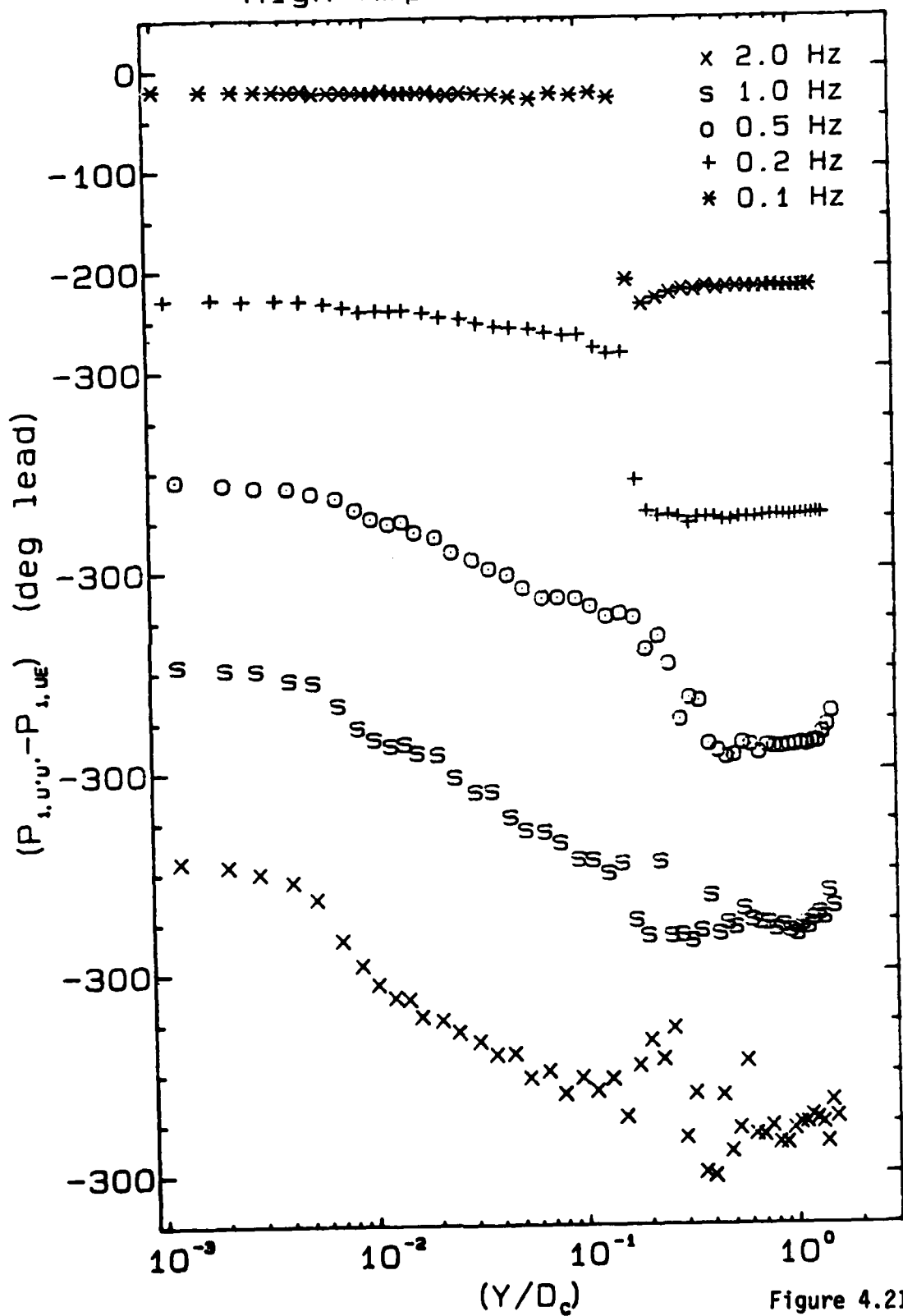


Figure 4.21b



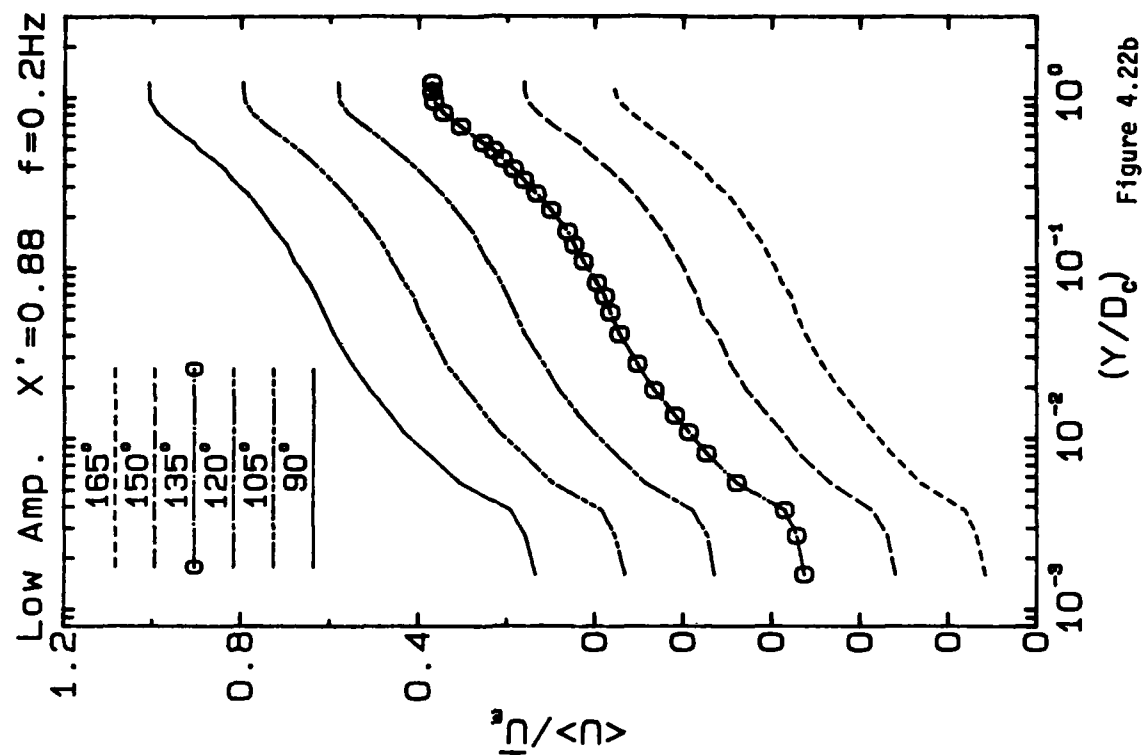


Figure 4.22b

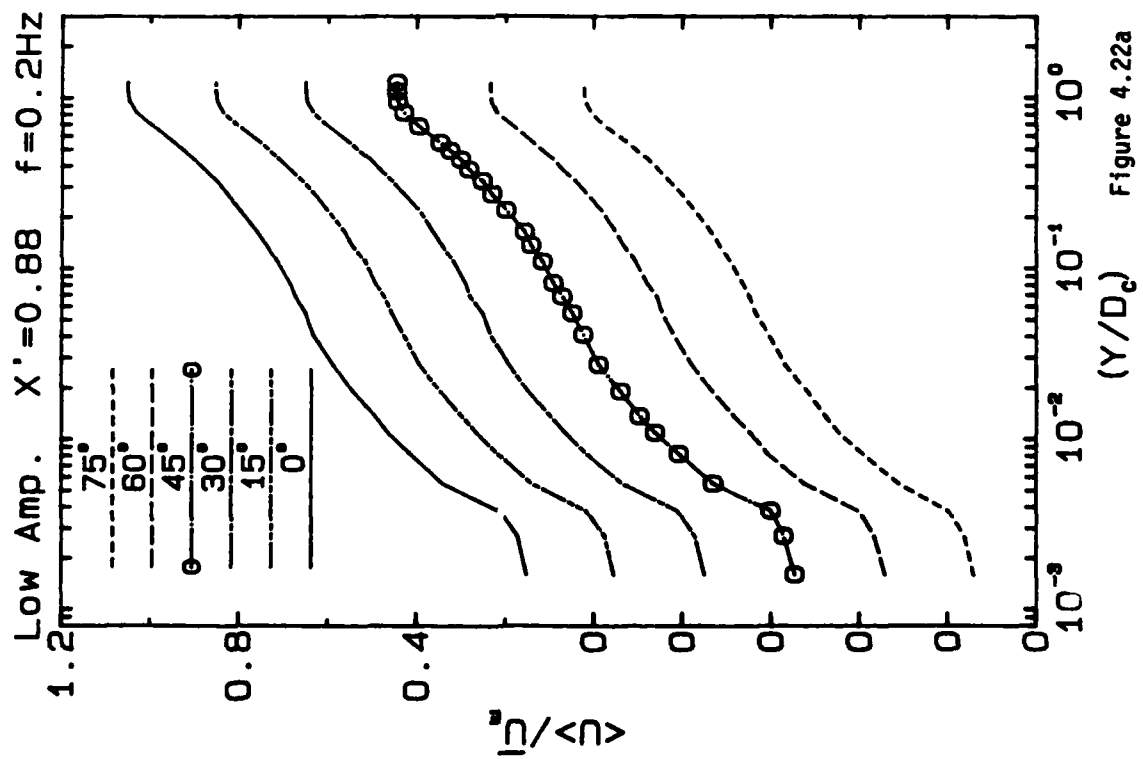


Figure 4.22a

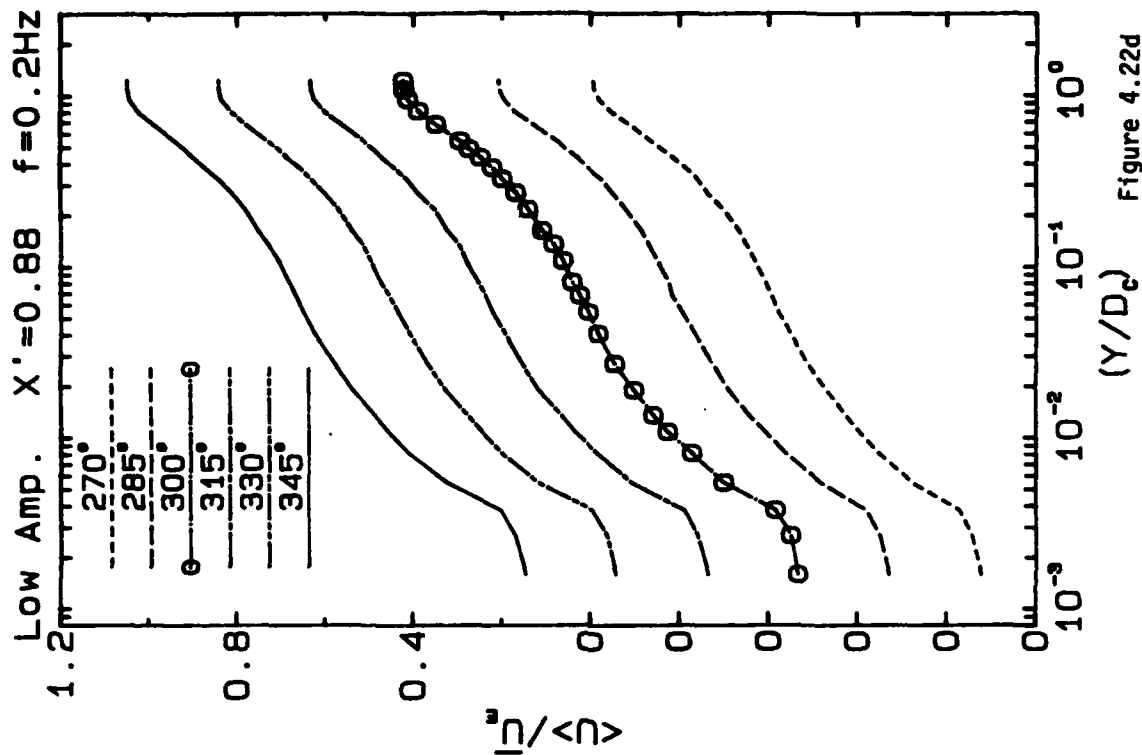


Figure 4.22d

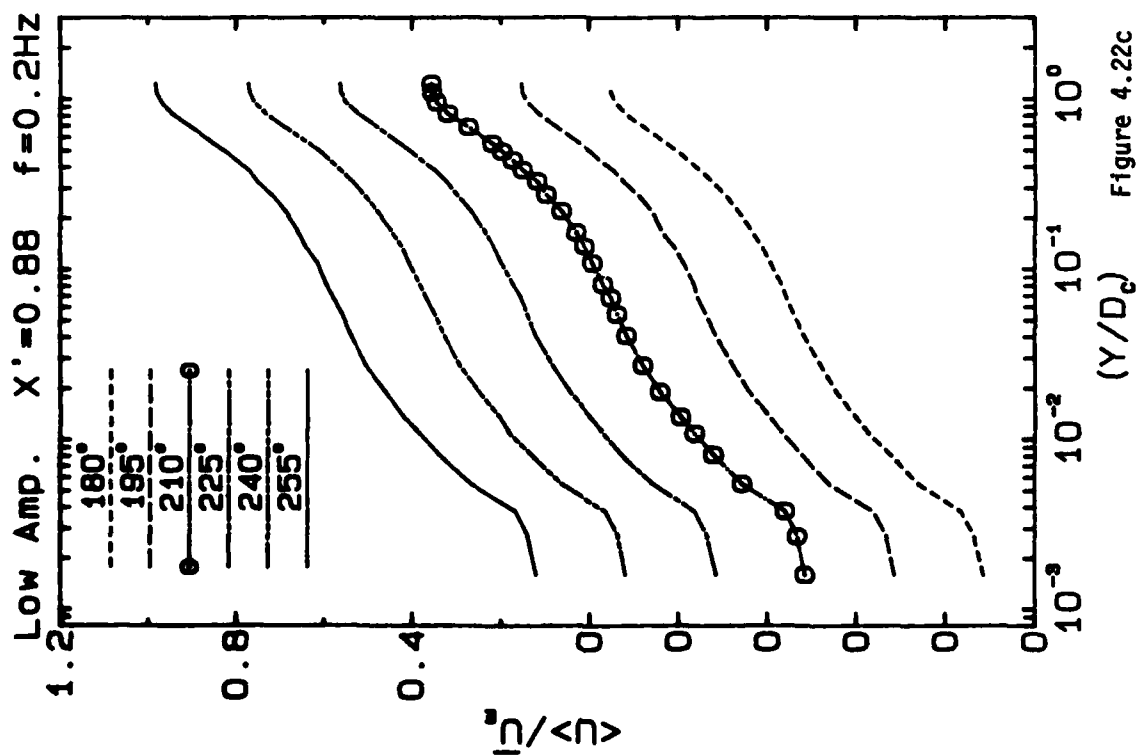


Figure 4.22c

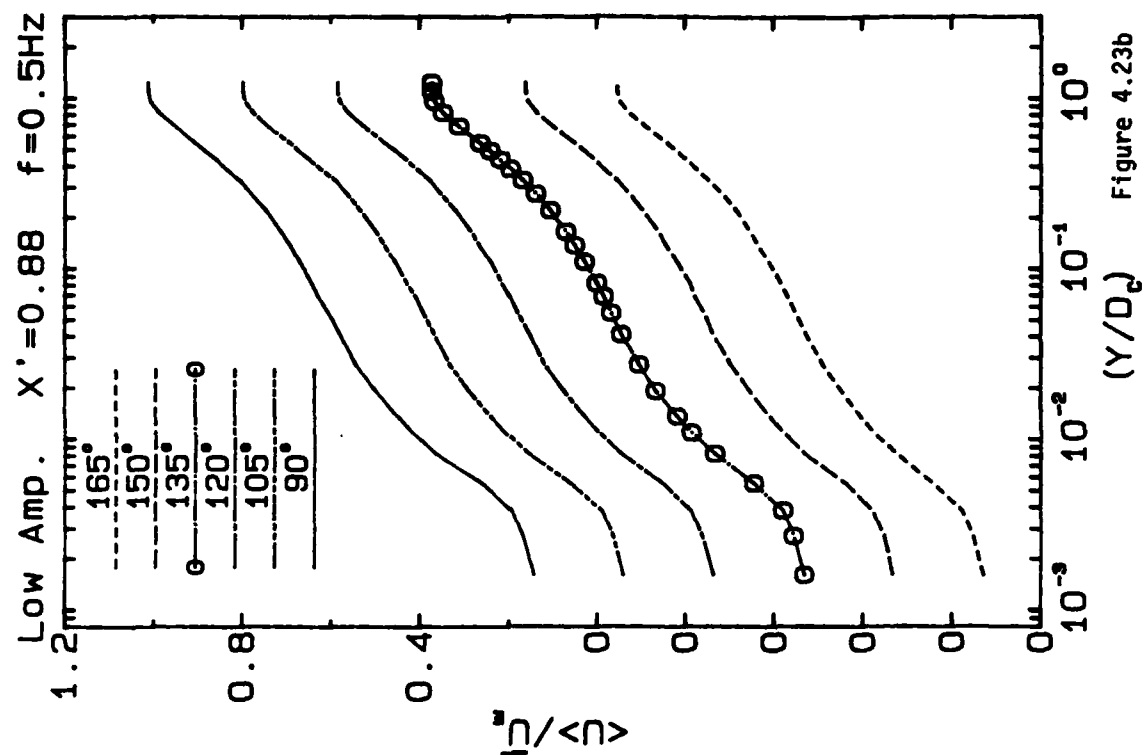


Figure 4.23b

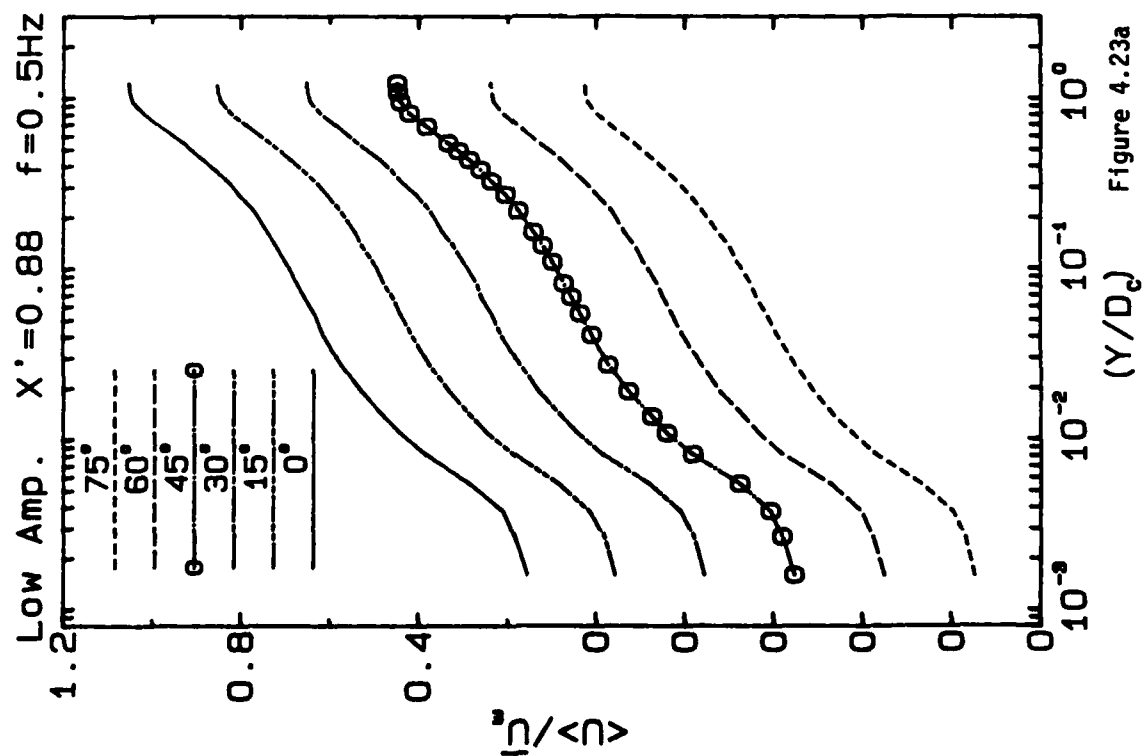


Figure 4.23a

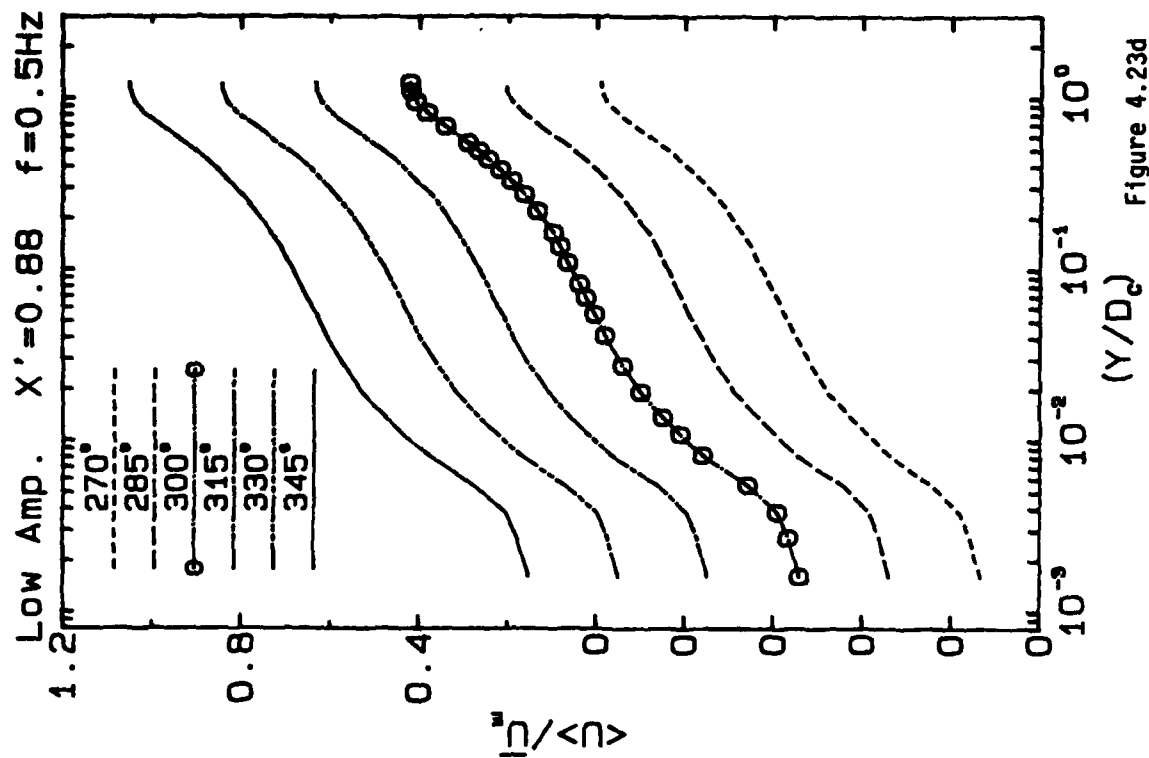


Figure 4.23d

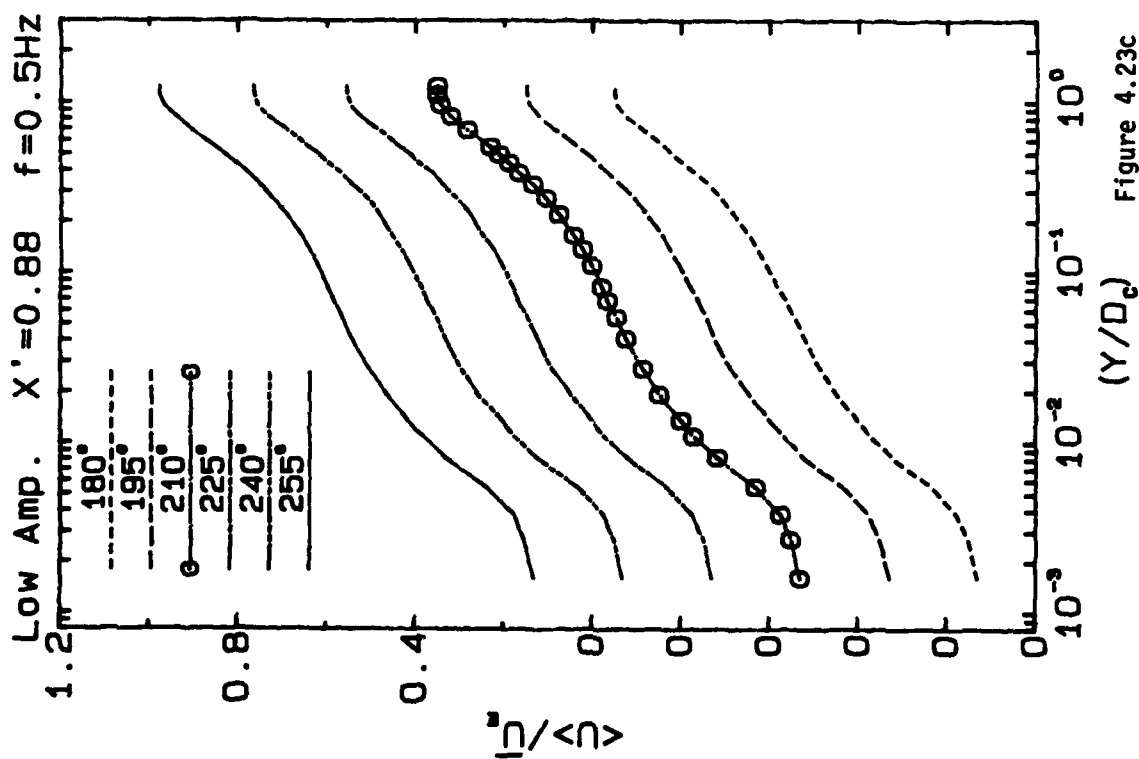


Figure 4.23c

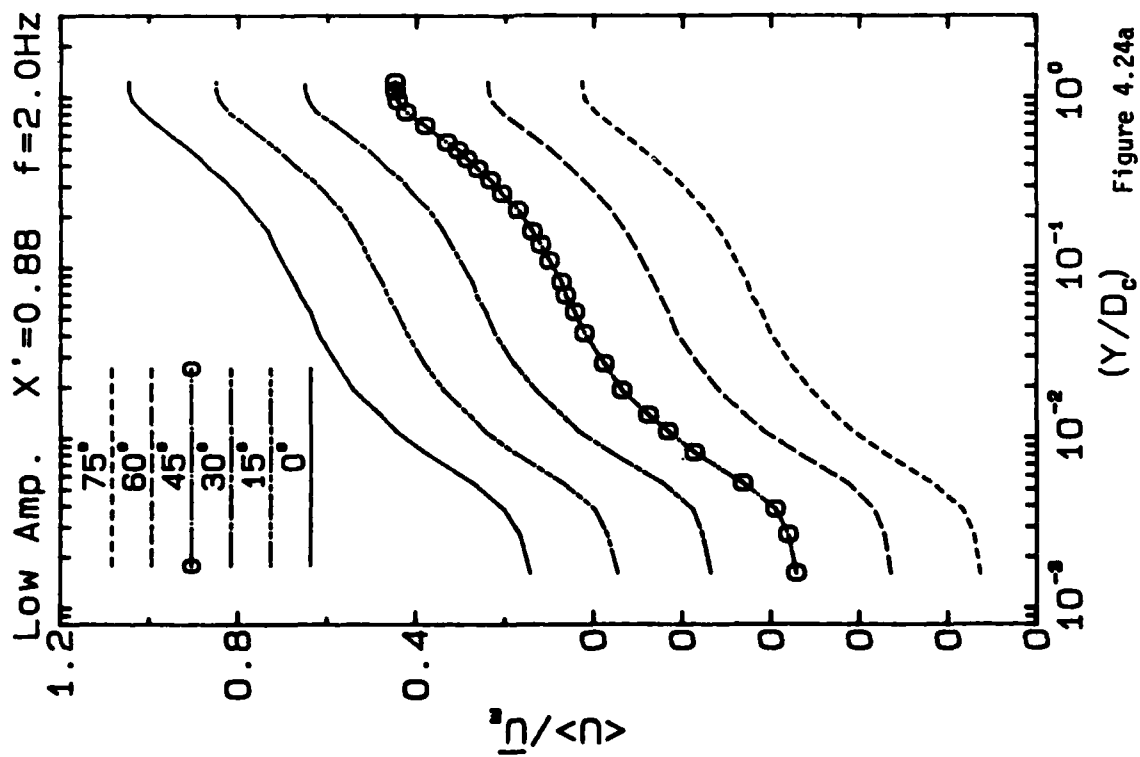


Figure 4.24a

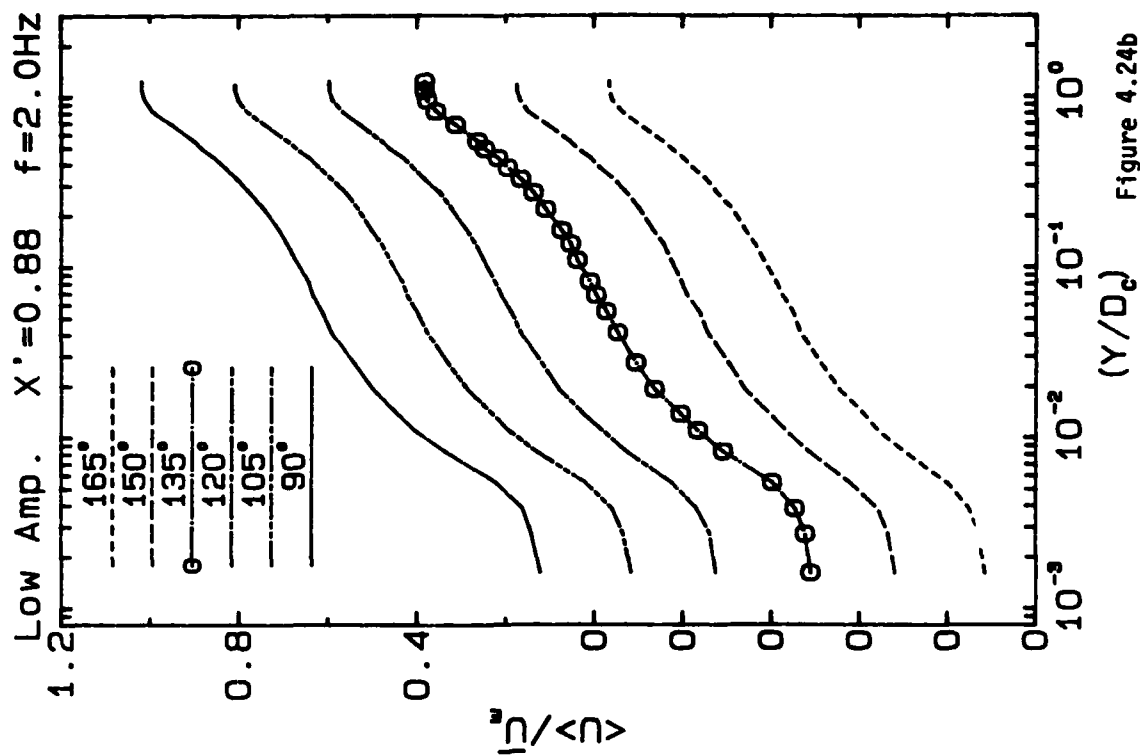


Figure 4.24b

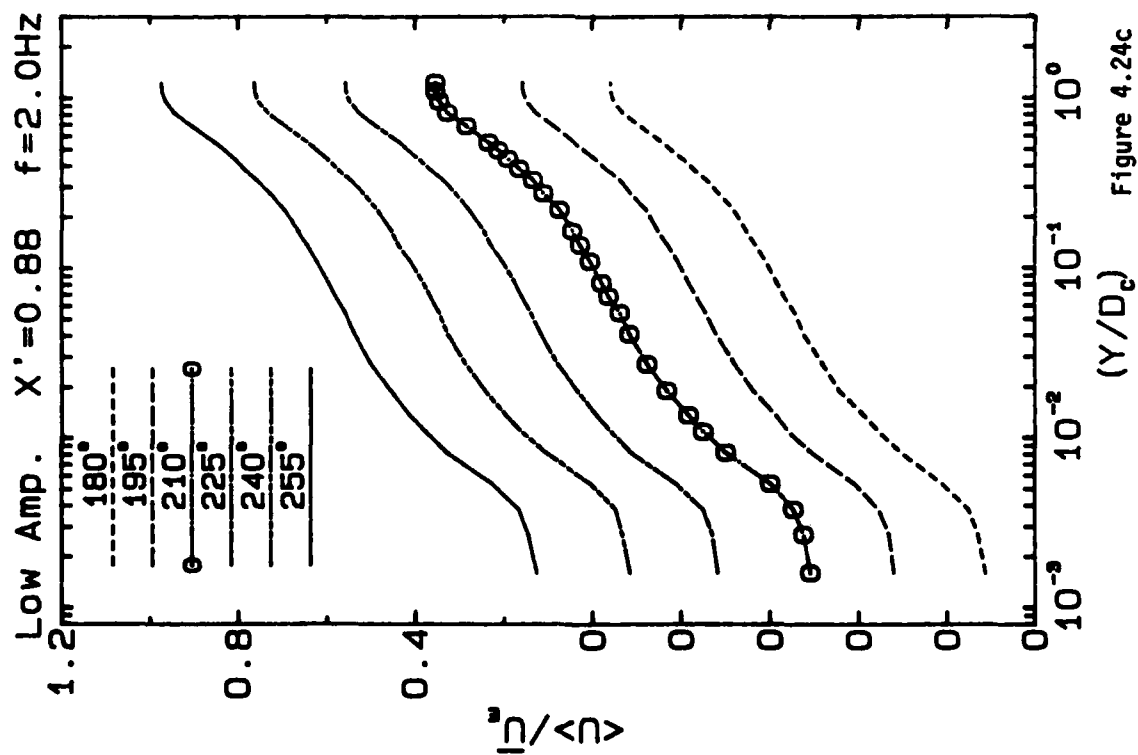


Figure 4.24c

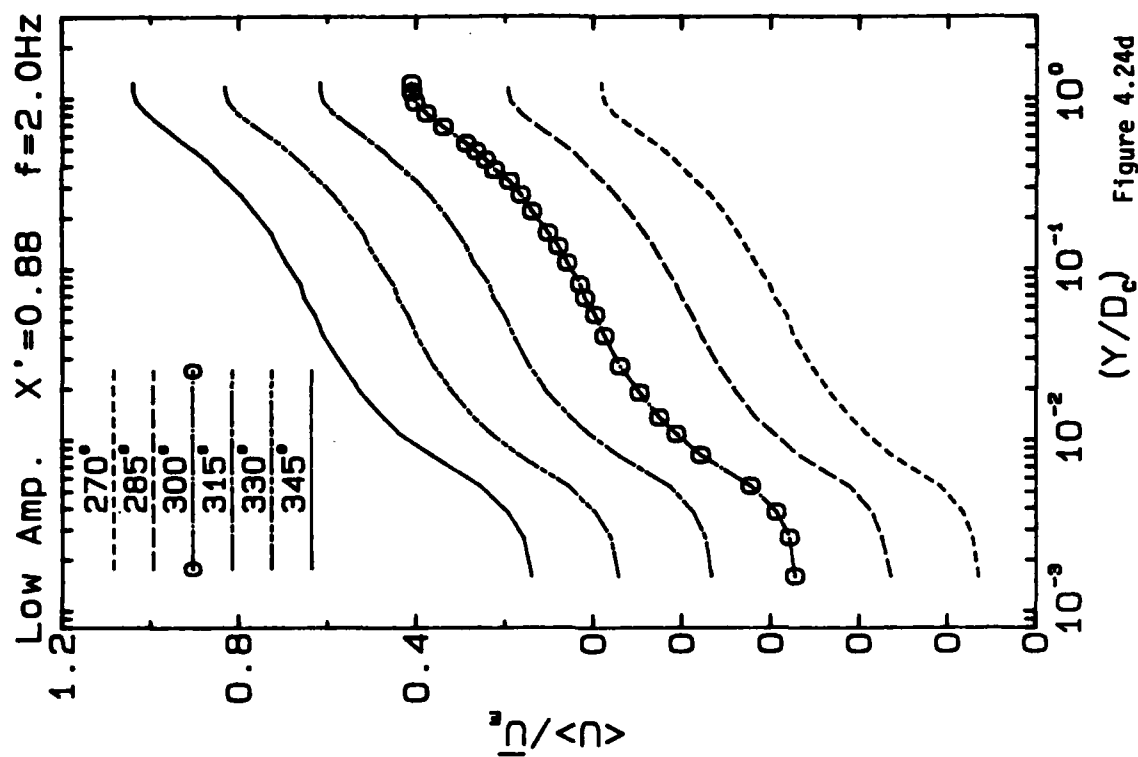


Figure 4.24d

High Amplitude  $X'=0.94$   $f=0.2\text{Hz}$   $f=0.2\text{Hz}$

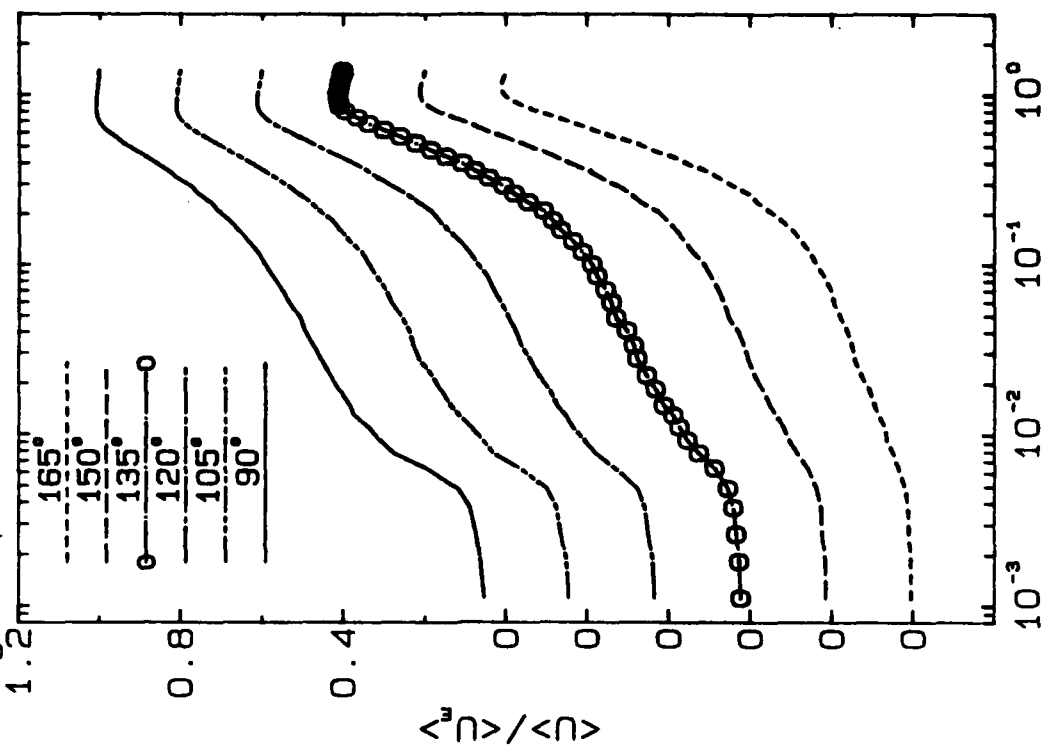


Figure 4.25a

High Amplitude  $X'=0.94$   $f=0.2\text{Hz}$   $f=0.2\text{Hz}$

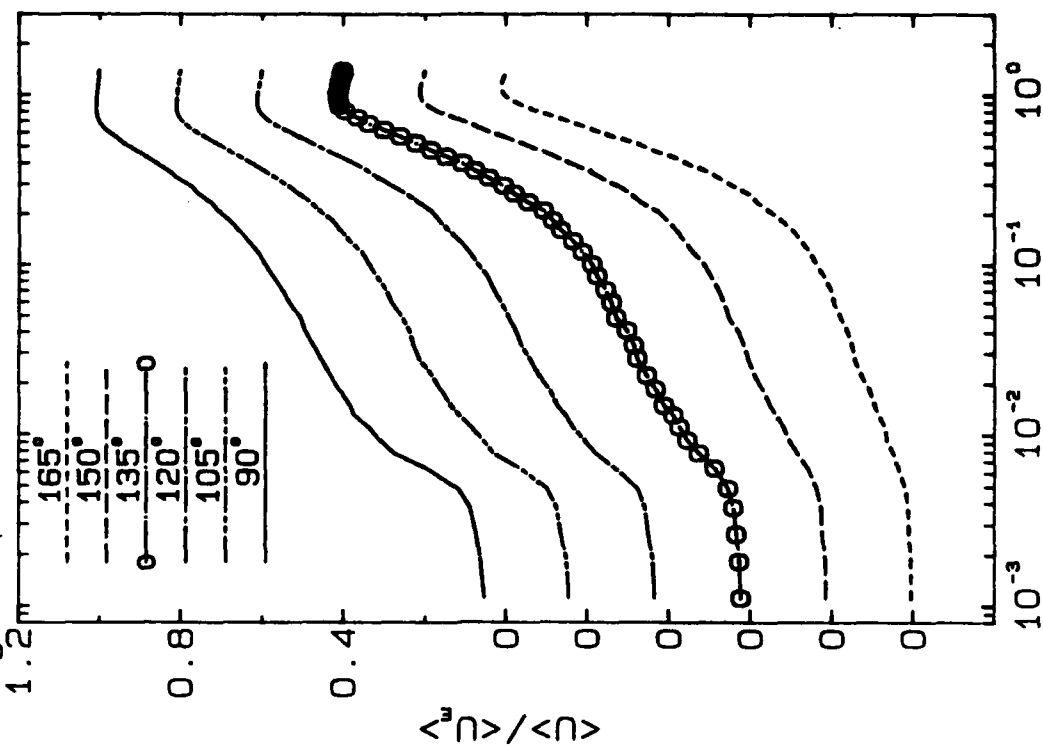
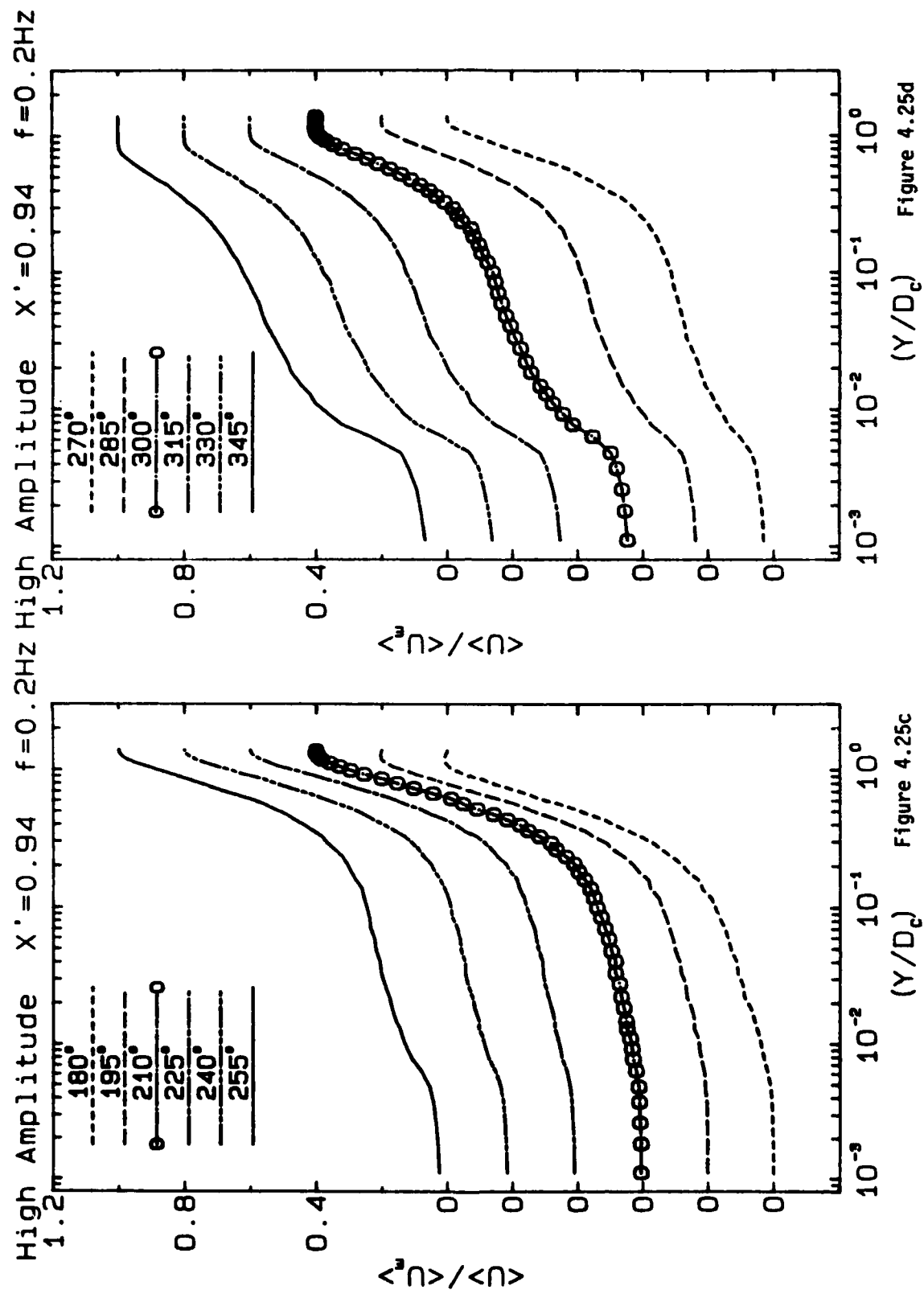
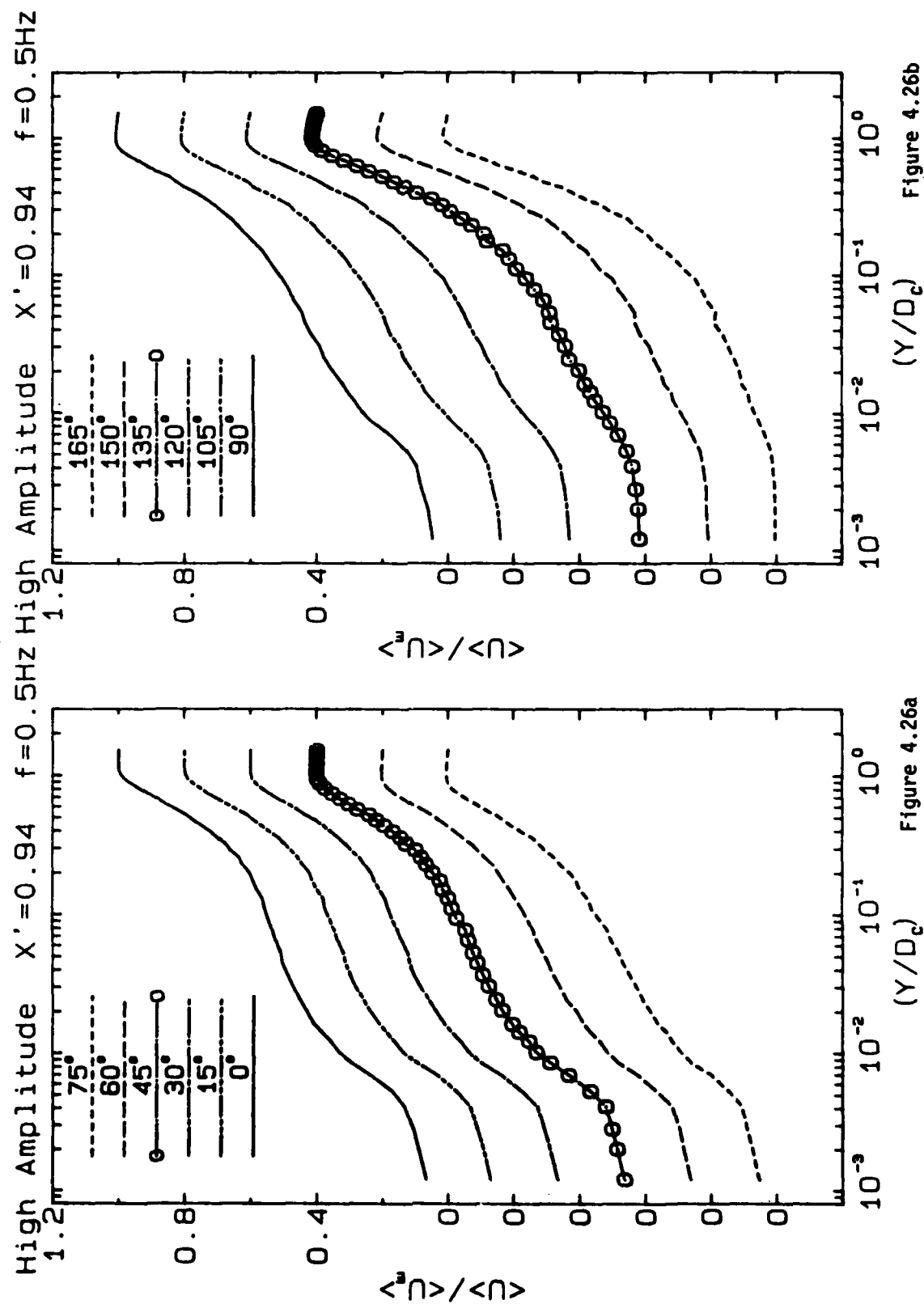


Figure 4.25b







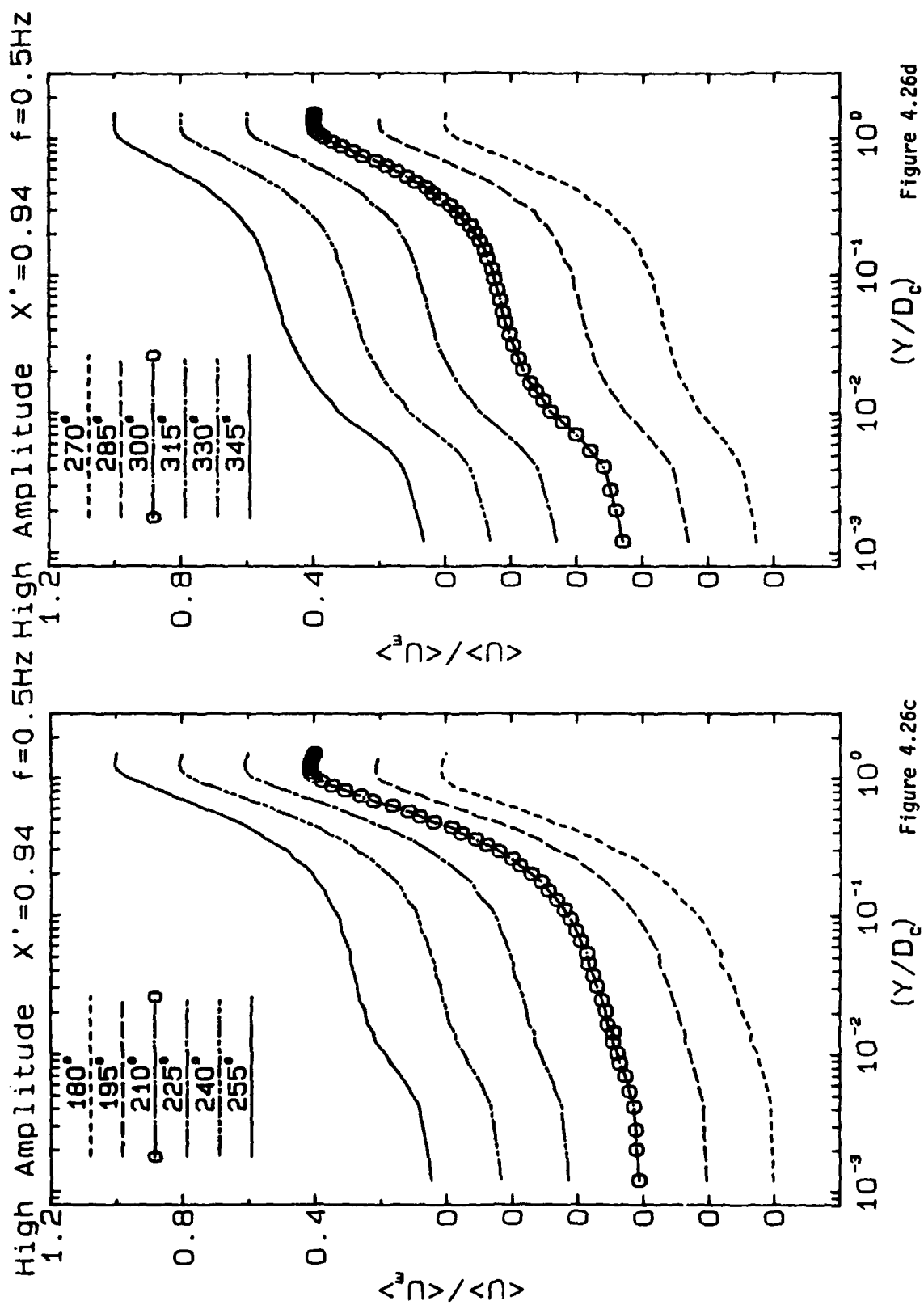


Figure 4.26d

Figure 4.26c

High Amplitude  $X'=0.94$   $f=2.0\text{Hz}$  High Amplitude  $X'=0.94$   $f=2.0\text{Hz}$

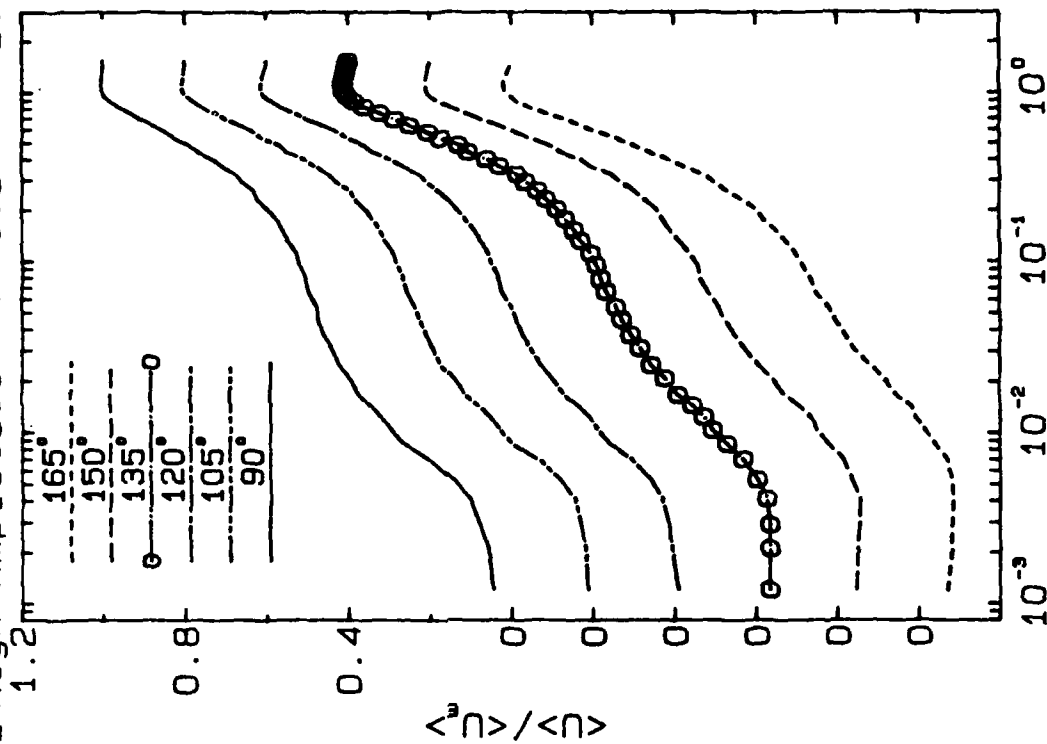


Figure 4.27a

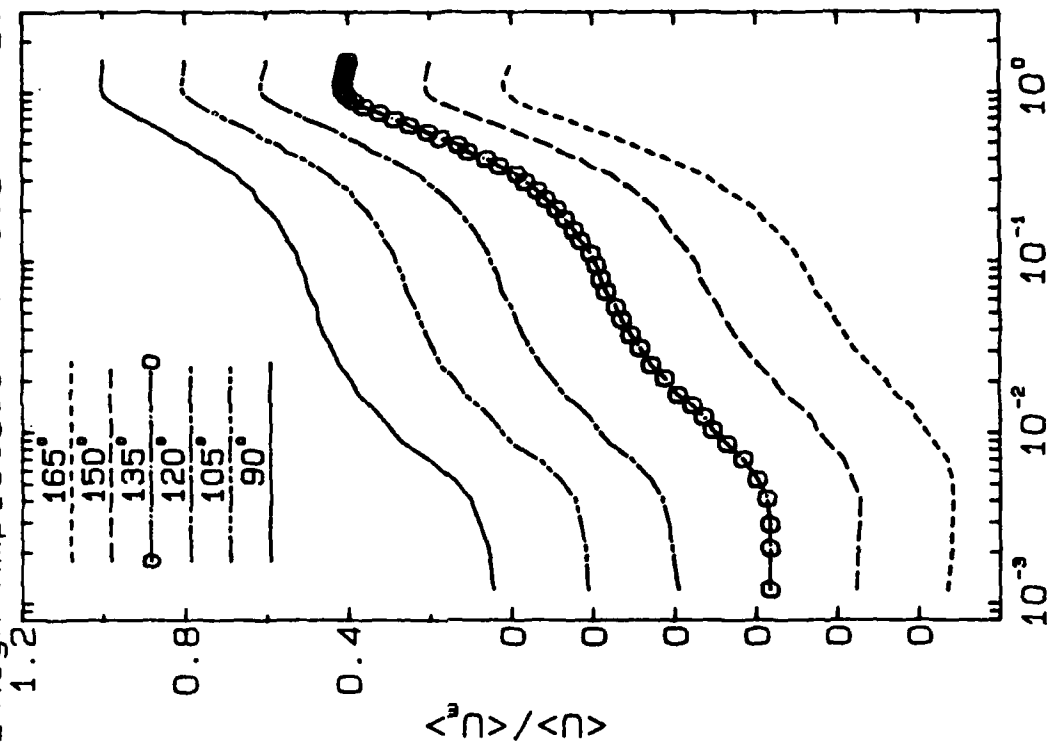
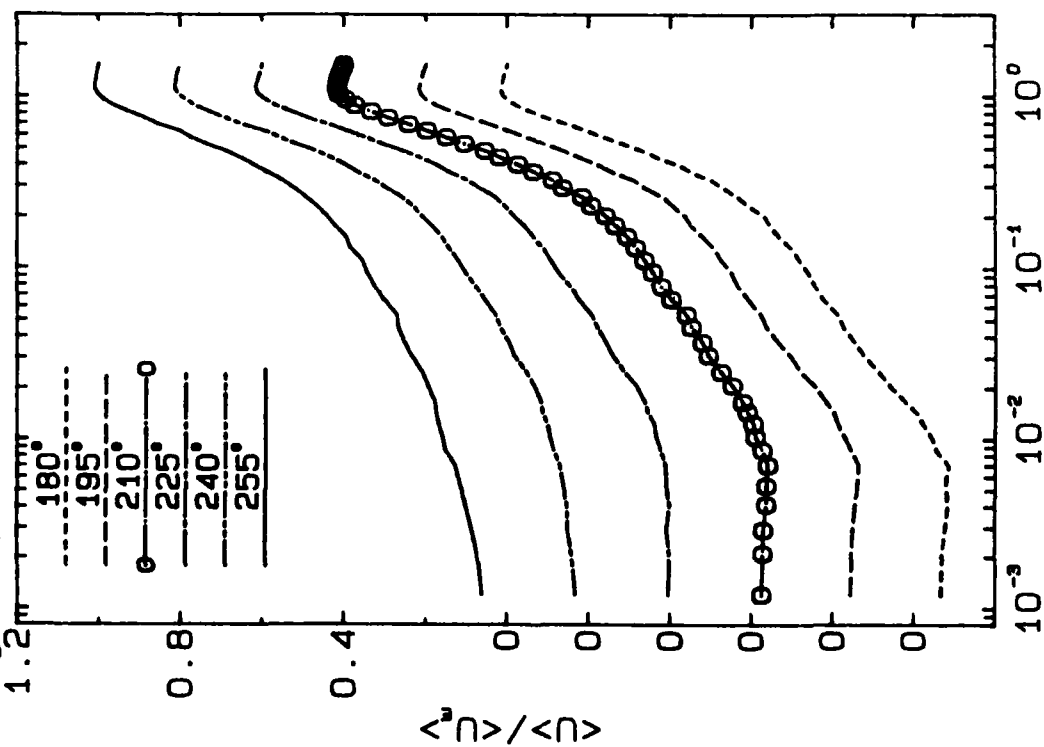


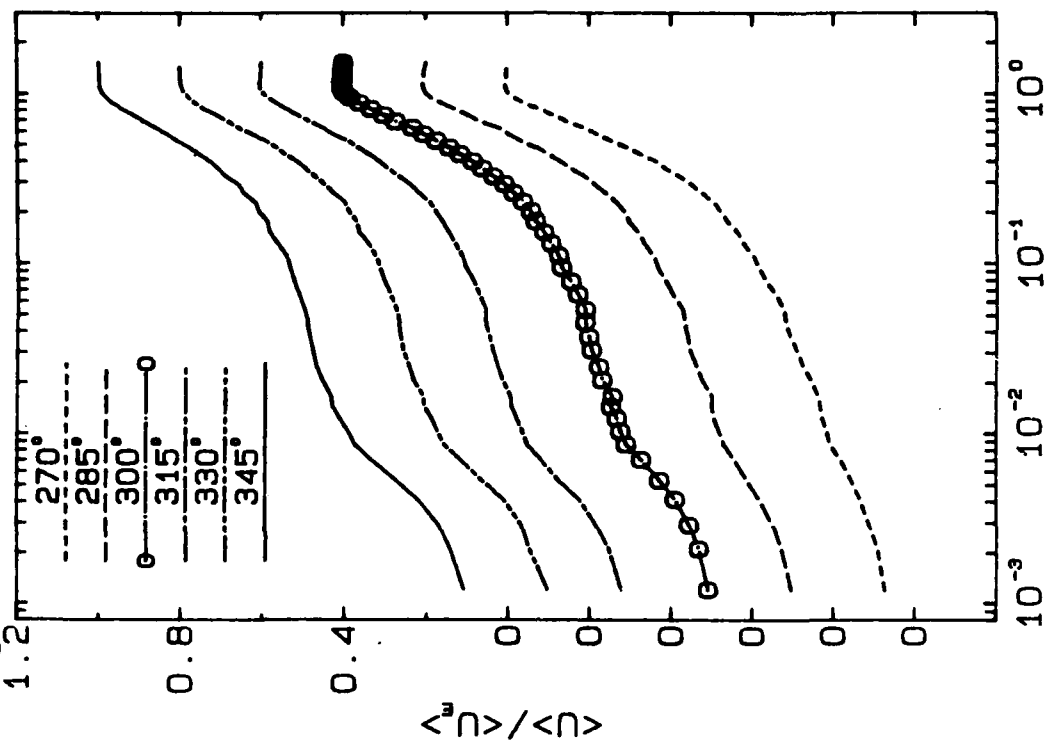
Figure 4.27b

High Amplitude  $X'=0.94$   $f=2.0\text{Hz}$



(Y/D<sub>0</sub>) Figure 4.27c

High Amplitude  $X'=0.94$   $f=2.0\text{Hz}$



(Y/D<sub>0</sub>) Figure 4.27d

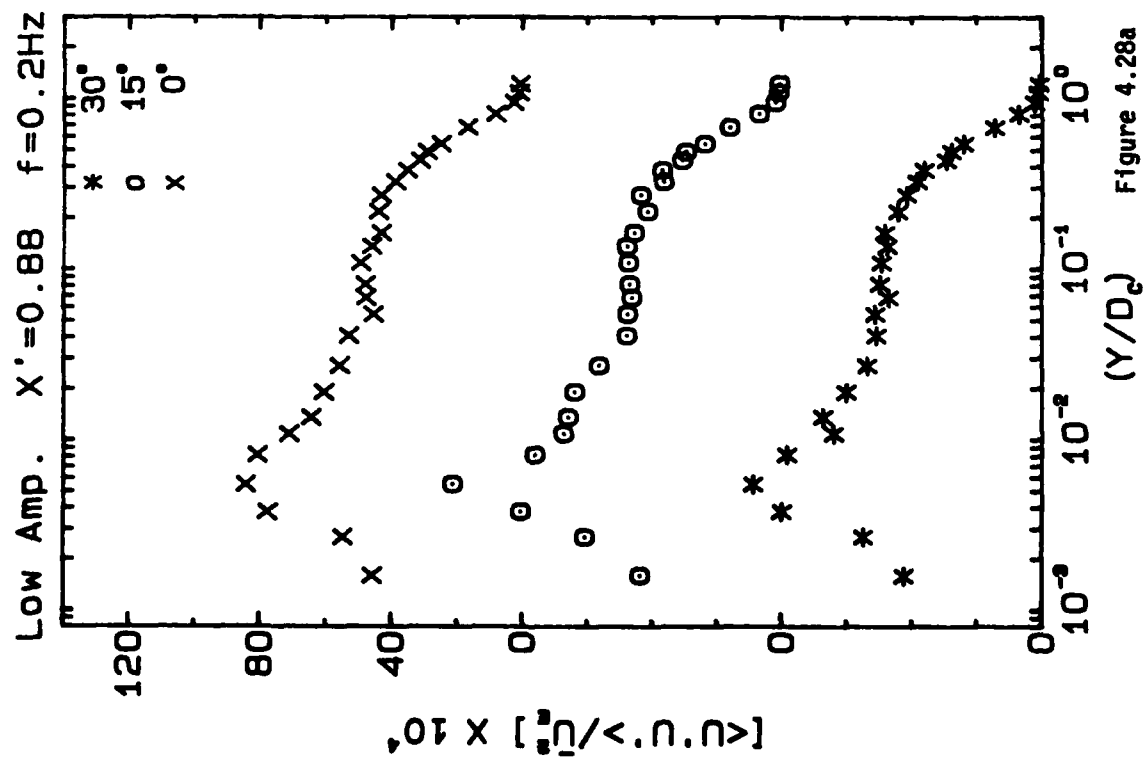


Figure 4.28a

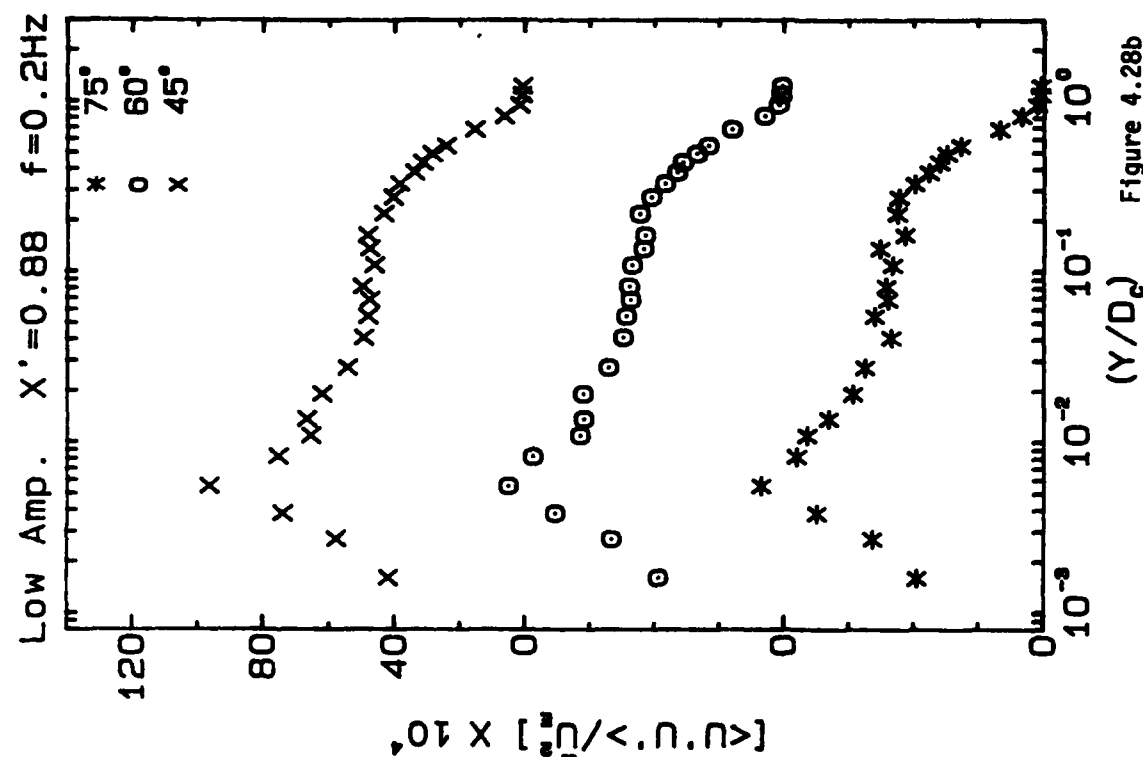


Figure 4.28b

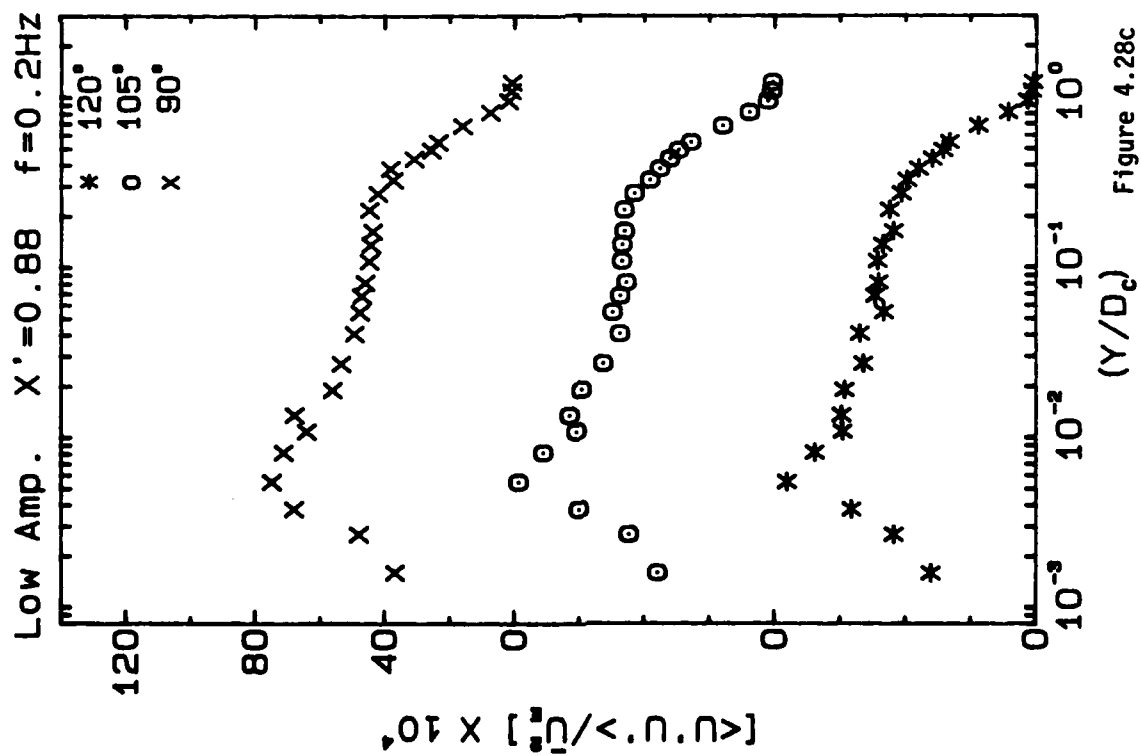


Figure 4.28c

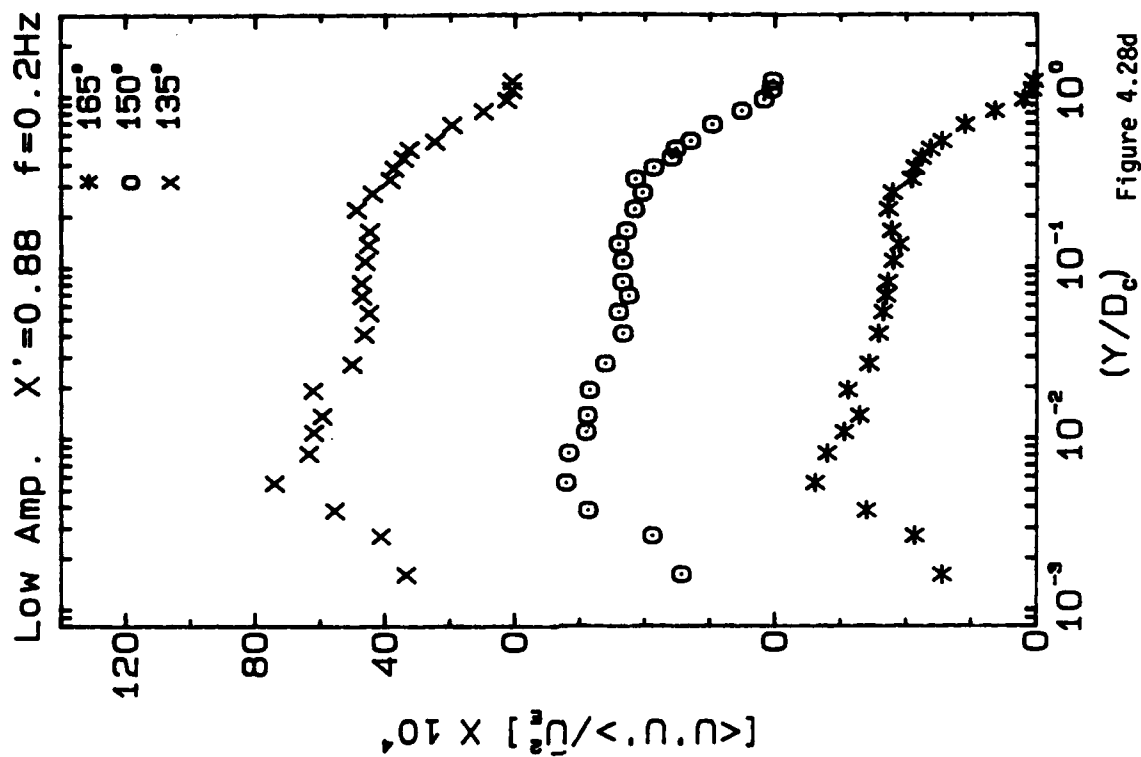


Figure 4.28d

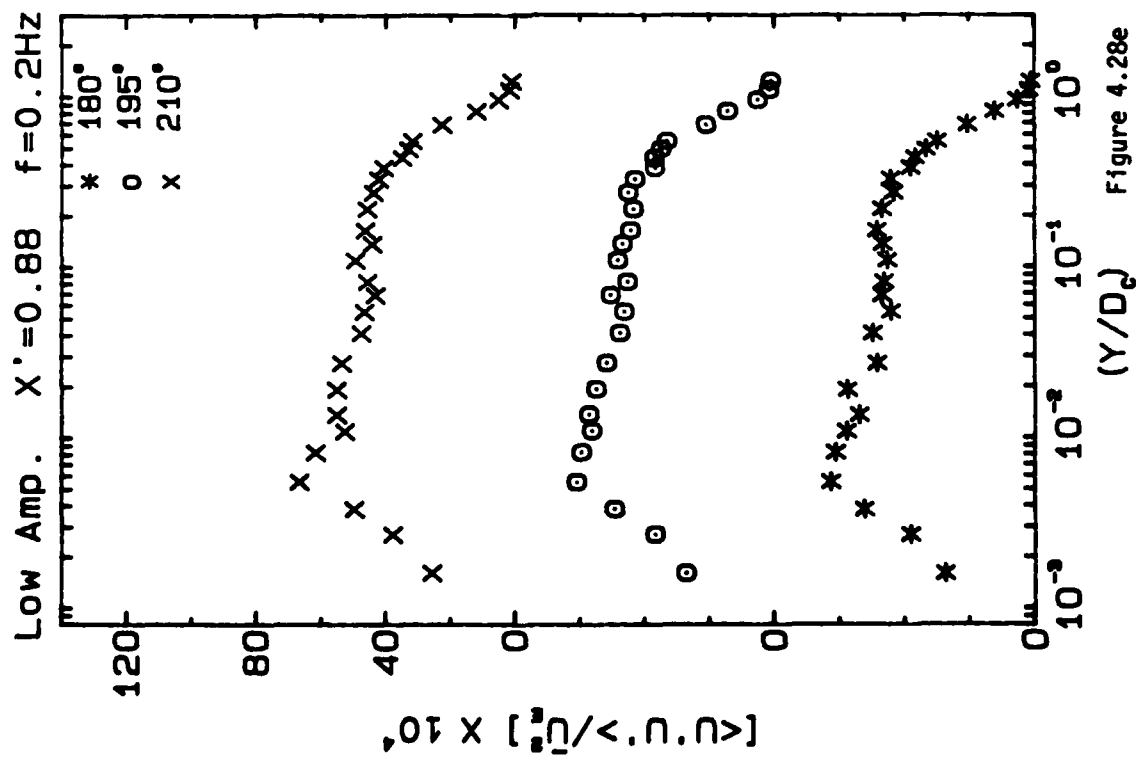


Figure 4.28e

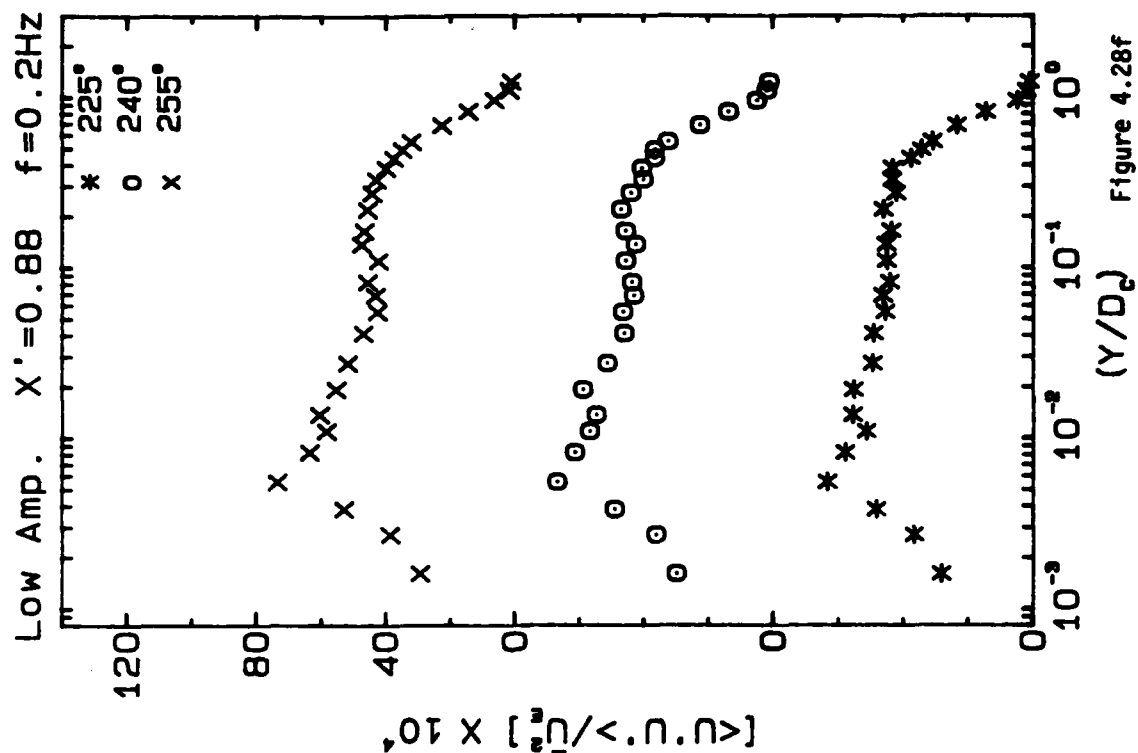


Figure 4.28f

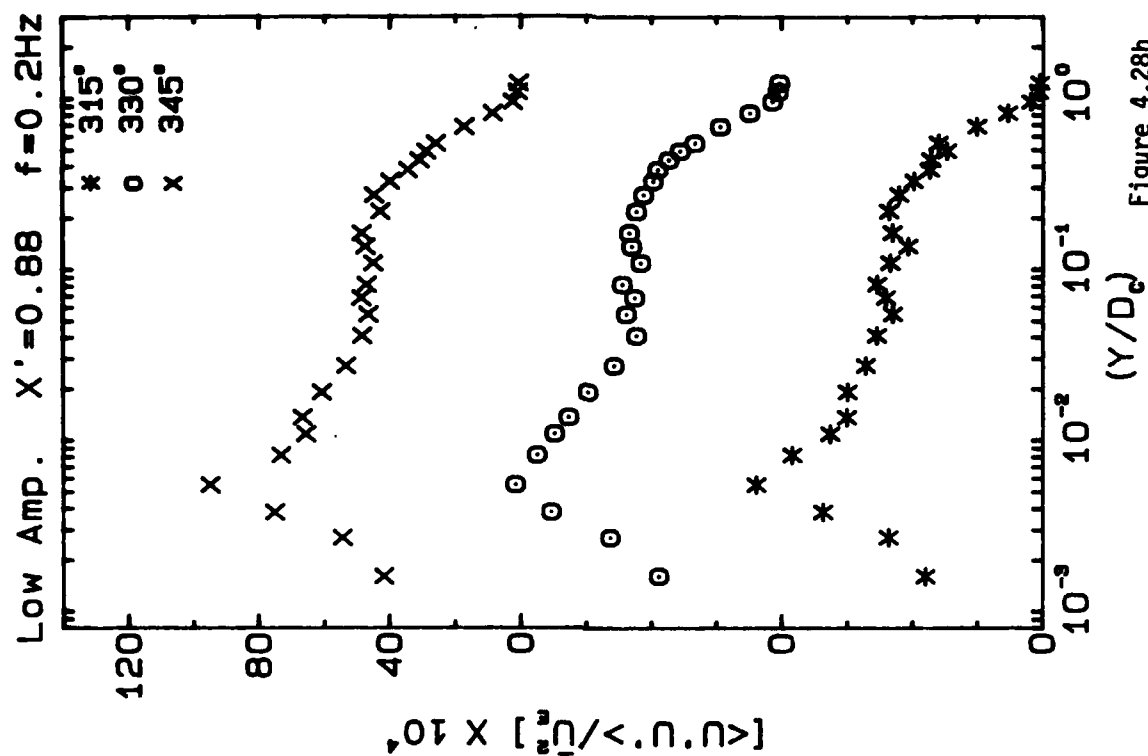


Figure 4.28h

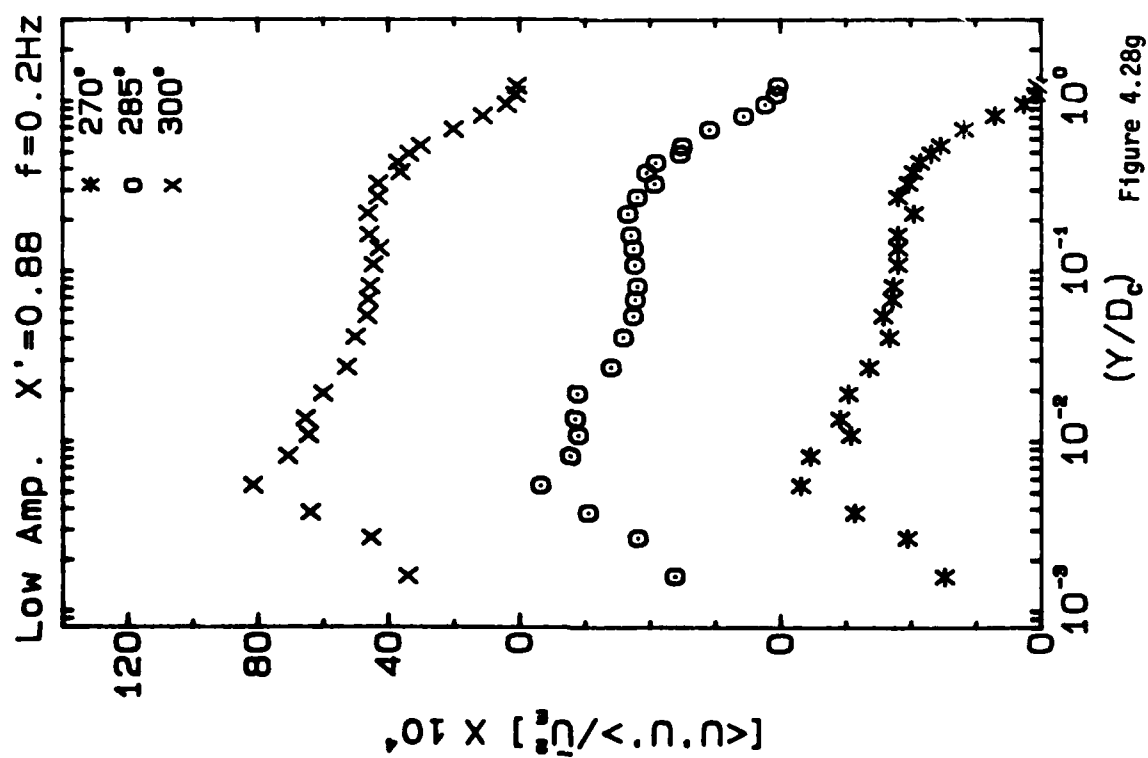


Figure 4.28g



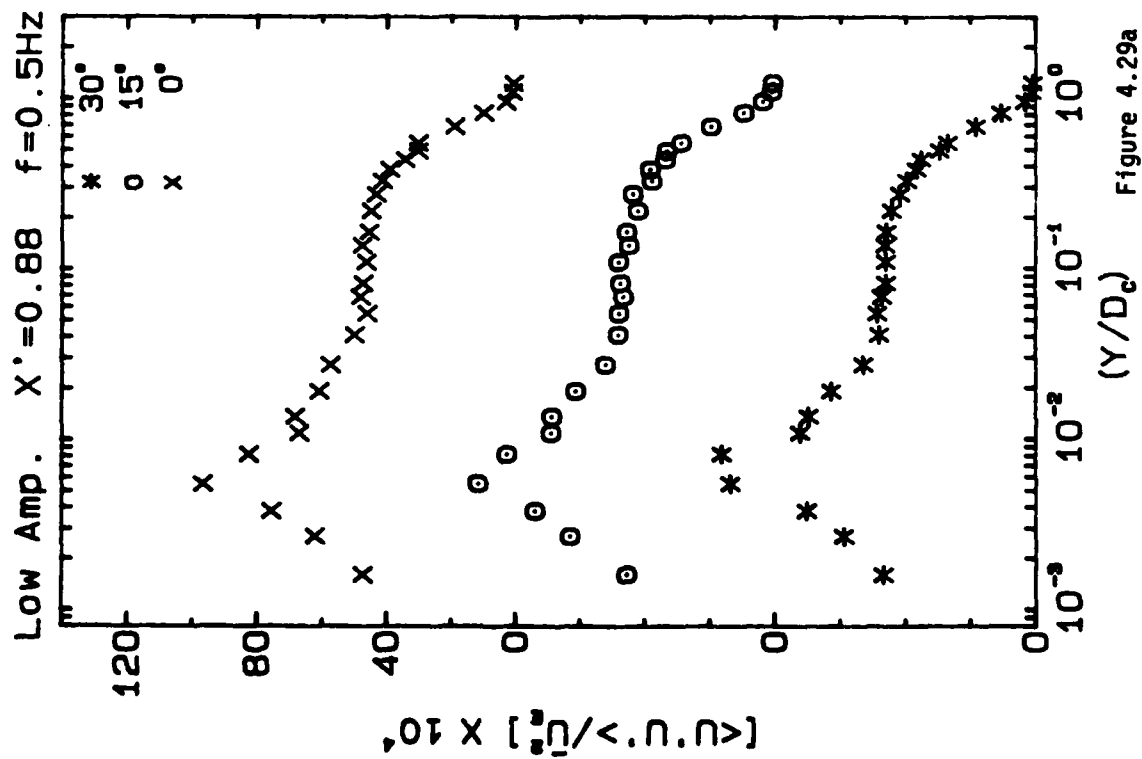


Figure 4.29a

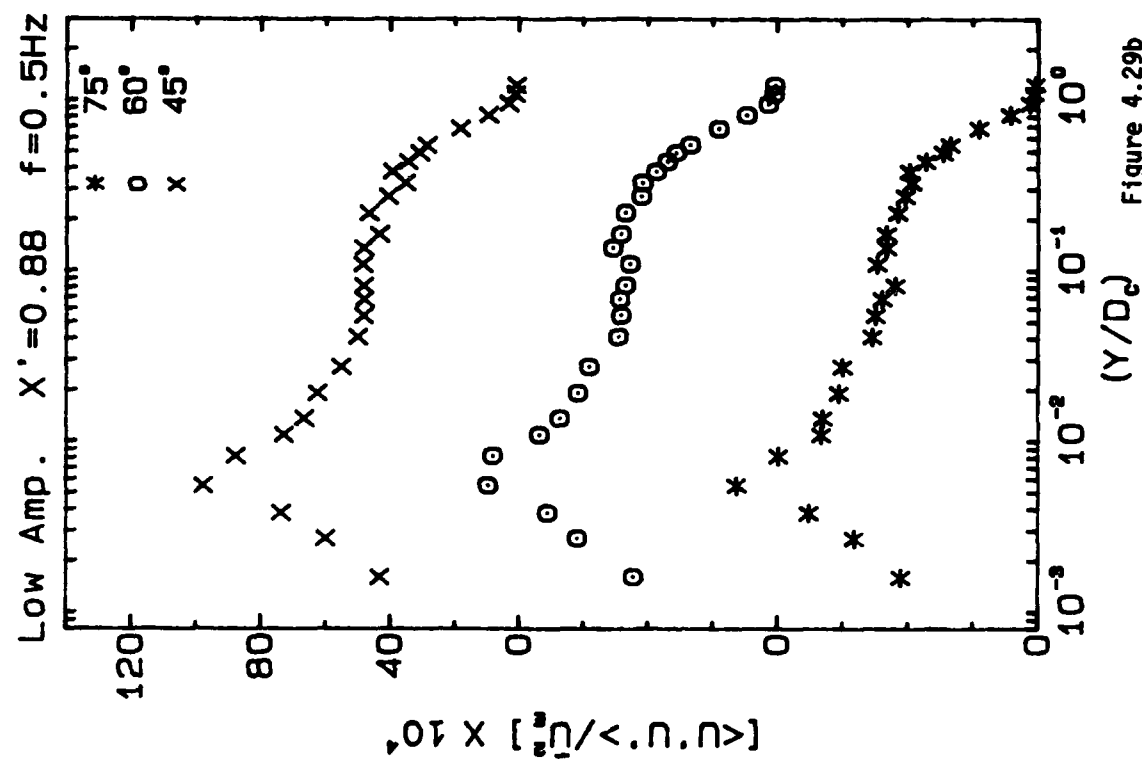


Figure 4.29b

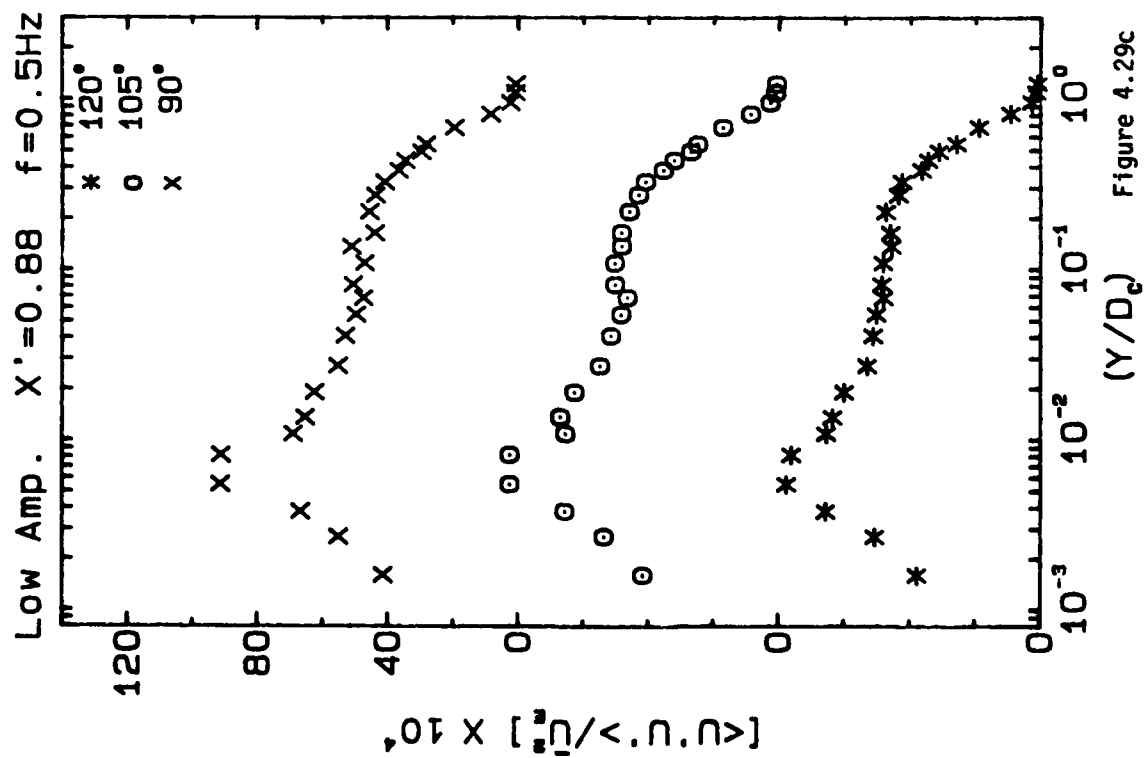


Figure 4.29c

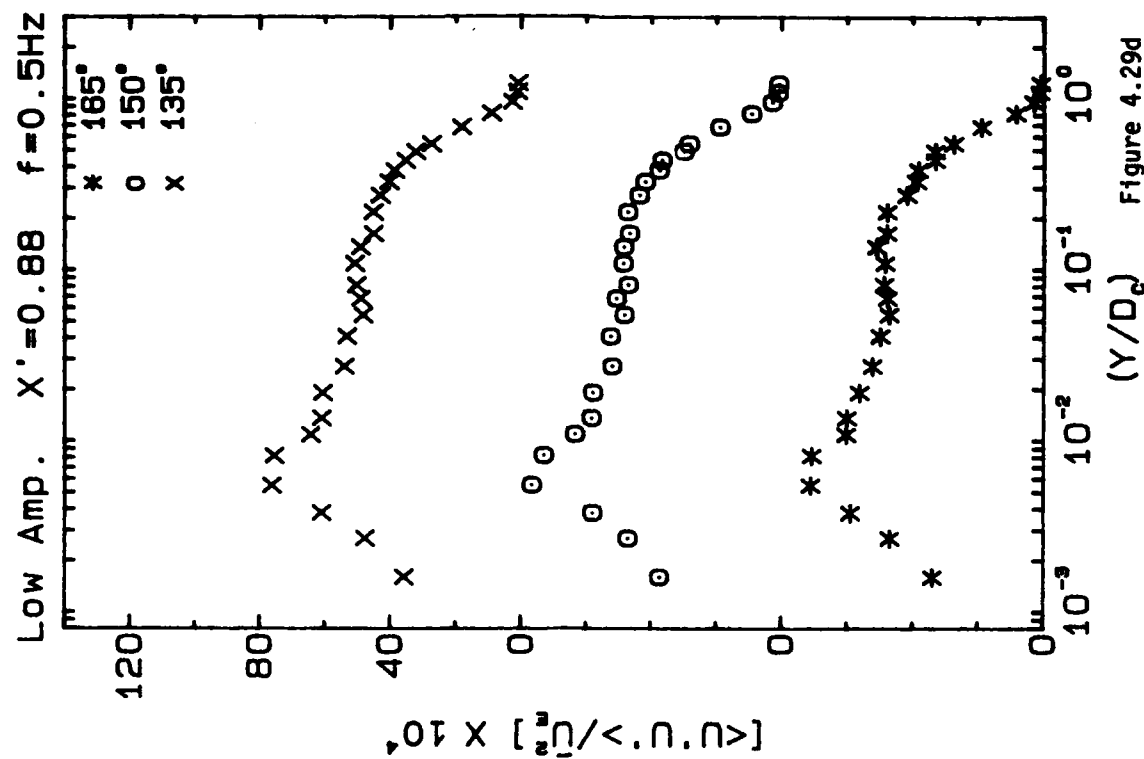


Figure 4.29d

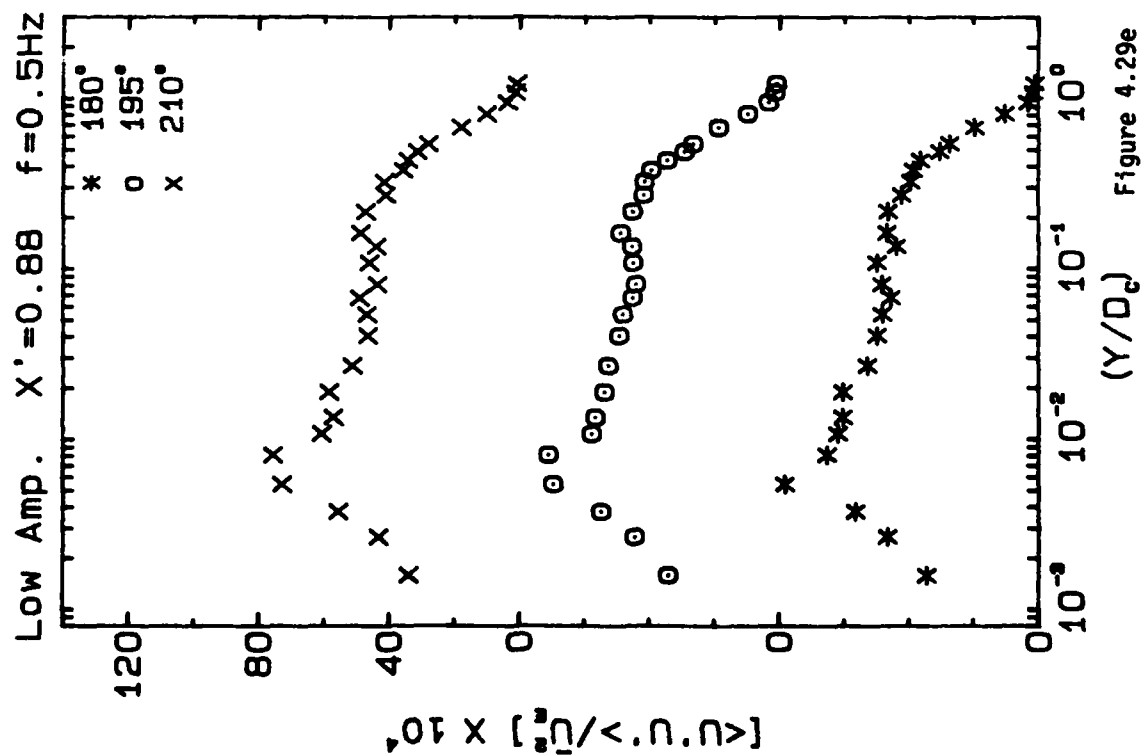


Figure 4.29e

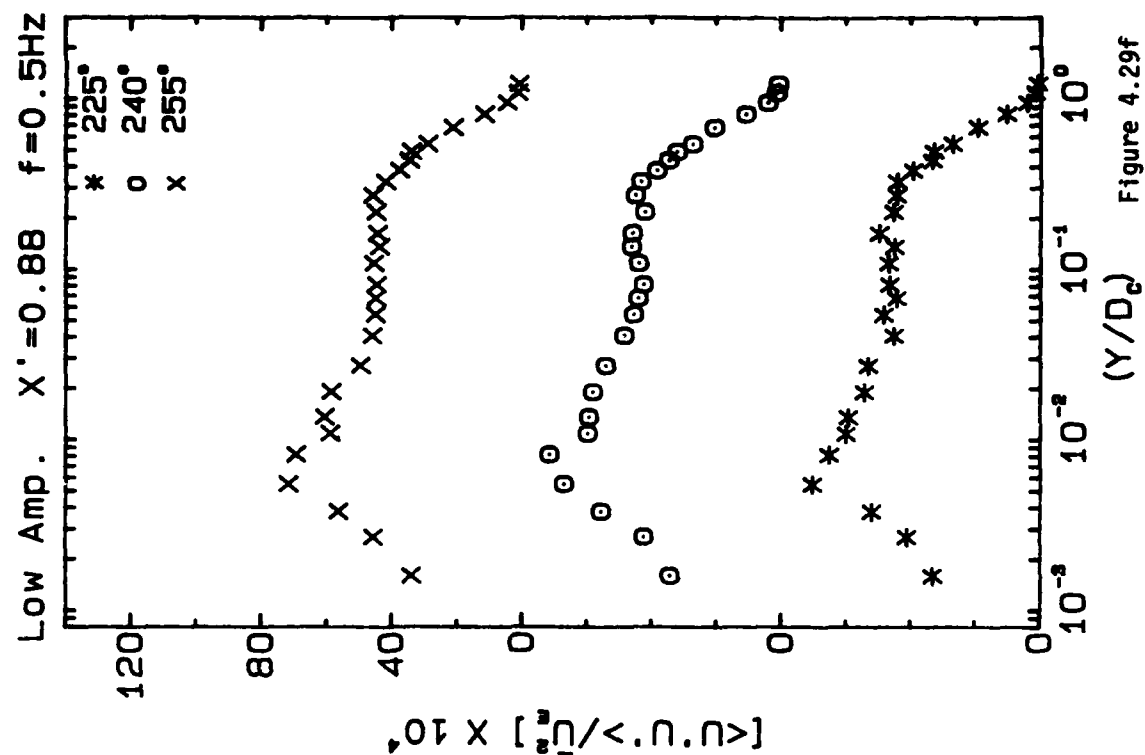


Figure 4.29f

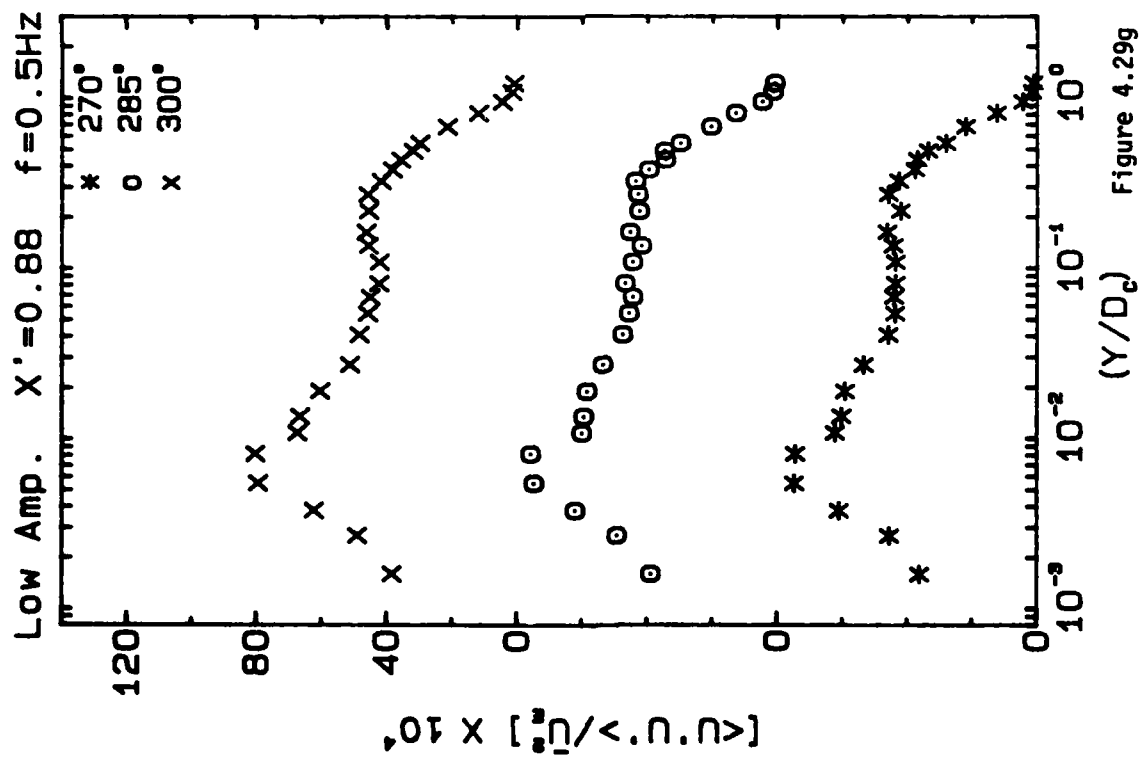


Figure 4.29g

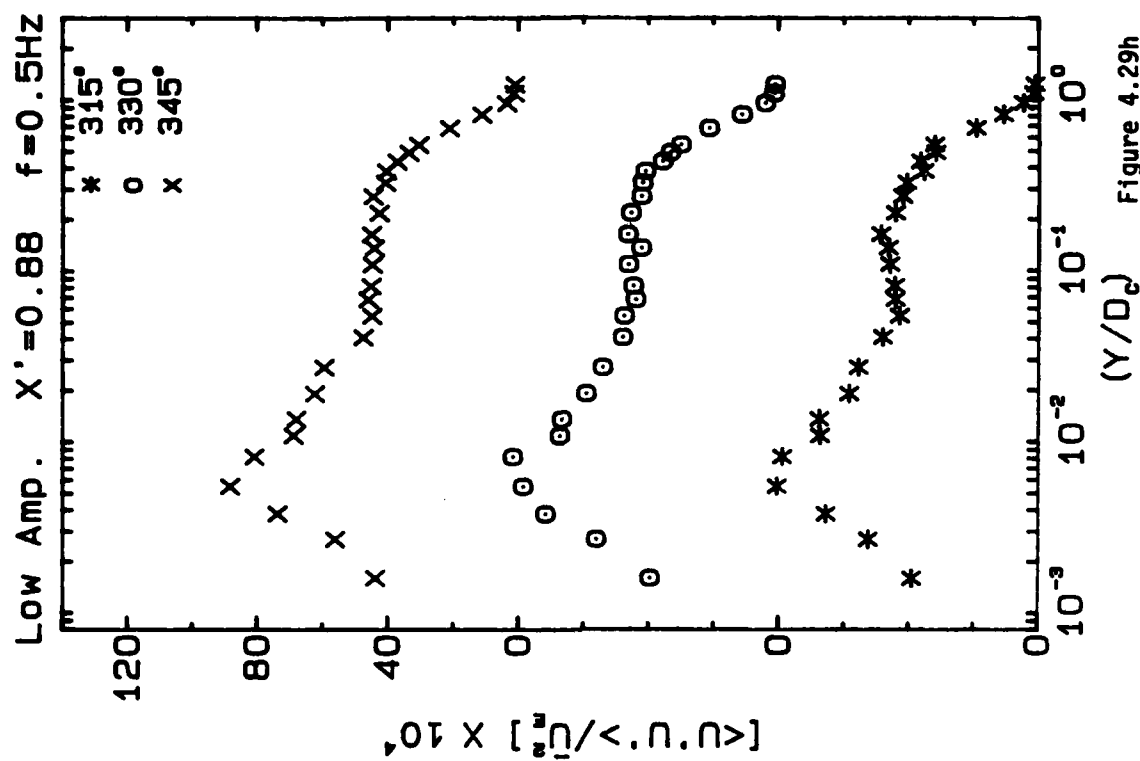


Figure 4.29h

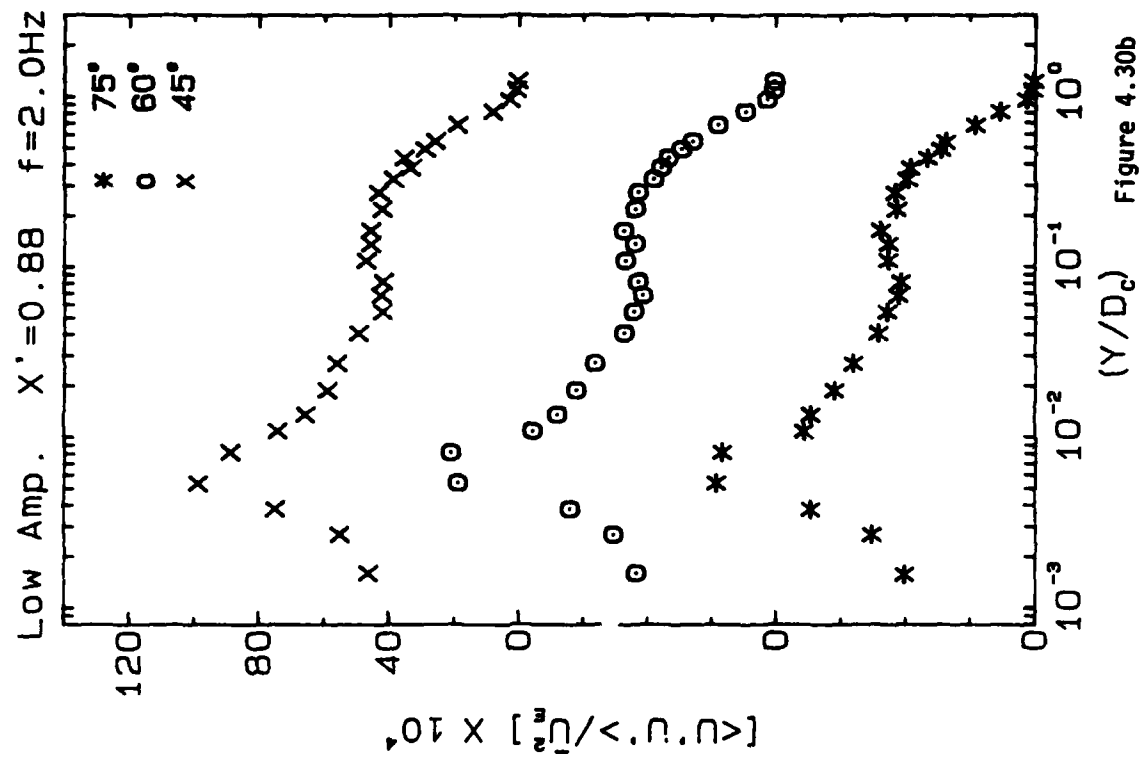


Figure 4.30b

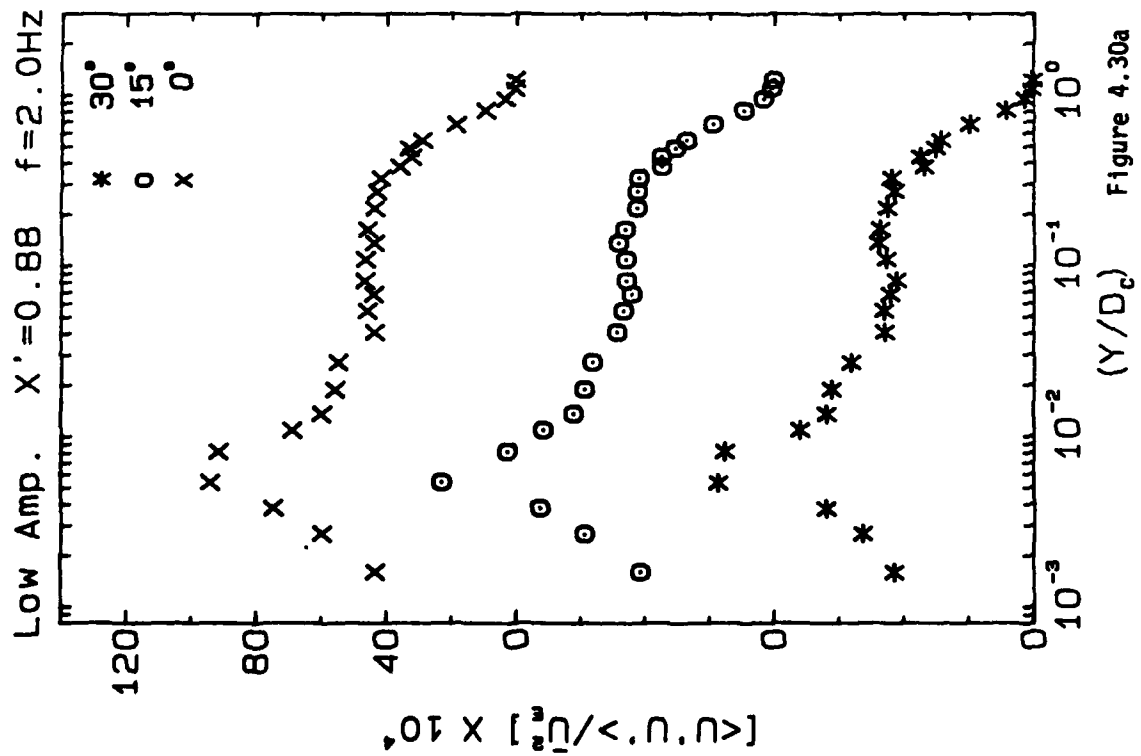


Figure 4.30a

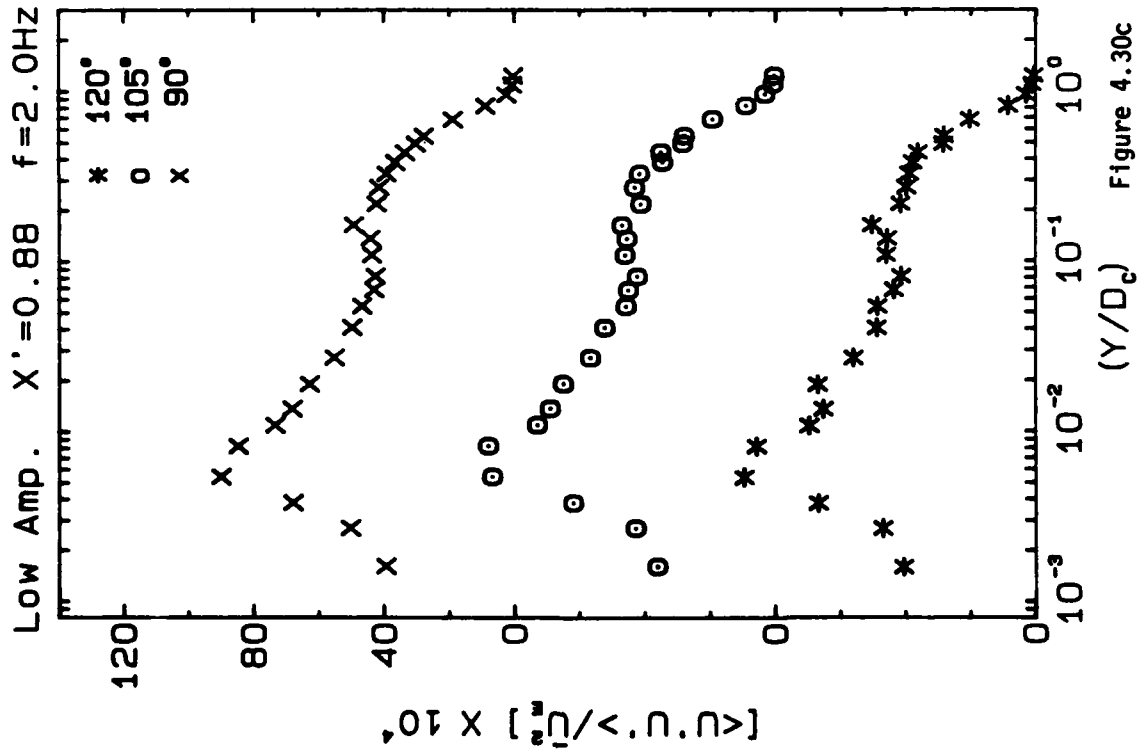


Figure 4.30c

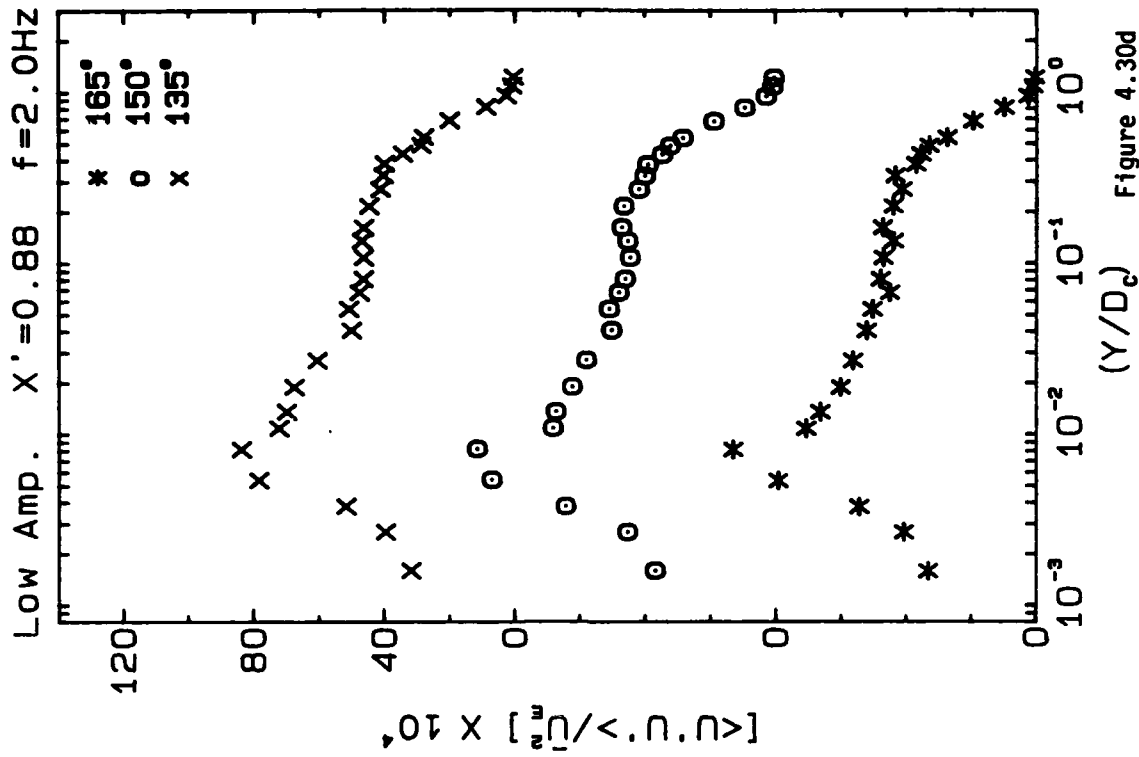


Figure 4.30d

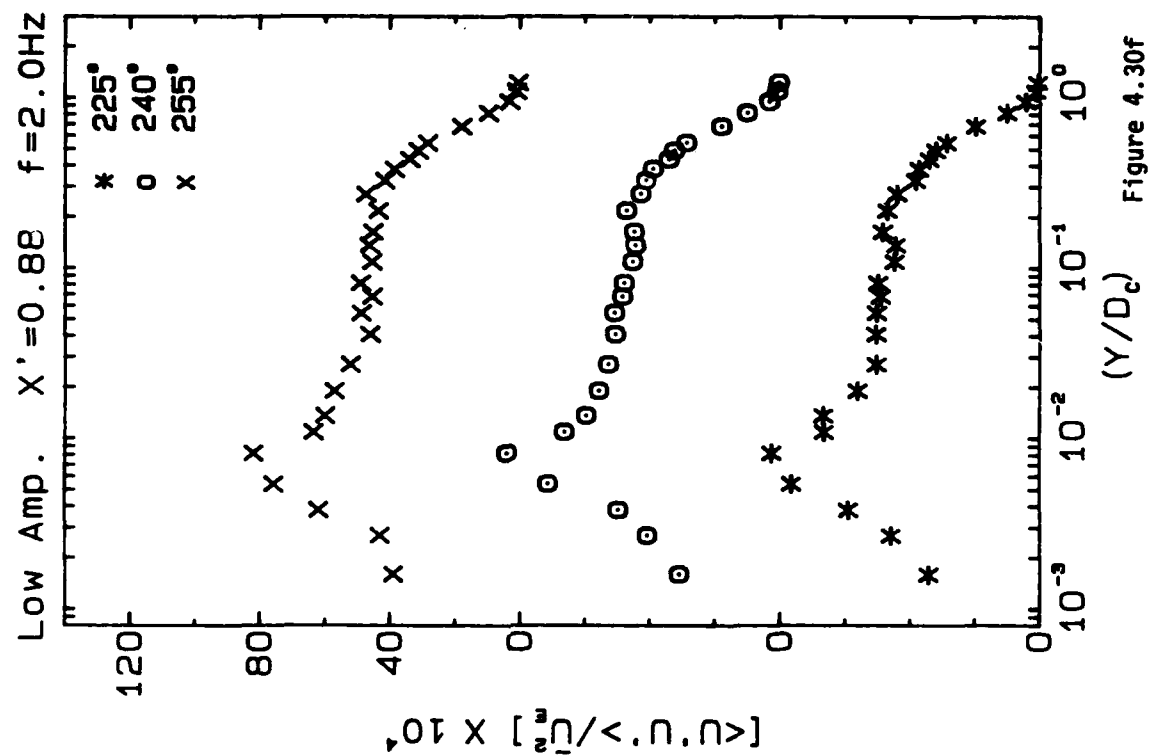


Figure 4.30f

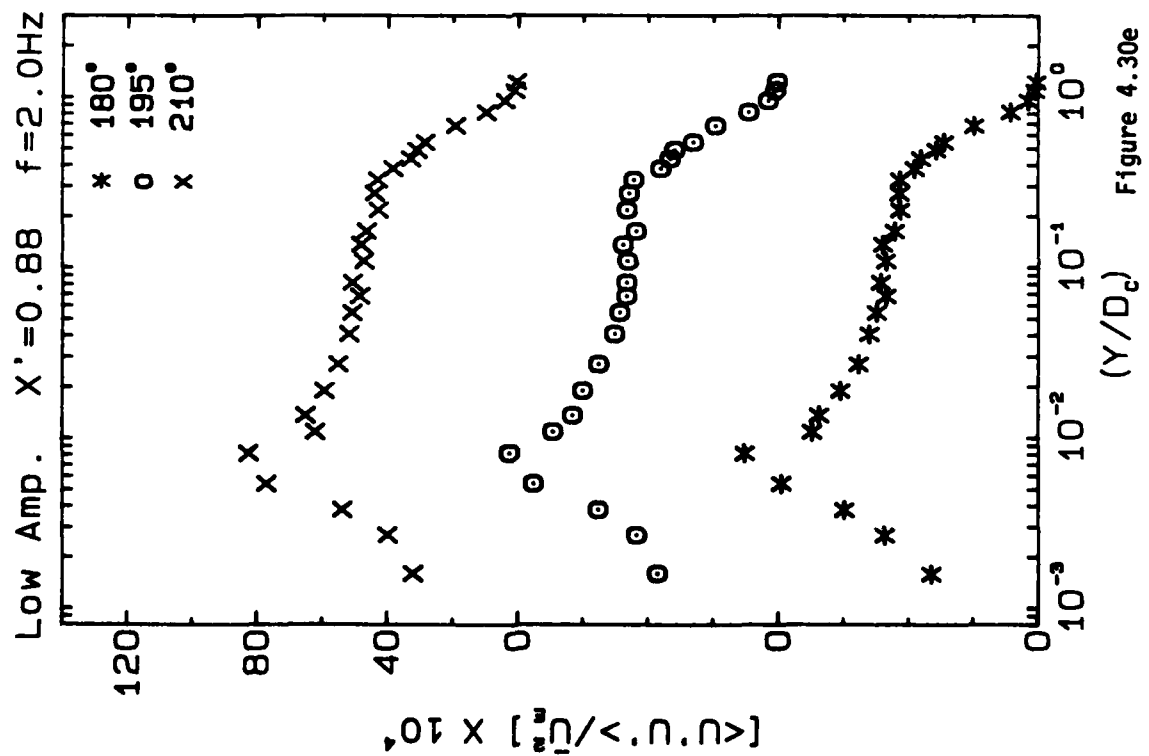
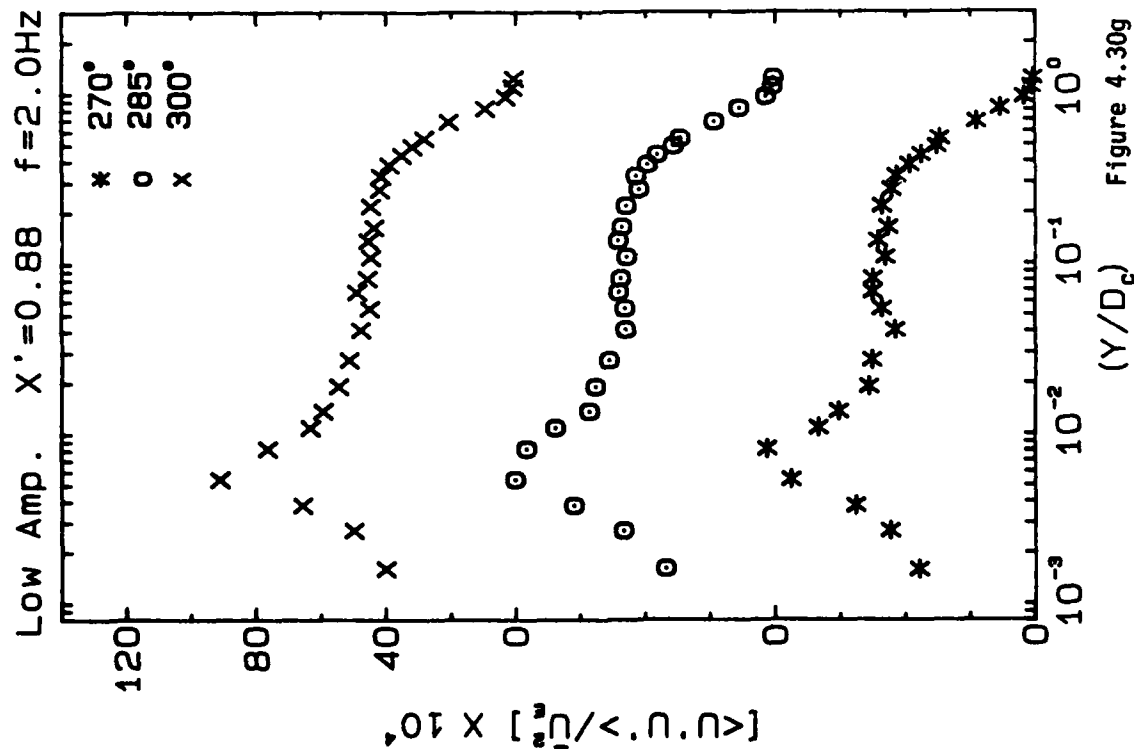
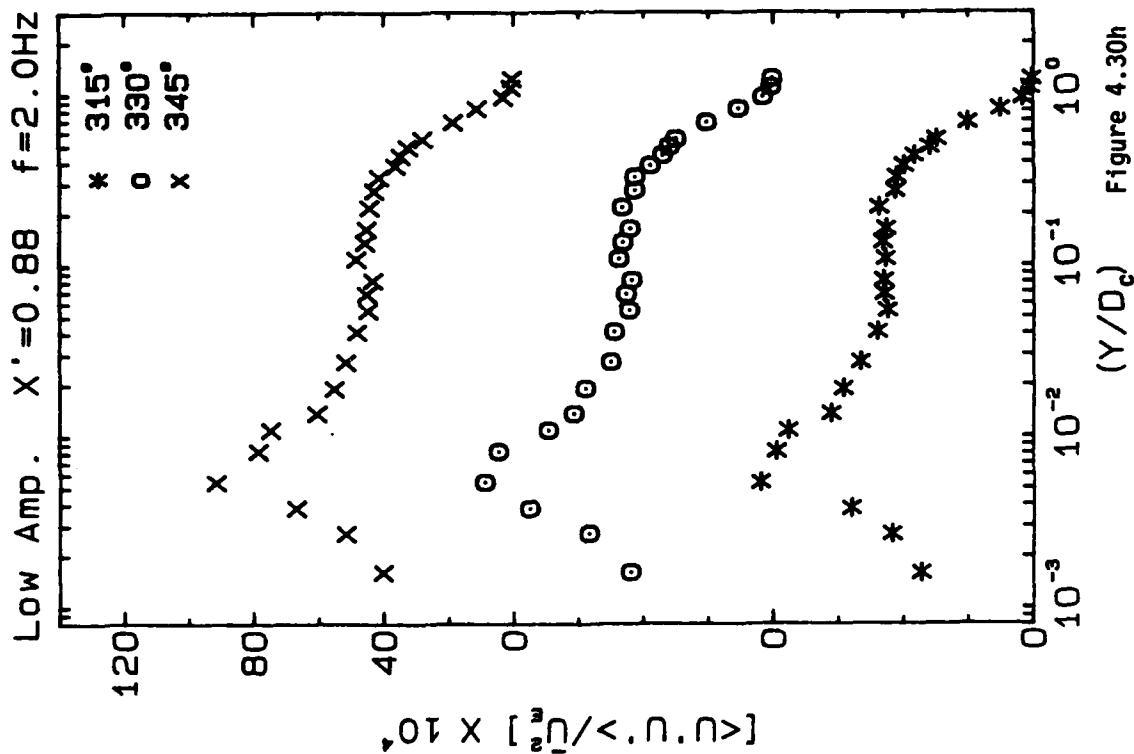


Figure 4.30e





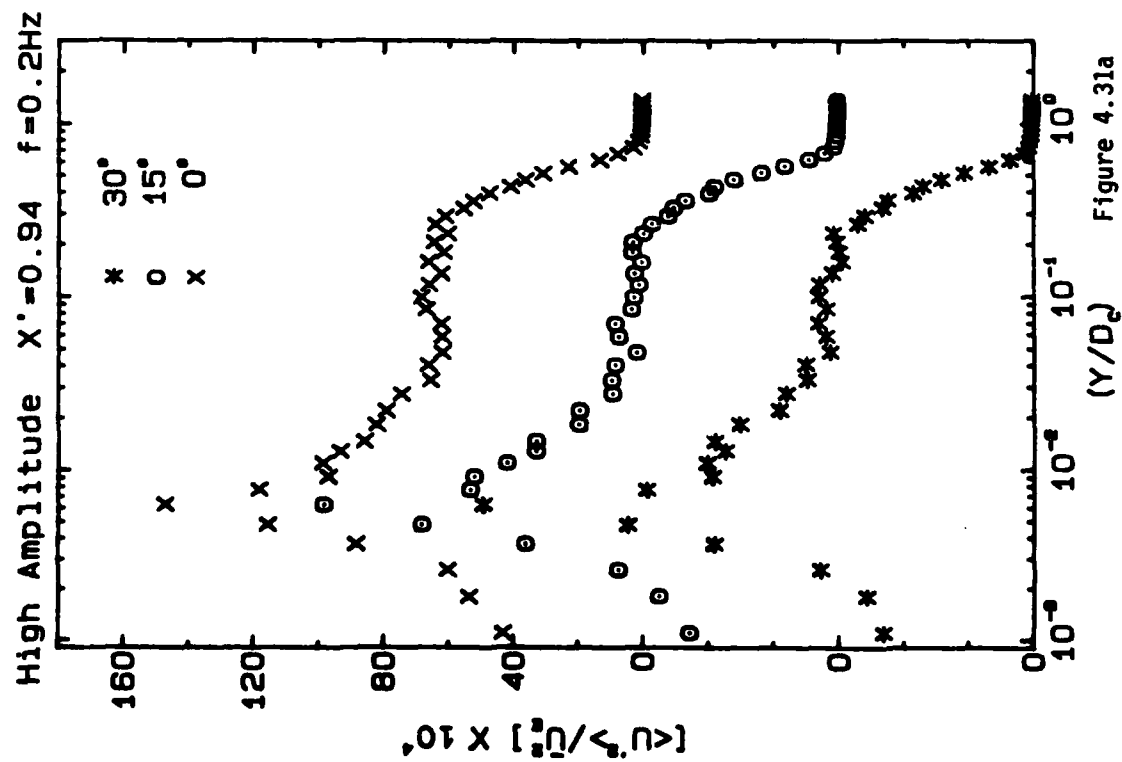


Figure 4.31a

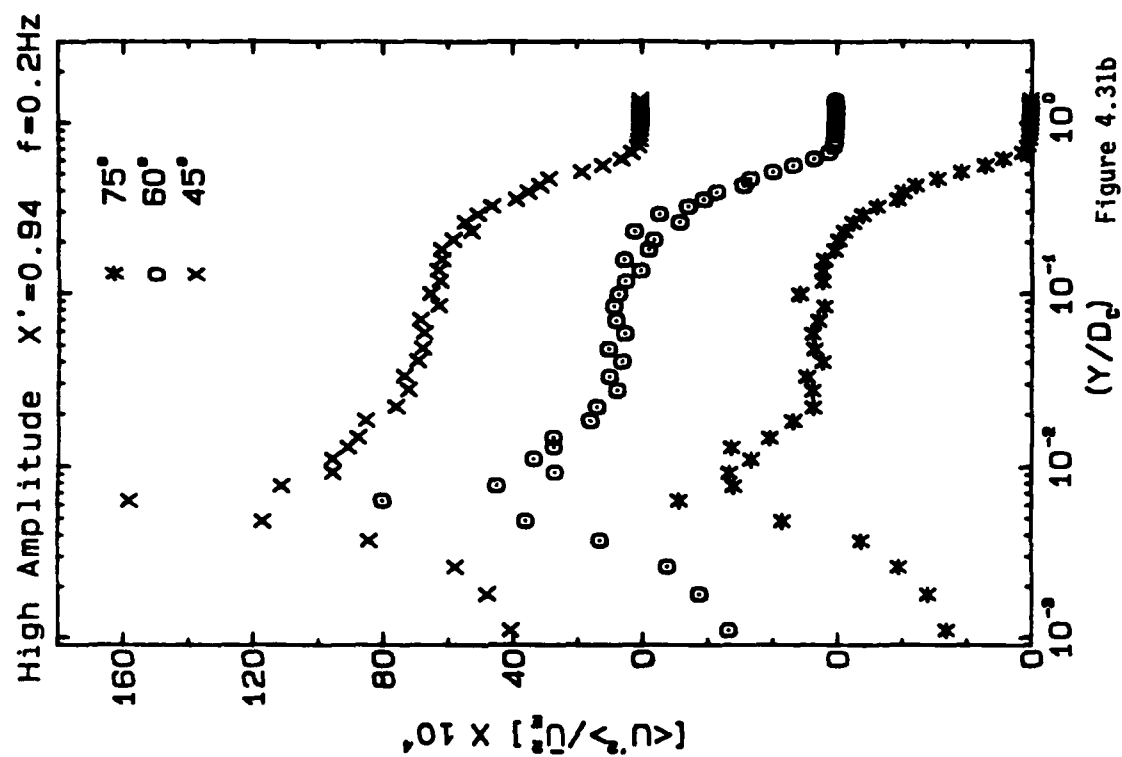


Figure 4.31b

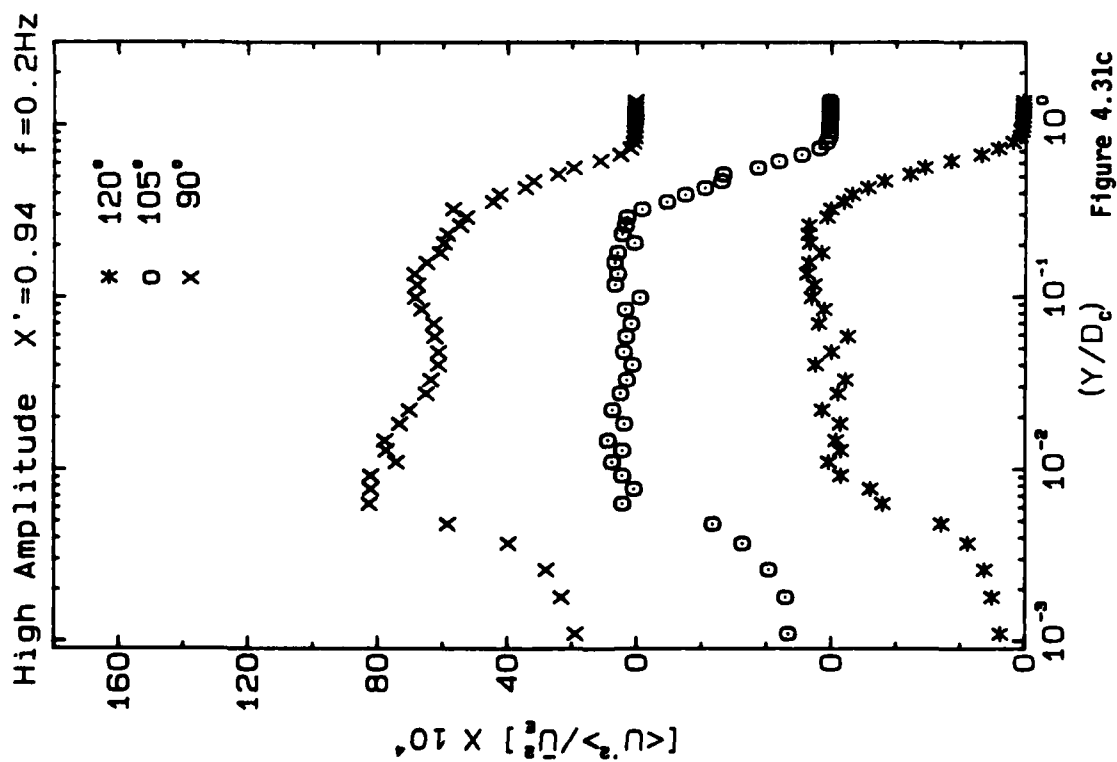


Figure 4.31c

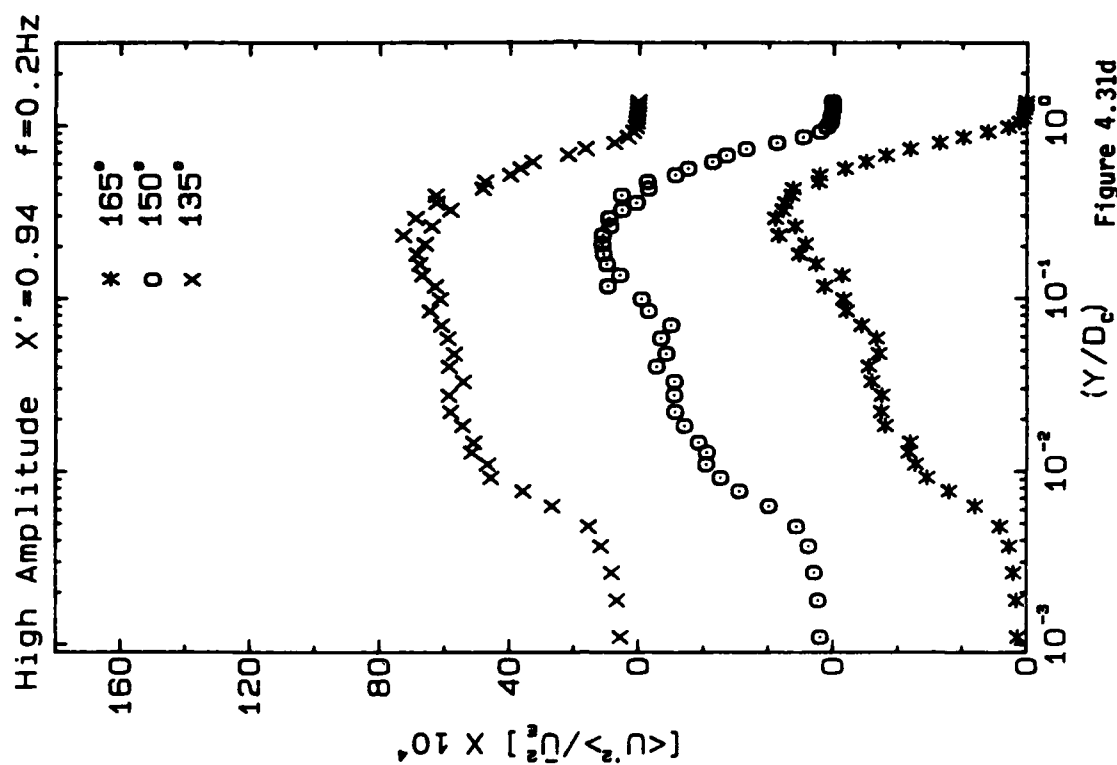
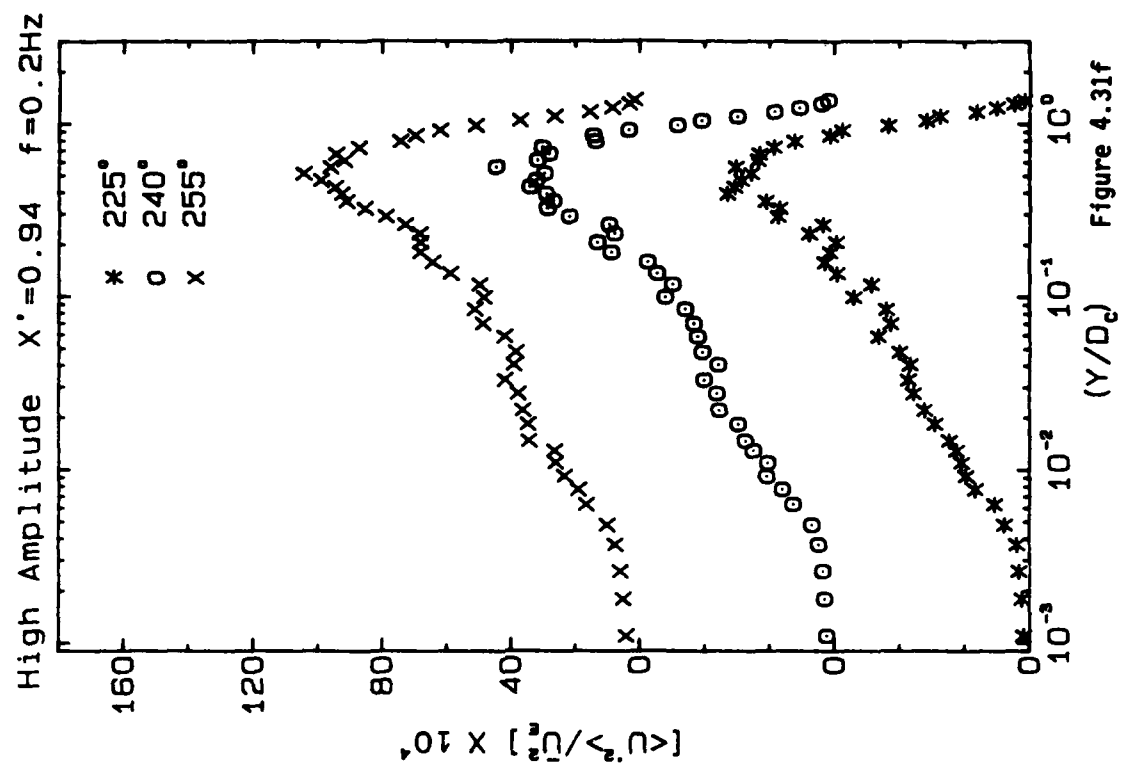
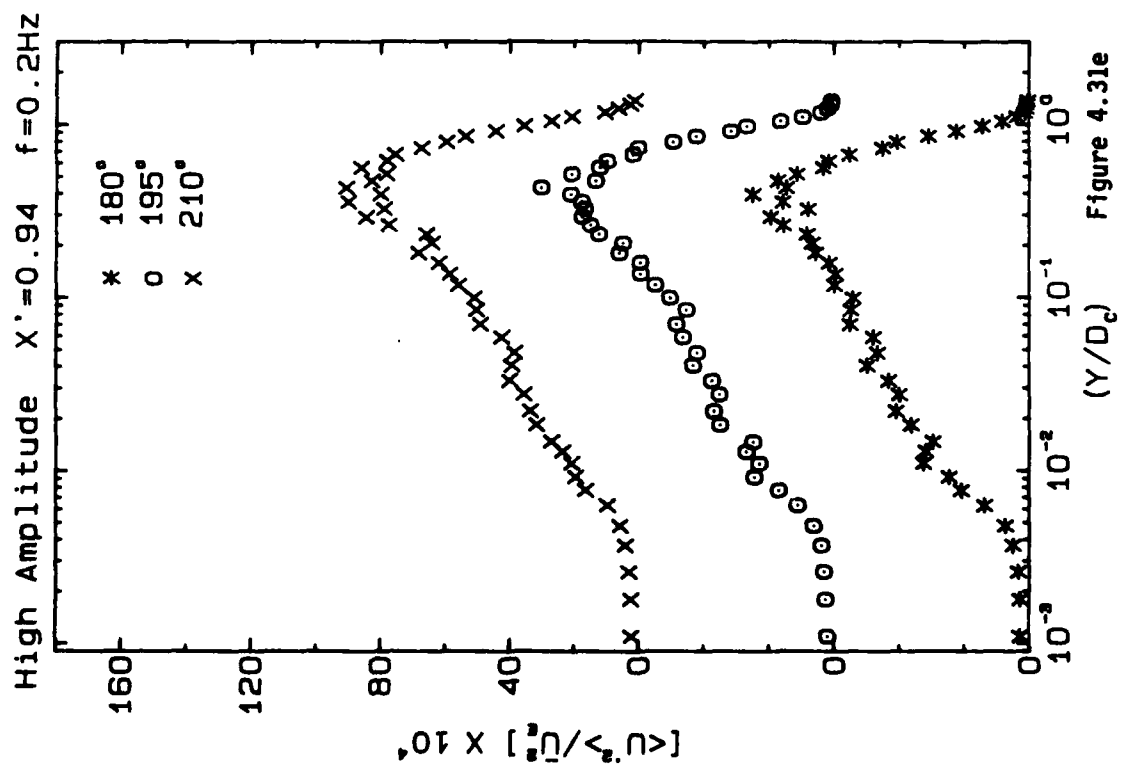


Figure 4.31d



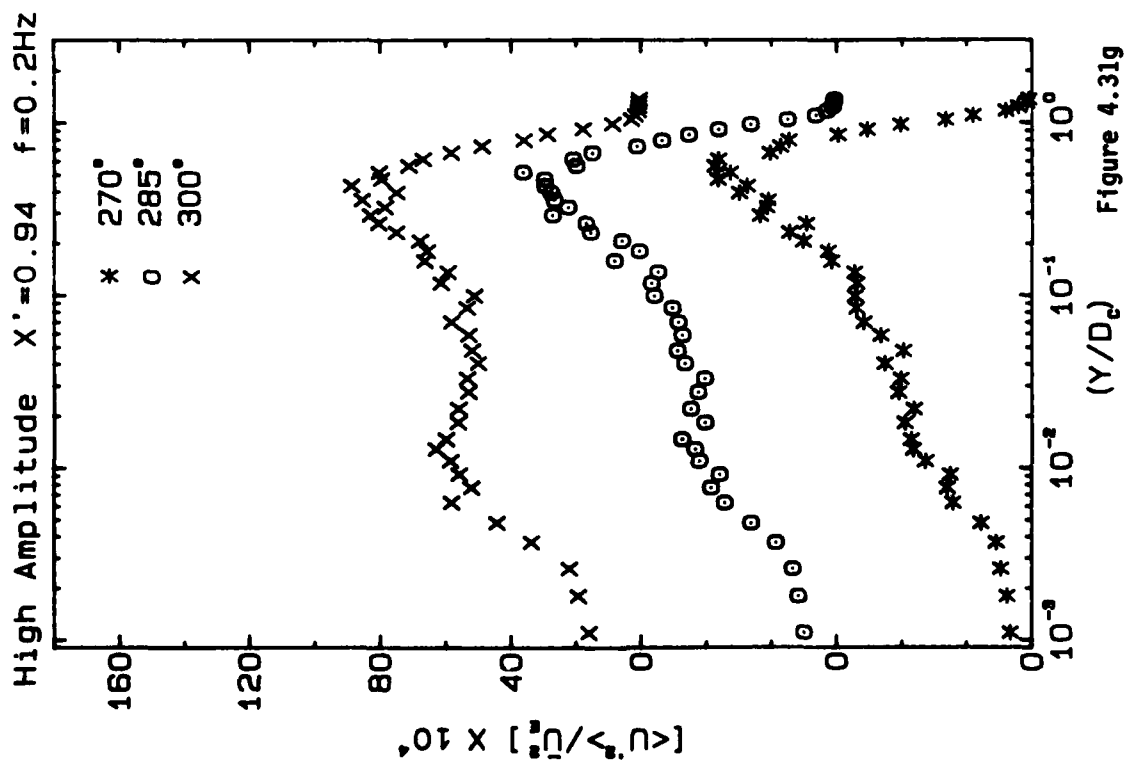


Figure 4.31g

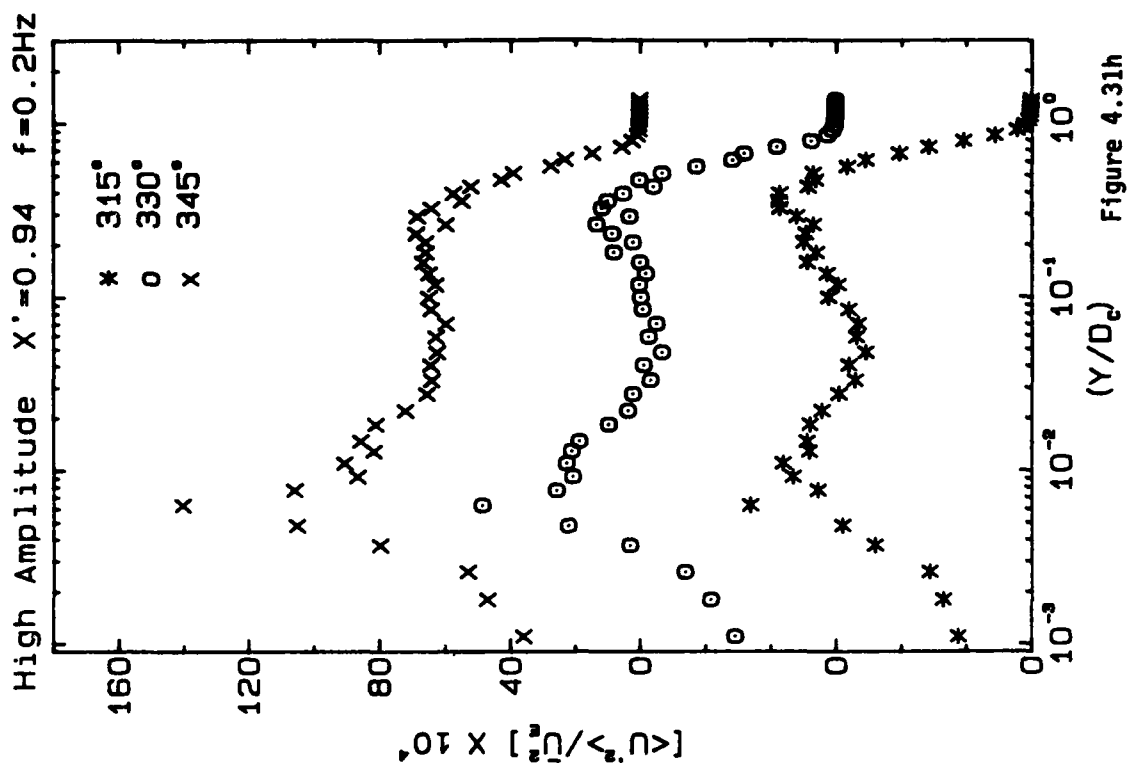


Figure 4.31h

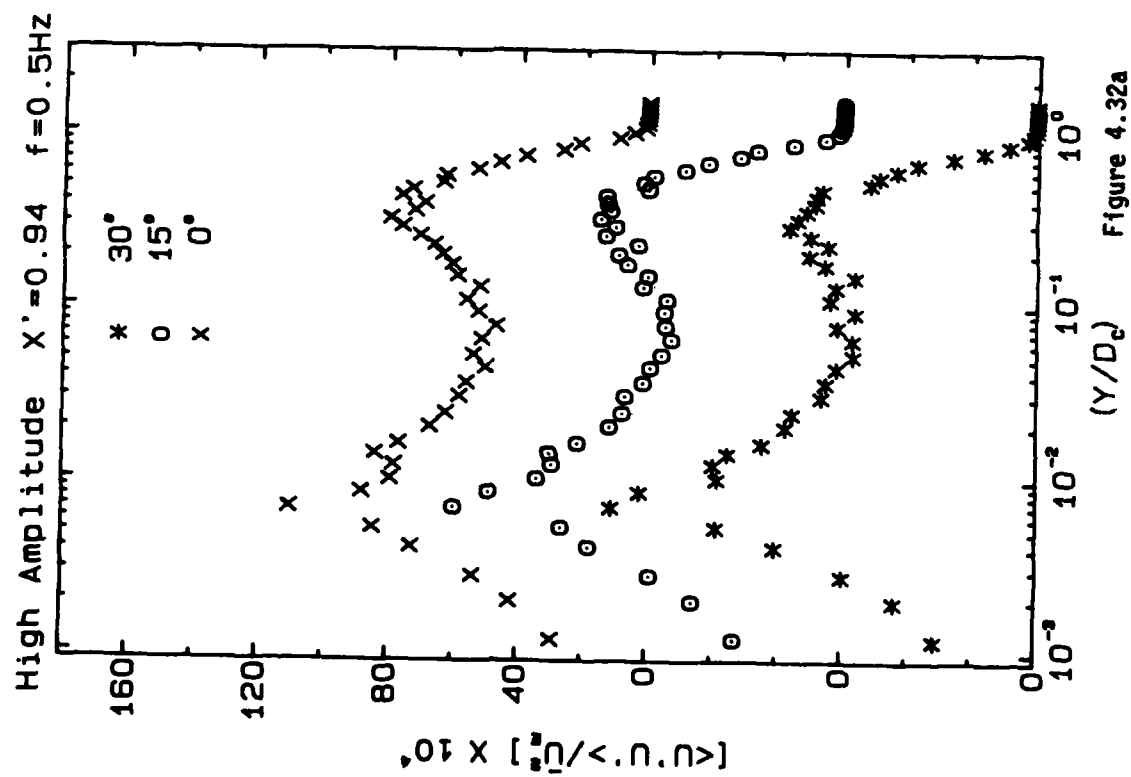


Figure 4.32a

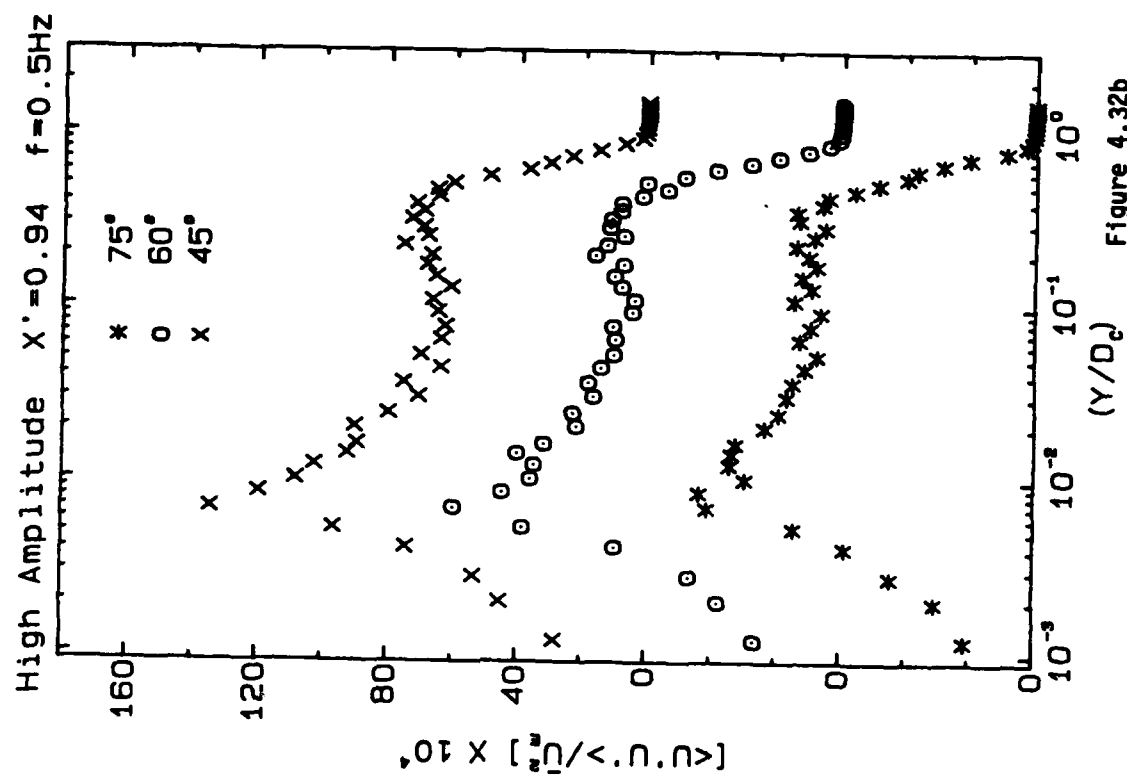


Figure 4.32b

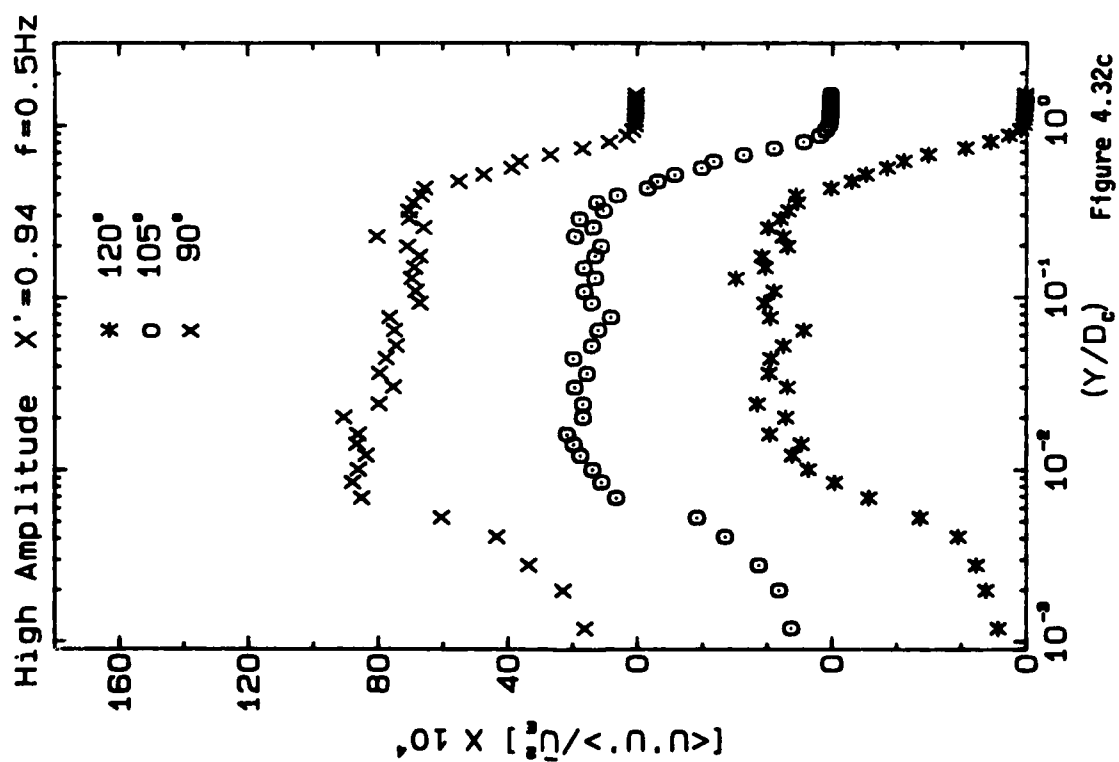


Figure 4.32c

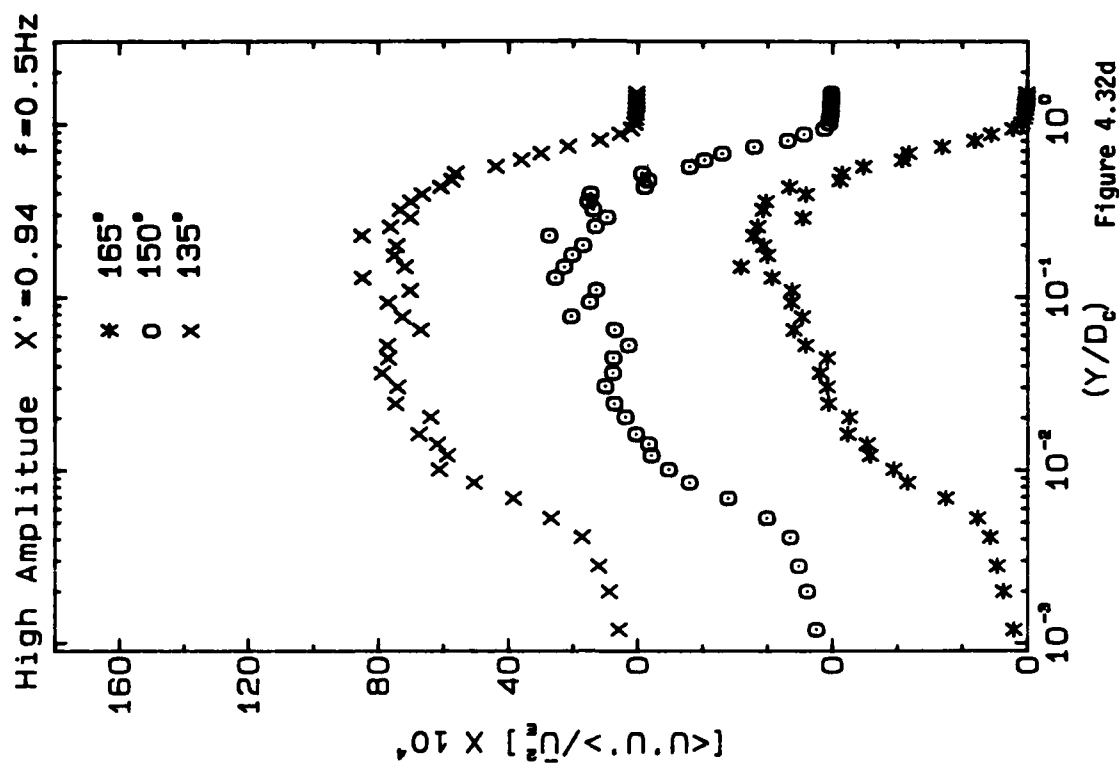


Figure 4.32d

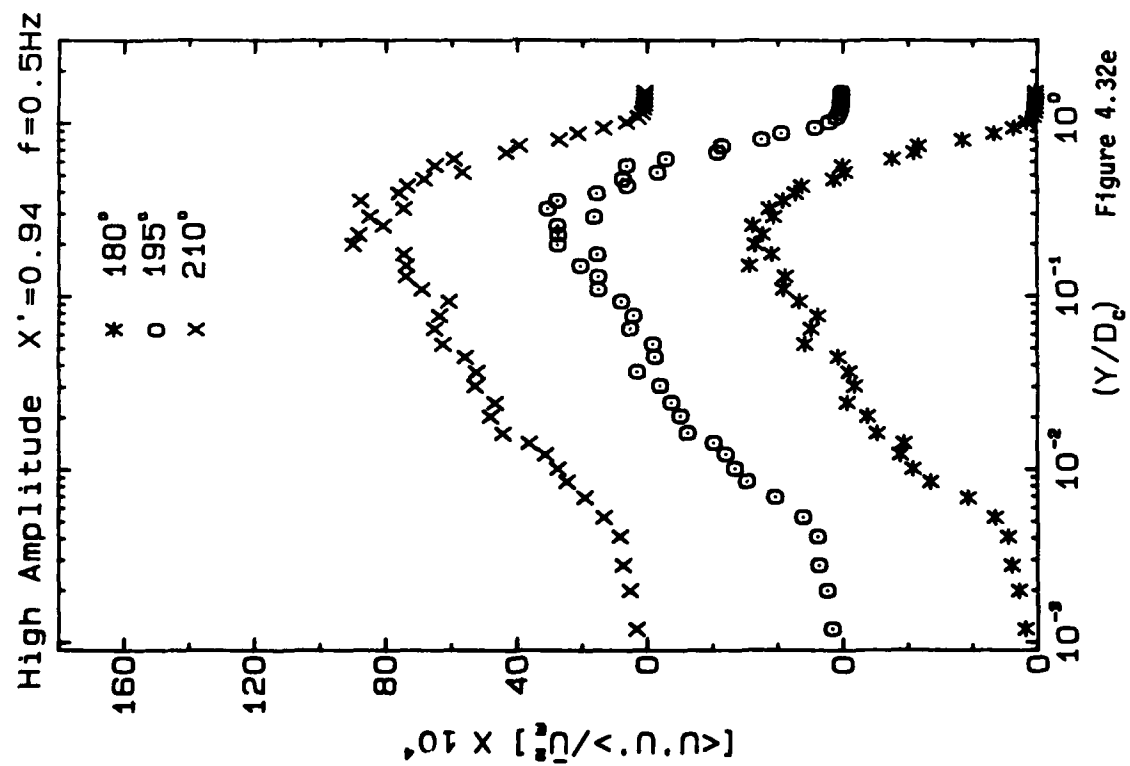


Figure 4.32e

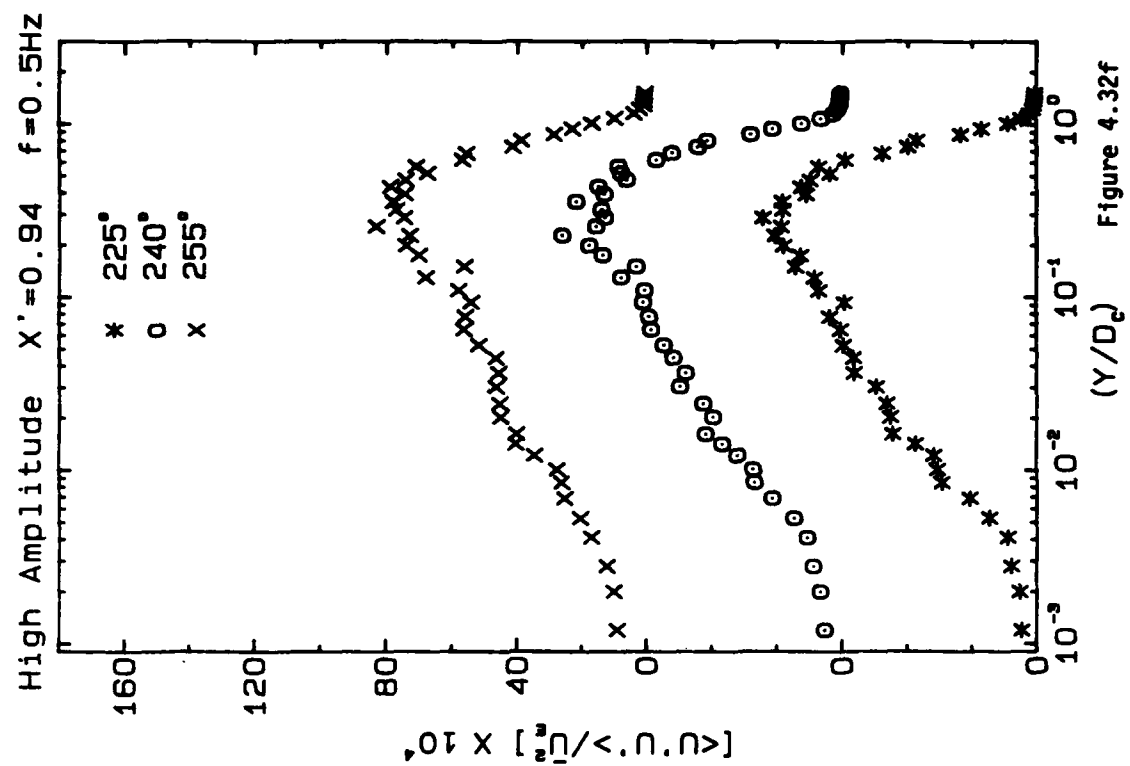


Figure 4.32f

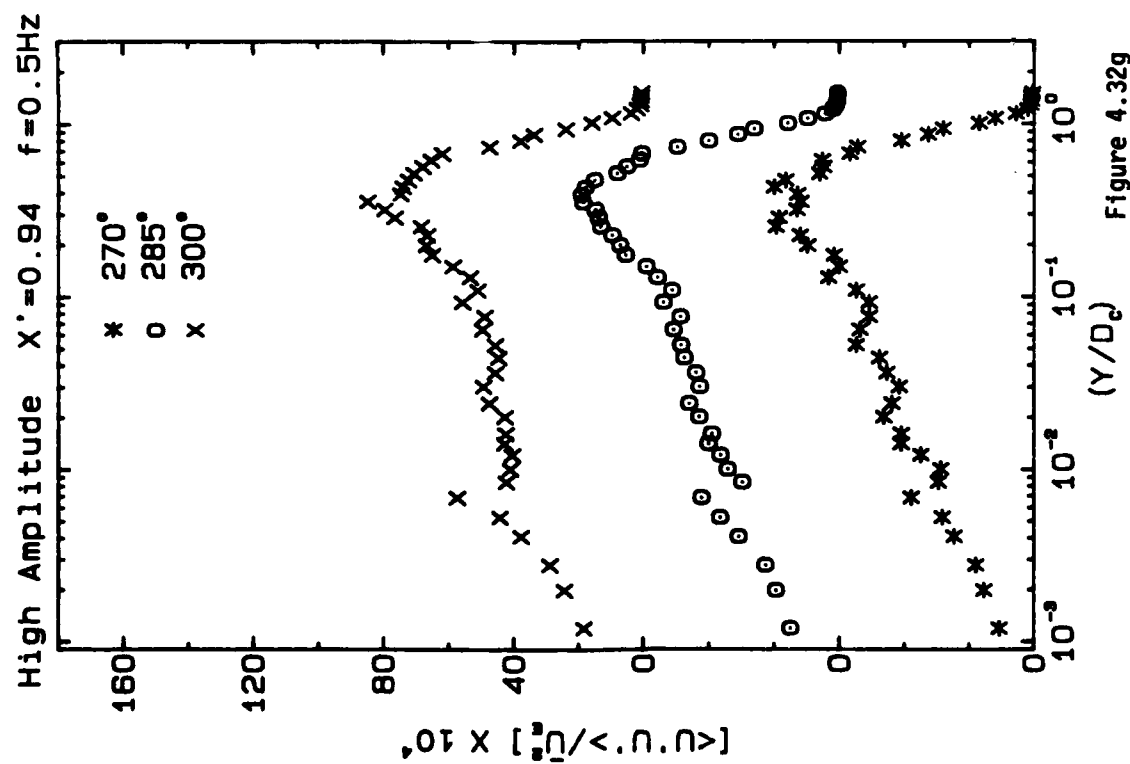


Figure 4.32g

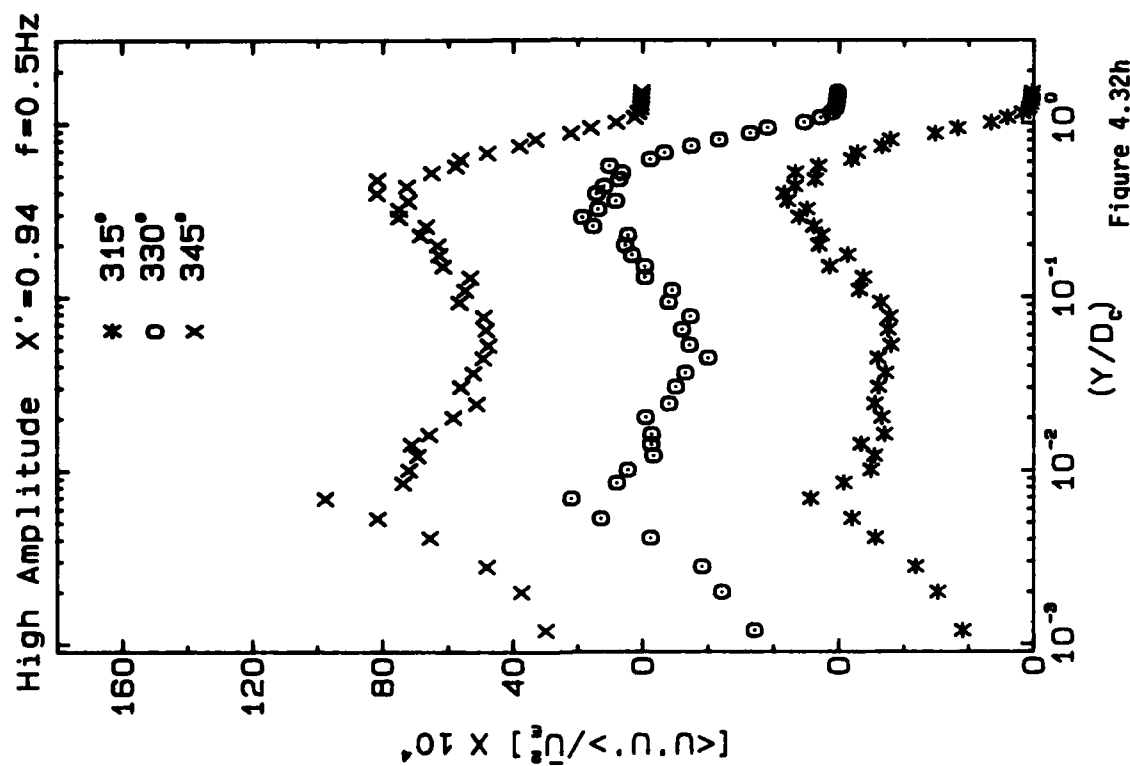


Figure 4.32h



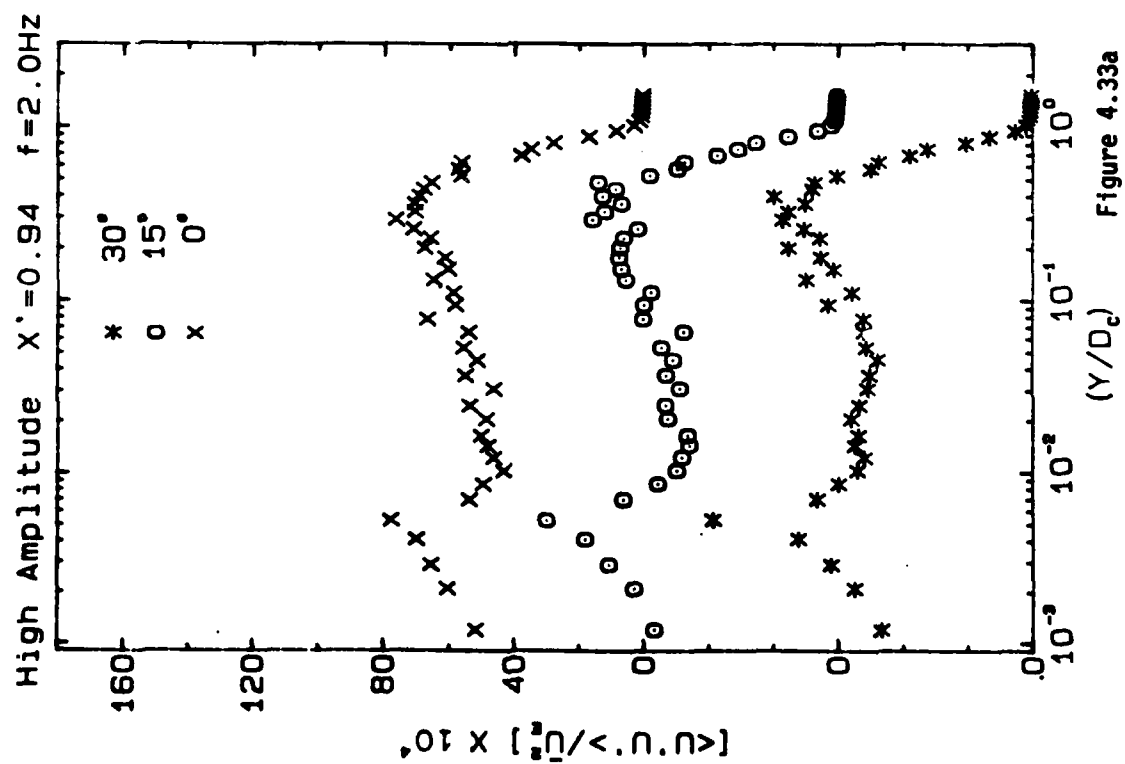


Figure 4.33a

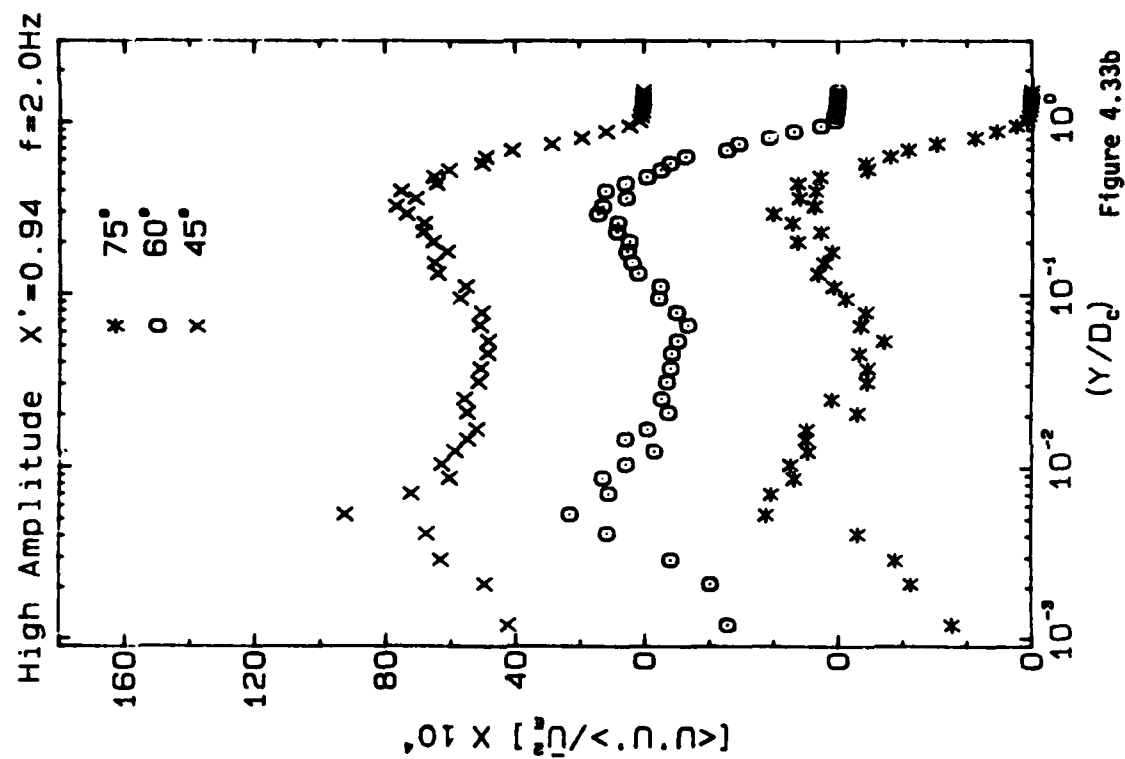


Figure 4.33b

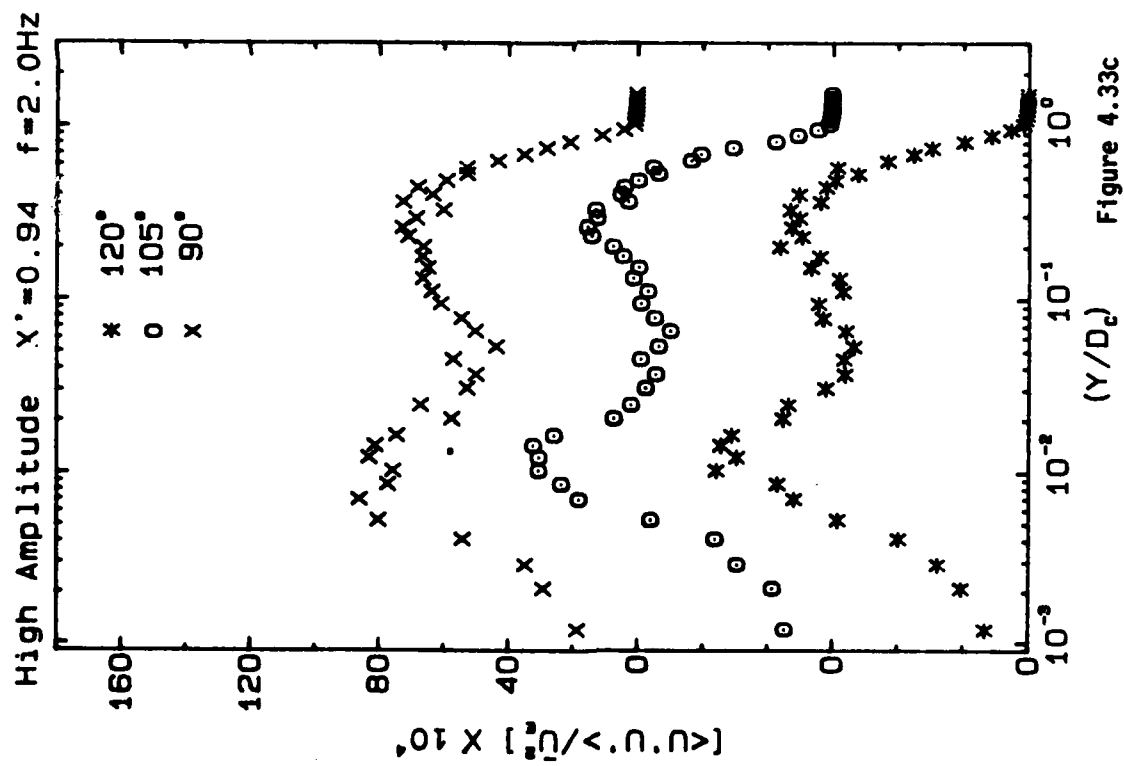


Figure 4.33c

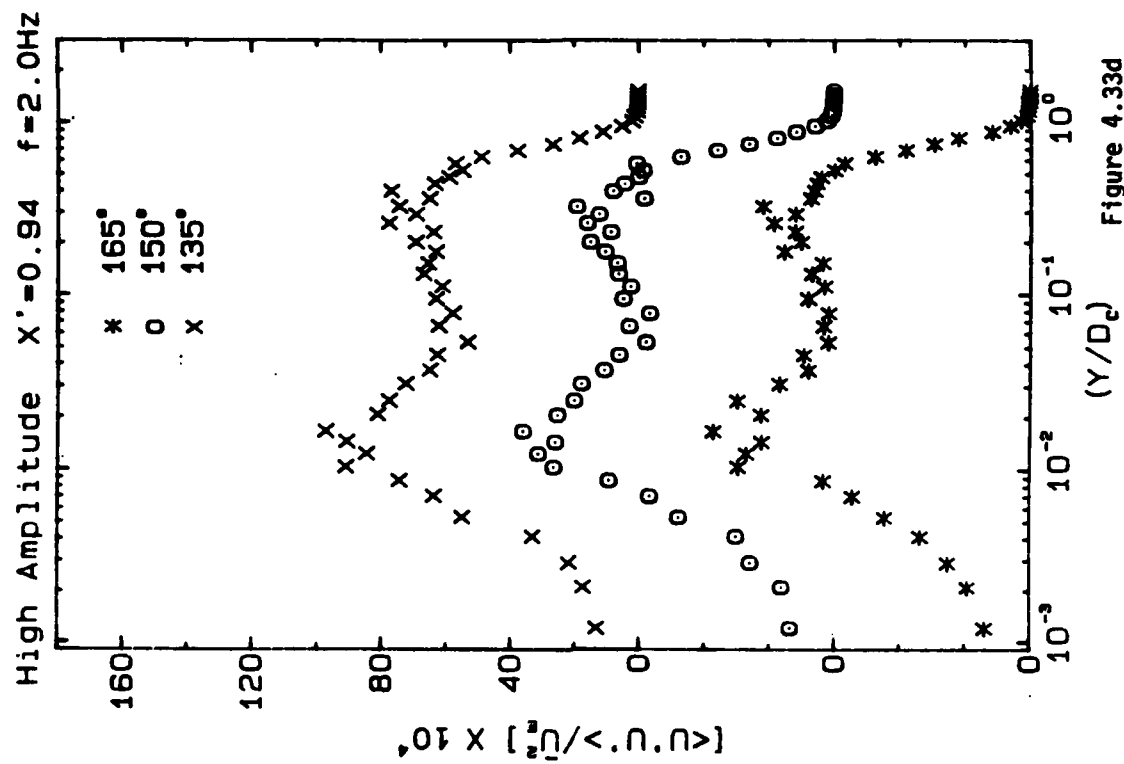


Figure 4.33d

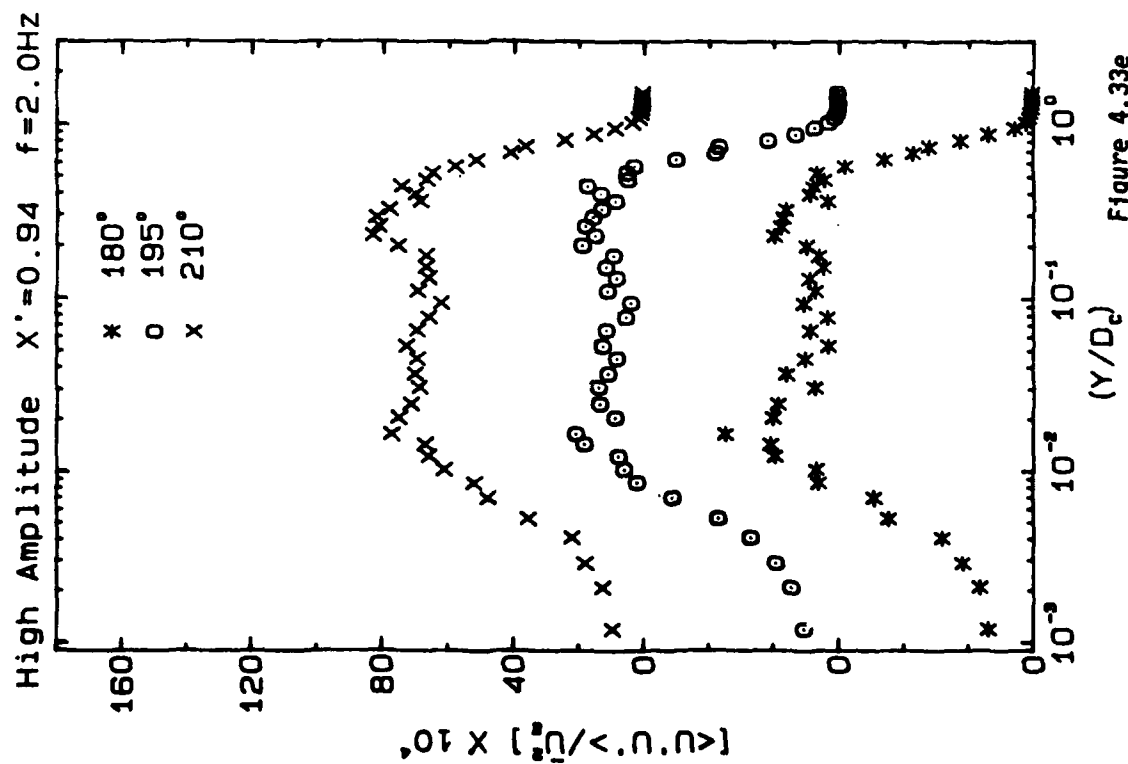


Figure 4.33e

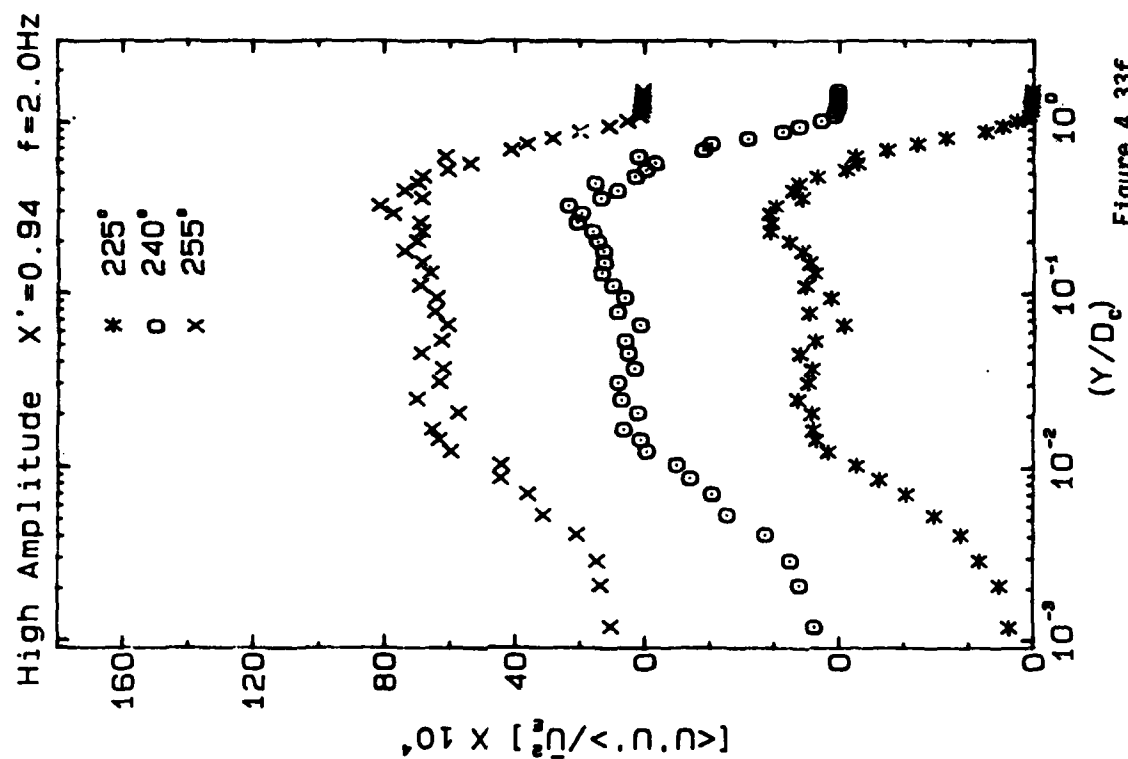


Figure 4.33f

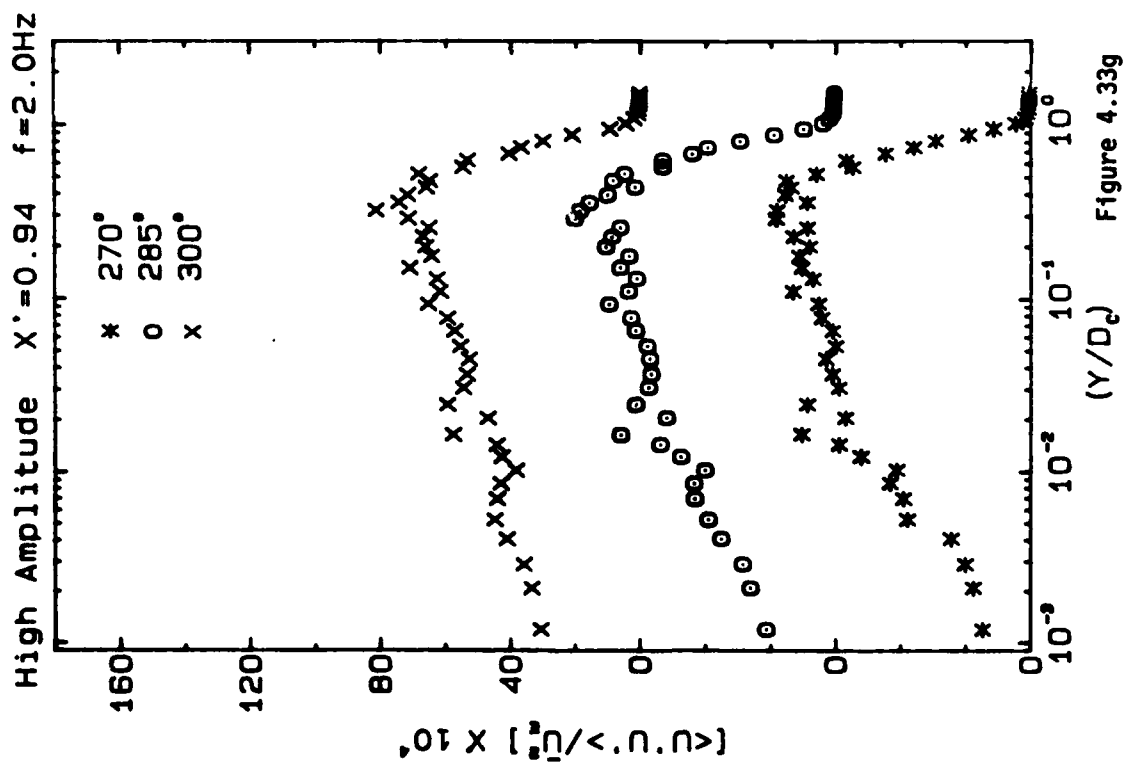


Figure 4.33g

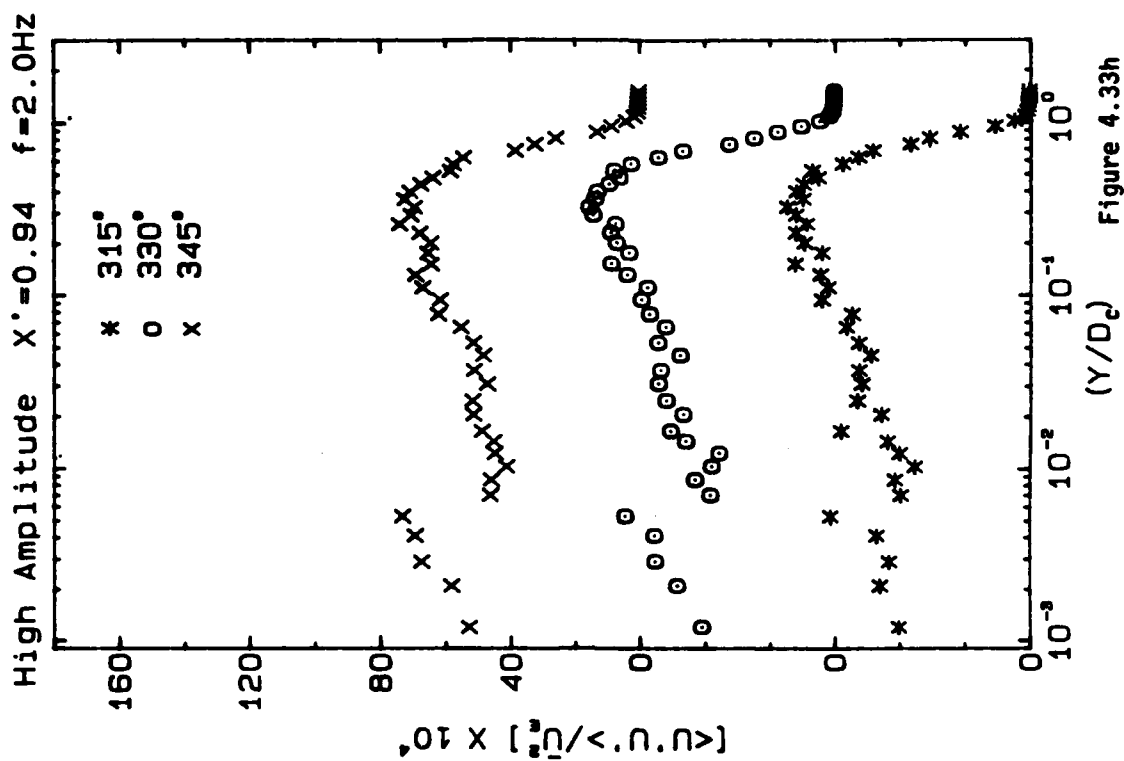


Figure 4.33h

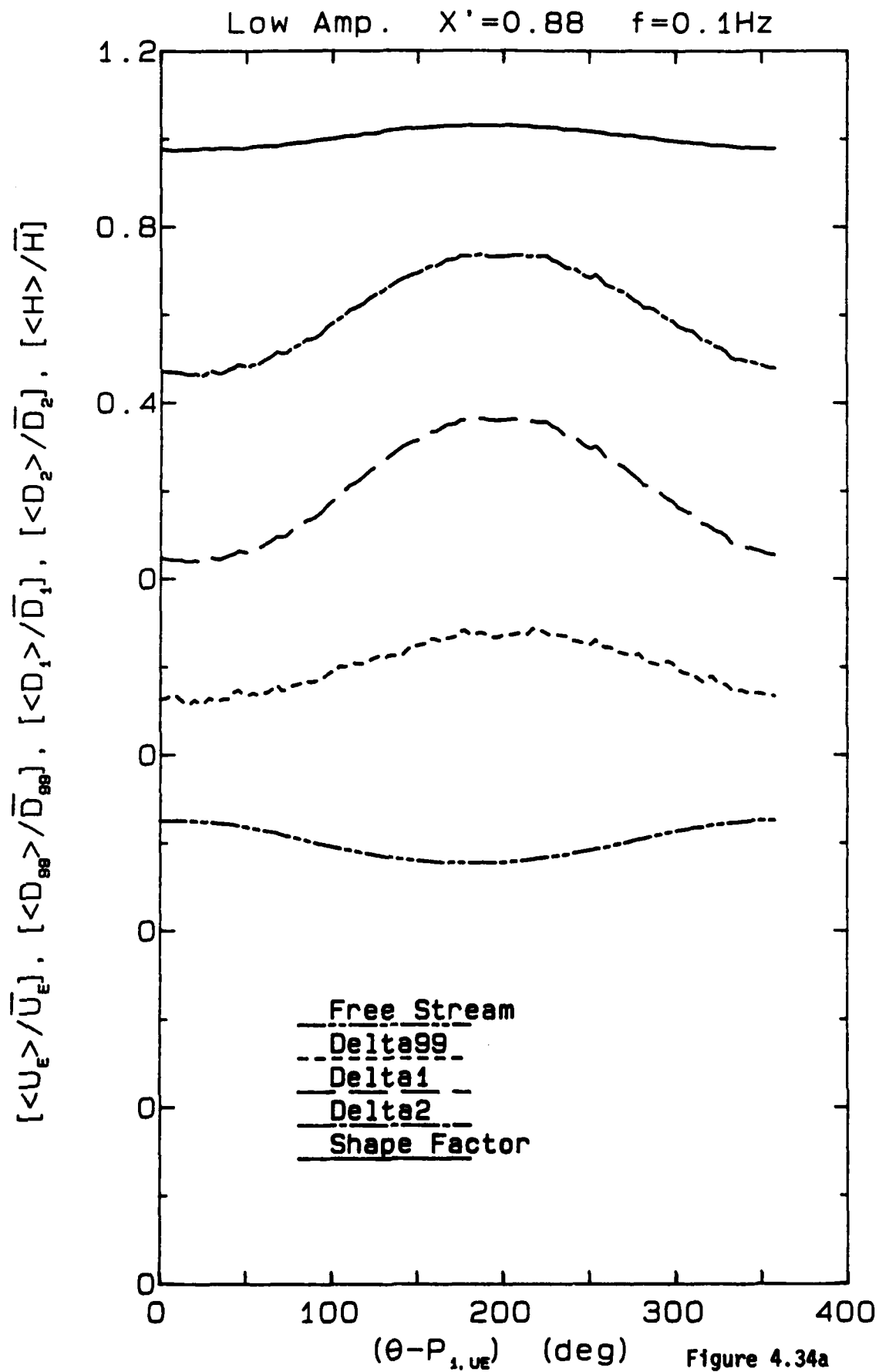


Figure 4.34a

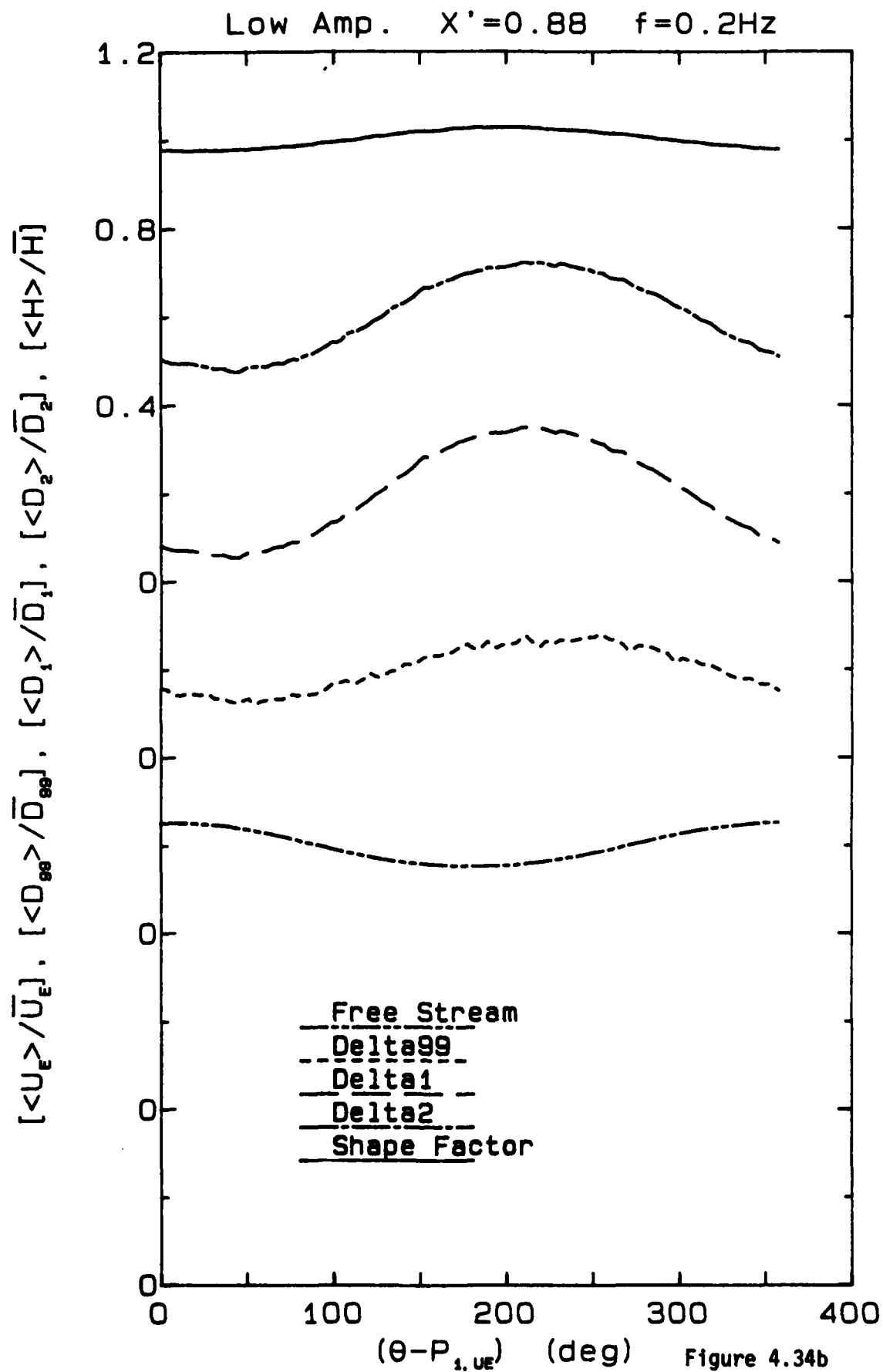


Figure 4.34b

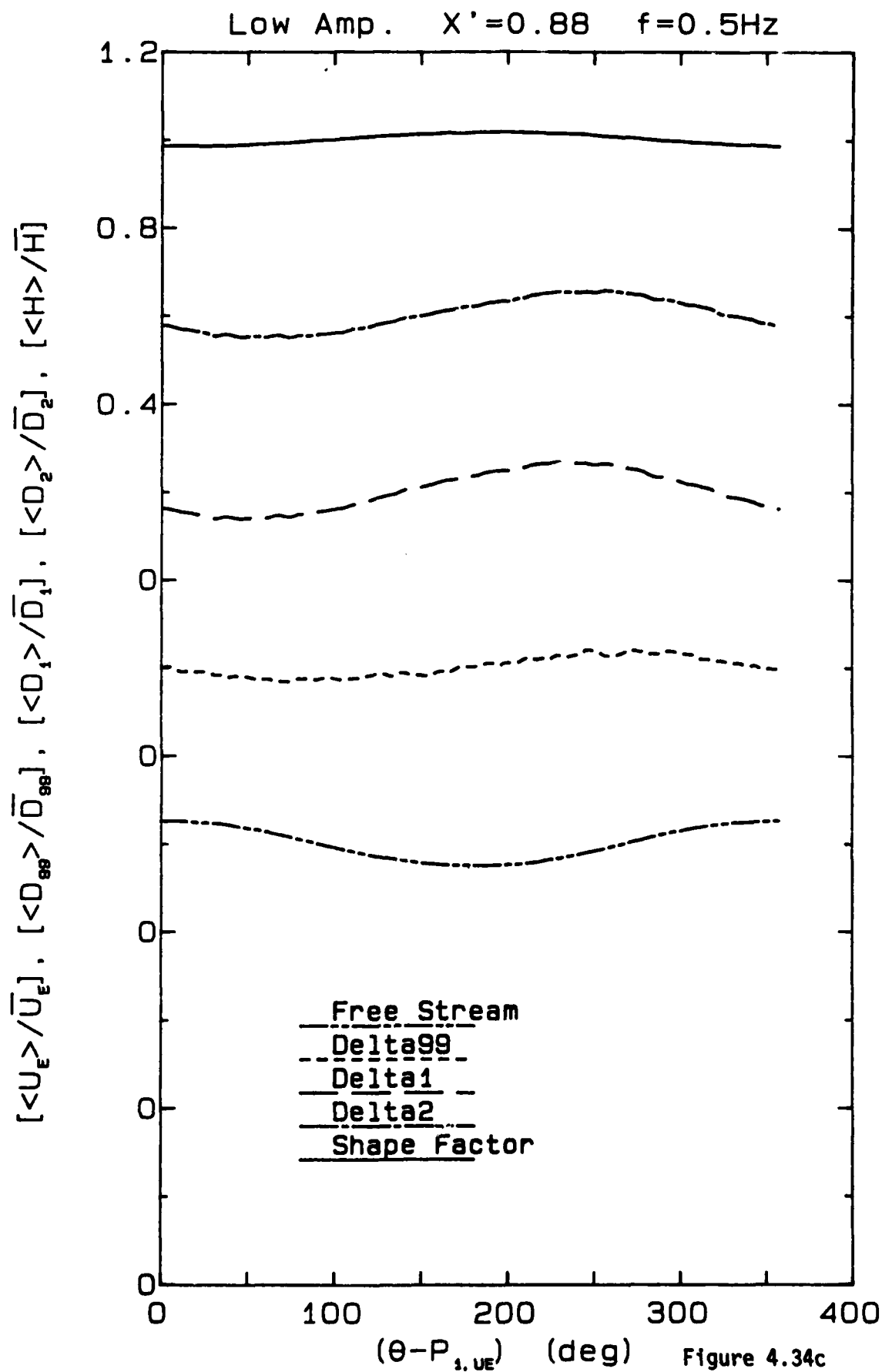


Figure 4.34c

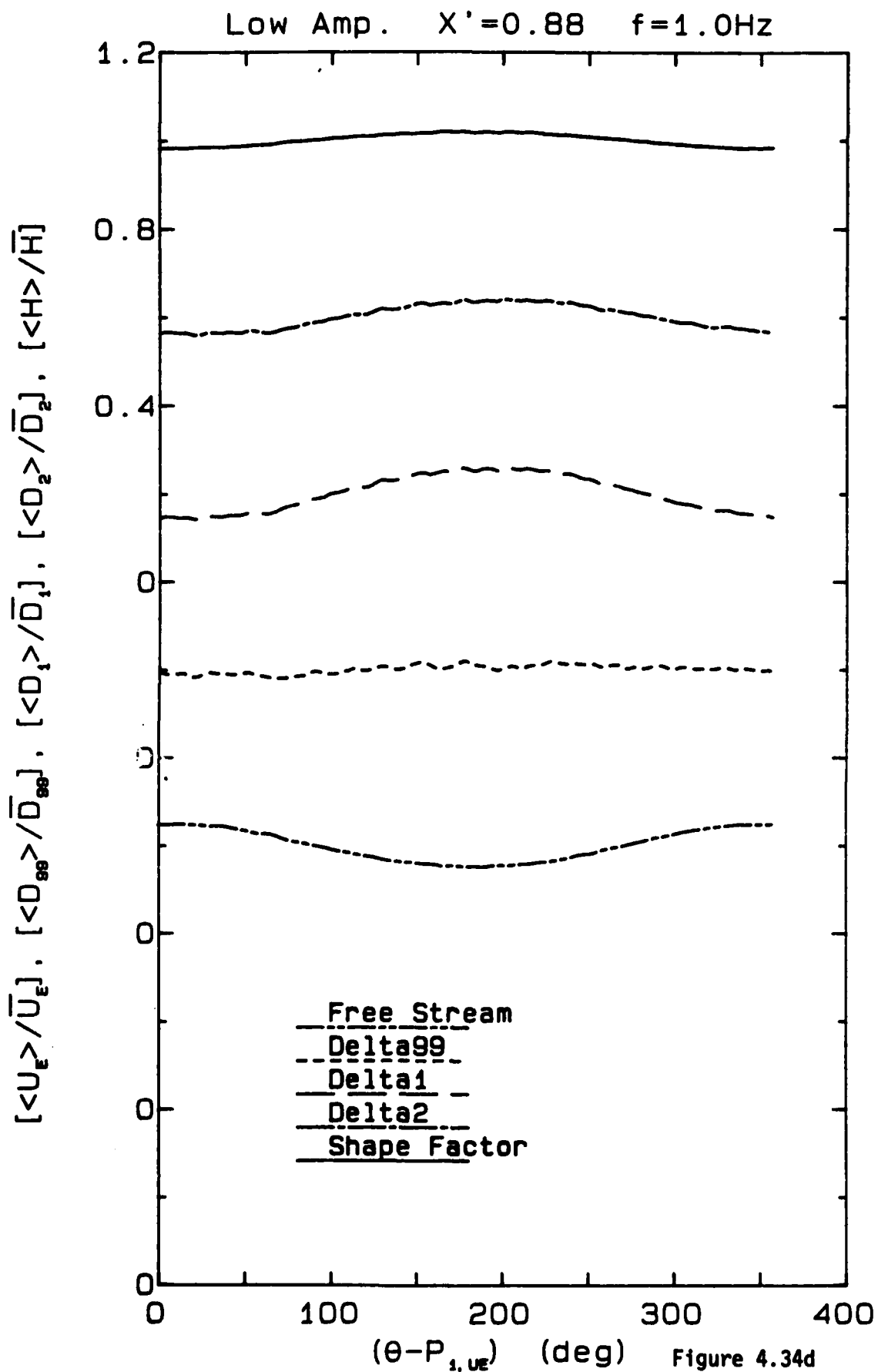


Figure 4.34d



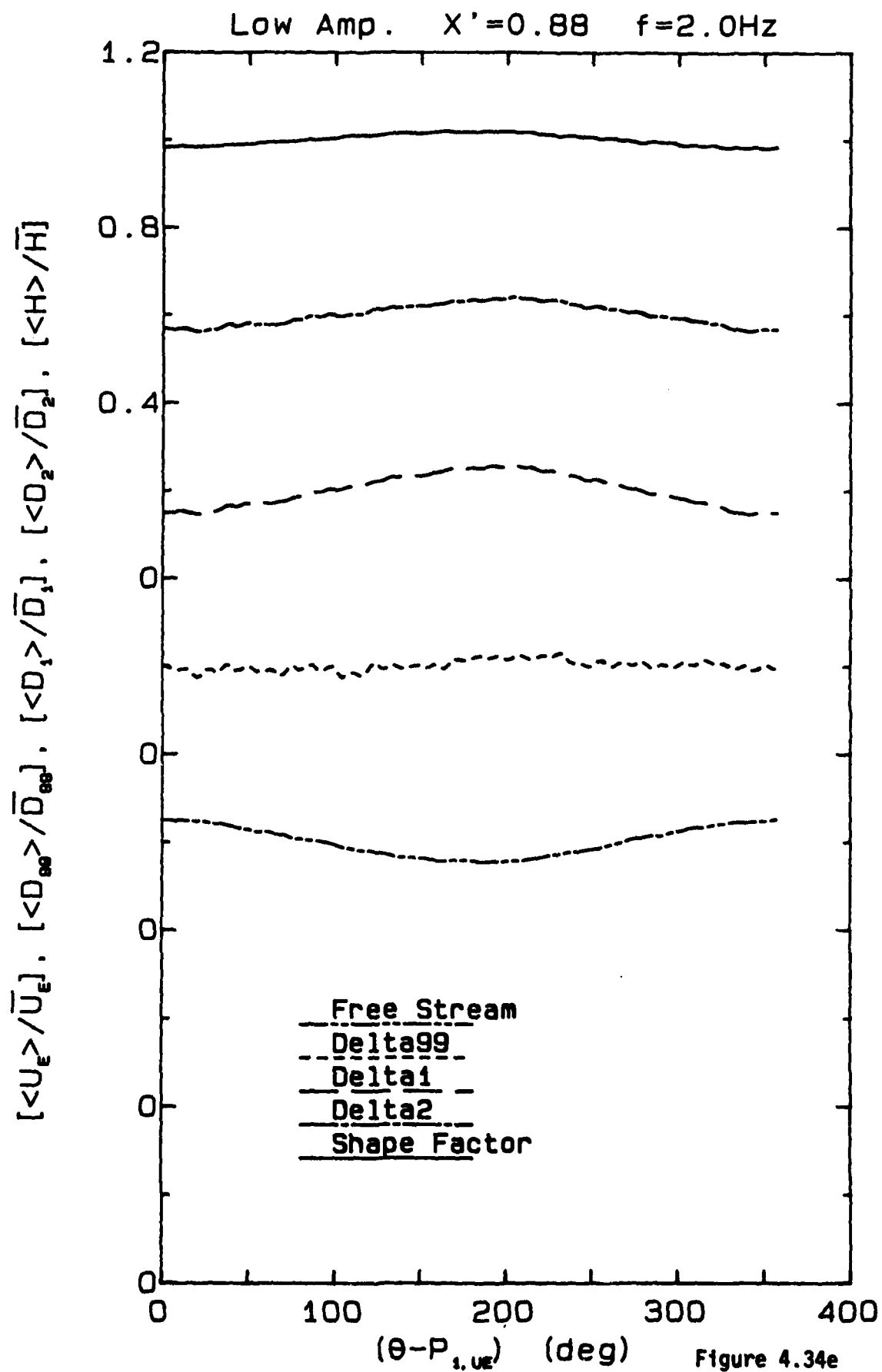


Figure 4.34e

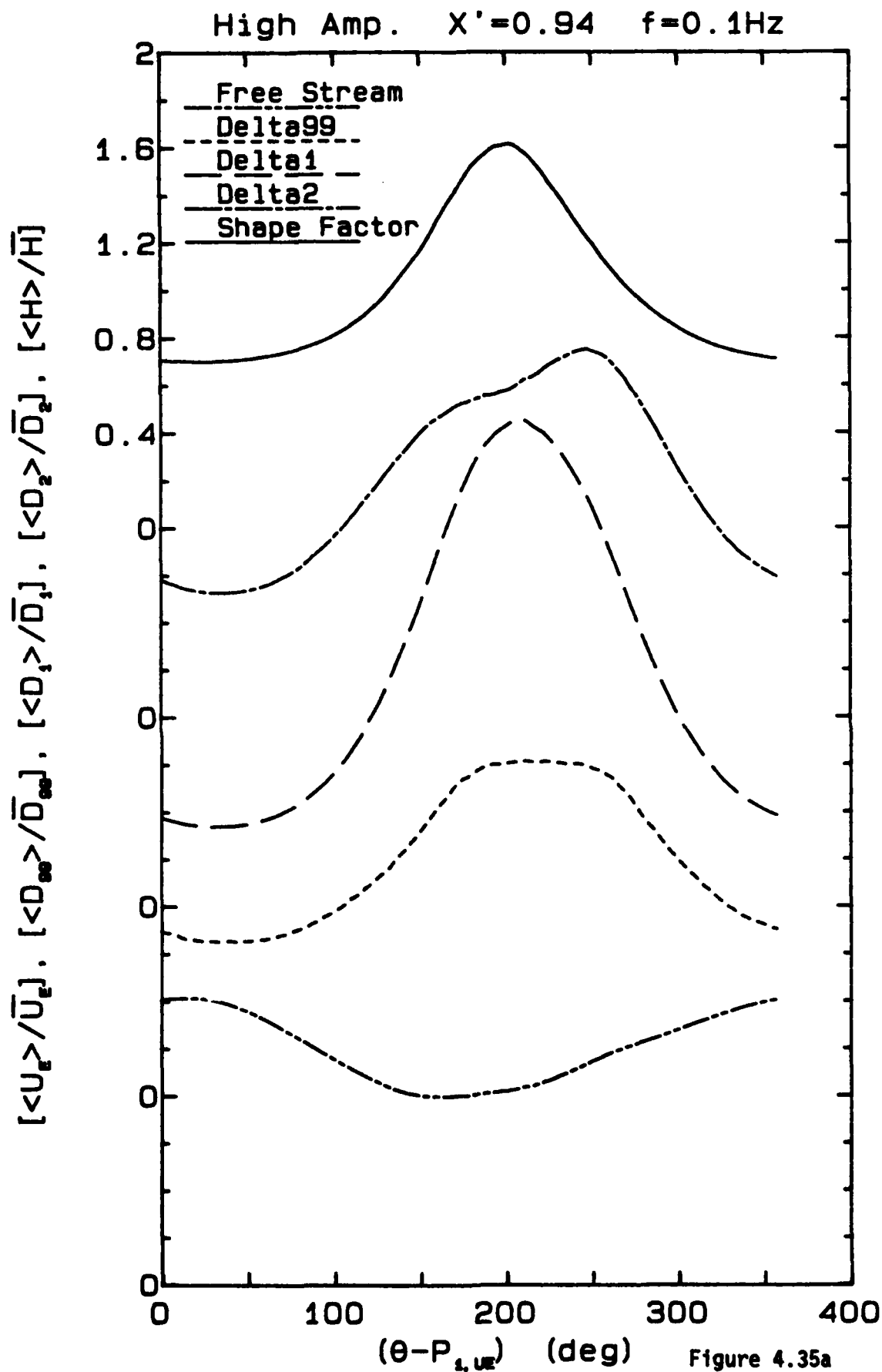


Figure 4.35a

High Amp.  $X'=0.94$   $f=0.2\text{Hz}$

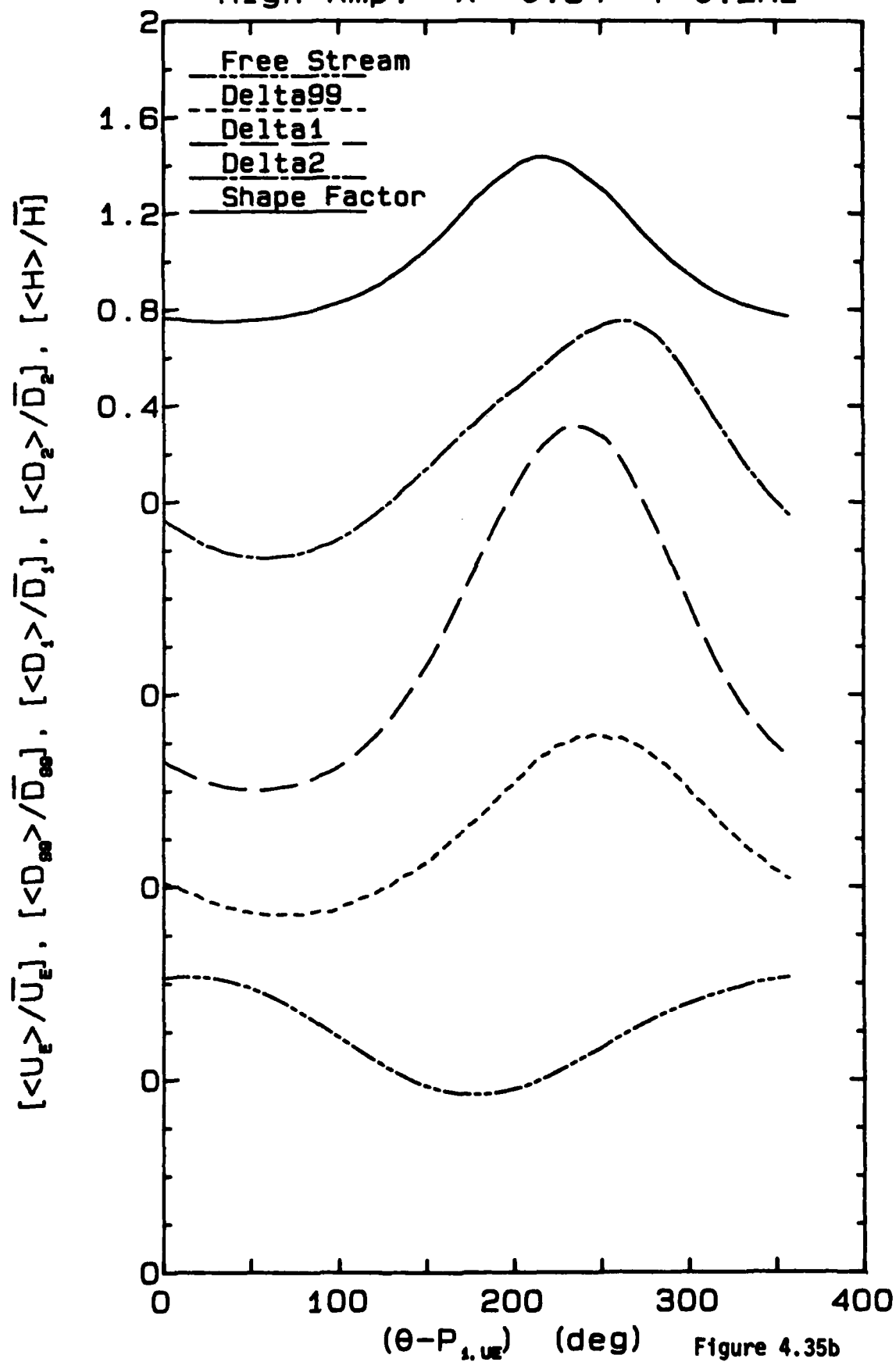


Figure 4.35b

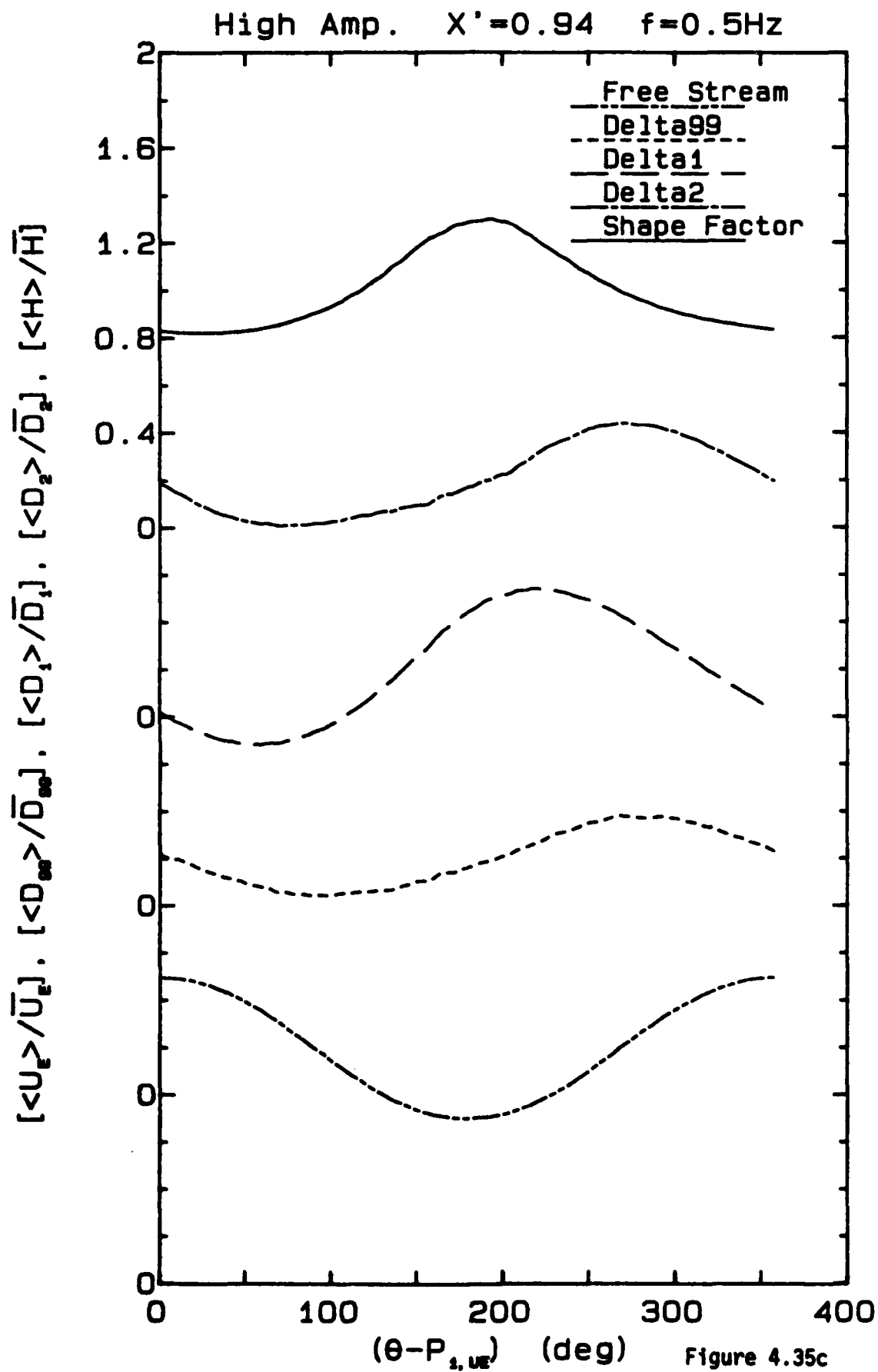
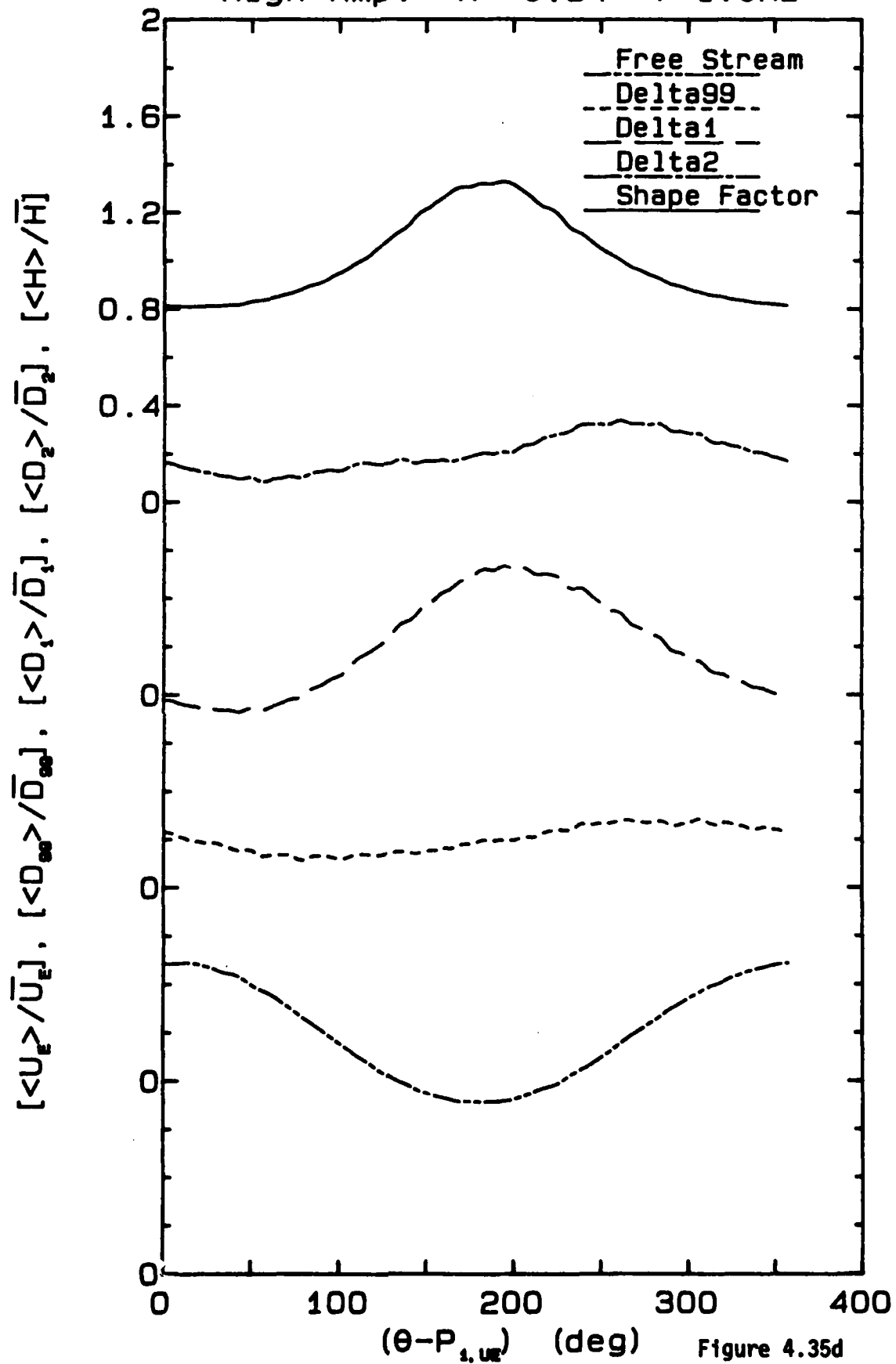


Figure 4.35c

High Amp.  $X' = 0.94$   $f = 1.0\text{Hz}$



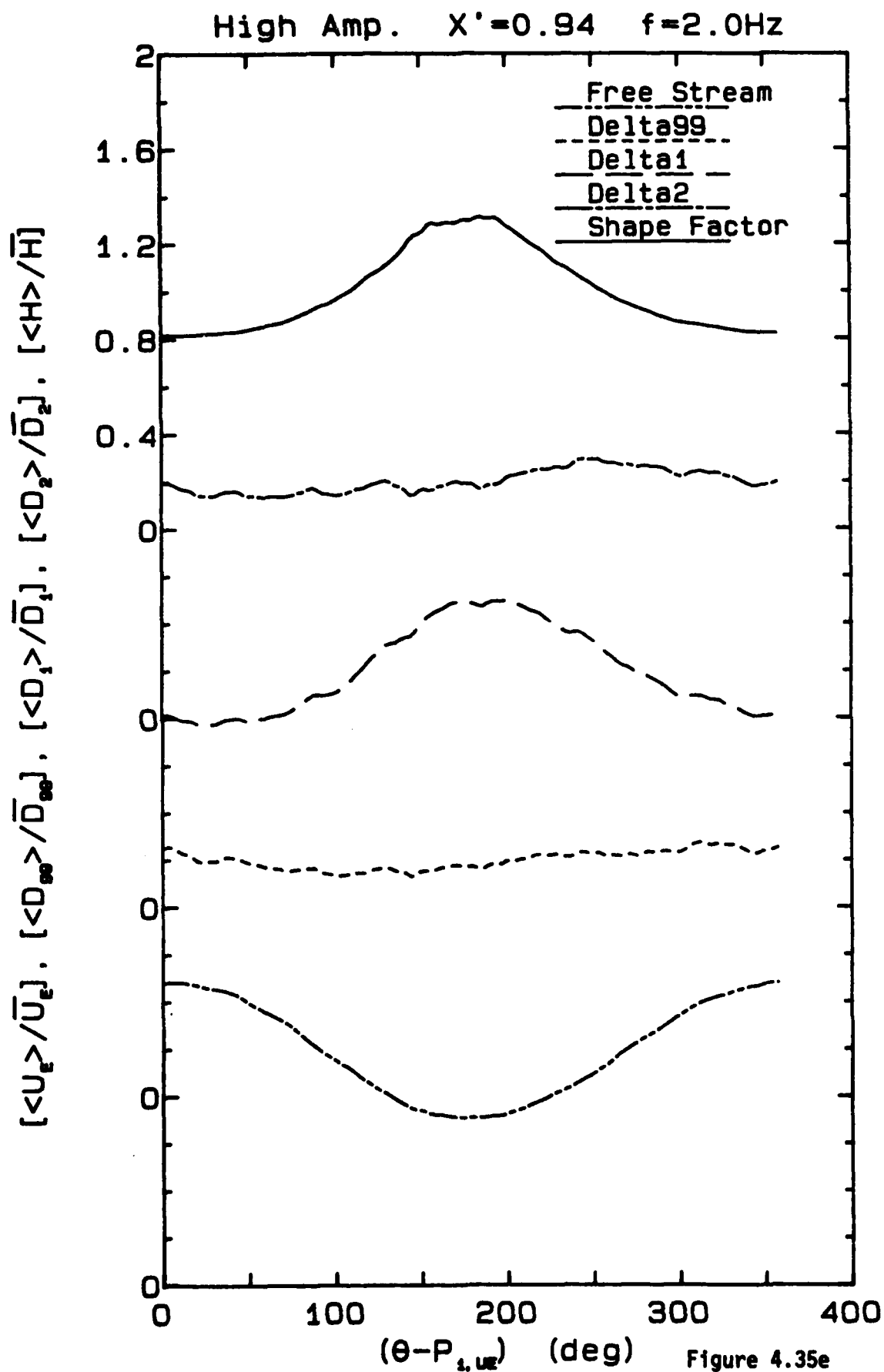


Figure 4.35e

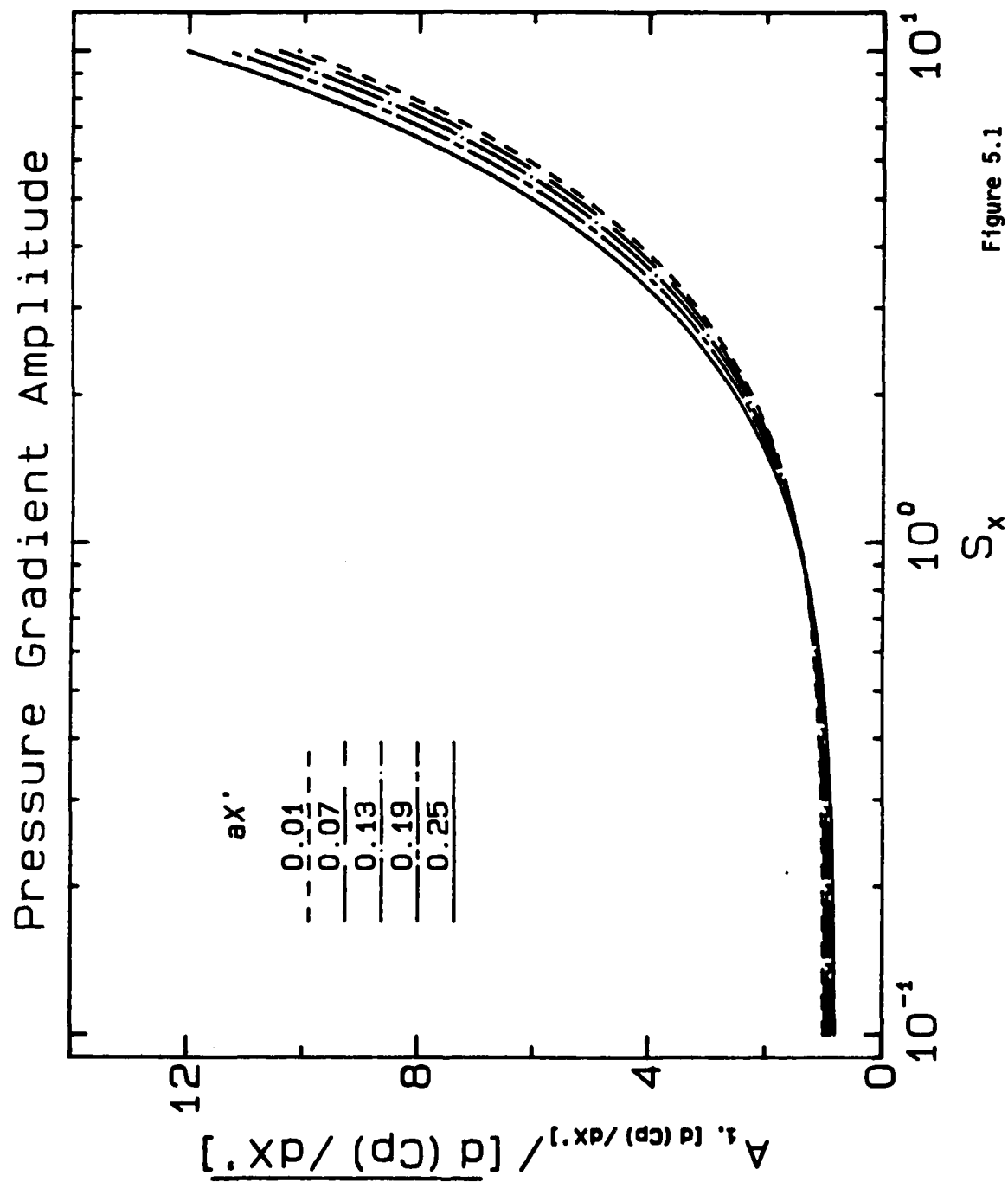


Figure 5.1

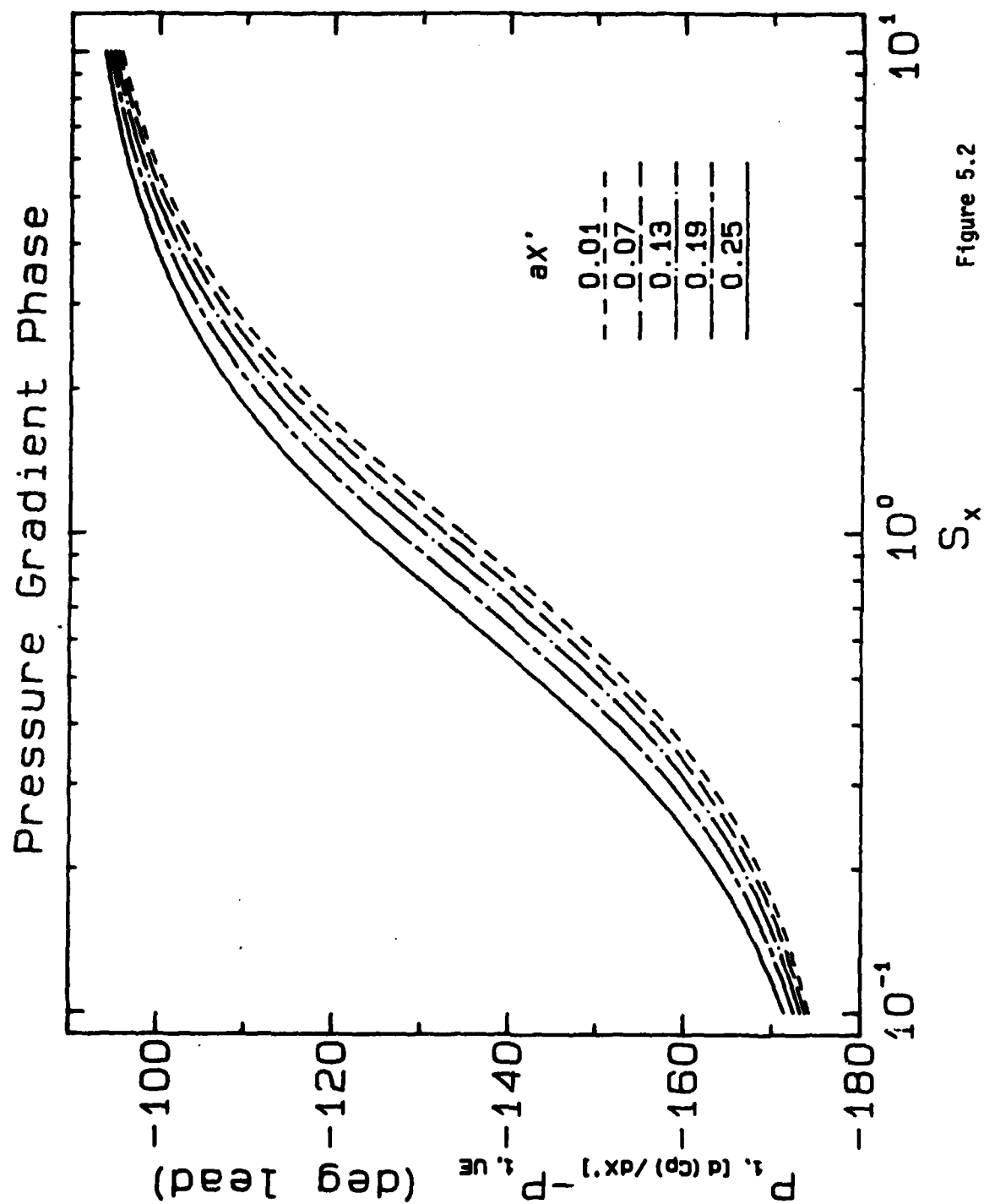


Figure 5.2



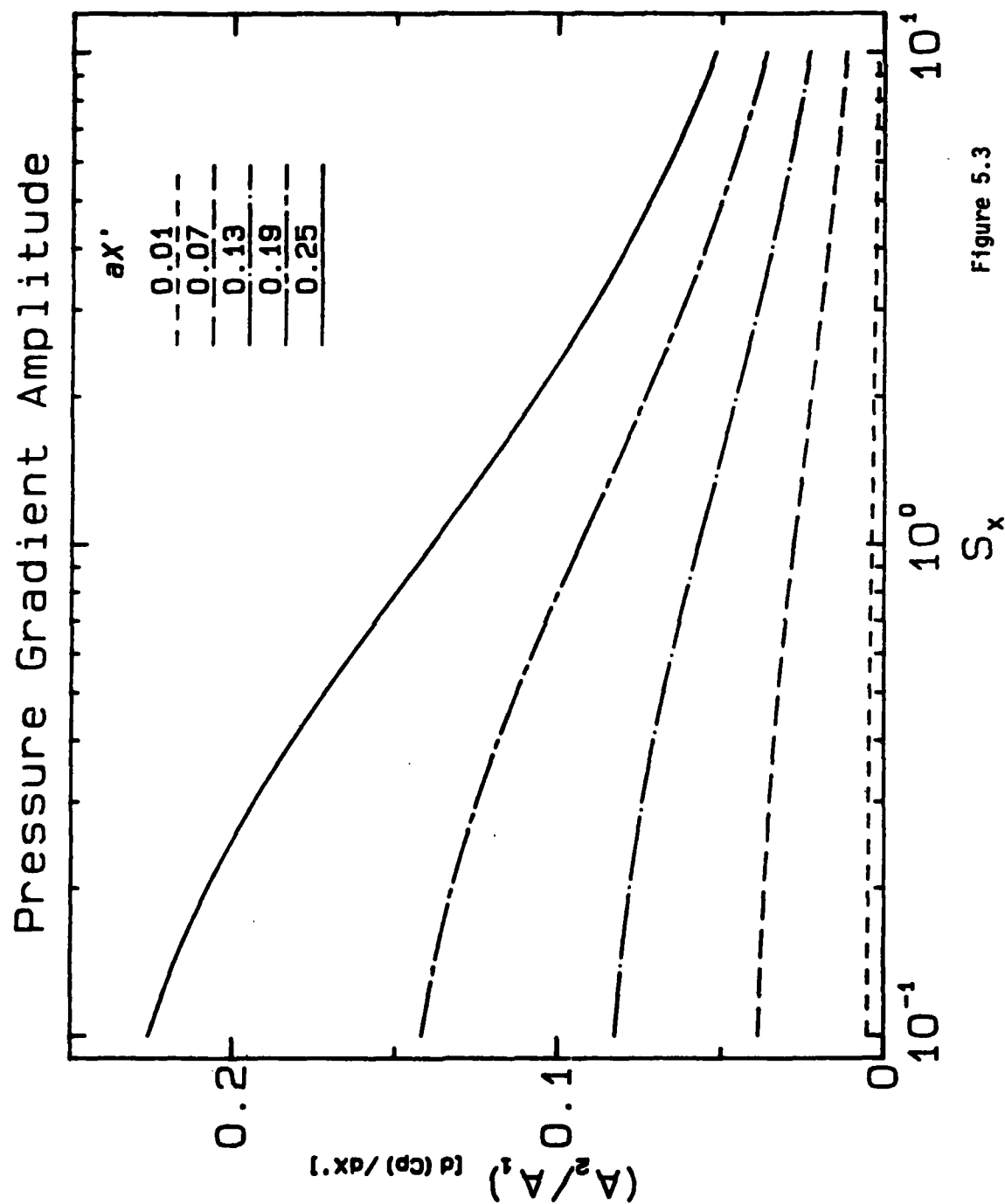


Figure 5.3

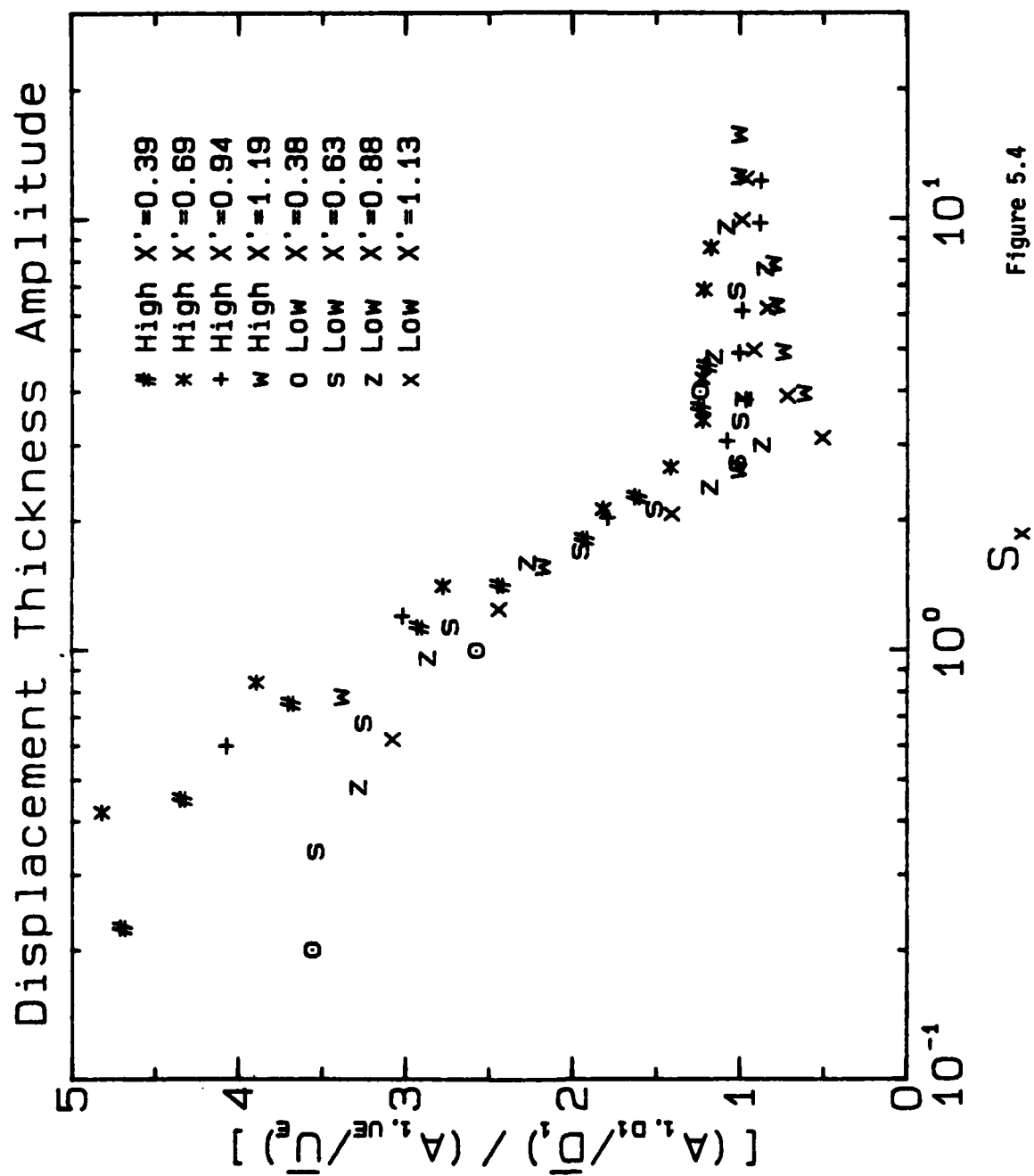


Figure 5.4

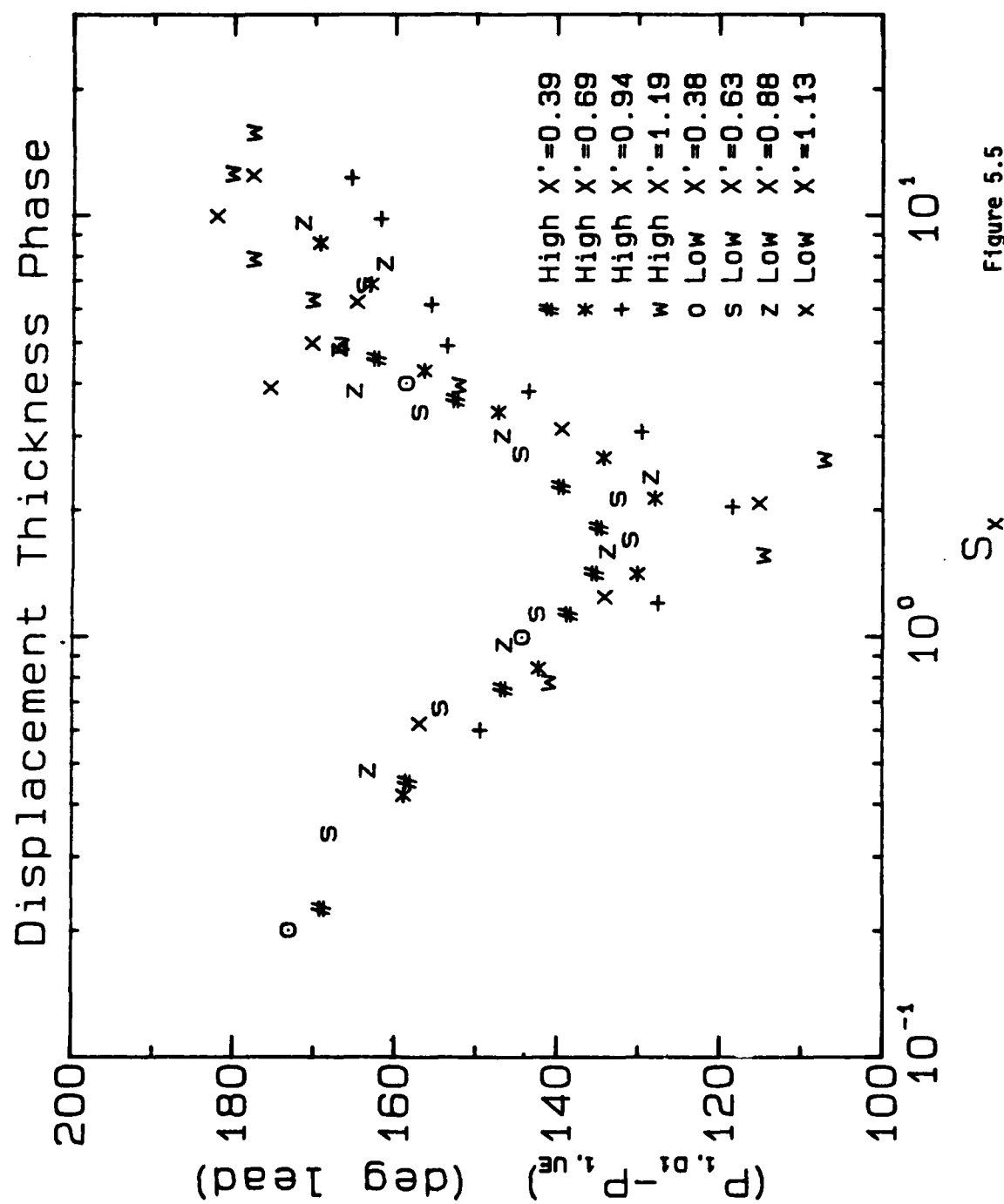


Figure 5.5

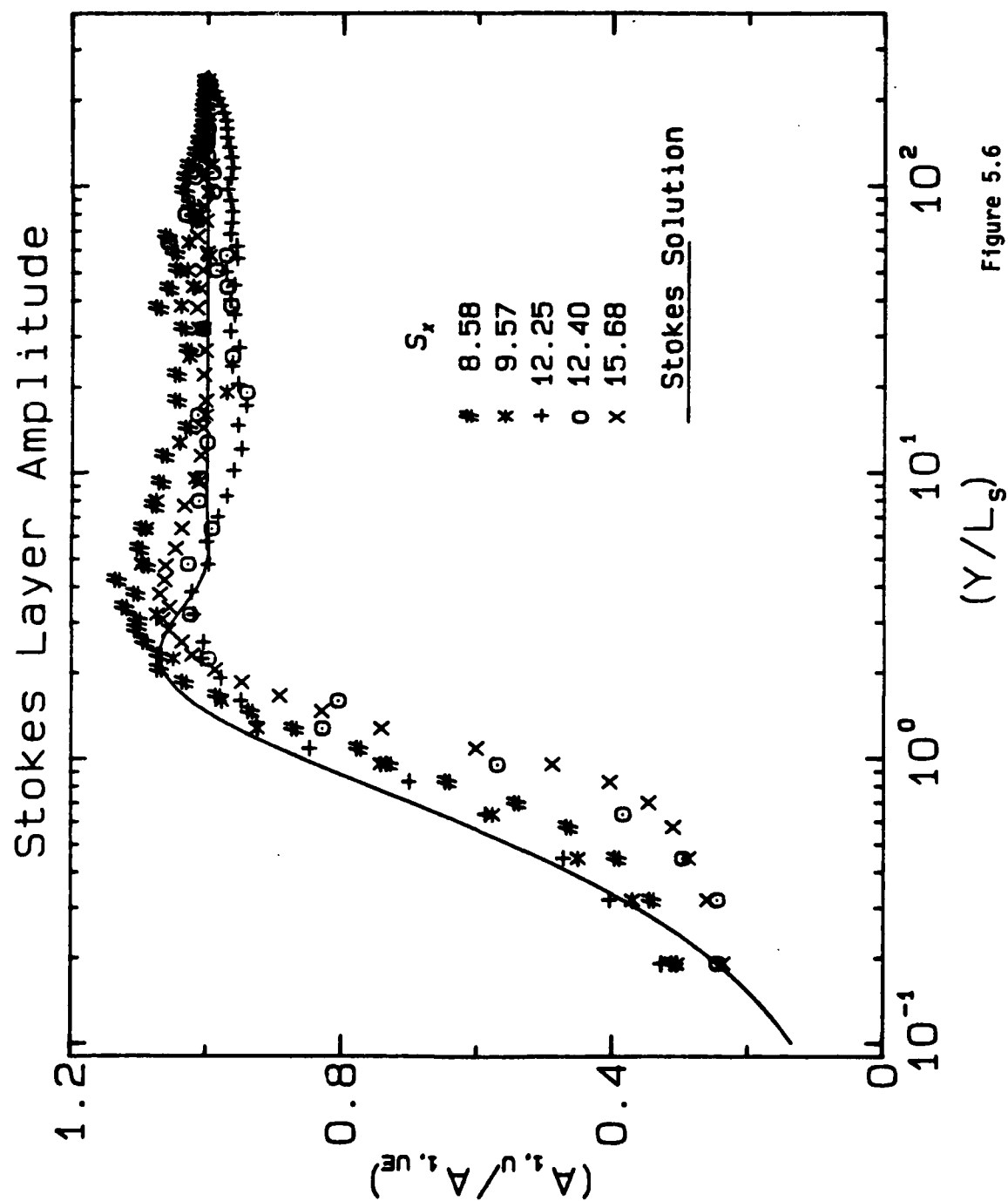


Figure 5.6

AD-A124 365

AN EXPERIMENTAL STUDY OF THE DYNAMICS OF AN UNSTEADY  
TURBULENT BOUNDARY LAYER(U) STANFORD UNIV CA  
THERMOSCIENCES DIV R JAYARAMAN ET AL. DEC 82 TF-18

3/3

UNCLASSIFIED

ARO-16760.2-EG ARO-1-80

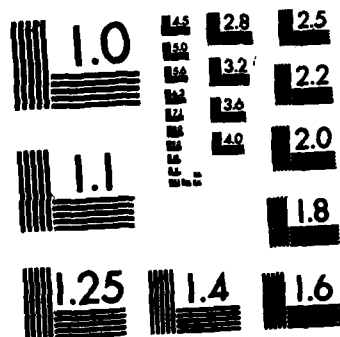
.F/G 20/4

NL

END

FILMED

DTIC



MICROCOPY RESOLUTION TEST CHART  
NATIONAL BUREAU OF STANDARDS-1963-A

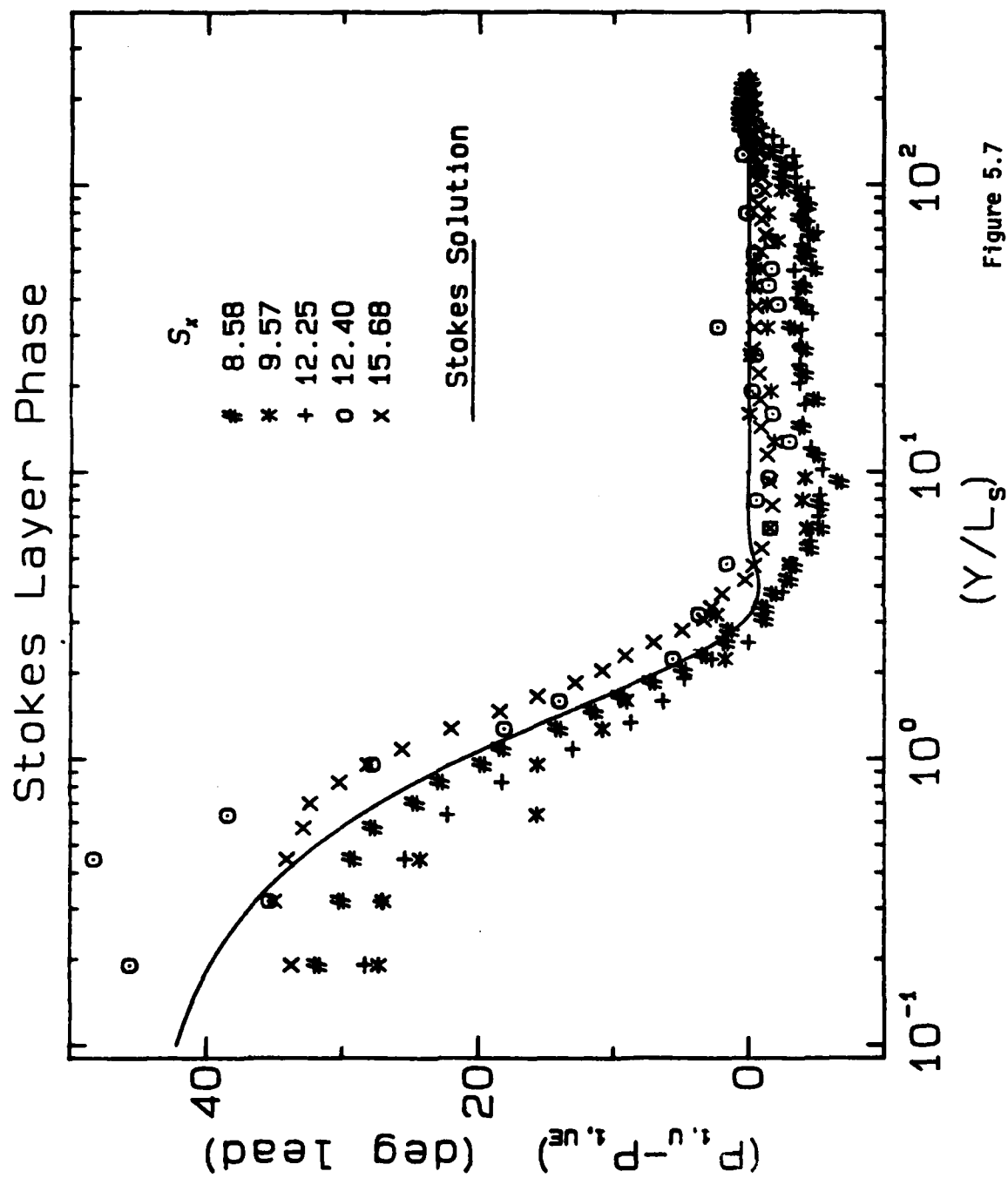


Figure 5.7

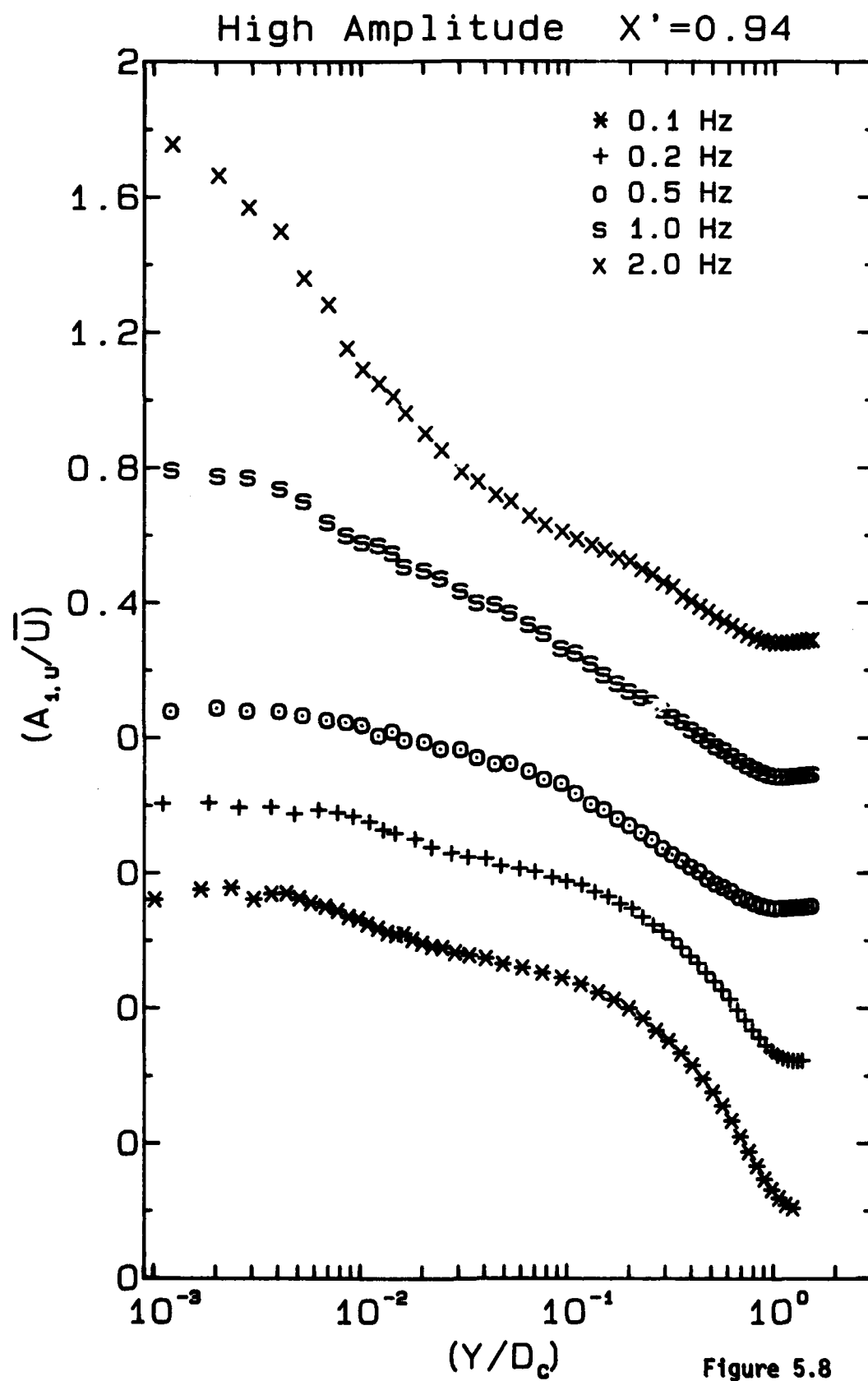


Figure 5.8



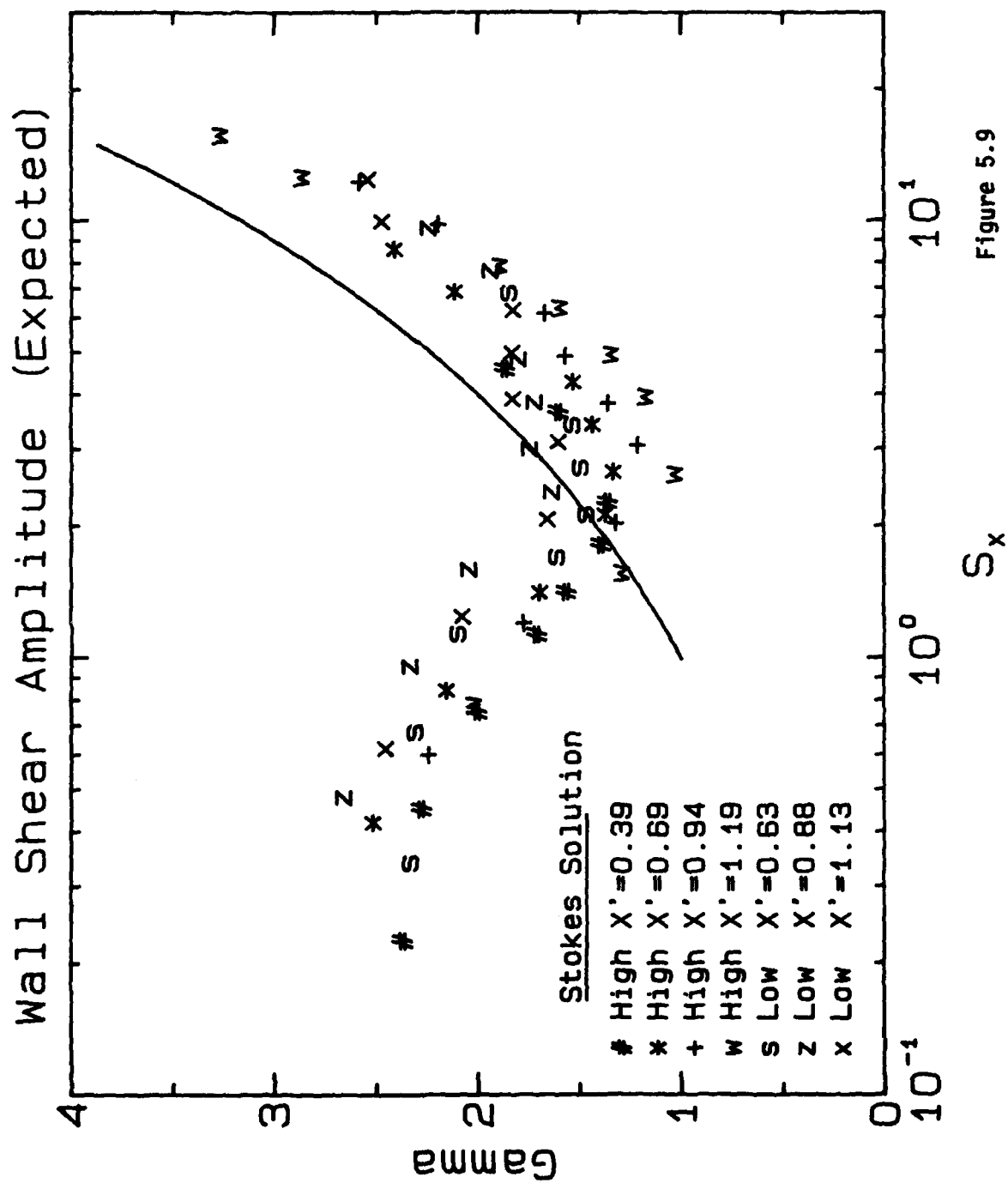
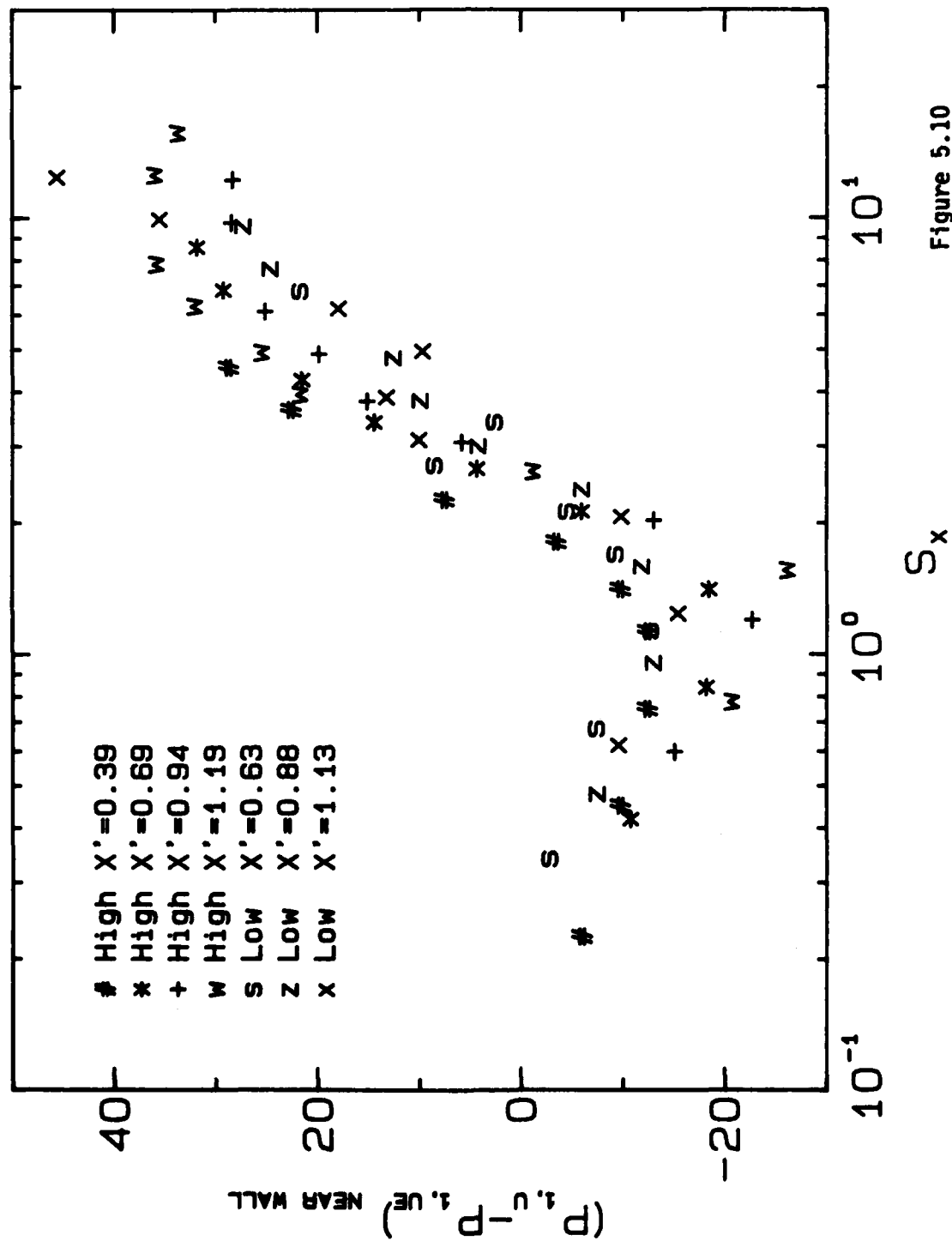


Figure 5.9

# Wall Shear Phase (Expected)



## Appendix A

### CONTENTS OF MICROFICHE REPORT

Detailed results for all the cases studied in the form of plots and tables are presented in Jayaraman, Parikh, and Reynolds [1982] in microfiches. There are 16 microfiches in the report. Their contents are summarized below.

#### A.1 Contents of Microfiche 1

Microfiche 1 contains the boundary layer growth under zero-pressure gradient conditions, the upstream disturbance during unsteady operation, and the imposed free-stream excitation in the test section. Table A.1 shows the data available, whether the data are in the form of tables or plots, and their locations in the microfiche. The number after the decimal point in the locations shown refers to the page number on the microfiche. The correspondence between the headings used in the tables and the present nomenclature is shown in Table A.4.

#### A.2 Contents of Microfiches 2 through 16

Microfiches 2 through 16 contain plots and tables for all the experimental cases studied (see Tables 4.1 and 4.2). Several different types of plots are presented. Table A.2 summarizes what the abscissas and the ordinates are in each plot type and the type of scaling used in the abscissas. Two different types of tables as described in Table A.3 are presented. The nomenclature used in the plots is the same as the present one. The correspondence between the present nomenclature and the headings used in the tables is shown in Table A.4. For convenience, the experimental cases are divided into eight groups, as shown in Table A.5.

Table A.6 shows the locations where plots can be found in the microfiches. Table A.7 presents the locations of the tables. As shown in these tables, there are two parts to the location of a table or a plot. The part before the decimal point refers to the number of the microfiche, and the part after the decimal point shows the page number within the microfiche.

Table A.1  
CONTENTS OF MICROFICHE 1

<u>Table-Plot</u>	<u>Location</u>
<u>Zero-Pressure Gradient Boundary Layer Development</u>	
Free-stream velocity: Table . . . . .	1.01
Mean velocity and turbulence: Tables . . . . .	1.02-1.15
<u>Upstream Disturbance</u>	
Low amplitude, $X' = -1.03$ :	
RMS free-stream disturbance: Table . . . . .	1.16
High amplitude, $X' = -1.03$ :	
RMS free-stream disturbance: Table . . . . .	1.17
High amplitude, $X' = -0.36$ :	
Mean velocity and turbulence: Tables . . . . .	1.18-1.26
<u>Imposed Free-Stream Excitation in Test Section</u>	
Low amplitude:	
Mean and first harmonic results, Tables . . . . .	1.27-1.29
Mean velocity and turbulence, Plots . . . . .	1.30-1.35
First harmonic amplitude and phase, Plots . . . . .	1.36-1.41
Phase-averaged velocity, Plots . . . . .	1.42-1.53
High amplitude:	
Mean and first harmonic results, Tables . . . . .	1.54-1.62
Mean velocity and turbulence, Plots . . . . .	1.63-1.71
First harmonic amplitude and phase, Plots . . . . .	1.72-1.80
Phase-averaged velocity, Plots . . . . .	1.81-1.98

Table A.2  
TYPES OF PLOTS

<u>Type</u>	<u>Ordinate</u>	<u>Abscissas</u>	<u>Abscissa Scaling</u>
1	$U^+$	$Y^+$	Logarithmic
2	$(\overline{U'U'}/\overline{U_E^2}) \times 10^4$	$(Y/D_C)$	Logarithmic
3	$(U/U_E)$	$(Y/D_C)$	Linear
4	$(\overline{U'U'}/\overline{U_E^2}) \times 10^4$	$(Y/D_C)$	Linear
5	$(A_{1,U}/A_{1,UE})$	$(Y/D_C)$	Logarithmic
6	$(P_{1,U} - P_{1,UE})$	$(Y/D_C)$	Linear
7	$(A_{1,U}/A_{1,UE})$	$(Y/D_C)$	Linear
8	$(P_{1,U} - P_{1,UE})$	$(Y/D_C)$	Linear
9	$(A_{1,U'U'}/\overline{U_E^2}) \times 10^4$	$(Y/D_C)$	Logarithmic
10	$(P_{1,U'U'} - P_{1,UE})$	$(Y/D_C)$	Logarithmic
11	$(A_{1U'U'}/\overline{U_E^2}) \times 10^4$	$(Y/D_C)$	Linear
12	$(P_{1,U'U'} - P_{1,UE})$	$(Y/D_C)$	Linear
13	$[\langle U_E \rangle / \overline{U_E}], [\langle D_{99} \rangle / \overline{D_{99}}]$ $[\langle D_1 \rangle / \overline{D_1}], [\langle D_2 \rangle / \overline{D_2}]$ $[\langle H \rangle / H]$	$(\theta - P_{1,UE})$	Linear
14	$\langle U \rangle / \overline{U_E}$	$(Y/D_C)$	Logarithmic
15	$[\langle U'U' \rangle / \overline{U_E^2}] \times 10^4$	$(Y/D_C)$	Logarithmic

Table A.3  
TYPES OF TABLES

<u>Type</u>	<u>Contents</u>
1	Time-averaged results with Coles analysis.
2	First harmonic amplitude and phase of velocity and turbulence.

Table A.4  
NOMENCLATURE USED IN TABLES

<u>Table Entry</u>	<u>Present Nomenclature</u>
A1	$A_{1,u}$
A1e	$A_{1,u_e}$
A1es	$A_{1,u_e}^2$
A1'	$A_{1,u'u'}$
CF	$C_f$
DELTA	$\delta$
DELTA1	$\delta_1$
DELTA2	$\delta_2$
P1	$\phi_{1,u}$
P1e	$\phi_{1,u_e}$
P1L	$P_L$
P1'	$\phi_{1,u'u'}$
REDEL1	$\bar{U}_e \delta_1 / \nu$
REDEL2	$\bar{U}_e \delta_2 / \nu$
Udef	$U_e^+ - U^+$
Umean	$\bar{U}$
Ue	$\bar{U}_e$
Uo	$U_o$
Uos	$U_o^2$
U+	$U^+$
U'ms	$\overline{u'u'}$
Ues	$\bar{U}_e^2$
UTAU	$u_\tau$
Utr	$\bar{u}_{rms}$
Y+	$\gamma^+$

**Table A.5**

**IDENTIFICATION OF GROUPS OF EXPERIMENTAL CASES**

<u>Experiment</u>	<u>X'</u>	<u>Group ID</u>
Low Amplitude	0.38	1
	0.63	2
	0.88	3
	1.13	4
High Amplitude	0.39	5
	0.69	6
	0.94	7
	1.19	8



Table A.6  
PLOT LOCATIONS

Plot Type	Group ID							
	1	2	3	4	5	6	7	8
1	2.01 - 2.03	3.01 - 3.08	5.01 - 5.09	7.01 - 7.09	9.01 - 9.09	11.01 - 11.09	13.01 - 13.09	15.01 - 15.10
2	2.01 - 2.03	3.01 - 3.08	5.01 - 5.09	7.01 - 7.09	9.01 - 9.09	11.01 - 11.09	13.01 - 13.09	15.01 - 15.10
3	2.04 - 2.06	3.09 - 3.16	5.10 - 5.18	7.10 - 7.18	9.10 - 9.18	11.10 - 11.18	13.10 - 13.18	15.11 - 15.20
4	2.04 - 2.06	3.09 - 3.16	5.10 - 5.18	7.10 - 7.18	9.10 - 9.18	11.10 - 11.18	13.10 - 13.18	15.11 - 15.20
5	2.07 - 2.09	3.17 - 3.24	5.19 - 5.27	7.19 - 7.27	9.19 - 9.27	11.19 - 11.27	13.19 - 13.27	15.21 - 15.30
6	2.07 - 2.09	3.17 - 3.24	5.19 - 5.27	7.19 - 7.27	9.19 - 9.27	11.19 - 11.27	13.19 - 13.27	15.21 - 15.30
7	2.10 - 2.12	3.25 - 3.32	5.28 - 5.36	7.28 - 7.36	9.28 - 9.36	11.28 - 11.36	13.28 - 13.36	15.31 - 15.40
8	2.13 - 2.15	3.33 - 3.40	5.37 - 5.45	7.37 - 7.45	9.37 - 9.45	11.37 - 11.45	13.37 - 13.45	15.41 - 15.50
9	2.16 - 2.18	3.41 - 3.48	5.46 - 5.54	7.46 - 7.54	9.46 - 9.54	11.46 - 11.54	13.46 - 13.54	15.51 - 15.60
10	2.16 - 2.18	3.41 - 3.48	5.46 - 5.54	7.46 - 7.54	9.46 - 9.54	11.46 - 11.54	13.46 - 13.54	15.51 - 15.60
11	2.19 - 2.21	3.49 - 3.56	5.55 - 5.63	7.55 - 7.63	9.55 - 9.63	11.55 - 11.63	13.55 - 13.63	15.61 - 15.70
12	2.22 - 2.24	3.57 - 3.64	5.64 - 5.72	7.64 - 7.72	9.64 - 9.72	11.64 - 11.72	13.64 - 13.72	15.71 - 15.80
13	2.25 - 2.27	3.65 - 3.72	5.73 - 5.81	7.73 - 7.81	9.73 - 9.81	11.73 - 11.81	13.73 - 13.81	15.81 - 15.90
14	2.28 - 2.33	4.01 - 4.16	6.01 - 6.18	8.01 - 8.18	10.01 - 10.18	12.01 - 12.18	14.01 - 14.18	16.01 - 16.20
15	2.34 - 2.45	4.17 - 4.48	6.19 - 6.54	8.19 - 8.54	10.19 - 10.54	12.19 - 12.54	14.19 - 14.54	16.21 - 16.60

Note: Location 9.46 refers to Page 46 in Microfiche No. 9

Table A.7

TABLE LOCATIONS

Table Type	Group ID							
	1	2	3	4	5	6	7	8
1	2.46 - 2.48	4.49 - 4.56	6.55 - 6.63	8.55 - 8.63	10.55 - 10.63	12.55 - 12.63	14.55 - 14.63	16.61 - 16.70
2	2.49 - 2.51	4.57 - 4.64	6.64 - 6.72	8.64 - 8.72	10.64 - 10.72	12.64 - 12.72	14.64 - 14.72	16.71 - 16.80

Note: Location 9.46 refers to Page 46 in Microfiche No. 9

## Appendix B

### EFFECTS OF PROBE/WALL RELATIVE VIBRATIONS

Significant errors in the near-wall unsteady measurements could result from periodic variation at the exciting frequency of the probe location with respect to the wall. The following is a simple analysis of the effects of such variation on the measured near-wall velocity.

Let

$$u(y,t) = \bar{U}(y) + A_{1,u}(y) e^{j[\omega t + \phi_{1,u}(y)]} + u'(y,t)$$

and

$$y_p(t) = \bar{y}_p + A_{1,y_p} e^{j(\omega t + \phi_{1,y_p})}$$

where  $y_p$  is the instantaneous location of the probe with respect to the wall. Assuming that the amplitude of the variation in the probe location is small and neglecting higher harmonics, it can be shown that

$$\bar{U}_m(y) = \bar{U}(\bar{y}_p)$$

and

$$\tilde{u}_m = A_{1,u}(\bar{y}_p) e^{j[\omega t + \phi_{1,u}(\bar{y}_p)]} + \left(\frac{\partial \bar{U}}{\partial y}\right)_{y_p} A_{1,y_p} e^{j(\omega t + \phi_{1,y_p})}$$

where

$$u_m(t) = u(y_p, t)$$

Clearly, the measured mean velocity is unaffected by the periodic variation in the probe location with respect to the wall. The relative error in the measured periodic velocity is higher for locations closer to the wall. To get an estimate of these errors, assume that

$$A_{1,u}(y) = \frac{A_{1,\tau_w}}{\mu} y$$

Further, for unseparated boundary layers,  $(\partial \bar{U} / \partial y)$  is a maximum at the wall. Thus, for a worst-case estimate,

$$\tilde{u}_m = \frac{A_{1,\tau_w}}{\mu} \bar{y}_p e^{j[\omega t + \phi_{1,u}(\bar{y}_p)]} + \frac{\bar{\tau}_w}{\mu} A_{1,y_p} e^{j(\omega t + \phi_{1,y_p})}$$

The maximum relative error in amplitude is

$$E_A = \frac{\bar{\tau}_w}{A_{1,\tau_w}} \frac{A_{1,y_p}}{\bar{y}_p}$$

and it corresponds to no error in the phase angle.

The maximum error in the phase angle is

$$E_p = 2 \sin^{-1} \left( \frac{1}{2} E_A \right)$$

and it corresponds to no error in the amplitude.

For a given amplitude of probe-location variation, clearly the errors are smaller for adverse pressure gradient boundary layers (small  $\bar{\tau}_w$ ) subjected to high-amplitude, high-frequency (large  $A_{1,\tau_w}$ ) excitations. In the present work, one should expect the amplitude of the variation of the probe location with respect to the wall to be larger in the high-amplitude, high-frequency cases, since the amplitude of the oscillations in pressure is larger for such cases.

Recall the LDA probe-volume positioning procedures described in Section 3.3.1. This positioning is done under steady operating conditions and is accurately repeatable to 0.025 mm. Observation of the shadow of the needle and the bright streaks of laser light on either side of it, during unsteady operation of the rig, showed no visible movement of the beams with respect to the needle. Since the positioning repeatability is about 0.025 mm, it can be concluded that any movement of the beams with respect to the needle during unsteady operation was less than 0.025 mm.

The results for the amplitude and the phase of the periodic velocity presented in Chapter 4 show no anomalous behavior near the wall. The low-frequency results show that the velocity phase in the near-wall

region is nearly a constant, as it would be if the steady form of the law of the wall is applicable to the phase-averaged velocity profiles. The results for the high-frequency cases are in essential agreement with the expected Stokes solution, as shown in Chapter 5.

Thus, the present experimental data show no evidence of significant periodic variation in the LDA measuring volume location with respect to the wall.